ELECTROCHEMISTRY EDITOR'S PICK 2021

EDITED BY: Nosang Vincent Myung
PUBLISHED IN: Frontiers in Chemistry

frontiers Research Topics

ISSN 1664-8714
ISBN 978-2-88966-884-7
DOI 10.3389/978-2-88966-884-7

About Frontiers

Frontiers is more than just an open-access publisher of scholarly articles: it is a pioneering approach to the world of academia, radically improving the way scholarly research is managed. The grand vision of Frontiers is a world where all people have an equal opportunity to seek, share and generate knowledge. Frontiers provides immediate and permanent online open access to all its publications, but this alone is not enough to realize our grand goals.

Frontiers Journal Series

The Frontiers Journal Series is a multi-tier and interdisciplinary set of open-access, online journals, promising a paradigm shift from the current review, selection and dissemination processes in academic publishing. All Frontiers journals are driven by researchers for researchers; therefore, they constitute a service to the scholarly community. At the same time, the Frontiers Journal Series operates on a revolutionary invention, the tiered publishing system, initially addressing specific communities of scholars, and gradually climbing up to broader public understanding, thus serving the interests of the lay society, too.

Dedication to Quality

Each Frontiers article is a landmark of the highest quality, thanks to genuinely collaborative interactions between authors and review editors, who include some of the world's best academicians. Research must be certified by peers before entering a stream of knowledge that may eventually reach the public - and shape society; therefore, Frontiers only applies the most rigorous and unbiased reviews.
Frontiers revolutionizes research publishing by freely delivering the most outstanding research, evaluated with no bias from both the academic and social point of view. By applying the most advanced information technologies, Frontiers is catapulting scholarly publishing into a new generation.

What are Frontiers Research Topics?

Frontiers Research Topics are very popular trademarks of the Frontiers Journals Series: they are collections of at least ten articles, all centered on a particular subject. With their unique mix of varied contributions from Original Research to Review Articles, Frontiers Research Topics unify the most influential researchers, the latest key findings and historical advances in a hot research area! Find out more on how to host your own Frontiers Research Topic or contribute to one as an author by contacting the Frontiers Editorial Office: frontiersin.org/about/contact

ELECTROCHEMISTRY EDITOR'S PICK 2021

Topic Editor:
Nosang Vincent Myung, University of Notre Dame, United States

Citation: Myung, N. V., ed. (2021). Electrochemistry Editor's Pick 2021. Lausanne: Frontiers Media SA. doi: 10.3389/978-2-88966-884-7

Table of Contents

frontiers in Chemistry

ORIGINAL RESEARCH
published: 25 February 2019
doi: 10.3389/fchem.2019.00089

Development of Electrochemical Nanosensor for the Detection of Malaria Parasite in Clinical Samples

Olaoluwa R. Obisesan[1,2], Abolanle S. Adekunle[1], John A. O. Oyekunle[1], Thomas Sabu[2], Thabo T. I. Nkambule[3] and Bhekie B. Mamba[3]*

[1] Department of Chemistry, Obafemi Awolowo University, Ile-Ife, Nigeria, [2] International and Inter University Center for Nanoscience and Nanotechnology, Mahatma Gandhi University, Kottayam, India, [3] Nanotechnology and Water Sustainability Research Unit, College of Science, Engineering and Technology, Univeristy of South Africa, Johannesburg, South Africa

In this study, electrochemical nanosensors were developed from the synthesized metal oxide (MO) nanoparticles by supporting it on a gold electrode (Au). The activity of the developed nanosensor toward the detection of malaria biomarker (β-hematin) was determined and the optimum conditions at which the maximum detection and quantification occurred were established. β-Hematin current response at the sensors was higher when compared with the bare Au electrode and followed the order Au-CuO (C) > Au-CuO (M) > Au-Fe_2O3 (M) > Au-Fe_2O3 (C) > Au-Al_2O3 (M) > Au-Al_2O3 (C) > bare Au. The developed sensors were stable with a relatively low current drop (10.61–17.35 %) in the analyte. Au-CuO sensor had the best performance toward the biomarker and quantitatively detected *P. berghei* in infected mice's serum samples at 3.60–4.8 mM and *P. falciparum* in human blood serum samples at 0.65–1.35 mM concentration.

Keywords: β-hematin, metal oxide nanoparticles, sensor, cyclic voltammetry, square wave voltammetry, malaria, clinical samples, biomarker

OPEN ACCESS

Edited by:
Elizabeth J. Podlaha, Clarkson University, United States

Reviewed by:
Edgar D. Goluch, Northeastern University, United States
Jiahua Zhu, University of Akron, United States

***Correspondence:**
Abolanle S. Adekunle
sadekpreto@gmail.com

Specialty section:
This article was submitted to Electrochemistry, a section of the journal Frontiers in Chemistry

Received: *20 October 2018*
Accepted: *04 February 2019*
Published: *25 February 2019*

Citation:
Obisesan OR, Adekunle AS, Oyekunle JAO, Sabu T, Nkambule TTI and Mamba BB (2019) Development of Electrochemical Nanosensor for the Detection of Malaria Parasite in Clinical Samples. Front. Chem. 7:89. doi: 10.3389/fchem.2019.00089

INTRODUCTION

Medical diagnosis and biological monitoring of diseases in the clinical laboratory are important because they're useful in detecting various diseases or onset of several diseases. The use of markers (biomarkers) has been the main cornerstone in the identification and quantification of target metabolites in biological fluids (blood, urine, and saliva) (Gil and Pla, 2001; Angerer et al., 2006). Detection of most diseases using sophisticated techniques mainly involves expensive and time-consuming processes. Development of sensitive, selective, accurate, rapid as well as affordable techniques for clinical diagnosis has been a major focus of researchers recently. Electrochemical sensors using nanoparticles have emerged as one of the suitable technologies for the detection of analytes of interest in clinical chemistry due to their high sensitivity and selectivity, rapid response time, and low cost (Wang, 1994).

Malaria is an intricate, infectious, hematologic disease instigated by a protozoan parasite named *Plasmodium falciparum* (Priyamvada et al., 2014). The parasite spends part of its life in humans and part in Anopheles mosquitoes. Malaria is transmitted to humans through infected Anopheles mosquitos. Although there are more than 50 species of *Plasmodium*, only four species, *P. falciparum, P. vivax, P. malariae,* and *P. ovale,* are known to cause malaria in humans (Priyamvada et al., 2014). The malaria parasite depends on iron for growth because many enzymes of the parasite metabolic pathways depend on iron (Weinberg and Moon, 2009). Malaria clinical symptoms occur during the intra-erythrocytic stage. At this stage, *P. falciparum* degrades more than 80% of

hemoglobin present in the food vacuoles to serve as a source of amino acids (Goyal et al., 2012). To illustrate this phenomenon, in an average patient with 750 g of healthy hemoglobin and a 20% parasitemia, as much as 100 g of hemoglobin can be degraded during this cycle (Ziegler et al., 2001). This hemoglobin degradation results in the release of free heme or iron protoporphyrin IX (FePPIX) along with oxygen. Since this free heme is toxic to the parasite, *P. falciparum* converts the reactive heme species into a compact, highly insoluble, weakly magnetic crystal known as hemozoin with decreased pro-oxidant capacity which is nontoxic to the parasite (Oliveira et al., 2005).

Hemozoin, also known as malaria pigment, is a visible marker chemically and structurally similar to a distinctive hematin pigment, called beta-hematin (Fitch and Kanjananggulpan, 1987). Beta-hematin has been extensively explored for the synthesis of antimalaria drugs and can also serve as a biomarker for the diagnosis of malaria. It is a microcrystalline cyclic dimer of ferriprotoporphyrin IX (Fe(III)PPIX) in which the propionate side chain of one protoporphyrin coordinates to the iron(III) center of the other. The dimers use hydrogen to bond with their neighbors via propionic acid group, forming extended chains through the macroscopic crystal (Pagola et al., 2000). Considerable studies have been done on using β-hematin as a biomarker in antimalarial drug synthesis in order to inhibit the formation of hemozoins in the host system (Kumar et al., 2007; Thomas et al., 2012), as a biomarker for diagnosis in a magnetic field-enriched surface (Yuen and Liu, 2012), and as a detection assay for malaria diagnosis (Rebelo et al., 2013). With so many studies on β-hematin, however, there is a paucity of data on electrochemical detection of β-hematin as a target toward malaria diagnosis.

The motivation for this study is based on providing a long-term solution to the challenges faced by physicians and patients with malaria diagnosis. This study, therefore, focused on the development and affirmation of an electrochemical sensor that integrates metal oxide nanoparticles as electroactive species for the diagnosis of malaria parasite with the use of a biomarker (β-hematin) as the identification medium.

METHODS

Materials and Reagents

Materials used include magnetic stirrer, microwave, sonicator, PG-581 biologic potentiostat, 3 mm diameter gold electrode (working electrode) from CHI Instruments, USA, silver/silver chloride reference electrode (in saturated KCl, 3.0 M) and platinum counter electrode from (Bio-Logic Science Instruments, France).

All reagents and solvents used in this study were of analytical grades. They include ethanol (C_2H_5OH), copper chloride ($CuCl_2$), copper acetate ($Cu(CH_3COO)_2$, ethylene glycol ($C_2H_6O_2$), urea ($CO(NH_2)_2$, aluminum nitrate nonahydrate ($Al(NO_3)_3{\cdot}9H_2O$), iron (II) chloride tetrahydrate ($FeCl_2.4H_2O$), ferriprotoporphyrin IX chloride (Hemin Chloride [Cl-Fe(III)PPIX]), ammonia (NH_3), sodium hydroxide (NaOH), acetic acid (CH_3COOH), hydrochloric acid (HCl), potassium phosphate dibasic (K_2HPO_4), potassium phosphate monobasic (KH_2PO_4), potassium ferrocyanide trihydrate ($K_4[Fe(CN)_6].3H_2O$), potassium hexacyanoferrate ($K_3[Fe(CN)_6]$).

Synthesis and Characterization of Metal Oxide Nanoparticles

Chemical Synthesis of Copper Oxide (CuO) Nanoparticles

Copper oxide nanoparticles were synthesized using the method described by Manimaran et al. (2014). One hundred milliliters of deionised water along with 1 g of NaOH pellets were added to 0.51 g of copper chloride ($CuCl_2$) in a 500 mL beaker. The mixture was heated with a magnetic stirrer for 1 h during which the color of the solution changed from blue to black. After the reaction, the mixture was cooled to room temperature. The chemical reaction can be represented as:

$$CuCl_2 + 2NaOH \longrightarrow Cu(OH)_2 + 2NaCl \quad (1)$$

$$Cu(OH)_2 \xrightarrow{\text{Calcination}} CuO + H_2O \quad (2)$$

The pH value of the so formed CuO wet precipitate was neutralized by adding droplets of hydrochloric acid. Then the CuO wet precipitate was washed with deionised water to remove the impurity ions present in the solution and calcined at 300°C for 2 h. The solid is represented as CuO (C) where "C" represents chemical synthesis.

Microwave Synthesis of Copper Oxide (CuO) Nanoparticles

Copper acetate ($Cu(CH_3COO)_2$ and urea ($CO(NH_2))_2$ were taken as a solute in the ratio 1:3 (1 g of copper acetate and 3 g of urea) and dissolved in 100 mL ethylene glycol. The prepared solution was kept in a domestic microwave oven (operated at frequency 2.45 GHz and power 800 W). Microwave irradiation was carried out till the solvent was evaporated completely. Acetone washing was used to remove the organic impurities from the black colloidal precipitate that was obtained. The sample obtained was dried in atmospheric air and annealed for 30 min at 100°C to improve the ordering (Rejith and Krishnan, 2012). The black product is represented as CuO (M) where "M" represents microwave synthesis.

Chemical Synthesis of Aluminum Oxide (Al_2O_3) Nanoparticles

Aluminum nitrate nonahydrate ($Al(NO_3)_3{\cdot}9H_2O$) was used as a precursor for the synthesis of aluminum oxide (Al_2O_3) nanoparticles. $Al(NO_3)_3{\cdot}9H_2O$ (9.38 g, 0.025 mol) was dissolved in 50 mL of distilled water to obtain a 0.5 M solution. The precursor solution obtained (8 mL) was added to a 100 mL conical flask containing a mixed solution of 50 mL distilled water, 3.5 mL NaOH (5 M), and then blended well by stirring for 15 min. Subsequently, the mixed solution was left for 5 days at room temperature. The white crystalline products formed were collected by centrifugation, washed with distilled water and ethanol several times and dried, then calcinated at 850°C for 10 h

(Maryam et al., 2014). The product is represented as Al_2O_3 (C) where "C" represents chemical synthesis.

Microwave Synthesis of Aluminum Oxide (Al_2O_3) Nanoparticles

Microwave synthesis of aluminum oxide (Al_2O_3) was carried out using the method described by Maryam et al. (2014) with some modifications. Aluminum nitrate nonahydrate ($Al(NO_3)_3{\cdot}9H_2O$) was used as a precursor for the synthesis of Al_2O_3. $Al(NO_3)_3{\cdot}9H_2O$ (9.38 g, 0.025 mol) was dissolved in 50 mL of distilled water to obtain a 0.5 M solution. The precursor solution obtained (8 mL) was added to a 100 mL conical flask containing mixed solutions of 50 mL distilled water, 3.5 mL NaOH (5 M), and then blended well by stirring for 15 min. Subsequently, the mixed solution was subjected to microwave heating at 540 W to dry it. The solid product obtained is represented as Al_2O_3 (M) where "M" represents microwave synthesis.

Chemical Synthesis of Iron Oxide (Fe_2O_3) Nanoparticles

The accurately prepared 0.25 M $FeCl_2{\cdot}4H_2O$ solution was mixed with 5.4 M NaOH solution and 1.34 M $NH_3{\cdot}H_2O$ solution, respectively. The resulting mixture solution was magnetically stirred and heated up to 90°C while kept under nitrogen. The duration time was 1.5 h. Meanwhile, the pH value was adjusted by dropwise addition of 0.1 M HCl solution. The color of the resulting slurry changed from grayish green to red. Then, the slurry was washed repeatedly with deionized water and the suspension of iron oxide nanoparticles was obtained (Yang et al., 2014).

Microwave Synthesis of Iron Oxide (Fe_2O_3) Nanoparticles

Accurately weighed 5.5 g of iron nitrate was mixed with 2–3 drops of ethylene glycol and placed in the microwave. The paste was boiled for a few seconds and underwent dehydration followed by decomposition with the evolution of gases (O_2, NO_2) with yellow colored fumes. After 30 s it began burning and releasing lots of heat with vaporization of all the solution instantly to form a foamy porous black solid powder (Virendra et al., 2013).

Structural and Morphological Characterization of Synthesized Nanoparticles

The synthesized nanoparticles were characterized using Ultra-violet visible (UV-visible) spectroscopy, X-ray diffraction (XRD) spectroscopy, Scanning electron microscopy (SEM).

Synthesis of β-Hematin

β-hematin crystals (a biomarker for malaria parasite) were synthesized using an acid-catalyzed method (Egan et al., 2001). Accurately measured 8 mL of 0.1 M NaOH solution was used to dissolve 7.9 mM of Ferriprotoporphyrin IX chloride [Cl-Fe(III)PPIX, hemin chloride], heated at 60°C and stirred at 150 rpm for 46 min. Also, 1.45 mL of HCl (1 M) and 8.825 mL of acetic acid were added to the mixture, after 10 min and 14 min, respectively. After 46 min, the mixture was left undisturbed in a dark environment for 24 h. The solute obtained was washed with methanol and deionized water sequentially, filtered and collected for drying.

$$\underset{\text{Hemin chloride}}{2Cl-Fe\,(III)\,PPIX} + \underset{\text{Acetic acid}}{CH_3COOH} \longrightarrow \underset{\beta-\text{Hematin}}{(Fe\,(III)\,PPIX)_2} + CH_3COOH^{+}Cl^{-} \quad (3)$$

Electrode Modification Procedure (Sensor Preparation)

Electrode modification was carried out using the drop-dry method. The surface of the working electrode (Au) was prepared by polishing in an aqueous slurry of alumina nanopowder (LabChem) on a Buehler felt pad. The electrode was put through the ultrasonic vibration for 5 min in distilled water and absolute ethanol to eliminate the remaining alumina particles that may be caught on the surface. The gold electrode was then treated with piranha solution for about 1 min and was followed by rinsing in distilled water and ethanol for another 5 min and dried.

Suspensions of metal oxide nanoparticles were prepared by dissolving 2.5, 5.0, 7.5, and 10.0 mg of each nanoparticle in 1.0 mL DMF and sonicated for 20 min. Ten (10) μL drops of the prepared suspension were dropped on the bare gold electrode and dried in an oven at 50°C for 5 min to obtain gold-metal oxide nanoparticles (Au-MO) modified electrodes. Thus, the developed sensors using this procedure include Au-CuO (C), Au-CuO (M), Au-Fe_2O_3 (C), Au-Fe_2O_3 (M), Au-Al_2O_3 (C), and Au-Al_2O_3 (M). The mass of the active material on the Au was obtained by measuring the weight of the Au electrode before and after deposition using the Mettler Toledo (Model: ML 54) analytical balance (Switzerland). The active materials were found to range between ∼0.5 and 1.5 mg with the highest weight (1.5 mg) recorded for Au-CuO electrode modified with a 10 μL drop of 10 mg nanoparticle in 1 mL DMF. Thus, it could be inferred that the chemical composition of the MO nanoparticles also played a role on their adsorption and film formation on the base electrode.

Electrochemical Studies

Electrochemical experiments were carried out to establish the successful modification of the electrodes, electron transport, and electrocatalytic properties of the bare and modified gold electrode (Au). The bare and modified Au electrode disk (d = 3.0 mm in Teflon) was used as the working electrode, the platinum disk as a counter electrode and Ag/AgCl, KCl (sat'd) as a reference electrode. A benchtop pH/ISE ORION meter was used for pH measurements. All solutions were de-aerated by bubbling with nitrogen prior to each electrochemical experiment. Electrochemical experiments were carried out using PG-581 biologic potentiostat driven by UiEChem Electrochemical software. CV experiments were carried out by running the bare and modified Au electrode in 0.1 M buffer solution (PBS, pH 9.0), 5 mM $[Fe(CN)_6]^{4-/3-}$ solution prepared in 0.1 M PBS, and 1.0 mM of β-Hematin in pH 9.0 phosphate buffer solution as supporting electrolyte.

Interference Study

Since malaria parasite could coexist with *Salmonella typhi* bacteria in the host system, simultaneous determination of β-hematin and *S. typhi* antiserum VI was carried out. Accurately prepared 1.0 mM β-hematin in pH 9.0 PBS was spiked with 1.0–4.0 mg/mL of *Salmonella typhi* antiserum VI. The interference study of the biomarkers on Au-MO modified electrodes was carried out using a cyclic voltammetry experiment at scan rate 50 mV/s. The study was repeated in malaria-infected humans and mice sera in pH 9.0 PBS, spiked with 1.0–4.0 mg/mL *Salmonella typhi* antiserum VI and detected simultaneously with the malaria biomarker using the best Au-MO modified electrode.

Real Sample Analysis

Prior to the collection of samples, ethical clearance certificate was obtained from the Ethics and Research Committee of Obafemi Awolowo University Health Center, Ile Ife, Nigeria. During the handling of clinical samples, disposable gloves, and laboratory coats were always used to prevent infection or transmission of diseases. All the glassware used during this experiment were cleaned with sodium hypochlorite and ethanol after each experiment.

Recovery Analysis Using Human Urine Sample

Analytical validation of the electrochemical sensor method developed in this study was carried out using a recovery analysis experiment. Five urine samples (belonging to patients screened negative for malaria parasite) were collected at the Obafemi Awolowo University Health Centre, Ile Ife. Each urine sample was centrifuged (500 rpm) and diluted 10 times with pH 9.0 PBS. Precisely measured 10 mL of the diluted urine sample in 25 mL standard flask was spiked with 10 μM β-hematin and the content was made up to mark with pH 9.0 PBS. The spiked sample was run using SWV experiment, where Au-CuO (C) was used as the working electrode, Ag|AgCl, saturated KCl as the reference electrode, and Pt as the counter electrode, respectively. The β-hematin concentration corresponding to SWV reduction current of the spiked sample was estimated from the regression equation for the β-hematin standard calibration curve. The experiment was repeated 4 times ($n = 4$) for each urine sample and the recovery percentage was determined as the difference in the β-hematin concentration before and after the spiking experiment.

Determination of β-Hematin in Human Serum

Human blood samples of five patients (screened positive to malaria parasite) were collected at Obafemi Awolowo University Health Center, Ile Ife, Osun State, Nigeria. The blood samples were allowed to clot and centrifuged (at 500 rpm) to separate the serum and the plasma. The sera were diluted 10 times with pH 9.0 PBS and 10 mL of each serum was analyzed for the presence of β-hematin using the standard addition method (SAM) and square wave voltammetry technique, where Au-CuO (C) was the working electrode, Ag|AgCl, sat'd KCl was reference electrode and Pt counter was the electrode, respectively. Ten milliliters of the diluted sera samples was replicated in six 25 mL standard flasks and all except one were spiked with different standard concentrations (2, 4, 6, 8, and 10 μM) of β-hematin and makeup to mark with pH 9.0 PBS. The current corresponding to each spiked sample was determined using SWV experiment. The experiment was repeated 4 times ($n = 4$) for each serum sample and β-hematin concentration in the unspiked serum was determined by extrapolation.

Determination of β-Hematin in Animal Serum

Blood samples from 5 malaria-infected mice and 2 uninfected mice (control sample) were collected from the Faculty of Pharmacy, Obafemi Awolowo University, Ile Ife, Osun State, Nigeria. The serum was separated from the plasma by centrifugation. The sera were diluted 10 times with pH 9.0 PBS and 10 mL of each serum was analyzed for the presence of β-hematin using the standard addition method (SAM) and square wave voltammetry technique as discussed in determination of β-hematin in human serum. The experiment was repeated 4 times ($n = 4$) for each serum sample and β-hematin concentration in the unspiked serum was determined by extrapolation.

RESULTS AND DISCUSSION

Microscopic Analysis

Scanning electron microscope (SEM) analysis was used for the size and morphology study of the synthesized metal oxide (MO) nanoparticles. **Figures 1A–F** show the SEM images of CuO, Al_2O_3, and Fe_2O_3 nanoparticles for both chemical and microwave synthesis. SEM image of CuO (C) nanoparticles showed uniformly dispersed particles that are aggregated together with an average size of 12.72 nm (**Figure 1A**), while CuO (M) nanoparticles showed rod-like shaped agglomerated particles with an average size of 11.16 nm (**Figure 1B**). The particle size of the CuO nanoparticles was lower than the 30–60 nm reported for CuO in the literature (Sutradhar et al., 2014; Dhineshbabu et al., 2016). The SEM image of Al_2O_3 (C) revealed a quasi-spherical shape, with the average size of the agglomerated particles of 30.37 nm (**Figure 1C**). The Al_2O_3 (M) nanoparticles showed a passivated layer with an average particle size of 20.92 nm (**Figure 1D**). The Al_2O_3 (C) particle size falls within 26–53 nm as reported for the nanocatalyst in the literature (Veeradate et al., 2012). The SEM image of Fe_2O_3 (C) showed flaky crystals with an average size of 6.91 nm (**Figure 1E**), while that of Fe_2O_3 (M) indicated uniformly distributed particles, aggregated together to form a nanocluster with an average particle size of 6.42 nm (**Figure 1F**). The particle sizes obtained for Fe_2O_3 nanoparticles resembled closely those reported by Sweta (2014), but were much lower than the 10 μM reported by Balamurughan et al. (2014). The SEM analysis showed that the microwave synthesized nanoparticles have smaller sizes than that of chemically synthesized.

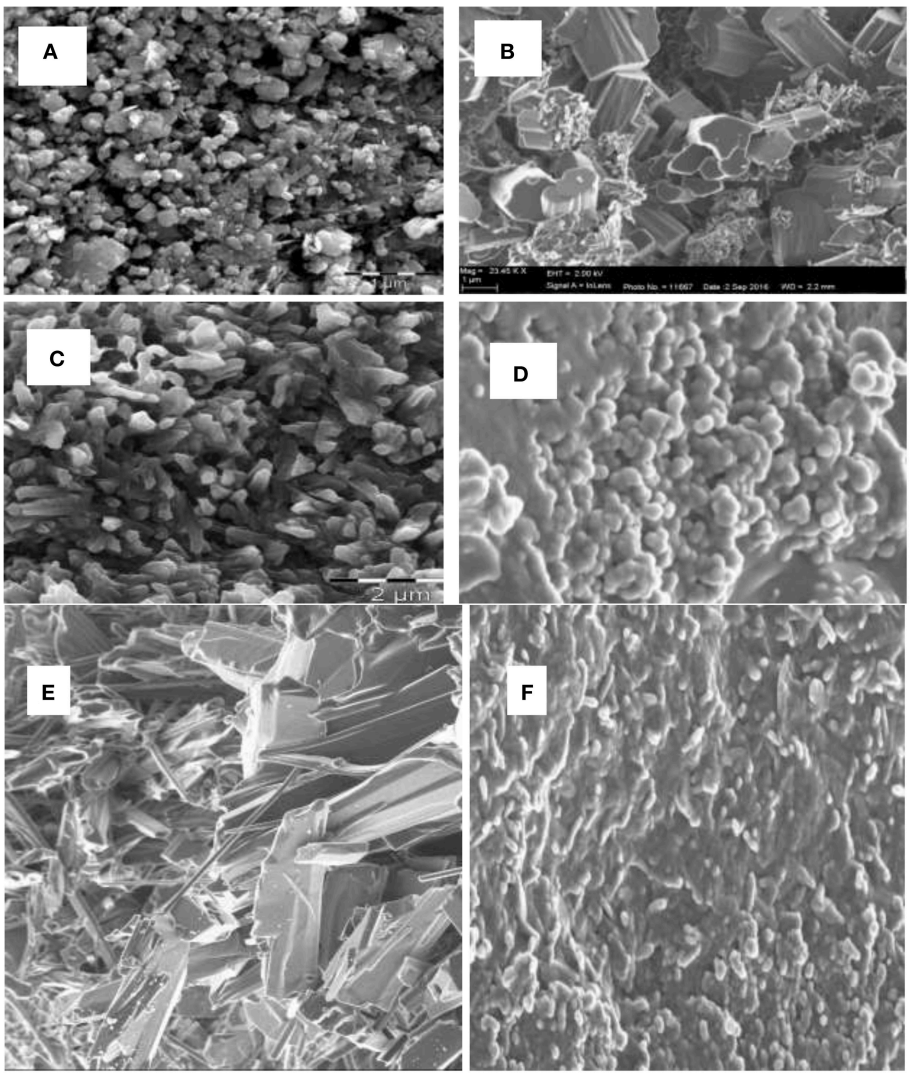

FIGURE 1 | SEM image of **(A)** CuO (C) nanoparticles, **(B)** CuO (M) nanoparticles, **(C)** Al_2O_3 (C) nanoparticles, **(D)** Al_2O_3 (M) nanoparticles, **(E)** Fe_2O_3 (C) nanoparticles, **(F)** Fe_2O_3 (M) nanoparticles.

UV–Visible and X-Ray Diffraction (XRD) Analyses

The UV absorption of the synthesized metal oxide nanoparticles at the ultraviolet region (not shown) arises from the electronic transition of electrons from the valence band to the conduction band, which might be due to the quantum size particles (Koole et al., 2014). Similar absorption bands has been observed and reported for CuO (Topnani et al., 2010), Al_2O_3 (Neethumol et al., 2014), and Fe_2O_3 (Balamurughan et al., 2014) nanoparticles.

X-ray diffraction is a potent and one of the most important methods for examining the structures of nanomaterials (Takeshi, 2007). X-ray diffractograms of the synthesized nanoparticles are shown in **Figures 2A–F**. X-ray diffraction pattern of CuO nanoparticles for both chemical and microwave synthesis match with JCPDS 05-0661 library for CuO and is similar to XRD pattern obtained by Dhineshbabu et al. (2016) and Meghana et al. (2015) for CuO nanoparticles. Distinct diffraction peaks at 32.213, 35.497, 38.712, 48.783, 53.551, 61.419, and 66.013 correspond to index planes (110), (−111), (111), (200), (202), (020), (220) (**Figure 2A**), suggesting a monoclinic structure of CuO (C) nanoparticles (Dhineshbabu et al., 2016). The peaks at 28.234, 35.420, 38.516, 48.650, 57.989, 61.472, 66.020, and 68.056, with index planes at (110), (−111), (200), (−202), (020), (202), (−113), and (311) (**Figure 2B**) correspond to cubic face CuO (M) nanoparticles (Rejith and Krishnan, 2012). Using Scherrer's formula (Equation 4) below (Neethumol et al., 2014):

$$D = \frac{K\lambda}{B\,(\mathrm{Cos}\,\theta)} \tag{4}$$

where D is the mean size of crystallites (nm), K is a factor 0.9, λ is x-ray wavelength, B is FWHM and θ is the Bragg angle, the average particle size for CuO (C) and CuO (M) nanoparticles,

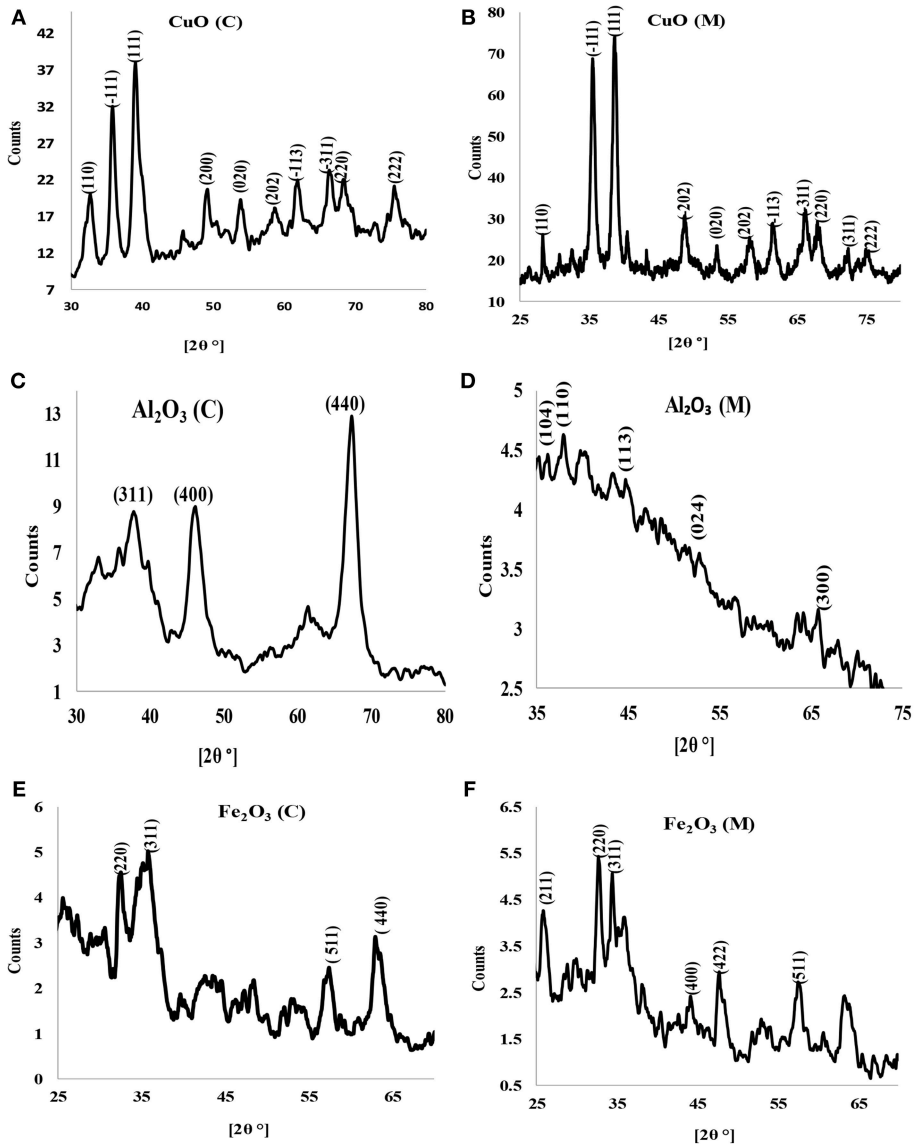

FIGURE 2 | X-ray diffractogram of **(A)** CuO (C) nanoparticles, **(B)** CuO (M) nanoparticles, **(C)** Al_2O_3 (C) nanoparticles, **(D)** Al_2O_3 (M) nanoparticles, **(E)** Fe_2O_3 (C) nanoparticles, and **(F)** Fe_2O_3 (M) nanoparticles.

estimated from full-width at half maximum of the diffraction were 21.75 nm and 21.41 nm, respectively.

X-ray diffractograms of Al_2O_3 (C) (**Figure 2C**) showed broad peaks at 38.421, 45.387, and 67.102, indexes at (311), (400), and (440) plane, correspondent to γ-Al_2O_3 phase (according to PDF card No. 00-001-1308) (Abbasian et al., 2010). A weak peak was obtained for Al_2O_3 (M) (**Figure 2D**). The peaks indicate fine crystallinity with an estimated average particle size of 13.05 nm and 9.01 nm for Al_2O_3 (C) and Al_2O_3 (M), respectively. The XRD pattern for iron oxide nanoparticles for both chemical and microwave synthesis showed that the crystallinity phase is γ-Fe_2O_3 (**Figures 2E,F**). The estimated average particle size for Fe_2O_3 (C) particles was 14.11 nm while that of Fe_2O_3 (M) was 21.50 nm.

UV-Vis and FTIR Analysis of Synthesized β-Hematin

In this study, synthetic hemozoin (β-hematin) was used as biomarker instead of the organism (*P. falciparum)* due to the challenges of culturing *P. falciparum* outside the biological system. Hemozoin (β-hematin) is a product of hemoglobin degradation in the bloodstream during infection by the malaria parasite.

The UV-visible spectroscopy results of hemin chloride (the starting material for β-hematin) and the synthesized β-hematin are showm in **Figures 3A,B**. The wavelength for maximum absorbance (λmax) for the two molecules is different, confirming the successful conversion of the hemin chloride (**Figure 3A**) to β-hematin (**Figure 3B**). Hemin chloride has a

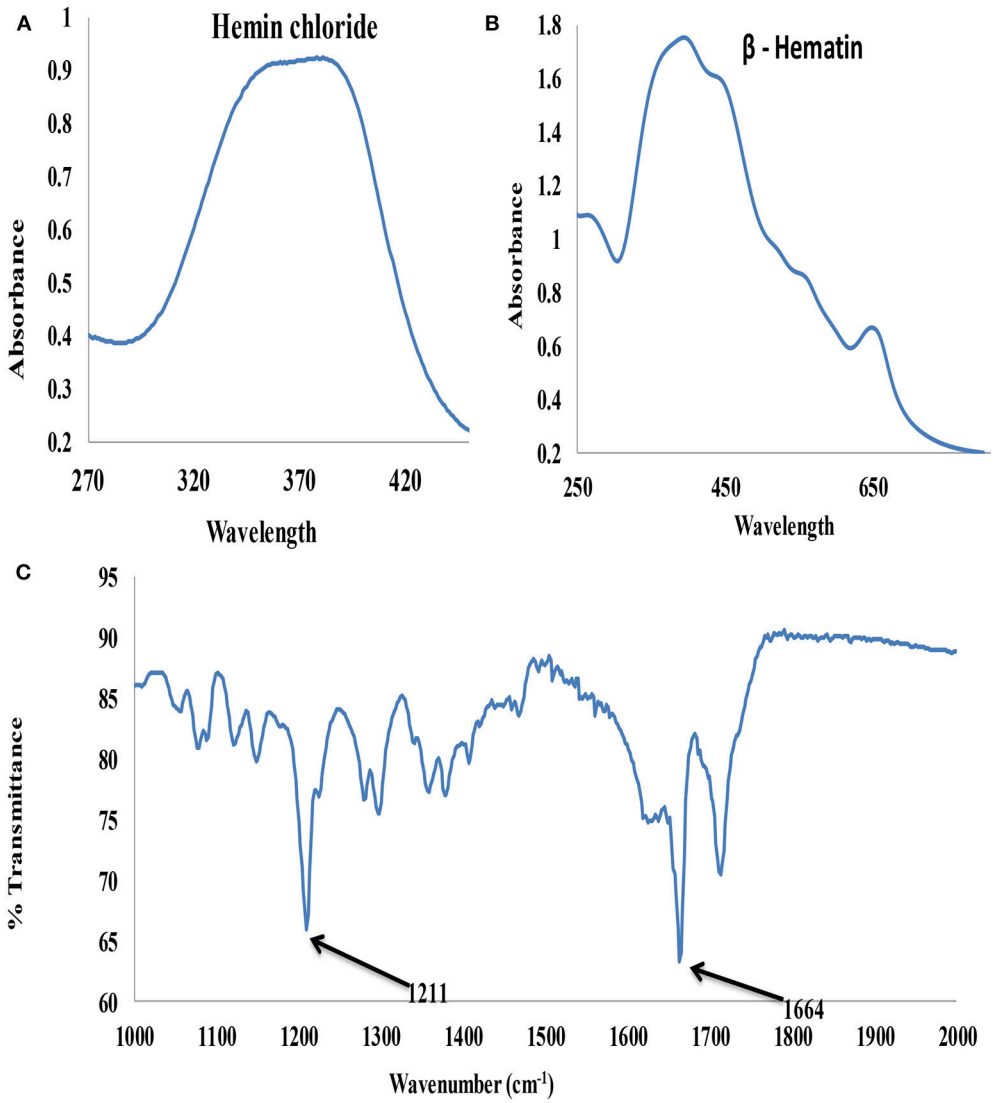

FIGURE 3 | UV–visible spectra **(A)** Hemin chloride **(B)** β-Hematin and **(C)** FTIR spectrum of β-Hematin.

broad absorbance at around 370 nm, while the synthesized β-hematin has its characteristic charge transfer (or absorption) band at around 650 nm and two broad soret bands at 383 and 400 nm. The differences in the absorbance of the two materials signify successful synthesis of β-hematin which can be used as a biomarker for the detection of malaria. The UV-visible result of β-hematin obtained in this study is in agreement with that reported by Fitch and Kanjananggulpan (1987) and Laure et al. (2012) for hemozoin or β-hematin.

The infrared spectroscopy analysis further confirmed the successful synthesis of β-hematin with hemozoin characteristic peaks at 1211 and 1664 cm^{-1} (**Figure 3C**) attributed to a dimeric ferriprotoporphyrin IX aggregate which is identical to *P. falciparum* hemozoin. The intense peak at 1,664 cm^{-1} indicates the presence of C=O stretching, an unidentate carboxylate coordination onto iron in the β-hematin. The peak at 1,211 cm^{-1} indicates an axial carboxylate ligand (C–O stretching frequency) from O-methyl groups linked to various metalloporphyrins (Slater et al., 1991).

Electrochemical Characterization of Fabricated Nanosensors

The electron transport properties of the Au-MO modified electrodes in 5 mM $[Fe(CN)_6]^{4-}/[Fe(CN)_6]^{3-}$ redox probe in 0.1 M PBS (scan rate, 50 mVs^{-1}) were investigated using cyclic voltammetry experiment. Cyclic voltammetric responses of the Au-MO modified electrodes (**Figure 4**) showed the characteristic one-electron oxidation-reduction peak in the region of 0–0.4 V attributed to $[Fe(CN)_6]^{3-/4-}$ redox probe but with higher current than that of the bare Au. Also, the characteristic $[Fe(CN)_6]^{3-/4-}$ redox peaks at the bare Au electrode were

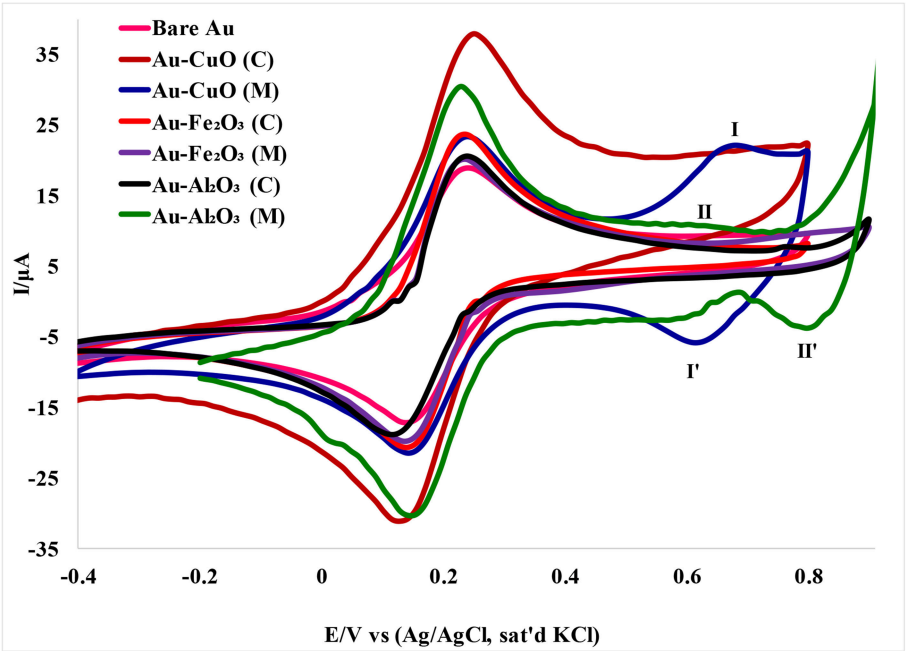

FIGURE 4 | Cyclic voltammograms of Au-MO modified electrodes in 5 mM $[Fe(CN)_6]^{4-}/[Fe(CN)_6]^{3-}$ redox probe in 0.1 M PBS (scan rate, 50 mV/s).

similar to those reported by Agboola et al. (2007) for bare Au in $[Fe(CN)_6]^{4-}/[Fe(CN)_6]^{3-}$ solution.

A pair of redox peaks was also observed for the Au-CuO modified electrode. The redox peaks at regions 0.63 (**I**) and 0.62 V (**I′**) appeared weak for CuO (C) and can be attributed to oxidation of CuO to Cu_2O_3 (Zaafarany and Boller, 2009). There were no observable peaks for the Fe_2O_3 redox process, probably because of the faster electron transfer process of Fe_2O_3 at the electrode, or overlap between the $[Fe(CN)_6]^{4-}/[Fe(CN)_6]^{3-}$ peaks and the Fe_3O_4 redox peaks. However, a peak at 0.80 V (**II′**) was attributed to reduction of Al_2O_3 nanoparticles.

The oxidation-reduction peaks observed for Au-Fe_2O_3 modified electrode in $[Fe(CN)_6]^{4-}/[Fe(CN)_6]^{3-}$ solution in this study were in agreement with the oxidation-reduction peaks reported by Fayemi et al. (2018) for Fe_2O_3 modified glassy carbon electrode. Electrochemical parameters such as formal potential ($E_{1/2}$), peak-to-peak separation potential (ΔEp), the ratio of anodic and cathodic peak current (I_{pa}/I_{pc}) were determined and summarized in **Table 1**. The ratios of the anodic to cathodic peak current (I_{pa}/I_{pc}) for the bare Au and Au-MO modified electrodes were ∼1.0 (unity) which indicates electrochemical reversibility process. Also, all the Au-MO electrodes have lower peak-to-peak separation, ΔEp (80.2–92.6 mV) and thus, enhanced electron transport properties when compared with the bare-Au electrode (ΔEp = 93.6). Factors responsible for enhanced electron transport at the modified electrodes might be the conductive nature of the metal oxide nanoparticle, its facile electronic nature, plus the ionic interaction between the metal oxide nanoparticle and underlying gold (Au) surface. However, Au-CuO (C) and Au-CuO (M) had the lowest ΔEp (80.2 mV) and therefore demonstrated the fastest electron transport among the bare-Au and other Au-MO modified electrodes investigated. It has been reported that the lower the ΔEp, the faster the electron transport at the electrode (Wang, 1994). Although the theoretical peak-to-peak potential separation value (ΔEp) is 59 mV for a fast one-electron process (Wang, 1994), the ΔEp values for all the electrodes were greater than that of the theoretical value.

Electrochemical Catalysis of β-Hematin Using Au-MO Modified Electrodes

The electrocatalytic behavior of the Au-MO modified electrode at different weights of MO nanoparticles (2.5, 5.0, 7.5, and 10.0 mg) toward 1.0 mM β-hematin in 0.1 M phosphate buffer solution (pH 9) was investigated using cyclic voltammetric experiment. **Figure 5** presents typical voltammogram obtained using Au-CuO modified electrodes. As shown in **Figure 5A**, the bare Au electrode gave a well-defined β-hematin reduction peak at −0.64 V and current of 17.9 μA not found in PBS (pH 9). However, modifying the Au electrode with 2.5 mg weight of the catalyst, Au-CuO (C) gave β-hematin reduction peak at −0.72 V but at very high current (99.7 μA) compared with bare Au (inset in **Figure 5B**). Compared with bare Au, the reduction peak of β-hematin at the Au-CuO (C) modified electrode occurred at a lower potential (energy) and higher current response (5 times higher) than those of the bare Au electrode. At 7.5 mg weight of the catalyst, Au-CuO (C) and Au-CuO (M) current responses were observed to be 25 and 18 times higher than that at bare Au (**Figures 5B,C**).

However, it is interesting to note that the reduction of β-hematin at Au-Fe_2O_3 and Au-Al_2O_3 modified electrodes still occurred at a lower potential (energy), although at a lower current response compared with the bare Au electrode (not

TABLE 1 | Cyclic voltammetric data obtained for the modified electrodes in 5 mM $[Fe(CN)_6]^{-3/-4}$ in 0.1 M PBS.

Electrode	I_{pc} (μA)	I_{pa}(μA)	I_{pa}/I_{pc}	E_{pc} (mV)	E_{pa} (mV)	$E^{o'}$ (mV)	ΔE_p (mV)
Bare Au	17.1	18.8	1.1	143.4	237.0	190.2	93.6
Au-CuO (C)	31.1	37.4	1.2	143.4	223.6	183.5	80.2
Au-CuO (M)	21.5	23.1	1.1	143.4	223.6	183.5	80.2
Au-Fe2O3 (C)	20.7	23	1.1	143.4	236.0	189.7	92.6
Au-Fe2O3 (M)	19.9	19.6	1.0	136.2	223.6	179.9	87.4
Au-Al2O3 (C)	18.8	20.4	1.1	141.6	223.6	182.6	82.0
Au-Al2O3 (M)	30.3	30.5	1.0	142.4	228.8	185.6	86.4

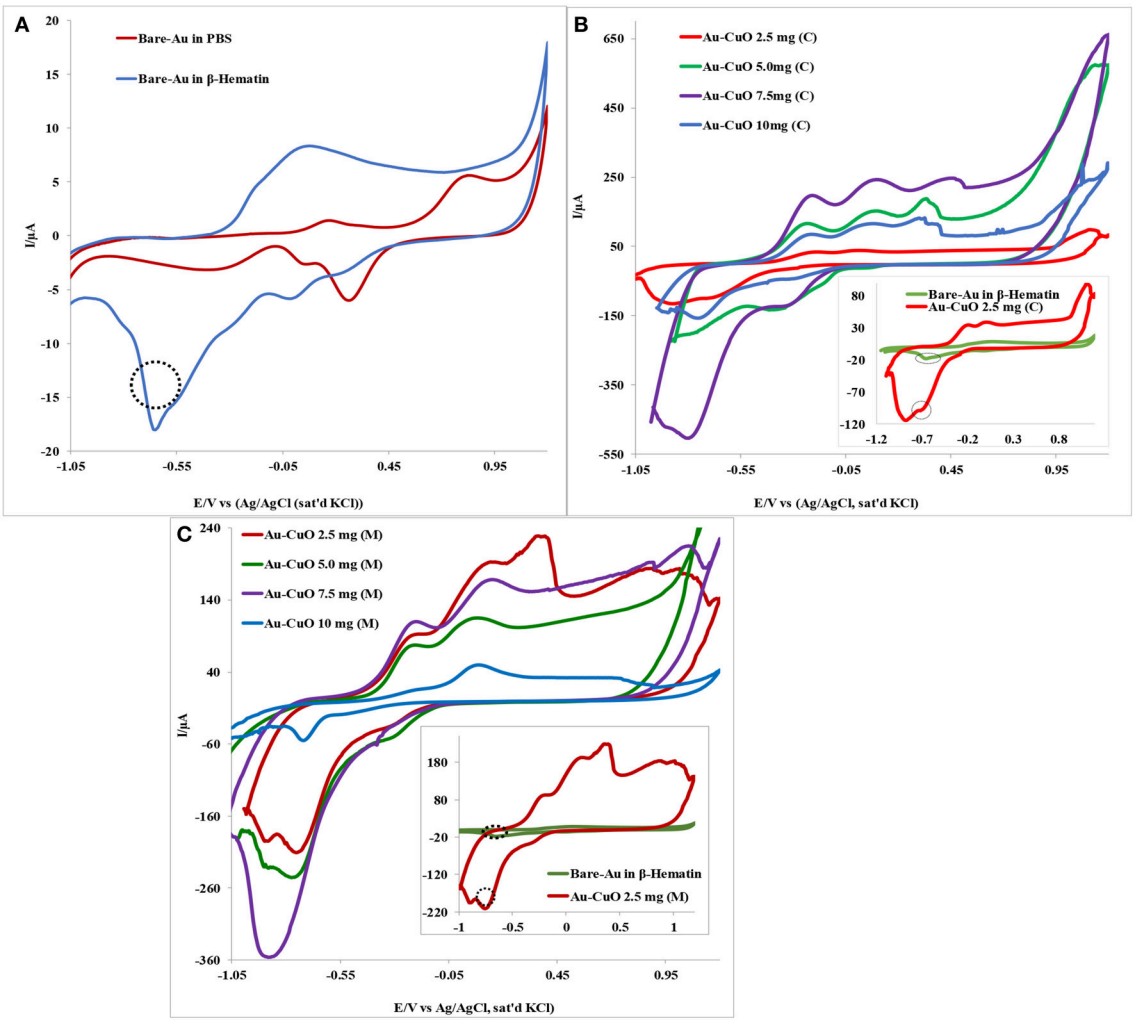

FIGURE 5 | Typical **c**yclic voltammetry evolution of: **(A)** Bare Au in 0.1 M PBS (pH 9) and 1.0 mM β-Hematin solution. **(B,C)** Are Au-CuO (C) and Au-CuO (M) (MO weights: 2.5–10.0 mg) modified electrodes in 0.1 M PBS (pH 9) containing 1.0 mM β-Hematin solution.

shown). The reason for the low β-Hematin reduction current at Au-Fe_2O_3 and Au-Al_2O_3 electrodes cannot be established at the moment but could be attributed to the formation of passive layers of Fe_2O_3 and Al_2O_3 films on Au electrode, thereby hindering electron transport at the electrode after catalysis. The reduction peak observed for β-hematin can be attributed to the reduction of Fe (III) atom at the center of the biomarker which is electrochemically active, to iron (II). Monti et al. (1999) reported the reduction of β-Hematin [(Fe (III) protoporphyrin IX)] to [Fe (II) protoporphyrin IXα] at −0.6 V using a bare platinum electrode as the working electrode, which is in agreement with the −0.64 V reduction potential recorded for β-Hematin at the bare Au electrode in this study. No oxidation peak was observed for β-hematin, suggesting irreversible electrochemical reaction.

In general, this result indicates that modifying Au with MO nanoparticles increases its electrode catalysis toward malaria biomarker (β-hematin), with enhanced sensitivity in terms of high reduction current and at lower energy. The remarkable results obtained undoubtedly proved the electrocatalytic sensing of Au-MO modified electrodes toward β-hematin. The results obtained confirmed the potential of the developed sensors for the detection and quantification of β-Hematin (malaria biomarker) or the parasite in biological fluids.

Scan Rate Study

Cyclic voltammetric experiments were carried out with a view to establishing the effect of scan rate (ν) (scan rates ranging from 25 to 500 mV/s) on the reduction current of β-hematin (1 mM) (**Figure S1**). It was observed that β-hematin reduction peak increases with an increase in scan rates. Using the Randles-Sevčik equation below, we obtained a linear plot of current (Ip) vs. the square root of scan rate $\nu^{1/2}$ (inset in **Figure S1**).

$$\mathrm{Ip} = 2.69 \times 10^5 \mathrm{n}^{3/2} \mathrm{D}^{½} \nu^{½} \mathrm{AC} \quad (5)$$

The non-zero intercept of the plots suggests that the electrode kinetic process is not completely controlled by the rate of diffusion of β-hematin from the solution to the surface of the electrode. Similar studies in literature have associated such deviation from diffusion to adsorption of reaction intermediates at the electrode surface. Adekunle and Ozoemena (2010) reported adsorption of DEAET intermediate at electrode surface during catalysis of the analytes using SWCNT-Ni modified electrode.

To further confirm the adsorption phenomenon, Tafel value (b) for the electrodes was obtained from plot of (Ep) vs. (log ν) using the Tafel equation (Equation 6) below:

$$\mathrm{E_p} = \left(\frac{\mathrm{b}}{2}\right) \log \nu + \text{constant} \quad (6)$$

Also, from Tafel value b = slope of the Tafel plot, charge transfer coefficient (α) was estimated using the relationship:

$$\text{Slope} = \frac{2.3\ \mathrm{RT}}{\alpha \mathrm{nF}} \quad (7)$$

where b = Tafel value, R = gas constant, T = temperature (in kelvin), α = charge transfer coefficient, n = number of electron and F = Faraday's constant.

The Tafel values ($\mathrm{mVdec^{-1}}$) and the charge transfer coefficient (α) in parenthesis are 1037.2 (0.06), 1042.6 (0.06), 296.2 (0.20), 279.6 (0.21), 174.6 (0.33), 301.8 (0.20) for Au-CuO (C), Au-CuO (M), Au-Fe_2O_3 (C), Au-Fe_2O_3 (M), Au-Al_2O_3 (C), and Au-Al_2O_3 (M) electrodes, respectively. The Tafel values are higher than 118.0 mV/dec for a one-electron process (Fayemi et al., 2018). High Tafel value had been attributed to adsorption of reactants or intermediates on the electrode surface (Ju and Leech, 2000). Therefore, it can be inferred from this study that there was adsorption of β-hematin or its intermediate on the surface of the Au-MO electrodes during electrocatalysis. It was also observed that the α values obtained were lower than the value 0.5 for standard reaction mechanism, which indicates that the reaction may be a neutralization reaction, while a value <0.5 means the reaction is an ionization reaction (Akira et al., 1989). Thus, the lower α values obtained in this study suggest an ionization reaction of the MO and β-hematin. This further confirms the redox process at the electrodes whereby at one point or the other, the MO nanoparticles and the analytes changed from one ionic state to the other with the resultant flow of electrons. The number of electrons (n) involved for each Au-MO electrode was calculated to be one (1). This also suggests that one electron was involved in the reduction of Fe^{3+} at the center of the analyte (β-hematin) by the MO catalyst on Au electrode. Thus, the following mechanism is suggested for the reduction of β-hematin. Assuming the metal ion M^{n+} in MO nanoparticles are represented as Cu^{2+}, Fe^{3+}, and Al^{3+}, respectively, therefore, the proposed mechanism is presented below using M^{2+} as example:

The interaction of the MO nanoparticles with aqueous β-hematin results in the formation of MO-β-hematin adducts (intermediates):

$$(\mathrm{MO})^{2+}_{\mathrm{film}} + \mathrm{Fe^{3+}PPIX_{(aq)}} \rightarrow [(\mathrm{MO})^{2+}_{\mathrm{film}} \ldots\ldots \mathrm{Fe^{3+}PPIX}]_{\mathrm{adduct}} \quad (8)$$

The adduct undergoes an internal rearrangement leading to the reduction of Fe^{3+} at the center of β-hematin to Fe^{2+} and oxidation of $(MO)^{2+}$ and $(MO)^{3+}$ simultaneously:

$$[(\mathrm{MO})^{2+}_{\mathrm{film}} \ldots\ldots \mathrm{Fe^{3+}PPIX}]_{\mathrm{adduct}} \rightarrow (\mathrm{MO})^{3+}_{\mathrm{film}} + \mathrm{Fe^{2+}PPIX} + \mathrm{e^-} \quad (9)$$

Equation 9 represents the one-electron process which is the rate-determining (slow) step. The catalyst is regenerated by the reduction process represented in Equation (10) below:

$$(\mathrm{MO})^{3+}_{\mathrm{film}} + \mathrm{e^-} \rightarrow (\mathrm{MO})^{2+}_{\mathrm{film}} \quad (10)$$

Stability Studies

The stability of the Au-MO modified electrodes in β-hematin was confirmed by repetitive cycling of the electrodes in a solution of β-hematin at a scan rate of 50 mV/s. It was observed that the current response at Au-CuO (C) electrode increases by 16.63% after 20 cycles probably due to surface activation (**Figure S2A**). The electrode was kept in a refrigerator at −4.0°C after use in β-hematin for 2 weeks and run again in the analyte, the current dropped by 14.20% (Inset in **Figure S2A**). This might be attributed to fouling (or poison) effect of the catalyst at the surface of the electrode after many uses. Similar effects have been noticed and reported for chemically modified electrodes (Ojani et al., 2005). However, the current drop is insignificant and there is assurance of the stability and reusability of the electrode with a reliable result. Other Au-MO electrodes studied showed a drop in β-hematin current after (20 cycles) (**Figures S2B–F**). The order of the current drop is: Au-Al_2O_3 (M) (7.02%) < Au-Al_2O_3 (C) (10.61%) < Au-CuO (M) (15.96%) < Au-Fe_2O_3 (C) (17.37%) < Au-Fe_2O_3 (M) (41.37%) (**Figure S2**).

In general, except for Au-Fe_2O_3 (M) with a high current drop (41.37%), all other developed sensors investigated have demonstrated good stability in the analyte with minimum current drop after 20 cycles. The high decrease in current response observed on Au-Fe_2O_3 (M) electrode can be attributed to the poisoning of the electrode surface during the repetitive cycling due to formation of degradation products of β-hematin.

Electroanalysis Study

The effect of change in concentration of β-hematin on current response at Au-MO modified electrodes was studied using square wave voltammetric (SWV) and chronoamperometric techniques (**Figures S3**, **S4**). The square wave analysis was carried out for a concentration range of 1.96–9.91 μM. The result showed that for all the electrodes, current increases with increase in the concentration of β-hematin, 1.96–9.91 μM in PBS (pH 9.0) (**Figures S3A–F**). The plot of current response (I) vs. β-hematin concentration gave a linear relationship (inset in **Figures S4A–F**). From these plots, limit of detection (LoD = 3.3 δ/m) and limit of quantification (LoQ = 10 δ/m) where "δ" is the relative standard deviation of the intercept of the y-coordinates from the line of best fit, and "m" the slope of the same line, were determined for the electrodes. The LoD values obtained are 0.83, 0.83, 1.08, 0.77, 0.71, and 0.43 μg/mL for Au-CuO (C), Au-CuO (M), Au-Fe_2O_3 (C), Au-Fe_2O_3 (M), Au-Al_2O_3 (C), and Au-Al_2O_3 (M) electrodes, respectively; while the LoQ values are 2.52, 2.52, 3.02, 2.32, 2.15, and 1.30 μg/mL for Au-CuO (C), Au-CuO (M),

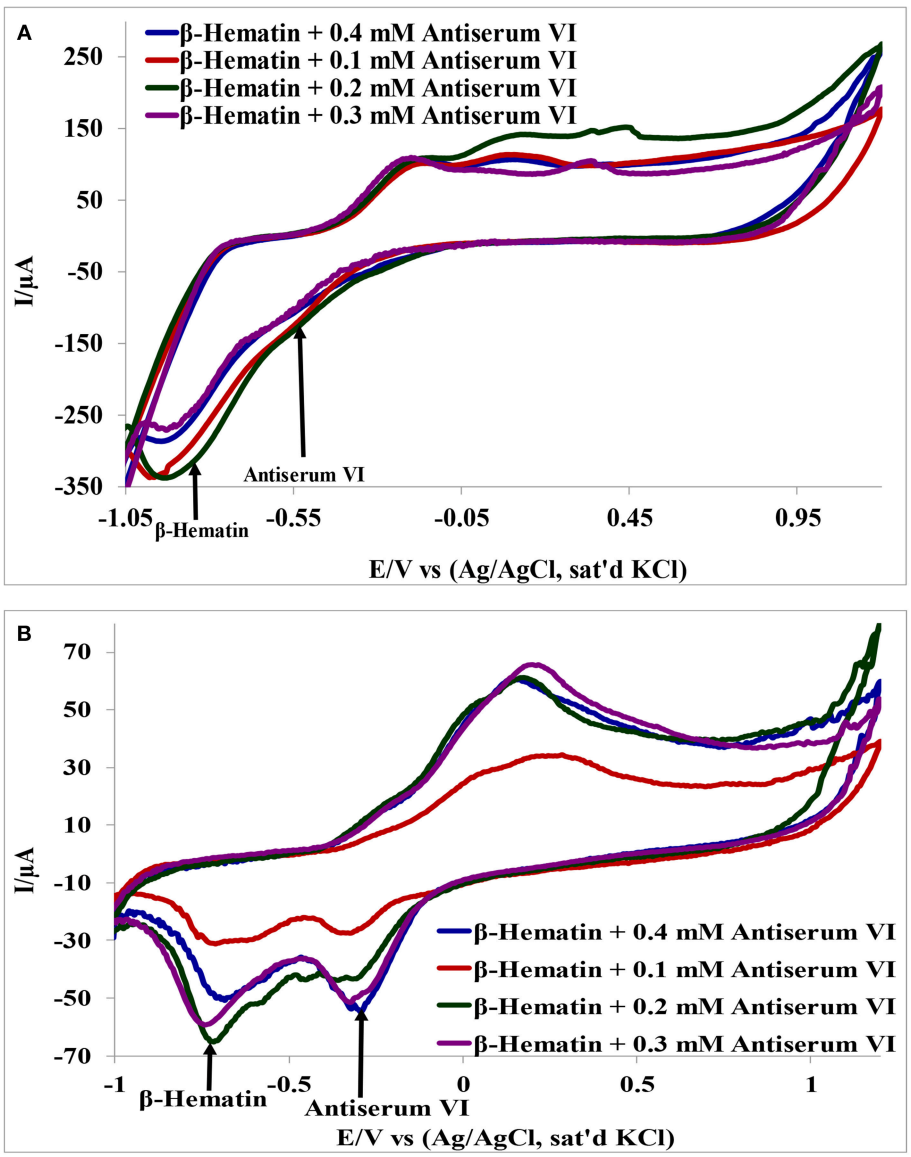

FIGURE 6 | Interference study of **(A)** Au-CuO (C), **(B)** Au-CuO (M) in 1 mM β-Hematin and Different Concentration of Antiserum VI.

Au-Fe_2O_3 (C), Au-Fe_2O_3 (M), Au-Al_2O_3 (C), and Au-Al_2O_3 (M) electrodes, respectively. It was observed that Au-Al_2O_3 (M) has the lowest LoD (0.43 μg/mL) and LoQ (1.30 μg/mL).

The LoDs recorded in this work are higher than 2.5 x 10^{-5} μg/mL and 4.0 x 10^{-5} μg/mL reported for *Plasmodium falciparum histidine-rich protein* 2 (PfHRP 2) detection on screen printed gold electrode (Gikunoo et al., 2014; Aver et al., 2017). Although the LoD is higher for the present study, the use of chemical biomarkers such as β-hematin should be encouraged because they are stable, affordable (cheaper), and easily available than PfHRP 2.

From the chronoamperometry study (**Figure S4**) and using the Cottrell equation (Bard and Faulkner, 2001), the plots of Ip vs. $t^{-1/2}$ for different concentrations of β-hematin were linear.

$$\mathrm{Ip} = \frac{\mathrm{nFAD}^{1/2}C}{\pi t^{1/2}} \tag{11}$$

where n is the number of electrons involved in the reaction, F is the Faraday Constant F (96,500 C/mol), and A is the experimentally determined area of the electrode, C is the bulk concentration of the β-hematin (mol/cm^3), while t is time (s), and D is the diffusion coefficient (cm^2/s). The diffusion coefficient (D) of β-hematin at the electrode was obtained from the slope of the curve as: Au-CuO (C) (3.5 x 10^{-2} ± 0.0006 cm^2/s), Au-CuO (M) (1.4 x 10^{-2} ± 0.001 cm^2/s), Au-Fe_2O_3 (C) (3.3 x 10^{-2} ± 0.0004 cm^2/s), Au-Fe_2O_3 (M) (2.4 x 10^{-2} ± 0.0005 cm^2/s), Au-Al_2O_3 (C) (0.5 x 10^{-2} ± 0.0002 cm^2/s), and Au-Al_2O_3 (M) (0.5 x 10^{-2} ± 0.0002 cm^2/s). The results obtained indicate that diffusion of β-hematin was best favored at Au-CuO (C) electrode and least favored at Au-Al_2O_3 electrodes (chemical and microwave synthesized). Also, the Au-MO electrode catalytic rate constants (k) toward β-hematin reduction were estimated from the relationship below (Bard and Faulkner, 2001):

$$\frac{I_{cat}}{I_{buff}} = \pi^{1/2}(\mathrm{kCt})^{1/2} \tag{12}$$

where I_{catt} and I_{buff} are the currents of analyte and buffer respectively, C is the analyte bulk concentration, k is the catalytic rate constant and t is the elapsed time. The result obtained follows the order: Au-CuO (C) (1.3 M/s), Au-CuO (M) (1.2 M/s), Au-Al_2O_3 (M) (0.6 M/s), Au-Fe_2O_3 (M) (0.5 M/s), Au-Al_2O_3 (C) (0.5 M/s), and Au-Fe_2O_3 (C) (0.3 M/s) The results suggest Au-CuO (C) having better catalytic activity toward the analyte, and that may explain its enhanced performance toward the detection of hematin as demonstrated in this study.

Interference Study

Detection of β-hematin on the Au-MO modified electrodes in the presence of *Salmonella typhi* VI antisera was carried out using cyclic voltammetry at a constant concentration of β-hematin (1.0 mM) and varying concentrations of the antiserum. It is interesting to know that β-hematin and antiserum VI could be detected simultaneously with well-defined signal separation of the analytes at their respective potential. A representative cyclic voltammograms using Au-CuO modified electrode is presented in **Figure 6**. On the other hand, this signal separation was not possible using the bare Au electrode. This result further confirmed the importance of chemically modified electrodes in sensor applications as it enhances the sensitivity and selectivity of bare electrodes. The respective analytes detected potentials and their signal separation at Au-MO electrodes are presented in **Table 2**. Au-CuO (both chemical and microwave synthesis) gave the highest current response and the best potential separation (500 mV) (**Table 2**). The result, therefore, suggests that the developed sensors can reliably be used for simultaneous detection of the malaria parasite and typhoid bacteria in clinical samples without signal interferences.

TABLE 2 | β-Hematin and *S. typhi* antiserum VI signal potentials at Au-MO modified electrodes and the corresponding signal/peak difference.

Electrodes	β-hematin (mV)	Antiserum VI (mV)	Peak difference (mV)
Au-CuO (C)	−910	−410	500
Au-CuO (M)	−900	−400	500
Au-Fe_2O_3 (C)	−600	−380	220
Au-Fe_2O_3 (M)	−680	−330	350
Au-Al_2O_3 (C)	–	–	Broad peak
Au-Al_2O_3 (M)	565	375	190

TABLE 3A | Recovery analysis of β-hematin in human urine samples ($n = 4$).

Sample	Amount added (μM)	Amount detected (μM)	Recovery (%)
Urine 1	10.00	11.41 ± 2.19	113.58 ± 1.37
Urine 2	10.00	8.98 ± 1.83	90.26 ± 3.22
Urine 3	10.00	9.27 ± 1.12	93.21 ± 7.22
Urine 4	10.00	9.56 ± 2.48	95.61 ± 4.50
Urine 5	10.00	10.19 ± 2.10	102.38 ± 2.18

TABLE 3B | Concentration of β-hematin (mM) in serum samples.

	Mice serum samples infected with *Plasmodium berghei* ($n = 4$)	Human serum samples diagnosed with malaria parasite ($n = 4$)
Sample	Concentration found (mM)	Concentration found (mM)
Serum 1	4.28 ± 0.11	1.20 ± 0.30
Serum 2	3.75 ± 0.21	0.65 ± 0.020
Serum 3	3.73 ± 0.24	0.88 ± 0.10
Serum 4	4.80 ± 0.57	1.15 ± 0.20
Serum 5	3.60 ± 0.33	1.35 ± 0.20

ANALYTICAL APPLICATION OF THE DEVELOPED SENSORS (AU-MO)

Recovery Analysis

Since the Au-CuO (C) modified electrode demonstrated superior and impressive electrochemical properties in terms of current response at lower energy with remarkable signal separation of the analytes without interference, its potential for analytical application in real life sample matrices was tested. Au-CuO (C) modified electrode was used for the detection of β-hematin in

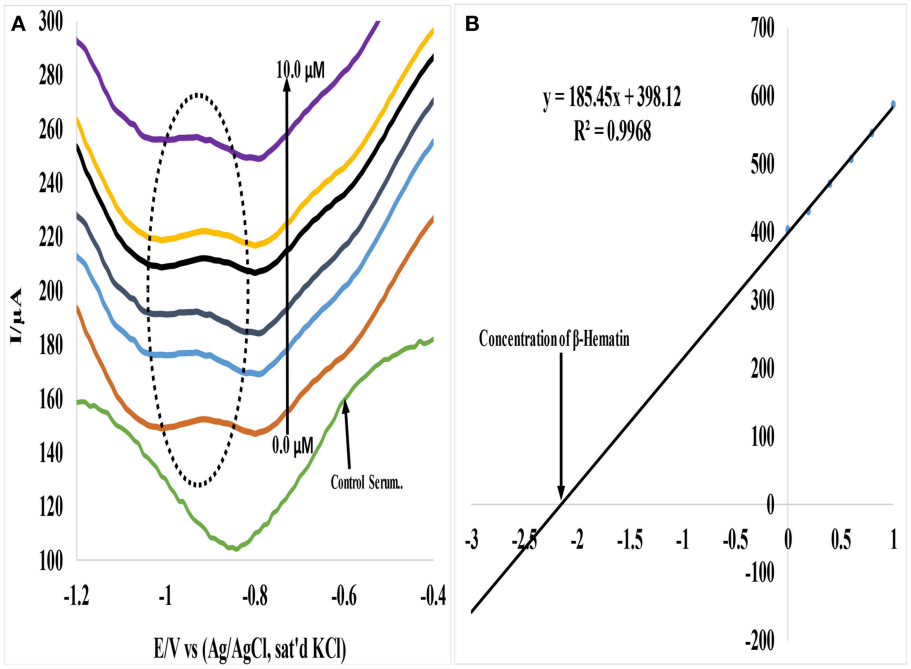

FIGURE 7 | (A) Typical SWV analysis of β-hematin in mice serum sample **(B)** Calibration curve for β-hematin determination in unspiked human urine sample using standard addition method (SAM).

urine samples (already screened negative) for malaria parasite infection. Five (5) urine samples were spiked with 10 μM of the β-hematin solution and the spiked samples current response at the Au-CuO (C) electrode was determined using square wave voltammetry techniques. It is interesting to know that the β-hematin was successfully detected in the spiked urine samples at around −0.75 V (**Figure S5B**). The procedure was repeated four (4) times for each urine sample, while β-hematin concentration in the spiked urine samples was determined by extrapolating the current measured from the regression equation of β-hematin standard calibration curve (inset of **Figure S5A**). The percentage recovery of the analyte in the urine samples was calculated and presented in **Table 3A**. The percentage recovery ranged from 90.26 ± 3.22 to 113.58 ± 1.37%, which falls within the recovery range (75–110%) expected for a reliable analytical procedure The result therefore further confirms the suitability and reliability of the Au-MO developed sensors for detection of β-hematin (malaria biomarker) in real life samples.

Determination of β-Hematin in Mice and Human Serum

In a similar study, Au-CuO (C) modified electrode was used for detection of β-hematin in the serum of infected mice and human sera diagnosed with malaria parasite using square wave voltammetry technique. The procedure followed the standard addition method (SAM). β-hematin peak was observed at around −0.80 V in animal serum and −0.91 V in human serum (**Figure 7**). This peak was absent in animal serum that was not infected with malaria parasite (control serum, **Figure 7A**). After spiking the infected serum samples with standard concentrations of β-hematin, the current response increased with increases in concentration (**Figure 7A**) and the current plot vs. concentration was obtained (**Figure 7B**). From the plot, the concentrations of β-hematin in the unspiked human and animal serum samples were estimated (**Table 3B**). The concentrations of β-hematin in the five animal sera analyzed were in the range 3.60 ± 0.33 to 4.80 ± 0.57 mM, while that in human sera were within the range of 0.65 ± 0.02 to 1.35 ± 0.20 mM. The concentrations found in the five human sera samples closely resembled one another and suggest the consistency and reliability of the developed sensor to detect the parasite quantitatively in human serum within the allowable threshold. Although the animal parasite was detected at much higher concentrations in the sera, the trend also suggests the possible threshold within which the parasite can exist in animals.

Cyclic voltammetry technique was also used to confirm the presence of β-hematin in human serum using Au-CuO (C) electrode and the reduction peak was successfully observed at around −0.82 V (inset in **Figure S6**). Infected animal serum was also spiked separately with each of *S. typhi* antiserum VI for simultaneous detection in the presence of the malaria biomarker (β-hematin) (**Figure S6**). The developed sensor successfully separated β-hematin from the antiserum with well-defined signal separation of 250 mV (**Figure S6**). The results also confirmed the potential of the Au-MO developed sensors as a device for detection and quantification of the malaria parasite and typhoid bacteria in human serum sample with little or no diagnosis confusion of malaria and a different antiserum.

CONCLUSION

This study describes the electron transport and electrocatalytic properties of both chemically and microwave synthesized metal oxide nanoparticles (MO) (where M = Cu, Fe, and Al) deposited on gold electrode toward the detection of malaria biomarker (β-Hematin) in clinical samples (e.g., blood serum, urine etc.). The study demonstrated that electrocatalysis of β-hematin was more favored on Au-electrode modified with CuO nanoparticles (chemical and microwave synthesized). The outstanding properties of the Au-CuO electrodes compared to others include enhanced current response at lower onset potential for catalysis, high electrochemical stability in the analytes (resistance to electrode fouling) and good signal separation between malaria and typhoid biomarkers (i.e., little or no interference) during detection. Au-CuO (C) gave the best sensing properties toward the detection of β-hematin in urine and blood serum. The sensor showed well-defined peaks of β-hematin and *S. typhi* antiserum VI in the clinical samples and was able to detect both analytes simultaneously with a potential separation of 250 mV in serum.

AUTHOR CONTRIBUTIONS

ASA and JAO designed the work and were part of the manuscript write-up, TS, TTIN and BBM provided the research platform for nanoparticles characterization, ORO carried out the experiment, interpreted the results and prepared the manuscripts. All authors reviewed the manuscript and agreed to its publication.

ACKNOWLEDGMENTS

Authors acknowledge Organization for Women in Science for the Developing World (OWSD) for providing fellowship for this research. Authors also acknowledge Obafemi Awolowo University, Ile Ife for providing research platform. ASA thank University of South Africa for research visit fellowship.

SUPPLEMENTARY MATERIAL

The Supplementary Material for this article can be found online at: https://www.frontiersin.org/articles/10.3389/fchem.2019.00089/full#supplementary-material

REFERENCES

Abbasian, A. R., Touradj, E., Suresh, K. B., and Mohamad, H. A. (2010). *Microwave-Assisted Synthesis of Alumina Nanoparticles From Aluminum Salt*. Conference paper, 1–12.

Adekunle, A. S., and Ozoemena, K. I. (2010). Electrocatalytic oxidation of diethylaminoethanethiol and hydrazine at single-walled carbon nanotubes modified with prussian blue nanoparticles. *Electroanalysis* 22, 2519–2528. doi: 10.1002/elan.201000289

Agboola, B., Westbroek, P., Ozoemena, K. I., and Nyokong, T. (2007). Voltammetric characterisation of the self-assembled monolayers (SAMs) of benzyl-and dodecyl-mercapto tetra substituted metallophthalocyanines complexes. *Electrochem. Commun.* 9, 310–316. doi: 10.1016/j.elecom.2006.08.047

Akira, Y., Kakitani, T., Enomoto, Y., and Mataga, N. (1989). Shapes of the electron-transfer rate vs energy gap relations in polar solutions. *J. Phys. Chem.* 93, 8316–8323. doi: 10.1021/j100363a009

Angerer, J., Bird, M. G., Burke, T. A., Doerrer, N. G., Needham, L., and Robison, S. H. (2006). Strategic biomonitoring initiatives: moving the science forward. *Toxicol Sci.* 93, 3–10. doi: 10.1093/toxsci/kfl042

Aver, H., Jon, A., and Ibtisam, E. T. (2017). Development of an immunosensor for PfHRP 2 as a biomarker for malaria detection. *Biosensors* 7, 1–14. doi: 10.3390/bios7030028

Balamurughan, M. G., Mohanraj, S., Kodhaiyolii, S., and Pugalenthi, V. (2014). *Ocimum sanctum* leaf extract mediated green synthesis of iron oxide nanoparticles: spectroscopic and microscopic studies. *J. Chem. Pharm. Sci.* 4, 201–204.

Bard, A. J., and Faulkner, L. R. (2001). *Electrochemical Methods: Fundamentals and Applications,* 2nd ed. Hoboken, NJ: John Wiley & Sons.

Dhineshbabu, N. R., Rajendran, V., Nithyavathy, N., and Vetumperumal, R. (2016). Study of structural and optical properties of cupric oxide nanoparticles. *Appl. Nanosci.* 6, 933–939. doi: 10.1007/s13204-015-0499-2

Egan, T. J., Mavuso, W. W., and Ncokazi, K. K. (2001). The mechanism of β-hematin formation in acetate solution. Parallels between hemozoin formation and biomineralization. *Biochemistry* 40, 204–213. doi: 10.1021/bi0013501

Fayemi, O. E., Adekunle, A. S., Swamy, B. K., and Ebenso, E. E. (2018). Electrochemical sensor for the detection of dopamine in real samples using polyaniline/NiO, ZnO, and Fe_3O_4 nanocomposites on the glassy carbon electrode. *J. Electroanal. Chem.* 818, 236–249. doi: 10.1016/j.jelechem.2018.02.027

Fitch, C. D., and Kanjananggulpan, P. (1987). The state of ferriprotoporphyrin IX in malaria pigment. *J Biol Chem.* 262, 15552–15555.

Gikunoo, E., Abera, A., and Woldesenbet, E. (2014). A novel carbon nanofibers are grown on glass microballoons immunosensor: A tool for early diagnosis of malaria. *Sensors* 14, 14686–14699. doi: 10.3390/s140814686

Gil, F., and Pla, A. (2001). Biomarkers as biological indicators of xenobiotic exposure. *J. Appl. Toxicol.* 21, 245–255. doi: 10.1002/jat.769

Goyal, M., Alam, A., and Bandyopadhyay, U. (2012). Redox regulation in malaria: current concepts and pharmacotherapeutic implications. *Curr. Med. Chem.* 19, 1475–1503. doi: 10.2174/092986712799828328

Ju, H., and Leech, D. (2000). Electrochemical study of a metallothionein modified gold disk electrode and its action on Hg2+ cations. *J. Electroanal. Chem.* 484, 150–156. doi: 10.1016/S0022-0728(00)00071-1

Koole, R., Groeneveld, E., Vanmaekelbergh, D., Meijerink, A., and de Mello Donegá, C. (2014). "Size effects on semiconductor nanoparticles," in *Nanoparticles*, ed C. de Mello Donegá (Berlin; Heidelberg:Springer), 13–51.

Kumar, S., Guha, M., Choubey, V., Maity, P., and Bandyopadhyay, U. (2007). Antimalarial drugs inhibiting hemozoin (β-hematin) formation: a mechanistic update. *Life Sci.* 80, 813–828. doi: 10.1016/j.lfs.2006.11.008

Laure, J., Don, A. L., Elisabeth, D., and Mourad, E. (2012). A physico-biochemical study on potential redox-cyclers as antimalarial and antischistosomal drugs. *Curr. Pharm. Design* 18, 3539–3566.

Manimaran, R., Palaniradja, K., Alagumurthi, N., Sendhilnathan, S., and Hussain, J. (2014). Preparation and characterization of copper oxide nanofluid for heat transfer applications. *Appl. Nanosci.* 4, 163–167. doi: 10.1007/s13204-012-0184-7

Maryam, L., Gholamali, F., and Nasrin, E. (2014). Synthesis and surface modification of aluminum oxide nanoparticles. *J. Ceramic Proc. Res.* 15, 316–319.

Meghana, S., Kabra, P., Chakraborty, S., and Padmavathy, N. (2015). Understanding the pathway of antibacterial activity of copper oxide nanoparticles. *RSC Advances* 5, 12293–12299. doi: 10.1039/C4RA12163E

Monti, D., Vodopivec, B., Basilico, N., Olliaro, P., and Taramelli, D. (1999). A novel endogenous antimalarial: Fe(II)-protoporphyrin IXR (Heme) inhibits hematin polymerization to β-hematin (malaria pigment) and kills malaria parasites. *Biochemistry* 38, 8858–8863. doi: 10.1021/bi990085k

Neethumol, V., Manjusha, H., Benny, C., Sreenivasan, P. V., Jenish, P., and Asmy, A. K. A. (2014). PVA - assisted synthesis and characterization of nano α -alumina. *Int. J. Sci. Res. Public.* 4, 1–5.

Ojani, R., Raoof, J. B., and Zamani, S. (2005). Electrochemical behavior of chloranil chemically modified carbon paste electrode. Application to the electrocatalytic determination of ascorbic acid. *Electroanalysis* 17, 1740–1745. doi: 10.1002/elan.200503277

Oliveira, M. F., Kycia, S. W., Gomez, A., Kosar, A. D., Bohle, D. S., Hempelmann, E., et al. (2005). Structural and morphological characterization of hemozoin produced by Schistosoma mansoni and Rhodnius prolixus, *FEBS Lett.* 579, 6010–6016 doi: 10.1016/j.febslet.2005.09.035

Pagola, S., Stephens, P. W., Bohle, D. S., Kosar, A. D., and Madsen, S. K. (2000). The structure of malaria pigment [beta]-haematin. *Nature* 404, 307–310. doi: 10.1038/35005132

Priyamvada, J., Babina, C., Sanjukta, P., and Pranab, G. (2014). Potential biomarkers and their applications for rapid and reliable detection of malaria. *BioMed Res. Int.* 2014:852645. doi: 10.1155/2014/852645

Rebelo, M., Sousa, C., Shapiro, H. M., Mota, M. M., Grobusch, M. P., and Hänscheid, T. (2013). A novel flow cytometric hemozoin detection assay for real-time sensitivity testing of Plasmodium falciparum. *PLoS ONE* 8:e61606. doi: 10.1371/journal.pone.0061606

Rejith, S. G., and Krishnan, C. (2012). Microwave synthesis of copper oxide nanoparticles: optical and structural characterizations. *J. Sci. Acta Xaveriana* 3, 65–72.

Slater, A. F., Swiggard, W. J., Orton, B. R., Flitter, W. D., Goldberg, D. E., Cerami, A., et al. (1991). An iron-carboxylate bond links the heme units of malaria pigment. *Proc. Natl. Acad. Sci. U.S.A.* 88, 325–329. doi: 10.1073/pnas.88.2.325

Sutradhar, P., Saha, M., and Maiti, D. (2014). Microwave synthesis of copper oxide nanoparticles using tea leaf and coffee powder extracts and its antibacterial activity. *J. Nanostruct. Chem.* 4:86. doi: 10.1007/s40097-014-0086-1

Sweta, P. (2014). *Antimicrobial Activity Of Iron Oxide Nanoparticles.* MSc Thesis. National Institute of Technology, Rourkela.

Takeshi, M. (2007). "Chapter 5, Section 53: Characterization methods for nanostructure of materials," in *Nanoparticle Technology Handbook*, eds M. Naito, T. Yokoyama, K. Hosokawa, and K. Nogi (Osaka: Elseivier).

Thomas, V., Gois, A., Ritts, B., Burke, P., Hänscheid, T., and McDonnell, G. (2012). A novel way to grow hemozoin-like crystals *in vitro* and its use to screen for hemozoin inhibiting antimalarial compounds. *PLoS ONE* 7:e41006. doi: 10.1371/journal.pone.0041006

Topnani, N., Kushwaha, S., and Athar, T. (2010). Wet synthesis of copper oxide nanopowder. *Int. J. Green Nanotechnol.* 1, M67–M73. doi: 10.1080/19430840903430220

Veeradate, P., Voranuch, T., Piyapong, A., and Pichet, L. (2012). Preparation and characterization of alumina nanoparticles in deionized water using laser ablation technique. *J. Nanomat.* 2012:819403. doi: 10.1155/2012/819403

Virendra, C., Gopal, C., Ravindra, S., and Nitish, G. (2013). Synthesis of nano crystalline ZnO by microwave-assisted combustion method: an eco-friendly and solvent-free route. *Int. J. Environ. Sci.* 4, 45–47.

Wang, J. (1994). *Analytical Electrochemistry*. New York, NY:VCH Publishers Inc.

Weinberg, E. D., and Moon, J. (2009). Malaria and iron: history and review. *Drug Metab Rev*. 41, 644–662. doi: 10.1080/03602530903178905

Yang, X. C., Shang, Y. L., Li, Y. H., Zhai, J., Foster, N. R., Li, Y. X., et al. (2014). Synthesis of monodisperse Iron oxide nanoparticles without surfactants. *J. Nanomat.* 2014:740856. doi: 10.1155/2014/740856

Yuen, C., and Liu, Q. (2012). Magnetic field enriched surface enhanced resonance Raman spectroscopy for early malaria diagnosis. *J. Biomed. Optics* 17:017005. doi: 10.1117/1.JBO.17.1.017005

Zaafarany, I., and Boller, H. (2009). Electrochemical behavior of copper electrode in sodium hydroxide solutions. *Curr World Environ.* 4, 277–284. doi: 10.12944/CWE.4.2.32

Ziegler, J., Linck, R., and Wright, D. W. (2001). Heme aggregation inhibitors: antimalarial drugs targeting an essential biomineralization process. *Curr. Med. Chem.* 8, 171–189. doi: 10.2174/0929867013373840

Conflict of Interest Statement: The authors declare that the research was conducted in the absence of any commercial or financial relationships that could be construed as a potential conflict of interest.

frontiers in Chemistry

ORIGINAL RESEARCH
published: 27 March 2019
doi: 10.3389/fchem.2019.00147

Carbon Nanotubes Modified With Au for Electrochemical Detection of Prostate Specific Antigen: Effect of Au Nanoparticle Size Distribution

Andrés Felipe Quintero-Jaime[1], *Ángel Berenguer-Murcia*[2], *Diego Cazorla-Amorós*[2] *and Emilia Morallón*[1]*

[1] Departamento de Química Física and Instituto Universitario de Materiales de Alicante (IUMA), University of Alicante, Alicante, Spain, [2] Departamento de Química Inorgánica and Instituto Universitario de Materiales de Alicante (IUMA), University of Alicante, Alicante, Spain

Different functionalized Multi-Wall Carbon Nanotube and gold nanoparticles (AuNPs) were synthesized as biosensor electrodes. These materials have been applied to the detection of the Prostate Specific Antigen (PSA). The synthesis of AuNPs was carried out using polyvinylpyrrolidone (PVP) as protecting agent. The PVP/Au molar ratio (0.5 and 50) controls the nanoparticle size distribution, obtaining a wide and narrow distribution with an average diameter of 9.5 and 6.6 nm, respectively. Nanoparticle size distribution shows an important effect in the electrochemical performance of the biosensor, increasing the electrochemical active surface area (EASA) and promoting the electron-transfer from the redox probe (Ferrocene/Ferrocenium) to the electrode. Furthermore, a narrow and small nanoparticle size distribution enhances the amount of antibodies immobilized on the transducer material and the performance during the detection of the PSA. Significant results were obtained for the quantification of PSA, with a limit of detection of 1 $ng{\cdot}ml^{-1}$ and sensitivities of 0.085 and 0.056 $\mu A{\cdot}mL{\cdot}ng^{-1}$ for the two transducer materials in only 5 min of detection.

Keywords: carbon nanotubes, PSA detection, chronoamperometry, gold nanoparticles, immunosensor

OPEN ACCESS

Edited by:
Vito Di Noto,
University of Padova, Italy

Reviewed by:
Pawel Jozef Kulesza,
University of Warsaw, Poland
Abhishek Lahiri,
Clausthal University of Technology, Germany

***Correspondence:**
Emilia Morallón
morallon@ua.es

Specialty section:
This article was submitted to Electrochemistry, a section of the journal Frontiers in Chemistry

Received: *03 December 2018*
Accepted: *28 February 2019*
Published: *27 March 2019*

Citation:
Quintero-Jaime AF, Berenguer-Murcia Á, Cazorla-Amorós D and Morallón E (2019) Carbon Nanotubes Modified With Au for Electrochemical Detection of Prostate Specific Antigen: Effect of Au Nanoparticle Size Distribution. Front. Chem. 7:147. doi: 10.3389/fchem.2019.00147

INTRODUCTION

Prostate Specific Antigen (PSA) or Kallikrein related peptidase-3, is a serine protease secreted by the prostate gland to seminal fluid, with a single chain of 32–33 kDa. According to the World Health Organization (WHO), prostate cancer is considered the second cause of death by cancer in men, with 307,000 deaths in 2012 (Ryerson et al., 2016; Siegel et al., 2017). One of the reasons for the high mortality of this illness is the application of medical therapy in advanced stages. Normally, blood levels of this protein in healthy men is below 4 $ng{\cdot}mL^{-1}$; then, higher values in the PSA concentration are related with development of tumors in the prostate gland, considering it as a reliable biomarker for early detection of prostate cancer (Villoutreix et al., 1994; Bélanger et al., 1995; Qu et al., 2008; Liu et al., 2012).

Thus, methods for early detection are required for a proper clinical treatment. Unfortunately, current methods for cancer diagnosis, such as a histological test or screening methods based on immunoassays as an ELISA test, are time-consuming and require qualified personnel, which implies high cost (Akter et al., 2012; Wang et al., 2015). In addition, low sensibility and

sensitivity makes detecting the disease difficult, especially in the first stages, where cancer shows an asymptomatic phase (Altintas et al., 2011). For that reason, many researches are trying to find low-cost techniques and improve the parameters of the detection, decreasing the time-response in the measurement.

Nowadays, sensitive detection and accurate quantification of chemical substances in physiological fluids has been a critical factor for a reliable clinical diagnostics of different diseases or medical disorders, for instance infectious diseases, diabetes melitus, Alzheimer's disease, DNA mutations, and cancer (Holliger and Hudson, 2005). Biomarkers are specific molecules (enzymes, proteins), whose concentrations increase during the development of a disease. Therefore, changes in the levels of a biomarker in physiological fluids might be related to the presence of a specific disease, and their measurement is useful for the early detection, monitoring drug therapy and medical control (Jayanthi et al., 2017).

Certainly, biosensors have been one of the most economical and functional analytical devices utilized in the last decade, as a result of their simple use in the detection of specific analytes, especially in complex samples, they are low-cost and easier handling (Turner, 2000). Biosensors are composed of two elements, a biorecognition element (enzymes, antibodies, hormones, proteins, or cells) which recognizes the target analyte, and a transducer material which converts the recognition event between the analyte and the bioreceptor in a measurable signal. Electrochemical biosensors are one of the most applied and commercialized at present (Ronkainen et al., 2010; Pisoschi, 2013).

Since the commercial implementation of electrochemical biosensors in the quantification of glucose in blood proposed by Clark and Lyons (Wang, 2002), recent advances in the biosensor field, especially in the application of nanomaterials, have brought a remarkable development in the miniaturization of electrochemical biosensors, translating in a small amount of sample required for the detection and a reduction of costs for manufacturing of the devices. Moreover, given that biological processes occur in nano and micro scales, nanostructured materials have shown an excellent platform to improve the interaction between the biological species of interest and the biosensor, guaranteeing a good measurement of the concentration. Proof of this concept has been the use of high surface area materials as metal nanoparticles (Au, Pt, Pd, Cu) (Corma and Garcia, 2008; Zhou et al., 2015), carbon materials (carbon nanotubes, graphene, and carbon nanohorns) (Wang and Dai, 2015; Bo et al., 2016), nanomanufactured electrodes, for instance interdigitated electrodes array (IDA), and screen printed electrodes (Abellán-Llobregat et al., 2017; González-Gaitán et al., 2017); producing electrochemical transducers for biosensors with high electroactive area and excellent electron transfer, key properties to provide an excellent sensitivity. At the same time, these materials might offer anchoring sites to promote the immobilization of the biorecognition element; or even promoting a direct electron transfer between the analyte and the electrode without the use of mediators or other species in the medium (Santos et al., 2015; González-Gaitán et al., 2017).

Integration between electrochemistry with other detection methods, such as enzyme immunoassays (EI), has created new platforms for biosensors with high sensibility and selectivity, benefitting from the specificity of the antigen-antibody reaction or the DNA chains hybridization, called electrochemical immunosensors, as several works have reported (Kavosi et al., 2014). Depending on the configuration of the immunosensors, they can be classified as "label-free" or "sandwich type." The first ones employ the interaction of the antibody (Ab) as biorecognition element with the antigen (Ag) to create an immunocomplex (Ab-Ag) onto the surface which will block the surface for electron transfer of some electroactive species (Okuno et al., 2007; Wang et al., 2013). On the other hand, sandwich type uses the coupling of a second antibody with antigen immobilized, creating an immunocomplex Ab_1-Ag-Ab_2, to increase the electrical barrier of the system. However, several works have developed sandwich type immunosensors with a second antibody labeled with peroxidase or phosphatase enzymes which catalyzes the hydrogen peroxide reduction, creating an increase in the electrochemical signal (Yu et al., 2006); (Yan et al., 2012).

Even though PSA detection has been widely studied using different electrochemical techniques, the high time consumption to quantify the concentration of the analyte has not been solved, taking at least 24 h for its analysis.

In this work a label-free electrochemical platform has been studied for the fast measurement of concentrations of PSA for the identification of the biomarker. Then, electrochemical detection of PSA was carried out with glassy carbon electrodes (GC) modified with functionalized multi-wall carbon nanotubes decorated with gold nanoparticles and the immobilization of monoclonal antibodies to the PSA.

EXPERIMENTAL SECTION

Reagents and Equipment

Multi-Wall Carbon Nanotubes (MWCNT) with purity 95% (8 nm of diameter) and 10–30 μm length were purchased to Cheap Tubes Inc. (Cambridgeport, USA). Nitric acid (65%) from Panreac was employed to functionalize and purify the carbon nanotubes. Purified mouse monoclonal PSA antibody (Ab) (Purified IgG-Ab) and native human PSA purified were purchased from Bio-Rad Laboratories (Munich, Germany).

Potassium dihydrogen phosphate (KH_2PO_4) and dipotassium hydrogen phosphate (K_2HPO_4) obtained from Merck and VWR Chemicals, respectively, were used to prepare phosphate buffer solutions (0.01 M PBS, pH = 7.2 and 0.1 M PBS, pH = 7.2) to dissolve the immunoreagents and as electrolyte, unless otherwise noted. Ferrocenium hexafluorophosphate (Fc-97%), employed as redox probe was purchased from Sigma Aldrich. All the solutions were prepared using ultrapure water (18 MOhm·cm, Purelab Ultra Elga equipment). The gases N_2 (99.999%) and H_2 (99.999%) were provided by Air Liquide.

Reagents employed in the gold nanoparticles synthesis included sodium tetrachloroaurate (III) dihydrate *(*$NaAuCl_4 \cdot 2H_2O$, 99%*)*, poly-n-vinylpyrrolidone (PVP, 40K), sodium

hydroxide (NaOH, 99,99% purity), anhydrous ethylene glycol and methanol (+98%) and were purchased from Sigma-Aldrich.

Preparation of the Transducer Material. Functionalized Multiwall Carbon Nanotubes (fMWCNT) With Gold Nanoparticles (AuNPs)

Functionalization of Multi-Wall Carbon Nanotubes

Multi-Wall carbon nanotubes (MWCNT) were subjected to a functionalization treatment by oxidation in nitric acid solution, according to the following procedure. In a two-necked, round-bottom flask, 200 mg of MWCNT were added in 100 mL of 3 M HNO_3 at 120°C for 24 h under reflux conditions.

MWCNTs were extracted after 24 h, filtered, washed with ultrapure water until the pH was neutral and dried in vacuum at 60°C for 24 h, and weighed. The sample was called fMWCNTs. These fMWCNTs were dispersed in water using sonication bath for 10 min, to get a concentration of 1 mg·mL^{-1}.

Gold Nanoparticles Synthesis

Gold nanoparticles were synthesized following the reduction-by-solvent method (Lu et al., 1999), adapting a previously published procedure (Domínguez-Domínguez et al., 2006). Given that, this procedure allows a control of the nanoparticle size distribution varying the molar ratio PVP/Au. In this research, two syntheses were carried out using two PVP/Au molar ratios (0.5 and 50). At the same time, all the chemical reactions during the synthesis were carried out in an inert atmosphere of argon, using a Schlenk system to avoid undesirable reactions. A typical synthesis is carried out as described in section S1.1 in supporting information (see **Figure S1**).

fMWCNT Decorated With AuNPs Dispersion

Transducer materials were prepared by the impregnation method in liquid phase, where the suspensions of the carbon material were put in contact with the nanoparticles colloid. Suspensions of fMWCNT (1 mg·mL^{-1}) were mixed with an appropriate amount of purified gold nanoparticles suspension (1 mg·mL^{-1}) to yield 5% (w/w) of metal loading. The dispersions were sonicated and stirred overnight in order to ensure the adsorption of the metal nanoparticles. Samples were filtered in vacuum to remove non-adsorbed nanoparticles and dried in vacuum at 60°C for 24 h. Based on the ratio PVP/Au used in the synthesis, transducer material will be named as fMWCNT-AuNPs-0.5 ratio and fMWCNT-AuNPs-50 ratio, for 0.5 and 50 ratios, respectively.

Immunosensor Electrode Preparation

A schematic diagram of the stepwise assembly procedure of the immunosensor is shown in **Scheme 1**. Prior to the modification, glassy carbon electrodes surface (3 mm diameter) was sanded with emery paper and polished using 1 and 0.05 μm alumina slurries, then rinsed with ultrapure water. Ten milligrams of the transducer material (fMWCNT-AuNPs) were dispersed in water with the aid of ultrasonic bath for 45 min, using an ice bath to avoid heating during the sonication. A 4 μL aliquot of the dispersion was dropped onto the glassy carbon (GC) surface and dried under an infrared lamp to remove the water. This procedure was repeated 3 times until completing 12 μL of the carbon material suspension on the electrode. Then, 5 μL of monoclonal antibodies solution (10 μg·mL^{-1}) were added onto the electrode surface and incubated at 4°C for 24 h, yielding the GC-fMWCNT-AuNPs-Ab electrode with 4.16 μg Ab·g^{-1}_{fMWCNT} of loading. Subsequently, electrodes were rinsed with PBS (0.01 M, pH = 7.2) to remove all non-reacted material. Afterwards, the electrodes were stored in PBS (0.1M, pH = 7.2) solution at 4°C before electrochemical detection of PSA in 0.1 M PBS + 0.5 mM Fc (pH = 7.2) by chronoamperometry.

Electrochemical Methods

Electrochemical characterization was performed in an EG&G Princeton Applied Research Model 263A Potentiostat/Galvonastat using a standard three-electrode cell configuration, in which GC-fMWCNT-AuNPs-Ab electrode was the working electrode (WE), a gold wire as counter electrode (CE), and a reversible hydrogen electrode (RHE) introduced in the same electrolyte as reference electrode (RE). All the measurements were carried out in 0.1 M PBS (pH = 7.2) and 0.1 M PBS + 0.5 mM Fc (pH = 7.2) solutions, deoxygenating the cell during the measurement by bubbling nitrogen. Previously, fMWCNT-AuNPs were submitted to a continuous cycling in 0.1 M PBS (pH = 7.2) to clean the electrode.

The electrochemical detection of PSA was carried out by chronoamperometry in a BIOLOGIC SP-300 potentiostat, applying a steady potential of 1.0 V in 0.1 M PBS + 0.5 mM Fc (pH = 7.2) solution. A total of 8–9 aliquots of PSA solution (500 ng·mL^{-1}) were added to the electrochemical cell, achieving concentrations between 1 and 10 ng·mL^{-1}. Three minutes of reaction were maintained after the addition of each aliquot under stirring during the immunoreaction to ensure a good homogenization of the analyte in the electrolyte and promoting the transport of the PSA to the electrode.

All the calibration curves and the electrochemical characterization, including the immobilization process, were performed by triplicate using 3 different electrodes, synthesized separately. Error bars are incorporated in the calibration curves considering the standard deviation. Afterwards the electrochemical determination of PSA, mass of carbon nanotubes modified with AuNPs were determined using the gravimetric capacitance in PBS; in this way, current was normalized to the mass to avoid effect of mass.

Physicochemical Characterization

Transmission electron microscopic measurements (TEM) were carried out using JEOL TEM, JEM-2010 model, which is equipped with and Oxford X-ray detector (EDS), INCA Energy TEM 100 model, and GATAN acquisition camera.

X-Ray photoelectron spectroscopy (XPS) was performed in a VG-Microtech Mutilab 3,000 spectrometer and Al Kα radiation (1253.6 eV). The deconvolution of the XPS Au4f, C1s, S2p, and N1s was done by least squares fitting using Gaussian-Lorentzian curves, while a Shirley line was used for the background determination. The S2p spectra have been analyzed considering the spin-orbit splitting into S2p3/2 and S2p1/2 with a 2:1 peak area ratio and 1.2 eV splitting (Castner et al., 1996). The XPS

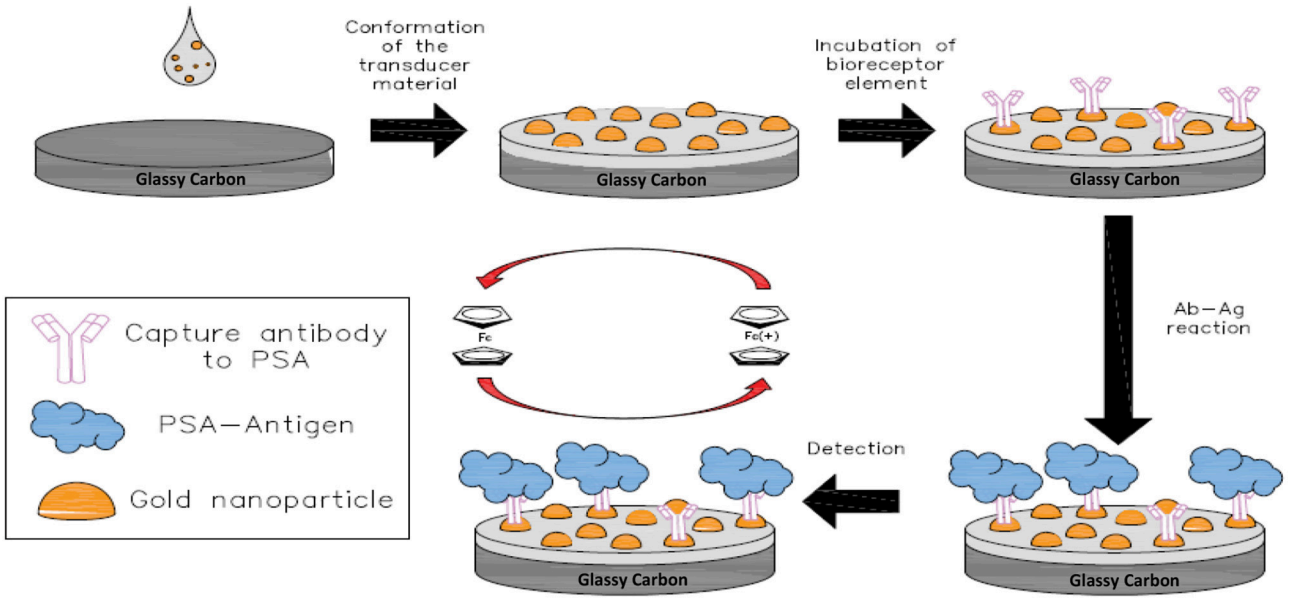

SCHEME 1 | Illustration of the stepwise process for PSA immunosensor electrode fabrication and detection of the cancer biomarker.

measurements were done in different parts of a given sample and repeated in two different samples, being the results similar.

To determine metal content, 10 mg of the carbon material modified with AuNPs were digested in an acid solution [1 HNO_3 (65%):3 HCl (37%)]. The suspension was sonicated for 20 min and heated at 80°C for 6 h until evaporation. Afterwards, 2 mL of HNO_3 were added and diluted with ultrapure water. Solutions were then analyzed using inductively coupled plasma optical emission spectroscopy (ICP-OES), Perkin-Elmer Optima 4,300.

RESULTS AND DISCUSSION

fMWCNT-AuNPs Electrodes Characterization

Physicochemical Characterization

MWCNT pristine material and fMWCNT were studied by temperature programmed desorption (TPD) to observe the nature of the different oxygen surface groups incorporated during the functionalization treatment and by Field Emission Scanning Electron Microscopy (FE-SEM) for studying possible morphological changes in the structure of the carbon material. The most relevant results are presented in section S2.1 in supporting information (see **Figures S2**–**S4** and **S6**, **Table S1** and discussion included in supporting information).

Figure 1 shows the TEM micrographs of the carbon materials with AuNPs. This Figure reveals the distribution and particle size of the AuNPs onto the surface of the carbon nanotubes after the impregnation procedure. As previously reported, PVP concentration during the synthesis of the metal nanoparticles is a key factor to control the nanoparticle size in the colloid (Bönnemann and Richards, 2001; Miguel-García et al., 2010). **Figures 1C,F** show the particle size distribution determined by TEM. As expected, the nanoparticle size distribution decreases to a narrow distribution with the increase of the amount of PVP. The average particle size changes from 9.5 to 6.6 nm with the increase in the PVP/Au ratio. Moreover, agglomeration and a non-spherical shape of the nanoparticles is observed for lower PVP/Au ratio.

Gold loading was quantified by ICP-OES, achieving values of 2.1 and 3.6 wt % for the ratios PVP/Au of 0.5 and 50, respectively (See **Table 1**). Furthermore, XPS spectra for Au-4f core level region of our samples in **Figure S5**, shows two doublets at 84.1 and 87.8 eV associated with Au^0 species and at 84.9 and 88.6 eV related with a higher oxidized state ($Au^{+\delta}$ species) (Jasmin et al., 2017; Liberman et al., 2017). The $Au^0/Au^{+\delta}$ ratio is for both samples 90.5%.

Electrochemical Characterization of fMWCNT-AuNPs

Figure 2 shows the cyclic voltammograms (CV) for fMWCNT and fMWCNT-AuNPs modified GC electrode between 0.1 and 1.8 V. The CV for fMWCNT shows an oxidation peak at ∼ 0.6 V, with the corresponding reduction peak at 0.55 V; which are associated with the surface oxygen groups formed during the functionalization treatment. At the same time, the capacitance of these fMWCNTs is 43 $F{\cdot}g^{-1}$, a value similar to that previously reported in similar conditions (González-Gaitán et al., 2017). However, incorporation of the gold nanoparticles in the carbon material generate an additional oxidation process at 1.5 V and the corresponding reduction at 1.15 V, corresponding with the oxidation-reduction of the gold oxide in the surface of the nanoparticles (Sukeri et al., 2015).

It is well-known that nanoparticle size has an important influence in the electrochemical active surface area (EASA) and smaller nanoparticle size implies an increase in the EASA (Zaragoza-Martín et al., 2007; Sukeri et al., 2015; Ayán-Varela et al., 2017). **Table 1** shows the EASA for the different transducer

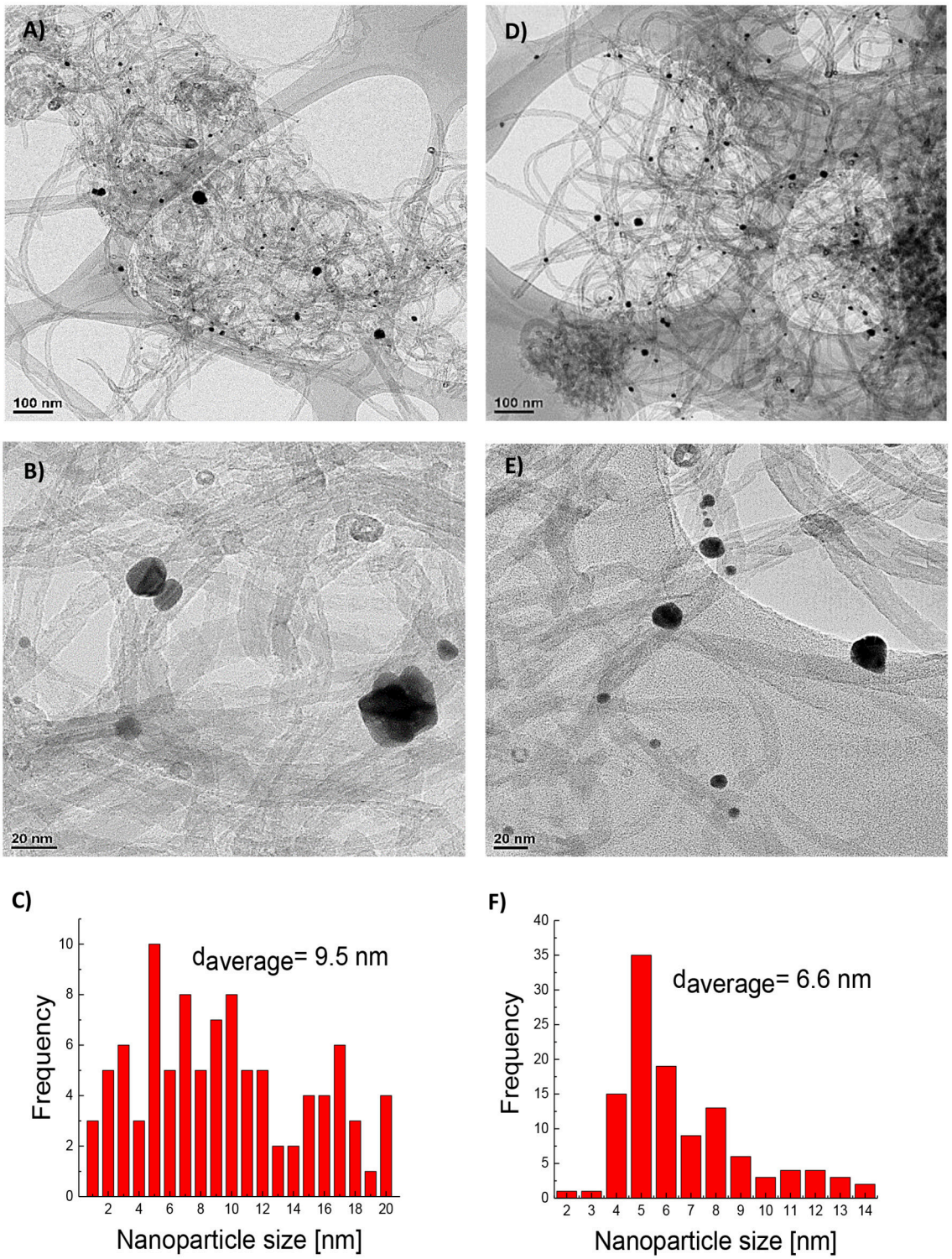

FIGURE 1 | (A–F) HR-TEM micrographs: **(A)** fMWCNT-AuNPs-0.5, **(B)** fMWCNT-AuNPs-0.5 magnified, **(C)** histogram of Au nanoparticle size distribution in fMWCNT-AuNPs-0.5 transducer material, **(D)** fMWCNT-AuNPs-50, **(E)** fMWCNT-AuNPs-50 magnified, and **(F)** histogram of Au nanoparticle size distribution in fMWCNT-AuNPs-50 transducer material.

TABLE 1 | Amount of Au obtained by ICP and EASA in the fMWCNT-AuNPs and fMWCNT-AuNPs-Ab materials.

Sample	Au ICP-OES (wt %)	EASA ($m^2\ g^{-1}$)	S-2p amount by XPS (wt %)	% of Au-S species in the total S-2p
fMWCNT-AuNP-0.5	2.1	28.6	–	–
fMWCNT-AuNP-50	3.6	33.4	–	–
fMWCNT-AuNP-0.5-Ab	–	–	0.16	9
fMWCNT-AuNP-50-Ab	–	–	0.32	28

Amount of S obtained by XPS and percentage of thiol group bound to Au.

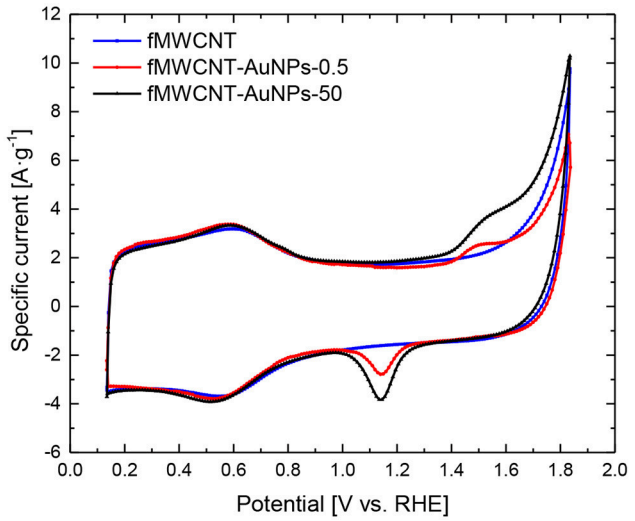

FIGURE 2 | CV for fMWCNT, fMWCNT-AuNPs-0.5 and fMWCNT-AuNPs-50 in 0.1 M PBS (pH = 7.2) and v_{scan} =50 mV·s^{-1}.

material synthesized in this work. It can be observed that the decrease in the particle size implies an increase in the EASA of around 17%.

Electrochemical Characterization of the Monoclonal Antibodies Immobilized on the fMWCNT-AuNPs Samples

Figure 3 shows the CV for the fMWCNT-AuNP electrode before and after immobilization of antibodies. It can be observed that no significant changes are appreciated on the double layer region of carbon nanotubes between 0.1 and 0.75 V for both materials. This result suggests that the immobilization of the antibody is not produced on the carbon nanotube surface. On the other hand, the redox processes for gold surface oxide shows a decrease in the current indicating a blockage of the surface area of AuNP and a decrease in the EASA of 16 and 24% for fMWCNT-AuNPs-0.5 (**Figure 3A**) and fMWCNT-AuNPs-50 (**Figure 3B**), respectively (Dey et al., 2012; Deiminiat et al., 2017). Section S2.2 of the supporting information includes, for comparison purposes, the electrochemical behavior of a polycrystalline gold electrode modified with monoclonal antibodies to PSA (see **Figures S7** and **S8**). The high affinity between thiol groups present in the antibody structure with the gold nanoparticles causes the immobilization of the antibody (Benvidi et al., 2015) producing the observed decrease in available Au surface area.

The covalent interaction between gold and the bioreceptor can be observed in the S2p spectra after immobilization (**Figure 4**), where, S2p3/2 peaks at binding energies of 163.9 and 162.7 eV, can be associated unbound and bound thiol groups (Castner et al., 1996). Considering the low amount of sulfur species, the XPS has significant noise and the deconvolution can only be considered as qualitative. The bound thiol species can be associated to the interaction between the antibody and the gold surface (Yam et al., 2003; Berner et al., 2007; Amendola et al., 2014; Venditti et al., 2017). Then, it can be suggested that the interaction between gold nanoparticles and thiol groups promote the covalent immobilization of the antibodies in the material. The samples with PVP/ratio of 50 presents a much higher intensity of the peak at 162.7 eV, indicating a higher quantity of thiol groups bonded to AuNPs, in contrast with the AuNPs prepared with a lower PVP/Au ratio. This suggests that a higher amount of antibodies are immobilized on the surface of the electrode which contains the smaller average Au nanoparticle size (**Table 1**). Moreover, the presence of a higher amount of covalently bounded Ab-Au in the fMWCNT-AuNPs-50-Ab samples permits either a proper immobilization or even a better orientation of the bioreceptor in the transducer (Trilling et al., 2013). Even though the interaction with thiol generates changes in the oxidation states of gold from Au^0 to $Au^{+\delta}$, authors have observed that the signal of Au^0 can scatter the intensity of the $Au^{+\delta}$, when low concentration of this latter species is present. For that reason no significant changes in gold spectra can be observed (Singh and Whitten, 2008).

Additional signals in the S2p spectra appear at higher binding energies, especially for fMWCNT-AuNPs-0.5-Ab, between 166.4 and 169.6 eV, which can be related with oxidized sulfur species, probably associated with the denaturalization which takes place in the antibody or other direct interactions with the functional groups of the carbon material. These interactions are more probable for the sample with the largest AuNPs size and this produces a larger proportion of inappropriate immobilization of the biorecognition element in the surface of the material (Singh and Whitten, 2008; Trilling et al., 2013).

Electrochemical Performance of the PSA Immunosensor

Despite the blocking effect of the Ab antibodies in the AuNPs surface and subsequent formation of the immunocomplex antibody-antigen, which can be used as a label-free platform

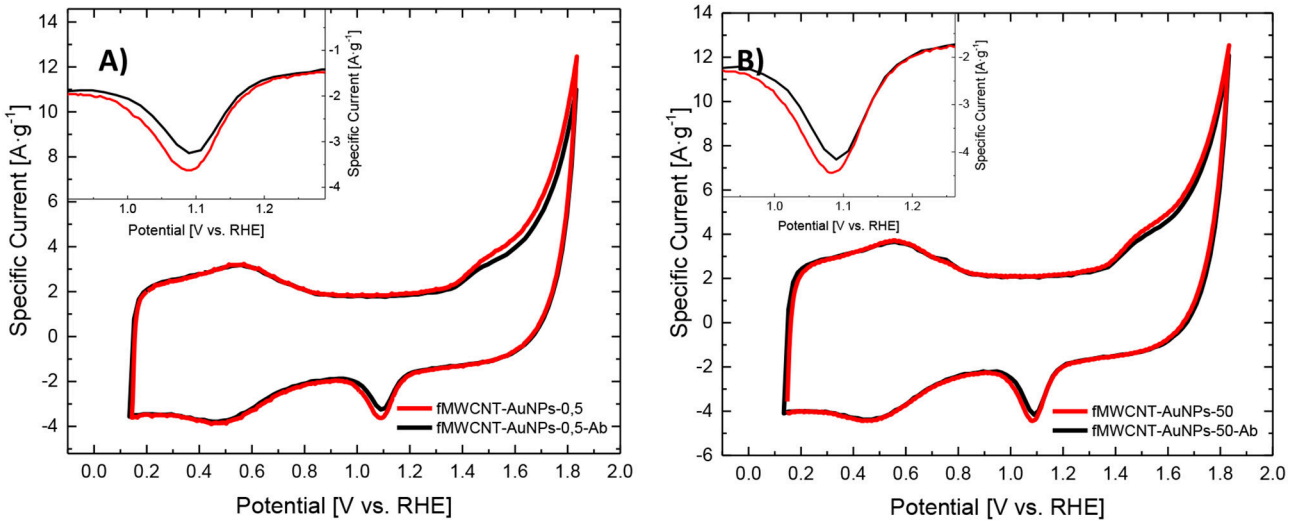

FIGURE 3 | (A,B) Electrochemical behavior of the immunosensor fMWCNT-AuNPs-Ab: **(A)** CV for transducer material before (red line) and after (black line) the immobilization with monoclonal antibodies of fMWCNT-AuNPs-0.5 in 0.1 M PBS (pH = 7.2), v_{scan} =50 mV·s^{-1}, **(B)** CV for transducer material before (red line) and after (black line) the immobilization with monoclonal antibodies of fMWCNT-AuNPs-50 in 0.1 M PBS (pH = 7.2), v_{scan} =50 mV·s^{-1}.

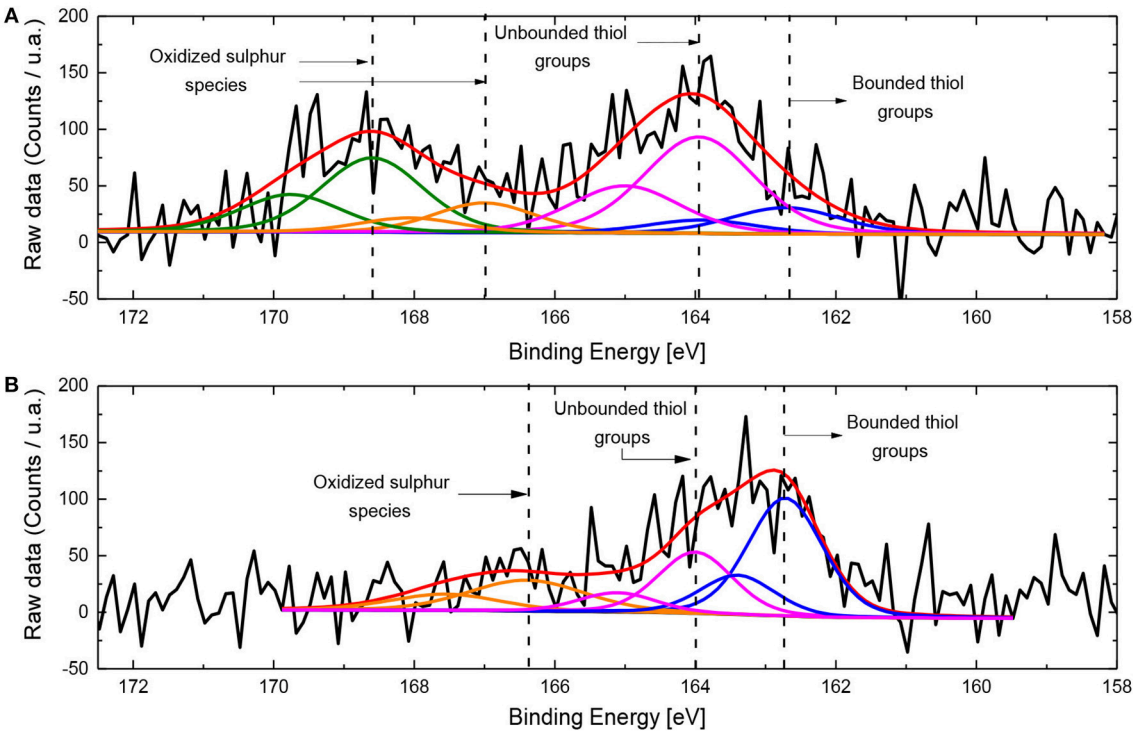

FIGURE 4 | (A,B) XPS spectra for S2p: **(A)** fMWCNT-AuNPs-0.5 and **(B)** fMWCNT-AuNPs-50 synthesized.

for detection, application of the high potential to achieve the oxidation-reduction reaction of gold nanoparticles produces the denaturalization and desorption of the bioreceptor [See Preparation of the transducer material. Functionalized multiwall carbon nanotubes (fMWCNT) with gold nanoparticles (AuNPs)]. Then, a redox mediator could be used in order to decrease the detection potential (Chuah et al., 2012), for this part ferrocene was used as redox mediator for the sensing process of the biomarker.

Figure 5A shows the CVs for the fMWCNT and fMWCNT-AuNPs with different PVP/Au ratios (0.5 and 50) in 0.1 M PBS + 0.5 mM Fc solution, where the corresponding

oxidation-reduction processes of ferrocene at 0.9 and 0.83 V can be observed. Current density for both processes increases with the incorporation of the AuNPs. Moreover, increasing the PVP/Au ratio causes a growth in the current density for both processes, as a result of a larger EASA.

As reported, the oxidation process of ferrocene in aqueous solution is characterized by a single-electron transfer mechanism preceded by a weak adsorption process (Salinas-Torres et al., 2011). In this case, the separation peak for the redox process of ferrocene in fMWCNT at 50 $mV \cdot s^{-1}$ is around 47 ± 1 mV, suggesting that the mechanism for the redox process of ferrocene involves adsorption on the carbon material. On the contrary, incorporation of the AuNPs in the carbon material causes an increase of the separation peak to around 72 ± 1 mV, suggesting that the catalyst avoids the adsorption step during the oxidation process, making the process more irreversible (Sieben et al., 2014). The electrochemical behavior with the scan rate for the different transducer material synthesized in presence of the Fc can be observed in section S2.3 of the **Supporting Information** (see **Figures S9** and **S10**).

Figures 5B, C show the decrease in the peak current for the oxidation process at 0.9 V for electrodes modified with Ab monoclonal antibodies, suggesting that the Fc redox processes are electrochemically impeded, presenting the higher current drop in fMWCNT-AuNPs-50-Ab biosensors. Some authors have suggested that, steric effects of the different functional groups of the antibodies immobilized on the surface, reduce the electron transfer between the electrode and the electroactive species (Fc), which might be used as a label-free platform for detection of the biomarker. These results agree with the XPS results and confirm the presence of the Ab on the surface of AuNPs (Deiminiat et al., 2017).

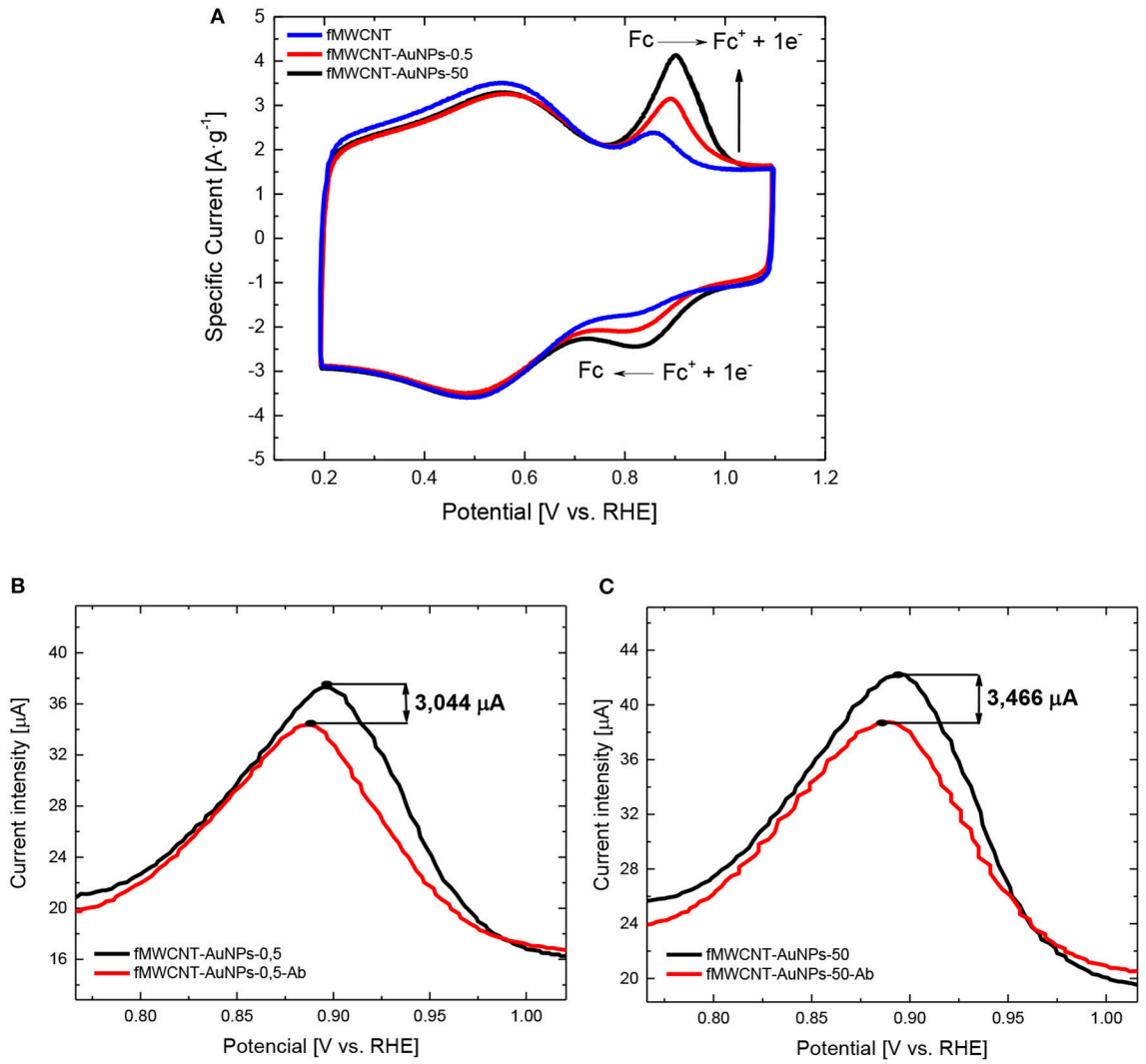

FIGURE 5 | (A–C) Electrochemical behavior of material synthesized in ferrocene: **(A)** CV for fMWCNT and fMWNCT-AuNP in PBS (0.1 M, 0.5 mM Fc, pH = 7.2) and v_{scan} =50 $mV \cdot s^{-1}$, **(B)** CV for transducer material in the oxidation peak before (red line) and after (black line) the immobilization with monoclonal antibodies of fMWCNT-AuNPs-0.5 in 0.1 M PBS + 0.5 mM Fc (pH = 7.2) and v_{scan} =50 mV/s, **(C)** CV for transducer material in the oxidation peak before (red line) and after (black line) the immobilization with monoclonal antibodies of fMWCNT-AuNPs-50 in 0.1 M PBS + 0.5 mM Fc (pH = 7.2) and v_{scan} =50 mV/s.

Immunosensor performance was investigated using chronoamperometry at 1 V with different concentrations of PSA in 0.1 M PBS + 0.5 mM Fc solution. Only 3 min were left between the additions of each aliquot for reaction between Ab immobilized in the AuNPs and PSA in solution. A decrease of the oxidation current associated to Fc is obtained with the increase of the PSA concentration. The change of the current with the addition of PSA can be used as electrochemical signal for detection of PSA. Given that antibody-antigen (Ab-Ag) reaction takes place after the addition of PSA in the solution, the immunocomplex Ab-Ag on the surface of the biosensor might increase the steric effects onto the surface of the electrode, which is translated in a decrease of the current for the ferrocene oxidation process ($Fc \rightarrow Fc + 1e^-$) (Torati et al., 2017). The calibration curves for both electrodes are shown in **Figures 6A,B**, with the chronoamperometric profiles (inset). First of all, decrease in the electrical current density of the oxidation process for ferrocene is observed with the increase of the concentration of PSA, demonstrating the blocking of the surface by the Ab-Ag complex which was mentioned above. Furthermore, all immunosensors show a typical Langmuir behavior, where an initial linear range can be observed and a plateau where the saturation of the biorecognition element takes place. In this case, saturation occurs as a consequence of the interaction of most of the immobilized antibodies with the

TABLE 2 | Analytical figures of merit for the quantification of PSA with both electrochemical modified electrodes (fMWCNT-AuNPs-0.5-Ab and fMWCNT-AuNPs-50-Ab).

Parameter	Sample	
	fMWCNT-AuNP-0.5-Ab	fMWCNT-AuNP-50-Ab
Sensitivity [(mA·g_{fMWCNT}^{-1})/(ng·mL^{-1})]	7.11 ± 0.82	4.74 ± 0.43
Intercept (ng·mL^{-1})	2.48 ± 2.02	2.32 ± 1.22
R	0.96	0.96
N	5	7
Linear range (ng·mL^{-1})	0–4	0–6
LOD (ng·mL^{-1})	1	1
LOQ (ng·mL^{-1})	3.3	3.3

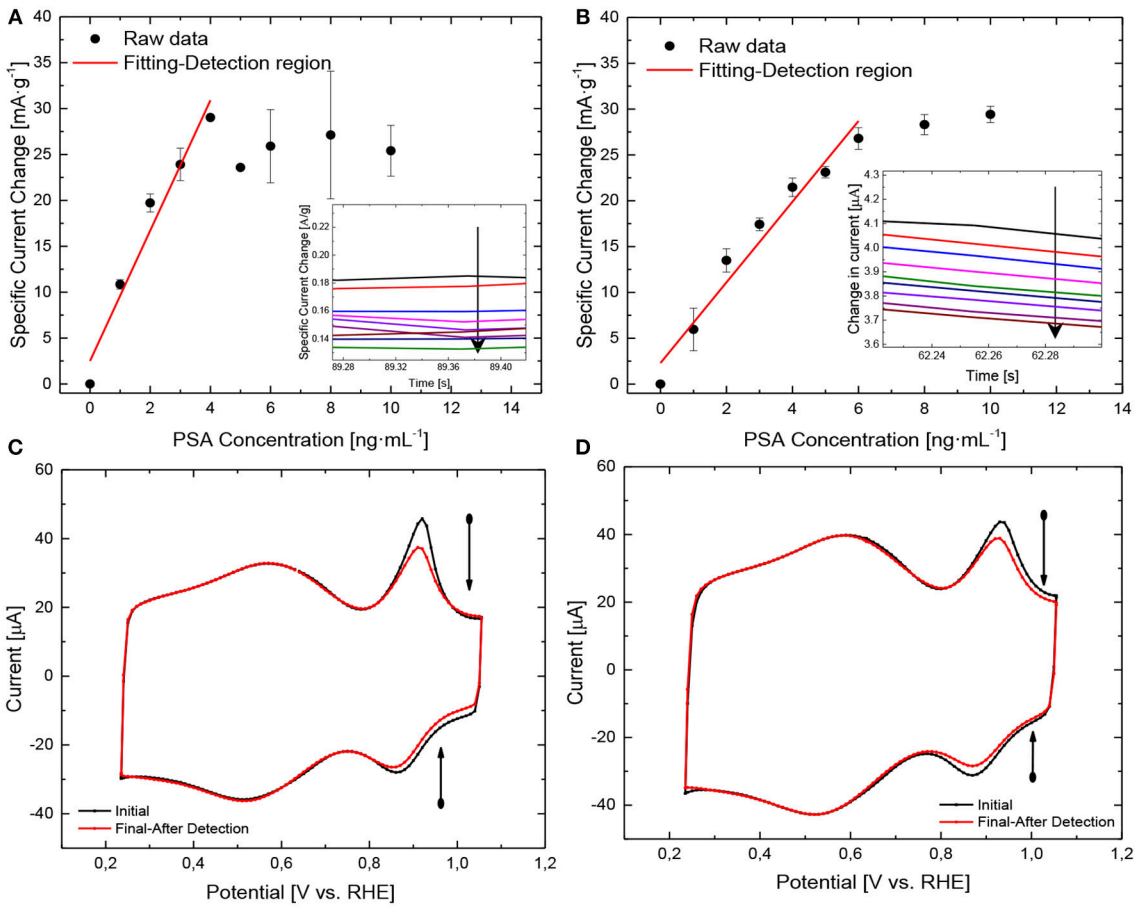

FIGURE 6 | (**A–D**) Electrochemical detection of the biomarker: **(A)** Calibration curve for fMWNCT-AuNPs-0.5-Ab, **(B)** Calibration curve for fMWNCT-AuNPs-50-Ab. All the measurements were performed in 0.1 M PBS + 0.5 mM Fc (pH = 7.2) and v_{scan} =50 mV·s^{-1}, **(C)** CV for fMWNCT-AuNPs-0.5-Ab before (black line) and after (red line) detection of PSA in 0.1 M PBS + 0.5 mM Fc (pH = 7.2) and v_{scan} =50 mV/s, **(D)** CV for fMWNCT-AuNPs-50-Ab before (black line) and after (red line) detection of PSA in 0.1 M PBS + 0.5 mM Fc (pH = 7.2) and v_{scan} =50 mV/s.

TABLE 3 | Analytical parameters for different PSA biosensors.

Electrode	Sample				
	Electrochemical technique (Time to measure)	Detection limit ($ng \cdot mL^{-1}$)	Concentration range ($ng \cdot mL^{-1}$)	Sensitivity ($\mu A \cdot mL \cdot ng^{-1}$)	References
fMWCNT-AuNPs-0.5-Ab	Amperometric (5 min)	1	0–4	0.085	This work
fMWCNT-AuNPs-50-Ab	Amperometric (5 min)	1	0–6	0.056	This work
GC-MWCNT-Reactor	Amperometric (24 h)	1	0–60	0.047	Panini et al., 2008
AuNPs-PANAM dendrimer/MWCNTs/Chitosan/Ionic liquid	Voltametric (24 h)	0.05	0.05–2 (Range 1)	0.0942	(Kavosi et al., 2014)
Pt/Ti patterned-SWCNT	DPV (24 h)	0.25	0–1	…	Okuno et al., 2007

antigen in solution, therefore, no more active sites are available for an enhanced detection of PSA after achieving this saturation and thus no current changes happen. Finally, only an important decrease in the oxidation-reduction processes for ferrocene can be observed in the cyclic voltammograms **Figures 6C, D**, before and after the sensing process, as result of the immune-complex onto the surface which blocks the electron transfer, proving the biosensing activity of the immunosensor synthetized.

The saturation range of the immunosensor takes place at higher concentration values with the increase of PVP/Au ratio, showing at the same time, a higher analytical linear range detection of (0–4 $ng \cdot mL^{-1}$) for fMWNCT-AuNPs-0.5-Ab and (0–6 $ng \cdot mL^{-1}$) for fMWCNT-AuNPs-50-Ab. This behavior can be attributed to the nanoparticle size distribution in the fMWCNT-AuNPs-50-Ab immunosensor, which can provide a higher surface area, promoting a higher amount of biorecognition element immobilized onto the surface, a critical factor in the proper interaction of the fragment antigen-binding (Fab) part of the antibody with the antigen, which is in concordance with the XPS spectra for sulfur observed in section Electrochemical characterization of the monoclonal antibodies immobilized on the fMWCNT-AuNPs samples (Tajima et al., 2011). The linear regression of the calibration curve for both electrodes (fMWCNT-AuNPs-0.5-Ab and fMWCNT-AuNPs-50-Ab) were: $\Delta i\ (mA/g_{\ fMWCNT}) = 7.112\ C_{PSA}\ (ng_{\ PSA} \cdot ml^{-1}) + 2.478$ and $\Delta i\ (mA/g_{\ fMWCNT}) = 4.743\ C_{PSA}\ (ng_{\ PSA} \cdot ml^{-1}) + 1.717$, respectively and with the same correlation coefficient ($R^2 = 0.96$) for both electrodes. On the other hand, the sensitivity of the immunosensor shows a higher value in fMWNCT-AuNPs-0.5-Ab biosensors, in comparison with the samples with the highest PVP/Au ratio, which can be attributed to the fast decrease in the amount of antibodies in the electrode during the detection process, which is also supported by the saturation limit of the immunosensor.

Table 2 shows the analytical parameters obtained with both immunosensors. It can be observed that the sensitivity is higher for the fMWCNT-AuNPs-0.5 electrodes; however, the linear range is higher for the fMWCNT-Au-50 electrode.

Table 3 shows a comparison of some analytical parameters obtained in this work, with data published in the literature. In most of the cases, the sensitivity is similar or higher than the published, being the proposed sensor competitive with respect to previously reported electrochemical sensors. Moreover, time consumption to detect the PSA is greatly improved with respect to other immunosensors.

CONCLUSIONS

Electrochemical PSA sensors based on fMWCNT-AuNPs-Ab with different nanoparticle size distribution were developed. In order to study the effect of the nanoparticle size in the performance of the electrochemical sensor, two different synthesis were carried out, controlling the PVP/Au molar ratio to obtain gold nanoparticles with a wide and narrow distribution, and an average diameter of 9.5 nm and 6.6 nm for PVP/Au ratios of 0.5 and 50, respectively. Incorporation of the metal nanoparticles was verified by CVs, which demonstrated that narrow nanoparticle size distribution has higher EASA.

The prepared electrodes with different Au nanoparticles sizes showed a decrease of the current density of the redox processes associated with the gold oxide formation after the immobilization process of the biorecognition element, as a consequence of the blocking effect of this molecule in the surface. This behavior was shown for ferrocene ($Fc\text{-}Fc^{+}$) employed as redox probe. At the same time, XPS spectra for S2p demonstrated the presence of the S-Au bound, due to the covalent immobilization of the antibodies on the nanoparticle surface. Moreover, narrow Au nanoparticle size distribution promotes a higher immobilization of the antibodies which was seen as an increase in the amount of S-Au bound.

In this work, the electrochemical detection of PSA by chronoamperometry provided a fast method for the detection of this compound, which profits from the steric effects in the surface of the electrode created by the formation of the immunocomplex antibody-antigen, which acts as a diffusional barrier for the electroactive species, which is translated in a decrease in the current intensity of the oxidation processes. Even though a

decrease in current with the increase of PSA concentration can be observed in both biosensors, the lineal range and saturation concentrations is influenced by the nanoparticle size, being fMWCNT-AuNPs-50-Ab the sample which presents the best performance with a higher linear range between 0 and 6 ng·mL^{-1} with a good sensitivity of 4.74 mA g^{-1}/ng mL^{-1}, allowing the detection in human samples.

AUTHOR CONTRIBUTIONS

All authors listed have made a substantial, direct and intellectual contribution to the work, and approved it for publication.

ACKNOWLEDGMENTS

The authors would like to thank MINECO and FEDER (MAT2016-76595-R) for the financial support. AFQJ gratefully acknowledges Generalitat Valenciana for the financial support through Santiago Grisolia grant (GRISOLIA/2016/084).

SUPPLEMENTARY MATERIAL

The Supplementary Material for this article can be found online at: https://www.frontiersin.org/articles/10.3389/fchem.2019.00147/full#supplementary-material

REFERENCES

Abellán-Llobregat, A., Vidal, L., Rodríguez-Amaro, R., Berenguer-Murcia, Á., Canals, A., and Morallón, E. (2017). Au-IDA Microelectrodes Modified with Au-Doped Graphene Oxide for the Simultaneous Determination of Uric Acid and Ascorbic Acid in Urine Samples. *Electrochim Acta* 227, 275–284. doi: 10.1016/j.electacta.2016.12.132

Akter, R., Rahman, M. A., and Rhee, C. K. (2012). Amplified electrochemical detection of a cancer biomarker by enhanced precipitation using horseradish peroxidase attached on carbon nanotubes. *Anal. Chem.* 84, 6407–6415. doi: 10.1021/ac300110n

Altintas, Z., Uludag, Y., Gurbuz, Y., and Tothill, I. E. (2011). Surface plasmon resonance based immunosensor for the detection of the cancer biomarker carcinoembryonic antigen. *Talanta* 86, 377–383. doi: 10.1016/j.talanta.2011.09.031

Amendola, V., Scaramuzza, S., Agnoli, S., Polizzi, S., and Meneghetti, M. (2014). Strong dependence of surface plasmon resonance and surface enhanced raman scattering on the composition of Au–Fe nanoalloys. *Nanoscale* 6, 1423–1433. doi: 10.1039/C3NR04995G

Ayán-Varela, M., Ruiz-Rosas, R., Villar-Rodil, S., Paredes, J. I., Cazorla-Amorós, D., Morallón, E., et al. (2017). Efficient Pt electrocatalysts supported onto flavin mononucleotide–exfoliated pristine graphene for the methanol oxidation reaction. *Electrochim. Acta* 231, 386–395. doi: 10.1016/j.electacta.2016.12.177

Bélanger, A., van Halbeek, H., Graves, H. C., Grandbois, K., Stamey, T. A., Huang, L., et al. (1995). Molecular mass and carbohydrate structure of prostate specific antigen: studies for establishment of an international PSA standard. *Prostate* 27, 187–197. doi: 10.1002/pros.2990270403

Benvidi, A., Firouzabadi, A. D., Moshtaghiun, S. M., Mazloum-Ardakani, M., and Tezerjani, M. D. (2015). Ultrasensitive DNA sensor based on gold nanoparticles/reduced graphene oxide/glassy carbon electrode. *Anal. Biochem.* 484, 24–30. doi: 10.1016/j.ab.2015.05.009

Berner, S., Lidbaum, H., Ledung, G., Åhlund, J., Nilson, K., Schiessling, J., et al. (2007). Electronic and structural studies of immobilized thiol-derivatized cobalt porphyrins on gold surfaces. *Appl. Surf. Sci.* 253, 7540–7548. doi: 10.1016/j.apsusc.2007.03.066

Bo, X., Zhou, M., and Guo, L. (2016). Electrochemical sensors and biosensors based on less aggregated graphene. *Biosens. Bioelectron.* 89, 1–20. doi: 10.1016/j.bios.2016.05.002

Bönnemann, H., and Richards, R. M. (2001). Nanoscopic metal particles – synthetic methods and potential applications. *Eur. J. Inorg. Chem.* 2001, 2455–2480. doi: 10.1002/1099-0682(200109)2001:10<2455::2001:10<2455::AID-EJIC2455>3.0.CO;2-Z

Castner, D. G., Hinds, K., and Grainger, D. W. (1996). X-Ray photoelectron spectroscopy sulfur 2p study of organic thiol and disulfide binding interactions with gold surfaces. *Langmuir* 12, 5083–5086. doi: 10.1021/la960465w

Chuah, K., Lai, L. M. H., Goon, I. Y., Parker, S. G., Amal, R., and Justin Gooding, J. (2012). Ultrasensitive electrochemical detection of prostate-specific antigen (psa) using gold-coated magnetic nanoparticles as "dispersible electrodes." *Chem. Commun.* 48, 3503–3505. doi: 10.1039/c2cc30512g

Corma, A., and Garcia, H. (2008). Supported gold nanoparticles as catalysts for organic reactions. *Chem. Soc. Rev.* 37:2096. doi: 10.1039/b707314n

Deiminiat, B., Rounaghi, G. H., Arbab-Zavar, M. H., and Razavipanah, I. (2017). A Novel Electrochemical aptasensor based on F-MWCNTs/AuNPs nanocomposite for label-free detection of bisphenol, A. *Sensors Actua. B Chem.* 242, 158–166. doi: 10.1016/j.snb.2016.11.041

Dey, A., Kaushik, A., Arya, S. K., and Bhansali, S. (2012). Mediator free highly sensitive polyaniline–gold hybrid nanocomposite based immunosensor for prostate-specific antigen (PSA) detection. *J. Mater. Chem.* 22:14763. doi: 10.1039/c2jm31663c

Domínguez-Domínguez, S., Berenguer-Murcia, Á., Cazorla-Amorós, D., and Linares-Solano, Á. (2006). Semihydrogenation of phenylacetylene catalyzed by metallic nanoparticles containing noble metals. *J. Catal.* 243, 74–81. doi: 10.1016/j.jcat.2006.06.027

González-Gaitán, C., Ruiz-Rosas, R., Morallón, E., and Cazorla-Amorós, D. (2017). Effects of the surface chemistry and structure of carbon nanotubes on the coating of glucose oxidase and electrochemical biosensors performance. *RSC Adv.* 7, 26867–26878. doi: 10.1039/C7RA02380D

Holliger, P., and Hudson, P. J. (2005). Engineered antibody fragments and the rise of single domains. *Nat. Biotechnol.* 23, 1126–1136. doi: 10.1038/nbt1142

Jasmin, J.-P., Miserque, F., Dumas, E., Vickridge, I., Ganem, J.-J., Cannizzo, C., et al. (2017). XPS and NRA Investigations during the fabrication of gold nanostructured functionalized screen-printed sensors for the detection of metallic pollutants. *Appl. Surf. Sci.* 397, 159–166. doi: 10.1016/j.apsusc.2016.11.125

Jayanthi, V. S. P. K. S. A., Das, A. B., and Saxena, U. (2017). Recent advances in biosensor development for the detection of cancer biomarkers. *Biosens. Bioelectron.* 91, 15–23. doi: 10.1016/j.bios.2016.12.014

Kavosi, B., Salimi, A., Hallaj, R., and Amani, K. (2014). A highly sensitive prostate-specific antigen immunosensor based on gold nanoparticles/PAMAM Dendrimer Loaded on MWCNTS/Chitosan/ionic liquid nanocomposite. *Biosens. Bioelectron.* 52, 20–28. doi: 10.1016/j.bios.2013.08.012

Liberman, E. Y., Naumkin, A., V; Tsodikov, M., V; Mikhailichenko, A. I., Kon'kova, T., V; Grunskii, V. N., et al. (2017). Synthesis, structure, and properties of a Au/MnOx–CeO2 Nanocatalyst for low-temperature oxidation of carbon monoxide. *Inorg. Mater.* 53, 406–412. doi: 10.1134/S0020168517040112

Liu, B., Lu, L., Hua, E., Jiang, S., and Xie, G. (2012). Detection of the human prostate-specific antigen using an aptasensor with gold nanoparticles encapsulated by graphitized mesoporous carbon. *Microchim Acta* 178, 163–170. doi: 10.1007/s00604-012-0822-5

Lu, P., Teranishi, T., Asakura, K., Miyake, M., and Toshima, N. (1999). Polymer-Protected Ni/Pd Bimetallic nano-clusters: preparation, characterization and catalysis for hydrogenation of nitrobenzene. *J. Phys. Chem. B.* 103, 9673–9682. doi: 10.1021/jp992177p

Miguel-García, I., Berenguer-Murcia, Á., and Cazorla-Amorós, D. (2010). Preferential Oxidation of CO catalyzed by supported polymer-protected palladium-based nanoparticles. *Appl. Catal. B Environ.* 98, 161–170. doi: 10.1016/j.apcatb.2010.05.025

Okuno, J., Maehashi, K., Kerman, K., Takamura, Y., Matsumoto, K., and Tamiya, E. (2007). Label-free immunosensor for prostate-specific antigen based on single-walled carbon nanotube array-modified microelectrodes. *Biosens. Bioelectron.* 22, 2377–2381. doi: 10.1016/j.bios.2006.09.038

Panini, N. V., Messina, G. A., Salinas, E., Fernández, H., and Raba, J. (2008). Integrated microfluidic systems with an immunosensor modified with carbon nanotubes for detection of prostate specific antigen (PSA) in human serum samples. *Biosens. Bioelectron.* 23, 1145–1151. doi: 10.1016/j.bios.2007.11.003

Pisoschi, A. M. (2013). Biosensors as bio-based materials in chemical analysis: a review. *J. Biobased Mater. Bioenergy* 7, 19–38. doi: 10.1166/jbmb.2013.1274

Qu, B., Chu, X., Shen, G., and Yu, R. (2008). A novel electrochemical immunosensor based on colabeled silica nanoparticles for determination of total prostate specific antigen in human serum. *Talanta* 76, 785–790. doi: 10.1016/j.talanta.2008.04.026

Ronkainen, N. J., Halsall, H. B., and Heineman, W. R. (2010). Electrochemical biosensors. *Chem. Soc. Rev.* 39, 1747–1763. doi: 10.1039/b714449k

Ryerson, A. B., Eheman, C. R., Altekruse, S. F., Ward, J. W., Jemal, A., Sherman, R. L., et al. (2016). Annual report to the nation on the status of cancer, 1975-2012, featuring the increasing incidence of liver cancer. *Cancer* 122, 1312–1337. doi: 10.1002/cncr.29936

Salinas-Torres, D., Huerta, F., Montilla, F., and Morallón, E. (2011). Study on electroactive and electrocatalytic surfaces of single walled carbon nanotube-modified electrodes. *Electrochim Acta* 56, 2464–2470. doi: 10.1016/j.electacta.2010.11.023

Santos, J. C. S. D., Barbosa, O., Ortiz, C., Berenguer-Murcia, A., Rodrigues, R. C., and Fernandez-Lafuente, R. (2015). Importance of the support properties for immobilization or purification of enzymes. *ChemCatChem* 7, 2413–2432. doi: 10.1002/cctc.201500310

Sieben, J. M., Ansón-casaos, A., Montilla, F., Martínez, M. T., and Morallón, E. (2014). Electrochimica acta electrochemical behaviour of different redox probes on single wall carbon nanotube buckypaper-modified electrodes. *Electrochim Acta* 135, 404–411. doi: 10.1016/j.electacta.2014.05.016

Siegel, R., Miller, K., and Jemal, A. (2017). Cancer Statistics, 2017. *Cancer J.* 67, 7–30. doi: 10.3322/caac.21387

Singh, J., and Whitten, J. E. (2008). Adsorption of 3-mercaptopropyltrimethoxysilane on silicon oxide surfaces and adsorbate interaction with thermally deposited gold. *J. Phys. Chem. C* 112, 19088–19096. doi: 10.1021/jp807536z

Sukeri, A., Saravia, L. P. H., and Bertotti, M. (2015). A facile electrochemical approach to fabricate a nanoporous gold film electrode and its electrocatalytic activity towards dissolved oxygen reduction. *Phys. Chem. Chem. Phys.* 17, 28510–28514. doi: 10.1039/C5CP05220C

Tajima, N., Takai, M., and Ishihara, K. (2011). Significance of antibody orientation unraveled: well-oriented antibodies recorded high binding affinity. *Anal. Chem.* 83, 1969–1976. doi: 10.1021/ac1026786

Torati, S. R., Kasturi, K. C. S. B., Lim, B., and Kim, C. G. (2017). Hierarchical gold nanostructures modified electrode for electrochemical detection of cancer antigen CA125. *Sensors Actuat. B Chem.* 243, 64–71. doi: 10.1016/j.snb.2016.11.127

Trilling, A. K., Beekwilder, J., and Zuilhof, H. (2013). Antibody orientation on biosensor surfaces: a minireview. *Analyst* 138, 1619–1627. doi: 10.1039/c2an36787d

Turner, A. P. F. (2000). Biosensors - sense and sensitivity. *Science* 290, 1315–1317. doi: 10.1126/science.290.5495.1315

Venditti, I., Fontana, L., Scaramuzzo, F., Russo, M., Battocchio, C., Carlini, L., et al. (2017). Nanocomposite based on functionalized gold nanoparticles and sulfonated Poly(Ether Ether Ketone) membranes: synthesis and characterization. *Materials* 10:258. doi: 10.3390/ma10030258

Villoutreix, B. O., Getzoff, E. D., and Griffin, J. H. (1994). A structural model for the prostate disease marker, human prostate-specific antigen. *Protein Sci.* 3, 2033–2044. doi: 10.1002/pro.5560031116

Wang, D., Zheng, Y., Chai, Y., Yuan, Y., and Yuan, R. (2015). Target protein induced cleavage of a specific peptide for prostate-specific antigen detection with positively charged gold nanoparticles as signal enhancer †. *Chem. Commun.* 51, 10521–10523. doi: 10.1039/C5CC02148K

Wang, H., Zhang, Y., Yu, H., Wu, D., Ma, H., Li, H., et al. (2013). Label-free electrochemical immunosensor for prostate-specific antigen based on silver hybridized mesoporous silica nanoparticles. *Anal. Biochem.* 434, 123–127. doi: 10.1016/j.ab.2012.11.012

Wang, J. (2002). Glucose biosensors: 40 years of advances and challenges. *Electroanalysis* 10, 107–119. doi: 10.1002/(SICI)1521-4109(199802)10:2<107::AID-ELAN107>3.0.CO;2-B

Wang, Z., and Dai, Z. (2015). Carbon nanomaterial-based electrochemical biosensors: an overview. *Nanoscale* 7, 6420–6431. doi: 10.1039/C5NR00585J

Yam, C. M., Cho, J., and Cai, C. (2003). Preparation, characterization, and heck reaction of multidentate thiolate films on gold surfaces. *Langmuir* 19, 6862–6868. doi: 10.1021/la0345385

Yan, M., Zang, D., Ge, S., Ge, L., and Yu, J. (2012). A disposable electrochemical immunosensor based on carbon screen-printed electrodes for the detection of prostate specific antigen. *Biosens. Bioelectron.* 38, 355–361. doi: 10.1016/j.bios.2012.06.019

Yu, X., Munge, B., Patel, V., Jensen, G., Bhirde, A., Gong, J. D., et al. (2006). Carbon nanotube amplification strategies for highly sensitive immunodetection of cancer biomarkers. *J. Am. Chem. Soc.* 128, 11199–11205. doi: 10.1021/ja062117e

Zaragoza-Martín, F., Sopeña-Escario, D., Morallón, E., and de Lecea, C. S. M. (2007). Pt/Carbon nanofibers electrocatalysts for fuel cells. effect of the support oxidizing treatment. *J. Power Sour.* 171, 302–309. doi: 10.1016/j.jpowsour.2007.06.078

Zhou, W., Gao, X., Liu, D., and Chen, X. (2015). Gold nanoparticles for *in vitro* diagnostics. *Chem. Rev.* 115, 10575–10636. doi: 10.1021/acs.chemrev.5b00100

Conflict of Interest Statement: The authors declare that the research was conducted in the absence of any commercial or financial relationships that could be construed as a potential conflict of interest.

frontiers in Chemistry

ORIGINAL RESEARCH
published: 26 April 2019
doi: 10.3389/fchem.2019.00286

A Printed and Flexible NO_2 Sensor Based on a Solid Polymer Electrolyte

Ru-bai Luo [1,2], Hai-bin Li [1], Bin Du [1,2], Shi-sheng Zhou [1,2] and Yu-heng Chen [1]*

[1] School of Print Packaging and Digital Media, Xi'an University of Technology, Xi'an, China, [2] Shaanxi Collaborative Innovation Center of Green Intelligent Printing and Packaging, Xi'an University of Technology, Xi'an, China

Solid polymer electrolyte (SPE) is an important part of printed electrochemical gas sensors and are of value to electrochemical sensors. Here, a new type of SPE was prepared by dissolving a poly-vinylidene fluoride (PVDF) matrix in a 1-methyl-2-pyrrolidone (NMP) to immobilize 1-ethyl-3-methylimidazolium tetrafluoroborate ([EMIM] [BF_4]), which was then used in a new electrochemical amperometric nitrogen dioxide sensor. The SPE was coated on a single electrode and attached to the electrode to construct a simple two-layer structure. Nitrogen dioxide in the air was reduced on the working electrode at a bias voltage of −500 V. We controlled the components and process parameters separately for control experiments. The results show that the SPE based on [EMIM] [BF_4], NMP, and PVDF coated on the electrode at a thickness of 1.25 mm with a 1:1:4 weight ratio under heat treatment conditions of 80°C for 2 min has the best sensitivity. The FTIR and XPS results indicated that SPE is prepared via physical miscibility. The SEM and XRD results showed that the sensitivity of the sensor is strongly dependent on the interconnected pore structure in SPE, and the pore structure is related to the synthesis ratio, morphology, and heat treatment mode of SPE. Moreover, the sensor sensitivity has a certain relationship with SPE conductivity. The reaction principle and cycle performance of the sensor were also studied.

Keywords: solid polymer electrolyte, gas sensor, screen printing, carbon electrode, double-layered composite structure

OPEN ACCESS

Edited by:
Mahendra Dashrath Shirsat, Dr. Babasaheb Ambedkar Marathwada University, India

Reviewed by:
Manwar Hussain, Hanyang University, South Korea
Yang Yang, University of Central Florida, United States

***Correspondence:**
Bin Du
dubin@xaut.edu.cn

Specialty section:
This article was submitted to Electrochemistry, a section of the journal Frontiers in Chemistry

Received: *14 June 2018*
Accepted: *08 April 2019*
Published: *26 April 2019*

Citation:
Luo R, Li H, Du B, Zhou S and Chen Y (2019) A Printed and Flexible NO_2 Sensor Based on a Solid Polymer Electrolyte. Front. Chem. 7:286. doi: 10.3389/fchem.2019.00286

INTRODUCTION

Air pollution is a major problem (Mattana and Briand, 2016) leading to the development and miniaturization of gas sensors (Li et al., 2016). Printed gas sensors have attracted increasing attention due to their low cost, small size, and ease of manufacture (Zhao et al., 2011). Solid polymer electrolyte (SPE) is widely used in sensor manufacturing. Crowley et al. reported a fully printed SPE-based gas sensor to detect hydrogen sulfide with a detection limit of 2.5 ppm at 10–100 ppm. It had a linear relationship between current and concentration in the 100-ppm region (Crowley et al., 2013; Sarfraz et al., 2013). However, printed gas sensors based on SPE often have defects such as poor stability, low selectivity, complex sensitivity mechanisms, and short lifetimes (Korotcenkov and Cho, 2011). Therefore, the development of a SPE that satisfies better stability and has a simple reaction mechanism is an important hot spot for current and future researchers. For example, Petr Kuberský et al. fabricated an electrochemical gas sensor based on a SPE on a flexible substrate through a complete screen-printing technique that had no metal electrode while also being inexpensive and easily mass produced (Kuberský et al., 2014).

Room temperature ionic liquids consist entirely of ions that possess several properties including negligible vapor pressure, wide potential windows, high thermal stability, and good intrinsic conductivity. This makes them attractive alternative electrochemical solvents and potentially advantageous in the development of stable and robust gas sensors (Buzzeo et al., 2004). To date, several ionic liquids have been widely used for the preparation of SPE. Electrochemical sensors based on different ionic liquids have been used to detect nitrogen dioxide (Silvester, 2011), ammonia (Silvester, 2011; Carter et al., 2016; Sekhar and Kysar, 2017), oxygen (Zevenbergen et al., 2011; Toniolo et al., 2012), ozone (Bidikoudi et al., 2014), and ethylene (Li and Compton, 2015). Nádherná et al. used direct radical polymerization of a mixture of room temperature ionic liquid to detect NO_2 at the platinum electrode (Kuberský et al., 2015). However, gas sensors based on SPE have a three-layer structure (Millet et al., 1996; Nádherná et al., 2011; Vonau et al., 2012; Manjunatha et al., 2014; Goto et al., 2015; Hodgson et al., 2015; Xie et al., 2015), and the fabrication process of this electrode-SPE-electrode composite structure is complicated. In addition, it is necessary to consider the surface bonding ability of the SPE and the double-layer electrode, which is often a constraint of large-scale mass production.

Based on this background, a new type of SPE was prepared from the synthesis of 1-ethyl-3-methylimidazolium tetrafluoroborate ([EMIM] [BF_4]), 1-methyl-2-pyrrolidone (NMP), and poly-vinylidene fluoride (PVDF). [EMIM] [BF_4] is a room-temperature ionic liquid with strong ions that make the liquid highly stable, and it becomes an ideal medium for gas detection. The application of ([EMIM] [BF_4]) in gas sensors can improve the detection limits and increase gas solubility and create wider potential windows (Rogers et al., 2010). The SPE and electrode formed a simple two-layer sensing structure. The results showed that the structure of the gas sensor can detect NO_2. The effect of the proportion of SPE and the control of the synthesis process parameters on the electrochemical performance of the gas sensor was studied to identify the best parameters. The microstructure, molecular properties, and material composition of different SPEs were also studied by scanning electron microscopy (SEM), Fourier transform infrared (FT-IR), X-ray diffraction (XRD), and X-ray photoelectron spectroscopy (XPS). The experiments confirmed the fabrication of a low-cost, fully-printed, and flexible gas sensor on a polyethylene terephthalate (PET) substrate.

EXPERIMENTAL

Materials and Characterizations

The 1-ethyl-3-methylimidazolium tetrafluoroborate ([EMIM] [BF_4], $C_6H_{11}BF_4N$, 99 wt%) and poly-vinylidene fluoride (PVDF, -(CH_2CF_2)n-, 98 wt%) were purchased from Love Pure Biological Technology (Shanghai, China) and used as received. The 1-methyl-2-pyrrolidone (NMP, C_5H_9NO, 99 wt%) was bought from Wuxi Yatai United Chemical (Wuxi, Jiangsu, China) and used as received. The morphology and cross-sectional microstructure of the SPE samples were investigated by field emission scanning electron microscopy (SEM, JEM3010, JEOL, Japan).

Fourier transform infrared (FT-IR) study was performed on a Fourier transform infrared spectrometer (IR, prestige-21/FTIR-8400S, Japan) in a KBr pellet. The resolution was 0.2 cm^{-1}, the number of scans was 16 s^{-1}, and the scan range was from 400 to 4,000 cm^{-1}. X-ray photoelectron spectroscopy (XPS, AXISULTRA, Kratos, UK) was recorded to study the chemical state of the molecules presented at the SPE by using Monochromatic Al Kα (1,486.71 V) line at a power of 100 W (10 mA, 10 KV) with the vacuum of about 10^{-8} Torr. X-ray diffraction (XRD) was performed by using a D/MAX-2550 diffractometer (Rigaku International Co., Japan). The conductivity of the SPE were measured by a four-point probe resistivity measurement system (NAPSON Corporation, RT-70V/RG-5). The electrochemical studies used a potentiometer (PS-12, from Hebei Huachuang Instrument Factory, Jiangsu, China) at a best bias voltage of −500 V.

Electrode Preparation

The interdigitated electrode was prepared by screen printing with carbon paste conductive ink. In a typical manufacturing process, the technological parameters of the JB-45CA screen printing machine (from Zhejiang Jinbao Machinery Co., Ltd. China) were set, the scraper pressure was 100 N/m, the scraper angle was 75°, and the scraper speed was 60 m/min. The carbon paste conductive ink was then evenly applied to one end of the printing plate, and the ink was transferred onto a PET film. The screen-printing plate had a screen number of 350 mesh/inch (1 inch = 0.0254 m) and had been exposed. Finally, the printed electrodes were vacuum dried at 120°C for 30 min.

Synthesis of SPE

The SPE is composed of [EMIM] [BF_4], PVDF, and NMP. Poly-vinylidene fluoride is the matrix and NMP is the solvent of PVDF. The ionic liquid determines the viscosity of the solid electrolyte

TABLE 1 | SPE parameters.

Sample	Ratio	Temperature (°C)	Teat treatment time (min)	Thickness (mm)
S1	1:1:3	80	2	1.25
S2	1:1:4	80	2	1.25
S3	1:1:5	80	2	1.25
S4	1:1:6	80	2	1.25
S5	1:1:4	80	2	1.25
S6	1:1:4	80	5	1.25
S7	1:1:4	80	8	1.25
S8	1:1:4	120	2	1.25
S9	1:1:4	160	2	1.25
S10	1:1:4	80	2	0.75
S11	1:1:4	80	2	1.00
S12	1:1:4	80	2	1.25
S13	1:1:4	80	2	1.50
S14	1:1:4	80	2	1.60

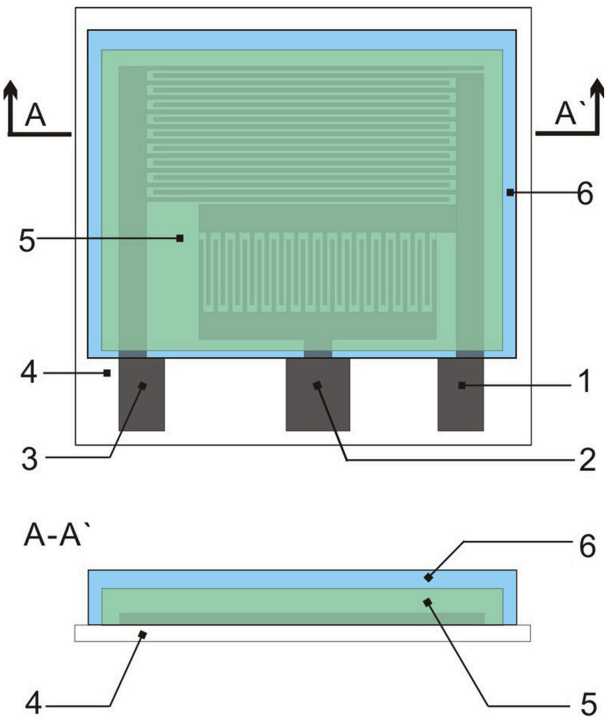

FIGURE 1 | Topology of the sensor: (1) Indicator electrode; (2) Reference electrode; (3) Auxiliary electrode; (4) PET film; (5) SPE; and (6) Hydrophobic membrane.

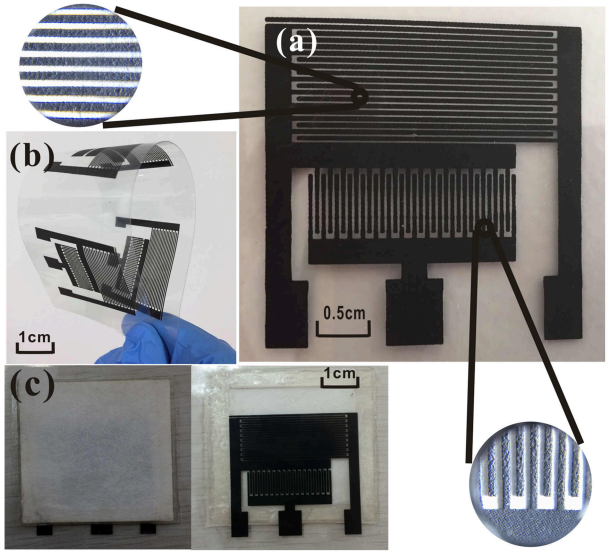

FIGURE 2 | (a) Interdigitated electrode; **(b)** curved electrode; **(c)** NO_2 sensor.

on PET film and the structure of the SPE layer. Gregorio and Borges (2008) described the effect of different temperatures on the crystalline phase of PVDF dissolved in NMP. Therefore, we studied the effect of temperature and blending ratio on the morphology and porosity of SPE. Under different crystallization conditions, we also explored the influence of the SPE coating thickness on sensor gas sensitivity. Here, we synthesized several groups of SPE with different mixing ratios and different processing conditions (**Table 1**). Samples S1–S4 represent four weight ratios of [EMIM] [BF_4], PVDF, and NMP. Samples S5–S9 represent SPE with different heat treatment conditions at optimum ratios. Samples S10–S14 represent the different thicknesses of the SPE coated on the interdigitated electrodes under optimum mixing and heat treatment conditions. We coated this via the equal displacement method. To obtain a uniform SPE, PVDF was gradually added to the mixed liquid in a CJJ78-1 magnetic heating stirrer (from Jintan Dadi Automation Instrument Factory, Wuxi, Zhejiang, China) over 20 min and stirred with a stirring capsule. The SPE was transferred to a D2F-1B vacuum drying oven (Shanghai Keheng Industrial Development Co., Ltd., China) until the SPE was transparent. This was then applied to uncooled SPE on the PET film substrate with interdigital electrode to completely cover the fork. Finally, the sample was held at a stable condition for 24 h under laboratory conditions, and the hydrophobic membrane was coated on the sample with a hot laminating machine.

Measurement Setup

The gas test system for the measurement of sensor characteristics consists of two gas tanks (the first filled with N_2 and the second filled with NO_2), exhaust gas collection devices, two flow controllers, and a sealed glass test room equipped with a potentiograph. The characteristics of all sensors were measured under identical conditions (unless otherwise stated: 20 ± 5°C, 50% RH). A potentiostat with stable potential was used to provide a stable voltage for the sensor. To prevent the influence of interfering substances from passing through a sufficient amount of N_2 to exclude the test room air and then pass in the quantitative NO_2, the required NO_2 concentration is quantitatively controlled by the flow controller for the two gas tanks. The output analog voltage levels from each potentiostat were sampled every other second with two four-channel 24-bit analog to digital converters (ADC; ADS1256, Kangwei Electronics, China), and data were subsequently transferred to a coordinator connected to the computer via wireless sensor data transmission technology. At the end of the sampling, the gas remaining after the reaction was collected and processed through an exhaust gas recovery device.

RESULTS AND DISCUSSION

Sensor Construction

The gas sensor has three patterns on the PET film pair (**Figure 1**). The sensor platform (**Figure 2c**) is prepared on a PET film substrate (4 × 4 cm). The three-electrode system is composed of a working electrode, a reference electrode, and an auxiliary electrode, which has better potential stability and reproducibility than the two-electrode system (Ianeselli et al., 2014; Wardak, 2014). The electrode is closely attached to the SPE and forms the basic part of the sensor. We used a three-electrode system

with interdigitated structures (**Figure 2a**) for capturing more components to be tested. This also saved samples, increased detection signals, and confirmed the distribution of the measured objects. **Figure 2b** shows that screen-printing technology allows the electrode to have a very clear grain, good stability, and good ductility in the bent state. The SPE covers most of the electrode area and only the three ports of the electrode are not attached. The hydrophobic breather membrane completely covers the SPE and is not in contact with the SPE.

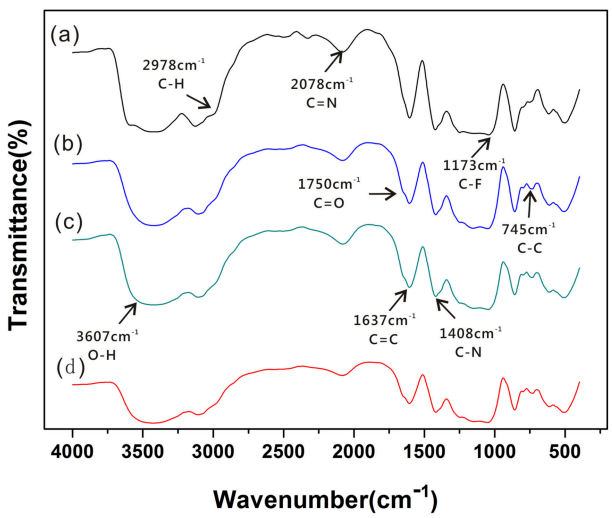

FIGURE 3 | FT-IR spectra of SPE under different NMP content conditions: **(a)** 1:1:3; **(b)** 1:1:4; **(c)** 1:1:5; and **(d)** 1:1:6.

FT-IR Spectral Analysis of SPE

Information on the structural characteristics of SPE was obtained from detailed analysis of the IR region between 200 and 4,200 cm^{-1}. **Figure 3** shows that different ratios of the prepared SPE have a similar molecular structure. **Figures 3**a,c show the characteristic bands at 1,637, 2,078, and 1,408 cm^{-1}. These are attributed to the stretching vibration of C=C, C=N, and C-N from [EMIM] [BF_4] (Sergeev et al., 2018). The intensity of C=C and C=N stretching vibration absorption peak decreases with decreasing [EMIM] [BF_4] concentration. There are characteristic bands at 3,607 cm^{-1} (attributed to stretching vibrations of O-H) and 2,978 cm^{-1} (attributed to stretching vibrations of saturated C-H). In addition, the intensities of the characteristic bands at 1,173 cm^{-1} are associated with stretching vibrations of C-F because of the continuous addition of PVDF during SPE production. Meanwhile, the presence of bands at 1,750 cm^{-1} in **Figure 3**b are attributed to stretching vibrations of C=O of NMP. The IR data shows that the positions of these absorption peaks did not change much indicating that [EMIM] [BF_4] and PVDF have good miscibility in NMP, and the crystal structure of PVDF remains constant. The peak due to the β-Phase is identified at 886 cm^{-1} (Ibtisam et al., 2014). With increasing of PVDF concentration, the β-phase intensity of PVDF increases gradually, and the β phase intensity in **Figure 3**a is obviously larger. This may be an important influencing factor affecting the formation of SPE pore structure and the gas sensitivity of the sensor.

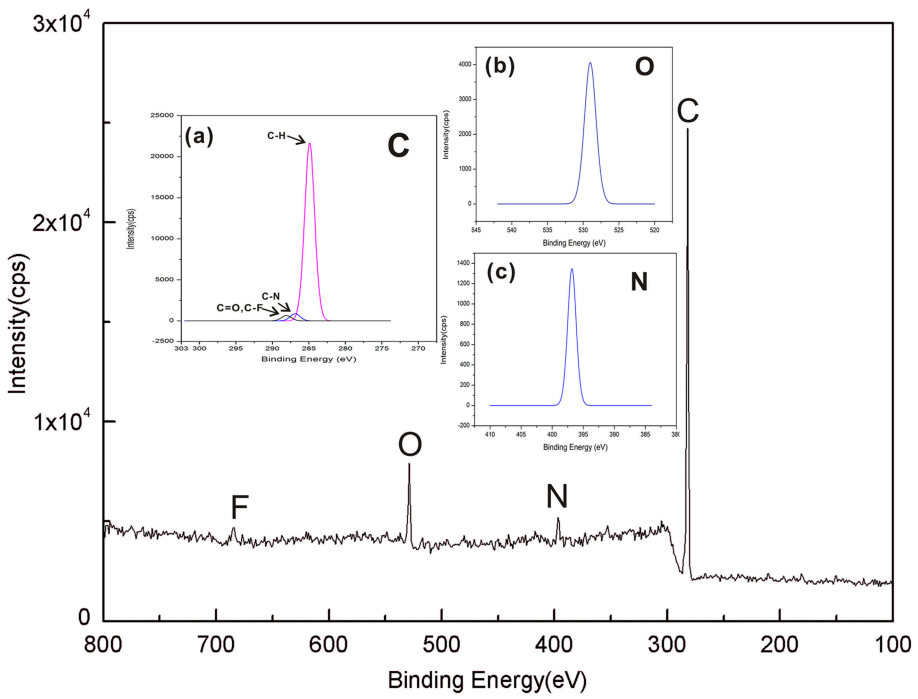

FIGURE 4 | Wide-scan XPS spectra of SPE; **(a)** C1s in SPE; **(b)** O1s in SPE; and **(c)** N1s in SPE.

XPS Analysis of SPE

XPS can investigate the surface elemental compositions and chemical structures of the SPE. The contents of C1s, O1s, F1s, and N1s are shown in **Figure 4**, and the XPS spectra of C1s, O1s, and N1s are shown in **Figures 4**a–c. There are four bands corresponding to C atoms, O atoms, N atoms, and F atoms, respectively, and the chemical composition ratio of C: N: O: F in SPE is as follows: 89.29: 3.15: 6.18: 1.38. **Figure 4**a shows that SPE has three specific peaks at 287.8 eV (C=O, C-F), 286.1 eV (C-N), and 284.7 eV (C-H). These peaks are consistent with the major chemical composition of the constructed SPE. This result confirms that the [EMIM] [BF_4] mixed with PVDF and did not produce a new binding energy. The SPE has specific peaks, which are seen separately in **Figures 4**b,c. These peaks confirm the existence of the two binding energies shown in **Figure 4**a, while further confirming that no new binding energy is produced between the substance that makes up the SPE.

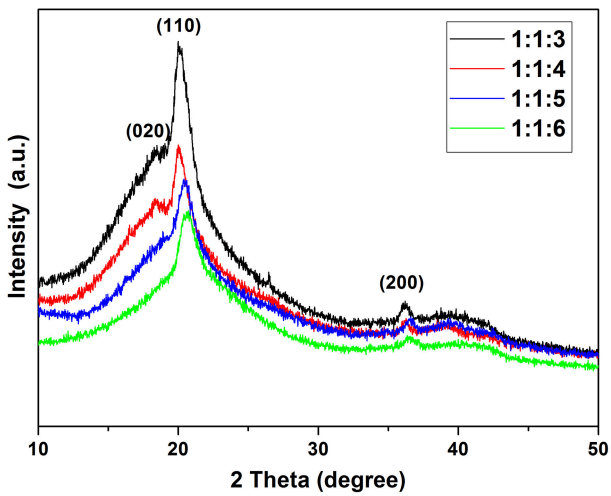

FIGURE 5 | XRD pattern of SPE under different NMP content conditions.

XRD Analysis of SPE

Figure 5 shows the XRD patterns of films of SPE. There are 3 phases in the SPE film, β-Phase (as major phase) at $2\theta = 20.3°$, α-Phase at $2\theta = 18.875°$, and γ-Phase at $2\theta = 36.1°$. These peaks correspond to the diffractions in planes (110), (020), and (200), respectively, all characteristic of the PVDF (Claudia et al., 2010). XRD patterns of different proportions of SPE show that the concentration of NMP in SPE significantly affects the crystallinity of PVDF and the increase of NMP content significantly reduces the β-Phase of PVDF. It can also be seen from the XRD patterns that excessively high NMP concentration will also cause the loss of α-Phase (at ratio of 1:1:6). The effect of NNP concentration on the crystallinity of the SPE sample was also confirmed by FTIR measurements. Versus other samples, the SPE prepared with 1:1:3 exhibits too high crystallinity, which may seriously affect the pore structure of SPE. The reduction of amorphous region will also decrease conductivity and affect gas sensitivity. None of the samples had new crystalline phases indicating that the NMP concentration has no effect on the crystalline phase.

Effect of the Type of SPE

SPE is an important factor for regular functioning of the sensor. [EMIM] [BF_4], PVDF, and NMP can form a solid electrolyte with a pore structure. We systematically studied the effect of different proportions and different heat-treated SPE on the gas sensitivity of the sensor. Gas sensitivity experiments were performed on SPE sensors coated with different ratios according to the test flow chart (**Figure 6**). After the gradual introduction of 175–700 mol of NO_2, sensor sensing data were

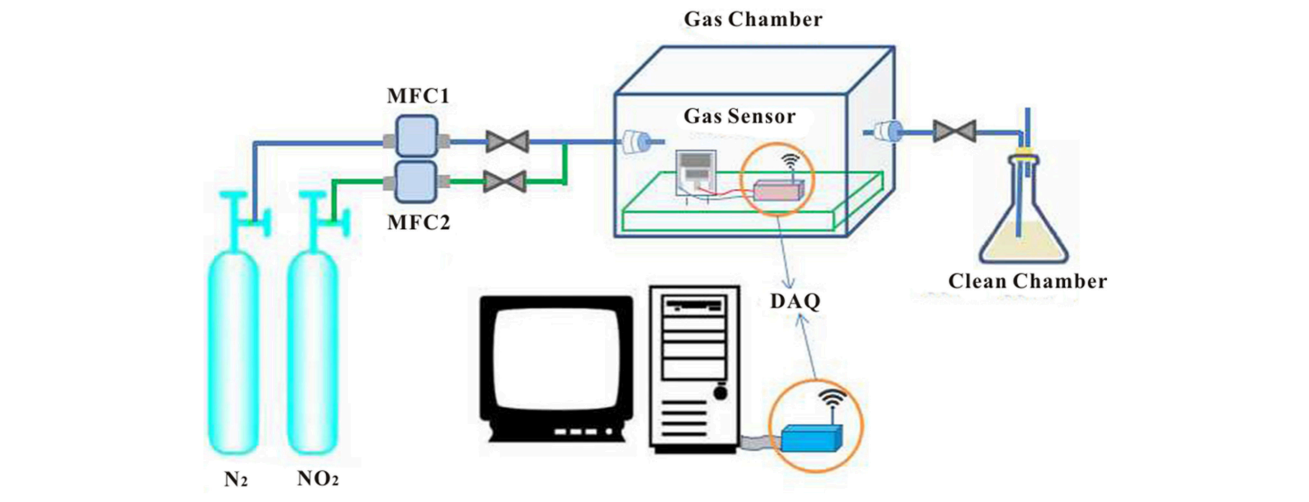

FIGURE 6 | NO_2 detection process (mixing N_2 and NO_2 to reach the test concentration is controlled by two flow controllers, and the gas sensor in the closed reaction chamber detects NO_2. The sensor detects NO_2 and generates a change in current, which is transmitted to the computer via wireless sensor technology. The detection system is also equipped with an exhaust gas recovery device).

acquired and fitted to the calibration curve of the specific sensor to present dependence of sensor current on NO_2 concentration. The sensitivity was determined as the slope of the calibration curve.

Figure 7A shows that the sensor based on a 1:1:4 ratio of SPE has the best gas sensitivity compared with other samples. This may be because PVDF forms a better pore structure at this ratio. As the concentration of [EMIM] [BF_4] increases in the low concentration range, free $[EMIM]^+$ and $[BF_4]^-$ increase in the SPE, and the solubility of SPE to NO_2 and conductivity is enhanced. This improves gas sensitivity. However, with further increases in PVDF concentration, the change of PVDF crystallinity may lead to the internal structure of SPE becoming tight with decreasing porosity. This affects the gas sensitivity.

Table 2 shows that as the concentration of the added ionic liquid increases, the conductivity of the SPE without PVDF also increases. However, this is not true for the relationship between sensor sensitivity and the conductance of the SPE. **Table 3** shows that the SPE prepared at a ratio of 1:1:4 has the highest conductivity. This may be because the concentration of PVDF is too high and results in excessive SPE crystallinity with too high of a viscosity; thus, the amorphous region of SPE is reduced, and the decrease in ion mobility leads to a decrease in electrical conductivity. The difference in sensor sensitivity shown in **Figure 7A** indicates that the conductivity of the SPE also plays an important role in the sensitivity of the NO_2 sensor.

The heat treatment time of the SPE at 80°C does not impact the gas sensitivity of the sensor (**Figure 7B**). Importantly, the heat treatment temperature is increased, and the gas sensitivity is lowered. This means that an increase in the

TABLE 2 | Conductance values of mixed [EMIM] [BF_4] and NMP.

[EMIM] [BF4]: NMP	**1:3**	**1:4**	**1:5**	**1:6**
AC conductance (ms/cm)	18.82	17.35	13.47	10.25

TABLE 3 | Conductance values of the SPE.

PVDF: [EMIM] [BF4]: NMP	**1:1:3**	**1:1:4**	**1:1:5**	**1:1:6**
AC conductance (ms/cm)	3.76	4.62	1.31	0.8

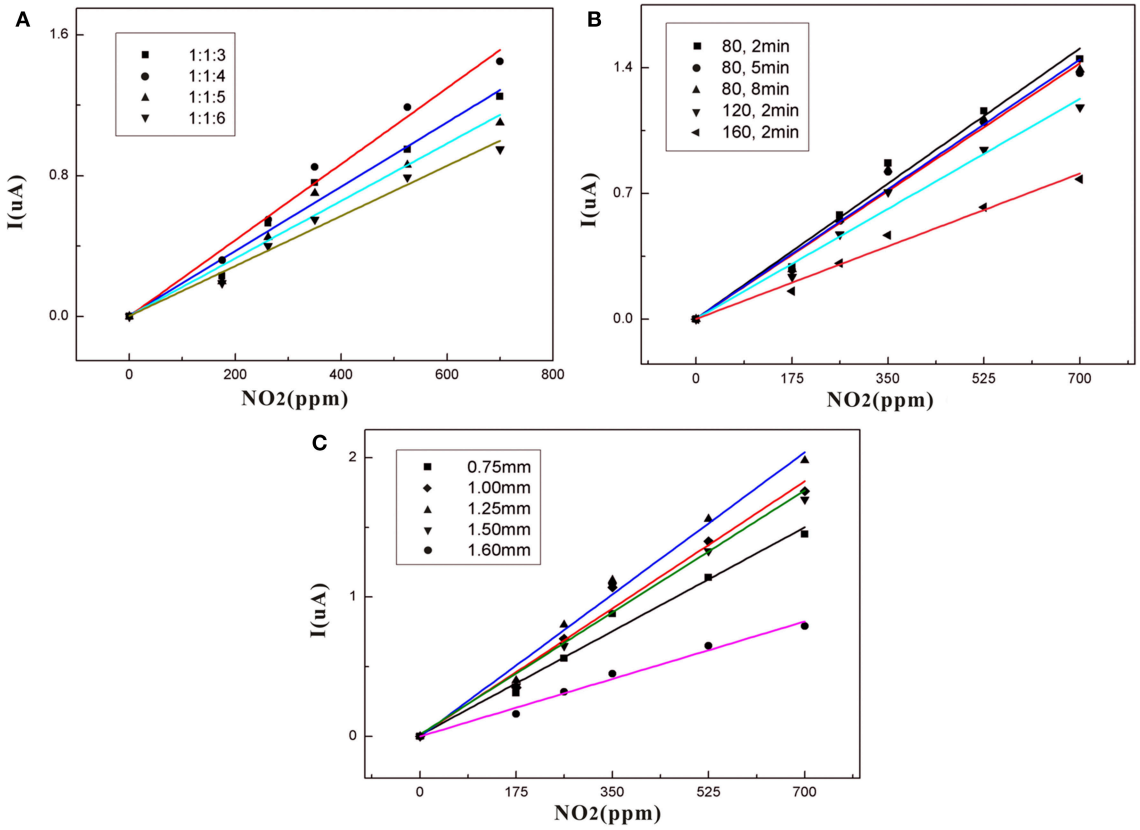

FIGURE 7 | (A) Dependence of sensor current on NO_2 concentration for different NMP contents in the SPE; **(B)** Dependence of sensor current on NO_2 concentration for different thermal treatments in SPE; **(C)** Dependence of sensor current on NO_2 concentration for different thicknesses in SPE.

heat treatment temperature may change the crystalline form of PVDF, which may affect gas sensitivity. The SPE based on the best gas-sensitivity ratio and heat treatment temperature was selected for further detailed study because it exhibited the highest sensitivity. This was coated on electrodes in five thicknesses. The five gas sensitivity curves (**Figure 7C**) indicate that the SPE has the best gas sensitivity at a sensor thickness of 1.25 mm. As the thickness increases, it becomes harder for the NO_2 involved in the redox reaction to come into contact with the electrode surface. However, the SPE volume is reduced when the thickness of the coating is <1.25 mm resulting in conductivity and gas solubility that are incompatible with normal sensor requirements. The sensor calibration fit curve in **Figure 7** is normalized for comparison. Here, *I* represents the current response of the sensor while analyzing the exposure.

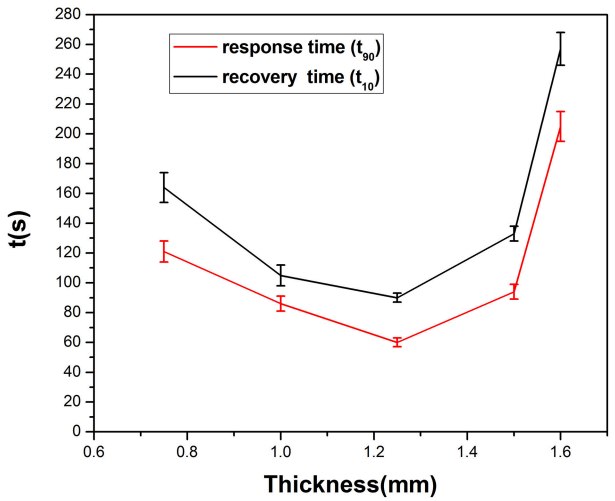

FIGURE 8 | Response time of different SPE thicknesses.

Figure 8 gives information on the relationship between response times (rise time and recovery time) and the thickness of the SPE. The rise/recovery time (t_{90}/t_{10}) was determined as the time period required to achieve 90 or 10% of the full response current upon a step increase/decrease in NO_2 exposure (Mason et al., 1994; Webb et al., 2012; Kuberský et al., 2013). There is longer response time when the thickness is over 1.25 mm and below 1.25 mm. This result indicates that NO_2 detection is strongly dependent on the SPE thickness. The suspected cause of this dependence is the degree of contact of NO_2 with the electrode and the conductivity of the SPE.

Morphology and Microstructure of SPE

We analyzed the morphology and microstructure of SPE to verify the difference in gas sensitivity. The SPE layer has different surface morphologies under different NMP ratios (**Figures 9a–d**). The SPE layer with the least amount of NMP (**Figure 9a**) is a compact plane with almost no pore mechanism indicating that PVDF and [EMIM] [BF_4] account for a larger proportion; it is difficult to form pore structures. In contrast, the SPE layer with the most NMP content (**Figure 9d**) is relatively loose. It has smaller pores, and the effective surface of both is less than the labeled portions in **Figures 7B,C**. **Figure 9b** shows that the SPE layer consists of [EMIM] [BF_4], PVDF, and NMP at a weight ratio of 1:1:4. This contains a significantly larger pore structure, which helps the interdigitated electrode to make better contact with NO_2. This confirms that the sensitivity difference shown in **Figure 7A** is closely related to the pore structure.

As shown in **Figures 9a–f**, the pore structure of the SPE is obvious on the surface of the SPE treated at 80°C for different times. The void ratio is similar. This indicates that the drying time has no significant effect on the formation of the pore structure of the SPE layer and does not affect the dispersion

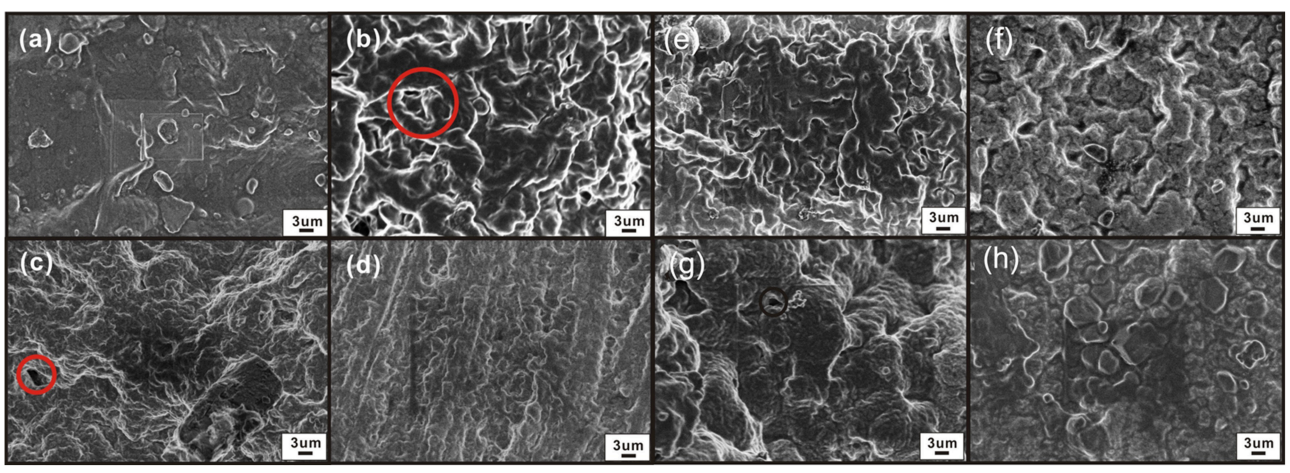

FIGURE 9 | Morphology of the SPE layer under different NMP contents, thermal treatment times, and drying temperature conditions (electron microscope, magnification 15,000×): **(a)** 1:1:3 weight ratio of an [EMIM] [BF_4], PVDF, and NMP, **(b)** 1:1:4; **(c)** 1:1:5; **(d)** 1:1:6; **(e)** 80°C for 5 min; **(f)** 80°C for 8 min.; **(g)** 120°C for 2 min; and **(h)** 160°C for 2 min.

and crystallization of PVDF in the NMP. This verifies that the SPE sensors prepared at different drying times have similar gas sensitivity results (**Figure 7B**).

Figures 9a,g,h are from the surface of the SPE layer: the pores are smaller and fewer in number when the temperature rises. The surface of the SPE is almost free of pores, and the surface is denser and smoother at 160°C. This may arise from the higher crystallization temperature causing excessive deformation and crowding of PVDF during heat treatment. As a result, the cross-linking capacity is destroyed, and the porosity is reduced—this affects the gas sensitivity of the sensor.

Gas Sensor Principle

The principle underlying this SPE-based amperometric NO_2 sensor is the measurement of the current produced by the electrochemical reduction of NO_2 on the electrode. NO_2 contacts the SPE and reaches the working electrode through the pores in the SPE followed by electrochemical reduction. At the same time, the ionic liquid contained in the SPE has a certain gas solubility—this promotes the reduction of NO_2 on the working electrode (Buzzeo et al., 2004). The generally accepted NO_2 reduction reaction at work electrode is represented by Equations (1) and (2).

$$NO_2 + e^- \rightarrow NO_2^- \quad (1)$$

$$NO_2^- + 2H^+ + e^- \rightarrow NO + H_2O \quad (2)$$

A more definite description of the reduction mechanism would require a specialized study involving identification and quantification of the reaction products. Most probably, water is oxidized at the auxiliary electrode:

$$H_2O \rightarrow 2H^+ + 2e^- + 1/2O_2 \quad (3)$$

Thus, the overall reaction occurring in the sensor can be expressed as

$$NO_2 \rightarrow NO + 1/2O_2 \quad (4)$$

The current through the sensor is controlled by the reduction reaction of NO_2 provided that the oxidation reaction of the water in the reaction produces protons and the proton transfer rate from the auxiliary electrode to the working electrode is sufficiently high. The sensor composition remains unchanged during the NO_2 detection. As shown in **Figure 10**, the sensor response has excellent stability and reproducibility with fast response/recovery times (60/90 s).

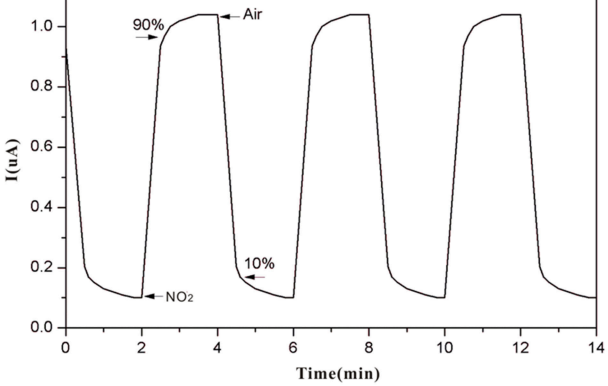

FIGURE 10 | Sensor response to repeated exposures to 100 ppm NO_2.

CONCLUSION

We report a systematic study of an electrochemical NO_2 sensor with an ionic liquid-based SPE and screen-printed carbon electrodes. The sensor gas sensitivity data showed that a 1:1:4 weight ratio [EMIM] [BF_4], PVDF, and NMP had the highest sensitivity. These were dried at 80°C for 2 min and coated on the PET film at a thickness of 1.25 mm. The results demonstrate that the two-layer sensing structure of the interdigital electrode and the SPE can reliably and reproducibly respond to NO_2. FTIR and XPS proved that the synthesis mode of SPE is physical miscibility. Combined with the sensitivity analysis, the effect of SPE on the NO_2 sensor is inseparable from the crystal morphology of PVDF. Moreover, the SEM and XRD of the SPE layer shows that the sensitivity of the sensor strongly depends on the interconnected pore structure formed by PVDF crystallization in SPE. A lower proportion of NMP will lead to a lower formation of pores. On the contrary, an excessive proportion of NMP causes the pore dispersion of PVDF in SPE to become smaller. The crowding of the PVDF substrate is increased with higher heat treatment temperature and longer heating time. In addition, gas sensitivity is also related to the thickness and conductivity of SPE. SPE containing room temperature ionic liquids expands the range of applications of solid electrolytes. The solid electrolyte prepared here can be used to design gas sensors operating at room temperature, and can be used as an alternative to the existing NO_2 sensor in future research and development.

AUTHOR CONTRIBUTIONS

RL, BD, and SZ contributed to the conception and design of the study. YC contributed to synthesis and analyses. HL contributed to manuscript writing and revision. All authors made substantial, direct, and intellectual contributions to the work, and approved it for publication.

FUNDING

This work was supported in part by NSF of the Science and Technology, Department of Shaanxi Province under Grant No. 2016JM5068, NSF of the Key Laboratory of Shaanxi Provincial Department of Education under Grant No. 15JS075

and Shanxi Province green smart printing and packaging collaborative innovation center. The valuable support of Prof. Dr.-Ing. Gunter Hübner at Stuttgart Media University is also gratefully acknowledged.

ACKNOWLEDGMENTS

We thank LetPub (www.letpub.com) for its linguistic assistance during the preparation of this manuscript.

REFERENCES

Bidikoudi, M., Zubeir, L., and Falaras, P. (2014). Low viscosity highly conductive ionic liquid blends for redox active electrolytes in efficient dye-sensitized solar cells. *J. Mater. Chem. A* 2, 15326–15336. doi: 10.1039/C4TA02529F

Buzzeo, C. B., Hardacre, C., and Compton, R. G. (2004). Use of room temperature ionic liquids in gas sensor design. *Anal. Chem*. 76, 4583–4588. doi: 10.1021/ac040042w

Carter, M. T., Stetter, J. R., Findlay, M. W., Meulendyk, B. J., Payel, V., and Peaslee, D. (2016). Amperometric gas sensors: from classical industrial health and safety to environmental awareness and public health. *ECS Trans*. 75, 91–98. doi: 10.1149/07516.0091ecst

Claudia, P., Alessandro, D., Roberto, M., Giancarlo, M., Giuseppe, R., Francesca, B. B., et al. (2010). Hydrophobin-stabilized dispersions of PVDF nanoparticles in water. *J. Fluorine Chem*. 177, 62–69. doi: 10.1016/j.jfluchem.2015.02.004

Crowley, K., Smyth, M. R., Killard, A. J., and Morrin, A. (2013). Printing polyaniline for sensor applications. *Chem. Pap*. 67, 771–780. doi: 10.2478/s11696-012-0301-9

Goto, T., Hyodo, T., Ueda, T., Kamada, K., Kaneyasu, K., and Shimizu, Y. (2015). CO-sensing properties of potentiometric gas sensors using an anion-conducting polymer electrolyte and au-loaded metal oxide electrodes. *Electrochim. Acta* 166, 232–243. doi: 10.1016/j.electacta.2015.03.045

Gregorio, R. Jr., and Borges, D. S. (2008). Effect of crystallization rate on the formation of the polymorphs of solution cast poly(vinylidene fluoride). *Polymer* 49, 4009–4016. doi: 10.1016/j.polymer.2008.07.010

Hodgson, A. W. E., Jacquinot, P., Jordan, L. R., and Hauser, P. C. (2015). Amperometric gas sensors of high sensitivity. *Electroanalysis* 11, 782–787. doi: 10.1002/(SICI)1521-4109(199907)11:10/11<782::AID-ELAN782>3.0.CO;2-S

Ianeselli, L., Grenci, G., Callegari, C., Tormen, M., and Casalis, L.,(2014). Development of stable and reproducible biosensors based on electrochemical impedance spectroscopy: three-electrode versus two-electrode setup. *Biosens. Bioelectron*. 55, 1–6. doi: 10.1016/j.bios.2013.11.067

Ibtisam, Y. A., Muhammad, Y., Mohd, H. H. J., and Haider, M. S. (2014). Effect of annealing process on the phase formation in poly(vinylidene fluoride). *AIP Conf. Proc*. 1614, 147–151. doi: 10.1063/1.4895187

Korotcenkov, G., and Cho, B. K. (2011). Instability of metal oxide-based conductometric gas sensors and approaches to stability improvement (short survey). *Sens. Actuators. B* 156, 527–538. doi: 10.1016/j.snb.2011.02.024

Kuberský, P., Altšmíd, J., Hamáček, A., Nešpurek, S., and Zmeškal, O. (2015). An electrochemical NO_2 sensor based on ionic liquid: influence of the morphology of the polymer electrolyte onsensor sensitivity. *Sensors* 15, 28421–28434. doi: 10.3390/s151128421

Kuberský, P., Hamáček, A., Nešpurek, S., Soukup, R., and Vik, R. (2013). Effect of the geometry of a working electrode on the behavior of a planar amperometric NO_2 sensor based on solid polymer electrolyte. *Sens. Actuators. B* 187, 546–552. doi: 10.1016/j.snb.2013.03.081

Kuberský, P., Syrový, T., Hamáček, A., Nešpurek, S., and Syrová, L. (2014). Fully printed electrochemical NO_2, sensor. *Procedia Eng*. 87, 1043–1046. doi: 10.1016/j.proeng.2014.11.340

Li, P., and Compton, R. G. (2015). Electrochemical high concentration oxygen sensing using a phosphonium cation based room temperature ionic liquid: analytical studies. *Electroanalysis* 27, 1550–1555. doi: 10.1002/elan.201500003

Li, S., Wang, W., Liang,F., and Zhang, W. X. (2016). Heavy metal removal using nanoscale zero-valent iron (nZVI): theory and application. *J. Hazard. Mater*. 322(Pt A), 163–171. doi: 10.1016/j.jhazmat.2016.01.032

Manjunatha, V., Subramanya, K., and Devendrappa, H. (2014). Structural optical and electrical conductivity properties of Li2SO4 doped polymer electrolytes. *Compos. Interfaces* 21, 121–131. doi: 10.1080/15685543.2013.838850

Mason, I. M., Guzkowska, M. A. J., Rapley, C. G., and Street-Perrott, F. A. (1994). The response of lake levels and areas to climatic change. *Clim. Change* 27, 161–197. doi: 10.1007/BF01093590

Mattana, G., and Briand, D. (2016). Recent advances in printed sensors on foil. *Mater. Today* 19, 88–99. doi: 10.1016/j.mattod.2015.08.001

Millet, P., Michas, A., and Durand, R. (1996). A solid polymer electrolyte-based ethanol gas sensor. *J. Appl. Electrochem*. 26, 933–937. doi: 10.1007/BF00242045

Nádherná, M., Opekar, F., and Reiter, J. (2011). Ionic liquid–polymer electrolyte for amperometric solid-state NO_2 sensor. *Electrochim. Acta* 56, 5650–5655. doi: 10.1016/j.electacta.2011.04.022

Rogers, E. I., O'Mahony, A. M., Aldous, L., and Compton, R. G. (2010). Amperometric gas detection using room temperature ionic liquid solvents. *ECS Trans*. 33, 473–502. doi: 10.1149/1.3484806

Sarfraz, J., Ihalainen, P., Määttänen, A., Peltonen, J., and Lindén, M. (2013). Printed hydrogen sulfide gas sensor on paper substrate based on polyaniline composite. *Thin Solid Films* 534, 621–628. doi: 10.1016/j.tsf.2013.02.055

Sekhar, P. K., and Kysar, J. S. (2017). An electrochemical ammonia sensor on paper substrate. *J. Electrochem. Soc*. 164, B113–B117. doi: 10.1149/2.0941704jes

Sergeev, A. S., Tameev, A. R., Zolotarevskii, V. I., and Vannikov, A. V. (2018). Electrically conductive inks based on polymer composition for inkjet printing. *Inorg. Mater*. 9, 147–150. doi: 10.1134/S2075113318010239

Silvester, D. S. (2011). Recent advances in the use of ionic liquids for electrochemical sensing. *Analyst* 136, 4871–4882. doi: 10.1039/c1an15699c

Toniolo, R., Dossi, N., Pizzariello, A., Doherty, A. P., Susmel, S., and Bontempelli, G. (2012). An oxygen amperometric gas sensor based on its electrocatalytic reduction in room temperature ionic liquids. *J. Electroanal. Chem*. 670, 23–29. doi: 10.1016/j.jelechem.2012.02.006

Vonau, C., Zosel, J., Paramasivam, M., Ahlborn, K., Gerlach, F., Vashook, V., et al. (2012). Polymer based materials for solid electrolyte sensors. *Solid State Ionics* 225, 337–341. doi: 10.1016/j.ssi.2012.04.015

Wardak, C. (2014). Solid contact nitrate ion-selective electrode based on ionicliquid with stable and reproducible potential. *Electroanalysis* 26, 864–872. doi: 10.1002/elan.201300590

Webb, D. J., Peng, G. D., and Zhang, W. (2012). Investigation into time response of polymer fiber bragg grating based humidity sensors. *J. Lightwave Technol*. 30, 1090–1096. doi: 10.1109/JLT.2011.2169941

Xie, L., Lu, J., and Yan,. H. (2015). A solid-state ozone sensor based on solid polymer electrolyte. *Electroanalysis* 10, 842–845. doi: 10.1002/(SICI)1521-4109(199809)10:12<842::AID-ELAN842>3.0.CO;2-S

Zevenbergen, M. A. G., Wouters, D., Dam, V. A., Brongersma, S. H., and Crego-Calama, M. (2011). Electrochemical sensing of ethylene employing a thin ionic-liquid layer. *Anal. Chem*. 83, 6300–6307. doi: 10.1021/ac2009756

Zhao, X., Lv, L., Pan, B., Zhang, W., Zhang, S. J., and Zhang, Q. X. (2011). Polymer-supported nanocomposites for environmental application: a review. *Chem. Eng. J*. 170, 381–394. doi: 10.1016/j.cej.2011.02.071

Conflict of Interest Statement: The authors declare that the research was conducted in the absence of any commercial or financial relationships that could be construed as a potential conflict of interest.

frontiers in Chemistry

ORIGINAL RESEARCH
published: 22 August 2019
doi: 10.3389/fchem.2019.00566

Characterization of Perturbing Actions by Verteporfin, a Benzoporphyrin Photosensitizer, on Membrane Ionic Currents

Mei-Han Huang[1], *Ping-Yen Liu*[2] *and Sheng-Nan Wu*[3,4]*

[1] College of Medical and Health Sciences, Fooyin University, Kaohsiung City, Taiwan, [2] Division of Cardiovascular Medicine, National Cheng Kung University Medical College, Tainan City, Taiwan, [3] Institute of Basic Medical Sciences, National Cheng Kung University Medical College, Tainan City, Taiwan, [4] Department of Physiology, National Cheng Kung University Medical College, Tainan City, Taiwan

OPEN ACCESS

Edited by:
Vito Di Noto,
University of Padova, Italy

Reviewed by:
Pramod K. Kalambate,
Huazhong University of Science and Technology, China
Man-Jiang Xie,
Fourth Military Medical University, China
Marta De Zotti,
University of Padova, Italy

***Correspondence:**
Sheng-Nan Wu
snwu@mail.ncku.edu.tw

Specialty section:
This article was submitted to Electrochemistry, a section of the journal Frontiers in Chemistry

Received: *21 February 2019*
Accepted: *25 July 2019*
Published: *22 August 2019*

Citation:
Huang M-H, Liu P-Y and Wu S-N (2019) Characterization of Perturbing Actions by Verteporfin, a Benzoporphyrin Photosensitizer, on Membrane Ionic Currents. Front. Chem. 7:566. doi: 10.3389/fchem.2019.00566

Verteporfin (VP), a benzoporphyrin derivative, has been clinically tailored as a photosensitizer and recently known to suppress YAP-TEAD complex accompanied by suppression of the growth in an array of neoplastic cells. However, the detailed information is little available regarding possible modifications of it and its related compounds on transmembrane ionic currents, despite its growing use in clinical settings. In this study, from whole cell recordings, VP (0.3–100 μM) increased the amplitude of Ca^{2+}-activated K^+ currents ($I_{K(Ca)}$) in pituitary tumor (GH_3) cells in a concentration-dependent manner with an EC_{50} value of 2.4 μM. VP-stimulated $I_{K(Ca)}$ in these cells was suppressed by further addition of either paxilline, iberiotoxin, or dithiothreitol, but not by that of tobultamide or TRAM-39. VP at a concentration of 10 μM mildly suppressed the amplitude of delayed-rectifier K^+ current; however, it had minimal effects on M-type K^+ current. In cell-attached current recordings, addition of VP to the recording medium enhanced the activity of large-conductance Ca^{2+}-activated K^+ (BK_{Ca}) channels. In the presence of VP, additional illumination with light intensity of 5.5 mW/cm^2 raised the probability of BK_{Ca}-channel openings further. Addition of VP decreased the peak amplitude of L-type Ca^{2+} current together with slowed inactivation time course of the current; however, it failed to modify voltage-gated Na^+ current. Illumination of GH_3 cells in continued presence of VP also induced a non-selective cation current. Additionally, VP increased the activity of BK_{Ca} channels in human 13-06-MG glioma cells with an EC_{50} value of 1.9 μM. Therefore, the effects of VP on ionic currents described herein tend to be upstream of its inhibition of YAP-TEAD complex and they are conceivably likely to contribute to the underlying mechanisms through which it and its structurally similar compounds effect the modifications in functional activities of pituitary or glial neoplastic cells, if the *in vivo* findings occur.

Keywords: verteporfin, Ca^{2+}-activated K^+ current, K^+ current, BKCa channel, Ca^{2+} current, pituitary tumor cell, glioma cell

INTRODUCTION

Verteporfin (VP, Visudyne®), a benzoporphyrin derivative, is a compound therapeutically tailored as a photosensitizer for photodynamic therapy, because this agent can effectively eliminate aberrant blood vessels in the eye associated with conditions such as either the wet form of macular degeneration or abnormal choroidal neovascularizations (Schmidt-Erfurth and Hasan, 2000; DeRosa and Crutchley, 2002; Renno et al., 2004; Rosenblatt et al., 2005; Hua et al., 2014; Hu et al., 2015; Chen and Hu, 2017; Ghazai et al., 2017; Konstantinou et al., 2017; AlAmri et al., 2018; Baskaran et al., 2018; Liu et al., 2018; Min et al., 2018; Iacono et al., 2019; Isildak et al., 2019).

Yes-associated protein (YAP) has been reported to be a main mediator of the Hippo pathway, which is thought to promote cancer development (Feng et al., 2016; Gibault et al., 2016; Kandoussi et al., 2017; Abe et al., 2018; Chen et al., 2019). A number of recent reports has demonstrated that VP can suppress the aberrant growth in a variety of tumor cell lines, including breast cancer, glioma, ovarian cancer, hepatocellular carcinoma, and retinoblastoma, through an intriguing mechanism linked to specific suppression of YAP-TEAD complex (Valero et al., 2015; Feng et al., 2016; Al-Moujahed et al., 2017; Gibault et al., 2017; Abe et al., 2018; Mulder et al., 2018; Li et al., 2019; Pellosi et al., 2019; Qin et al., 2019; Zhang et al., 2019). This compound has been indeed long supposed to be an inhibitor of YAP-TEAD complex and hence to play the roles in growth inhibition in different types of neoplastic cells including pituitary tumors and gliomas (Feng et al., 2016; Gibault et al., 2016, 2017; Al-Moujahed et al., 2017; Deng et al., 2018; Eales et al., 2018; Liao et al., 2018; Pellosi et al., 2019; Zhang et al., 2019).

The photodynamic therapy with different photosensitizers such as hypericin or VP has been previously demonstrated to be effective in the treatment of different types of hyper- or neoplastic tissues, including the residual small tumor in pituitary gland (Faustino et al., 1997; Marks et al., 2000; Valenzeno and Tarr, 2001; DeRosa and Crutchley, 2002; Rahimipour et al., 2003; Brown et al., 2004; Renno et al., 2004; Solban et al., 2006; Triesscheijn et al., 2006; Zhou et al., 2006; Cole et al., 2008; Tekrony et al., 2011; Nemes et al., 2016; Deng et al., 2018). Previous work indeed reported the capability of photosensitizers (e.g., rose bengal) to modify membrane ionic current in pituitary tumor (GH_3) cells or heart cells (Tarr et al., 1994; Valenzeno and Tarr, 1998, 2001). Alternatively, earlier reports have also revealed that VP could induce anterior ischemic optic neuropathy in rodents (Karacorlu et al., 2004; Min et al., 2018). However, surprisingly, little information has been thus far available concerning any possible modifications of VP on the level of surface membrane including ionic channels in a variety of neoplastic cells, despite its clinical approval for photodynamic therapy.

Because of the considerations described above, we sought to determine whether VP and its related compounds could exert any possible perturbations on different types of ionic currents which include Ca^{2+}-activated K^+ current ($I_{K(Ca)}$), delayed-rectifier K^+ current ($I_{K(DR)}$), M-type K^+ current ($I_{K(M)}$), large-conductance Ca^{2+}-activated K^+ (BK_{Ca}) channel, L-type Ca^{2+} current ($I_{Ca,L}$), and voltage-gated Na^+ current (I_{Na}). In this study, we provide substantial evidence to unravel that VP is indeed capable of modifying membrane ionic currents in pituitary tumor (GH_3) cells and in glioma (13-06-MG) cells, the actions of which are apparently of clinical relevance and appear to be upstream of its inhibition at YAC-TEAD complex.

MATERIALS AND METHODS

Drugs and Solutions

Verteporfin (VP, Visudyne®, BPD-MA, CL-318,952, $C_{41}H_{42}N_4O_8$,), rose bengal, tetraethylammonium chloride (TEA), tetrodotoxin (TTX), and tolbutamide were acquired from Sigma-Aldrich (St. Louis, MO), iberiotoxin and paxilline from Alomone (Jerusalem, Israel), and A-803467 (5-(4-chlorophenyl)-*N*-(3,5-dimethoxyphenyl)-2-furancarboxamide), A-887826 (5-(4-butoxy-3-chlorophenyl)-*N*-[[2-(4-morpholinyl)-3-pyridinyl]methyl-3-pyridine carboxamide), 2-guanidine-4-methylquinazoline (GMQ), S(-)-Bay K 8644 (Bay K 8644), nifedipine, NS1619, PF573228 (3,4-dihydro-6-[[4-[[[3-(methylsulfonyl)phenyl]methyl]amino]-5-(trifluoromethyl)-2-pyrimidinyl]amino]-2(1H)-quinolinone) and TRAM-39 (2-cholo-α,α-diphenylbenzeneacetonitrile) were from Tocris Cookson Ltd. (Bristol, UK), and pioglitazone was obtained from Takeda (Tokyo, Japan). Chlorotoxin was kindly provided by Professor Dr. Woei-Jer Chuang, Department of Biochemistry, National Cheng Kung University Medical College, Tainan, Taiwan. To protect VP from light, stock solution containing this compound was wrapped in aluminum foil. Cell culture media were obtained from Invitrogen (Carlsbad, CA), unless stated otherwise, and other chemicals or solvents such as $CdCl_2$, CsCl, CsOH, and *N*-methyl-D-glucamine$^+$ ($NMDG^+$) were of analytical reagent grade. The twice-distilled water that had been de-ionized through a Millipore-Q system was used in all experiments.

The composition of bath solution (i.e., HEPES-buffered normal Tyrode's solution) for GH_3 or 13-06-MG cells was as follows (in mM): NaCl 136.5, KCl 5.4, $CaCl_2$ 1.8, $MgCl_2$ 0.53, glucose 5.5, and HEPES-NaOH buffer 5.5 (pH 7.4). To measure K^+ currents [i.e., $I_{K(Ca)}$, $I_{K(DR)}$, and $I_{K(M)}$], we filled the patch pipette with a solution (in mM): KCl 140, $MgCl_2$ 1, Na_2ATP 3, Na_2GTP 0.1, EGTA 0.1, and HEPES-KOH buffer 5 (pH 7.2); however, in some separate set of experiments of reducing the level of intracellular Ca^{2+}, EGTA concentration in the solution was changed to 10 mM. To record $I_{K(M)}$, high K^+-bathing solution was composed of the following (in mM): KCl 145, $MgCl_2$ 0.53, and HEPES-KOH 5 (pH 7.4). In order to measure I_{Na}, $I_{Ca,L}$, or I_{NS} precisely, we replaced K^+ ions inside the pipette solution with

Abbreviations: BK_{Ca} channel, large-conductance Ca^{2+}-activated K^+ channel; EC_{50}, the concentration required for half-maximal stimulation; GMQ, 2-guanidine-4-methylquinazoline; *I-V*, current vs. voltage; $I_{Ca,L}$, L-type Ca^{2+} current; IK_{Ca} channel, intermediate-conductance Ca^{2+}-activated K^+ channel; $I_{K(Ca)}$, Ca^{2+}-activated K^+ current; $I_{K(DR)}$, delayed-rectifier K^+ current; $I_{K(M)}$, M-type K^+ current; I_{Na}, voltage-gated Na^+ current; I_{NS}, non-selective cation current; TEA, tetraethylammonium chloride; TEAD, TEA domain transcription factor; $\tau_{inact(s)}$, slow component of inactivation time constant for ionic current; TTX, tetrodotoxin; VP, verteporfin (Visudyne®); YAP, yes-associated protein.

equimolar Cs^+ ions, and pH was then appropriately adjusted to 7.2 with CsOH. In order to fully suppress Na^+, Ca^{2+} or K^+ currents, TTX (1 μM), $CdCl_2$ (0.5 mM) or TEA (10 mM) was added to the recording medium, respectively. The pipette solution and culture medium were commonly filtered on the day of use with Acrodisc® syringe filter with 0.2 μm Supor® membrane (Pall Corp., Port Washington, NY).

Cell Culture

GH_3 pituitary tumor cells, obtained from the Bioresources Collection and Research Center ([BCRC-60015]; Hsinchu, Taiwan), were maintained in Ham's F-12 media supplemented with 15% horse serum (v/v), 2.5% fetal calf serum (v/v), and 2 mM L-glutamine (Wu et al., 2003; Lin et al., 2014; So et al., 2018). The glioblastoma multiforme cell line (13-06-MG) was kindly provided by Professor Dr. Carol A. Kruse, Department of Neurosurgery, Ronald Reagan UCLA Medical Center, LA, CA, USA. Cells were grown in high-glucose (4 g/l) Dulbecco's modified Eagle media supplemented with 10% heat-inactivated fetal bovine serum (Huang et al., 2015). GH_3 or 13-06-MG cells were maintained at 37°C in a humidified environment of 5% CO_2/95% air and sub-cultured weekly and fresh media were generally added every 2–3 days to maintain a healthy cell population. Glial cells were verified by identifying glial fibrillary acidic protein, a cytoskeletal protein. The experiments were performed after 5 or 6 days of subcultivation (60–80% confluence).

Electrophysiological Measurements

Shortly before experimentation, we dissociated the cells and then placed a few drops of cell suspension onto a custom-built recording chamber affixed on the stage of a DM-IL inverted microscope (Leica, Wetzlar, Germany). As being settled down the bottom of the chamber, cells were bathed at a room temperature of 20–25°C in normal Tyrode's solution, the composition of which is describe above. Once cells were placed in the VP-containing medium, the recordings were carried out under very dim room light. For illumination system, we focused visible light onto a spot on the recording chamber which covered completely the area of cells exposed to VP in the central region with an illumination intensity of ∼5.5 mW/cm^2. We fabricated the recording pipette from Kimax-51 capillary tubes (#34500; Kimble, Vineland, NJ) using a vertical PP-83 (Narishige, Tokyo, Japan) or a horizontal P-97 Flaming/Brown (Sutter, Novato, CA) puller, and their tips were fire-polished with an MF-83 microforge (Narishige). During the measurements, the pipette with a resistance of 3–5 MΩ, which was inserted into holder, was gently maneuvered by using a WR-98 micromanipulator (Narishige). Patch-clamp experiments were measured in either cell-attached, inside-out, or whole-cell arrangement by using an RK-400 patch-clamp amplifier (Bio-Logic, Claix, France) connected with a personal computer with 64-bit processor (Lin et al., 2004; Wu et al., 2017; So et al., 2019). Shortly before giga-seal formation was achieved, the potentials were appropriately corrected for the liquid junction potential that commonly develop at the pipette tip as the composition of the pipette solution was quite different from that in the bath. Tested compounds were applied by perfusion or added to the bath to obtain the final concentration indicated.

Data Recordings

The data comprising both potential and current traces were stored online in an ASUS VivoBook Flip-14 touchscreen laptop computer (TP412U; Taipei City, Taiwan) at 10 kHz equipped with the 12-bit Digidata 1440A interface (Molecular Devices, Inc., Sunnyvale, CA). The latter device was used for efficient analog-to-digital/digital-to-analog conversion. During the experiments, data acquisition system was electronically driven by pCLAMP 10.7 software (Molecular Devices) run under Windows 10 (Redmond, WA), and the signals were simultaneously monitored on LCD monitor (MB169B+; ASUS, Taipei, Taiwan) through a USB type-C connection. Current signals were low-pass filtered at 2 kHz with FL-4 four-pole Bessel filter (Dagan, Minneapolis, MN) to minimize background noise. Through digital-to-analog conversion, the pCLAMP-generated voltage-clamp profiles with different waveforms were applied to determine the current-voltage (*I-V*) relationships for different types of ionic currents such as $I_{K(Ca)}$, $I_{K(DR),}$ or $I_{Ca,L}$. When high-frequency stimuli used to elicit the cells were required, an Astro-med Grass S88X dual output pulse stimulator (Grass Technologies, West Warwick, RI) was used.

Data Analyses

To evaluate concentration-dependent effect of VP on the stimulation of $I_{K(Ca)}$ in GH_3 cells, each cell was depolarized to +50 mV from a holding potential of 0 mV. Current amplitude measured at the end of each depolarizing pulse during cell exposure to 100 μM VP was taken to be 100%, and those in the presence of different VP concentrations were then compared. To determine concentration-dependent stimulation of VP on BK_{Ca} channels recorded from human 13-06-MG glioma cells, channel activity at +60 mV relative to the bath during the exposure to 100 μM VP was considered as 100%, and the channel open probabilities at different VP concentrations were compared. The mean values for concentration-dependent relation of VP on the stimulation of $I_{K(Ca)}$ or BK_{Ca} channels were least-squares fitted to a modified Hill function. That is,

$$Percentage\ increase\ (\%) = \frac{E_{\max}}{1 + \frac{EC_{50}^{n_H}}{[VP]^{n_H}}},$$

where [VP] is the VP concentration applied, EC_{50} the concentration required for half-maximal stimulation of $I_{K(Ca)}$ or BK_{Ca} channels, n_H the Hill coefficient, and E_{max} VP-induced maximal stimulation of either $I_{K(Ca)}$ in GH_3 cells or BK_{Ca} channels in 13-06-MG cells.

Single-BK_{Ca} channel currents were analyzed by pClamp 10.7 software (Molecular Devices). Multi-gaussian adjustments of the amplitude distributions among channels were commonly used to determine single-channel currents. Functional independence between channels was verified by comparing the observed stationary probabilities with the values calculated according to the binomial law. The open-state probability of the channels

was expressed as $N{\cdot}P_O$ which can be estimated using the following equation:

$$N \cdot P_O = \frac{A_1 + 2A_2 + 3A_3 + \ldots + nA_n}{A_0 + A_1 + A_2 + A_3 + \ldots + A_n},$$

where N is the number of active channels in the patch examined, A_0 the area under the curve of an all-points histogram corresponding to the closed state, and A_1-A_n are the histogram areas reflecting the levels of distinct open state for 1 to n channels in the patch.

Statistical Analyses

To perform linear or non-linear (e.g., sigmoidal or exponential function) curve fitting to the data set (i.e., the goodness of fit) was appropriately utilized by using OriginPro (OriginLab, Northampton, MA) or Prism version 5.0 (GraphPad, La Jolla, CA). Data were analyzed and are plotted using OriginPro (OriginLab), and they were expressed as mean±standard error of the mean (SEM). The paired or unpaired Student's *t*-test, or one-way analysis of variance (ANOVA) followed by *post-hoc* Fisher's least-significance difference test for multiple comparisons, were implemented for the statistical evaluation of differences among means. We further used non-parametric Kruskal-Wallis test, as the assumption of normality underlying ANOVA was likely to be violated. Statistical analyses were commonly performed by using IBM SPSS® version 20.0 (IBM Corp., Armonk, NY). $P < 0.05$ was considered significant, unless stated otherwise.

RESULTS

Stimulatory Effect of VP on Ca^{2+}-Activated K^+ ($I_{K(Ca)}$) Measured From Pituitary Tumor (GH_3) Cells

The whole cell configuration of the patch-clamp technique was initially carried out to evaluate any possible perturbations of VP on $I_{K(Ca)}$ amplitude in these cells. In the experiments designed to measure $I_{K(Ca)}$, we immersed the cells in normal Tyrode's solution containing 1.8 mM $CaCl_2$, and the recording pipette was filled with a solution which contained a low concentration 140 mM K^+, 0.1 mM EGTA, and 3 mM ATP. As whole-cell mode was achieved, the examined cell was maintained at the level of 0 mV to inactivate other types of voltage-gated K^+ currents which are enriched in these cells (Stojilkovic et al., 2010; So et al., 2018), and ionic currents in response to a series of the voltage pulses between 0 and +60 mV were robustly elicited. Current amplitude was progressively increased as the test voltage became more positive (**Figure 1**). When extracellular Ca^{2+} was removed, current amplitudes were greatly reduced; meanwhile, an increase in intracellular EGTA concentration from 0.1 to 10 mM also abolished these currents. This type of outward currents with an outwardly rectifying property has been hence regarded as $I_{K(Ca)}$ (Lin et al., 2004; Wu et al., 2017), the amplitudes of which become greatly small as intracellular Ca^{2+} level is decreased (i.e., intracellular EGTA with 10 mM).

As cells were exposed to VP, the amplitude of $I_{K(Ca)}$ in response to depolarizing step was considerably increased (**Figures 1A,B**). For example, VP at a concentration of 3 μM significantly raised $I_{K(Ca)}$ measured at the level of +50 mV from 184 ± 13 to 257 ± 24 pA ($n = 11$, $P < 0.05$). Washout of VP, current amplitude returned to 197 ± 14 pA ($n = 10$, $P < 0.05$). Similarly, as cells were exposed to 10 μM NS1619, an activator of BK_{Ca} channels, $I_{K(Ca)}$ amplitude at +50 mV increased from 179 ± 14 to 235 ± 25 pA ($n = 8$, $P < 0.05$). **Figure 1B** illustrates the averaged current-voltage (*I-V*) relationships of $I_{K(Ca)}$ with or without addition of VP (3 μM).

Concentration-dependent stimulation of $I_{K(Ca)}$ on GH_3 cells by VP was further derived and then constructed. In these experiments, we bathed the cells in normal Tyrode's solution, the examined cell was clamped at 0 mV, and depolarizing pulse from 0 to +50 mV was then delivered. As illustrated in **Figures 2A,B**, the presence of different VP concentrations (0.1–100 μM) could be efficacious at raising $I_{K(Ca)}$ amplitude in a concentration-dependent manner. According to least-squares minimization procedure, the half-maximal concentration required for the stimulatory effect of VP on $I_{K(Ca)}$ amplitude was estimated to be 2.4 μM, and it at a concentration of 100 μM fully increased current amplitude elicited by voltage depolarization. The experimental results thus demonstrate that VP has a stimulatory action on $I_{K(Ca)}$ seen in GH_3 cells in a concentration-dependent manner.

Comparison of Effects of VP, VP Plus Tolbutamide, VP Plus TRAM-39, VP Plus Paxilline, VP Plus Iberiotoxin, and VP Plus Dithiothreitol on $I_{K(Ca)}$ Amplitude in GH_3 Cells

An earlier work has demonstrated that VP might disrupt mitochondrial inner membrane potential in cancer cells (Belzacq et al., 2001). On the other hand, the activity of different types of K^+ channels present in pituitary cells including GH_3 cells (Stojilkovic et al., 2010) might contribute synergistically to VP-mediated effect on $I_{K(Ca)}$. Therefore, during cell exposure to VP, subsequent addition of different compounds including tolbutamide, TRAM-39, paxilline, iberiotoxin, and dithiothreitol was further studied to evaluate whether those agents exert any modulation on $I_{K(Ca)}$ stimulated by VP. As depicted in **Figure 2C**, subsequent application of neither tolbutamide nor TRAM-39 could attenuate VP-mediated increase of $I_{K(Ca)}$ amplitude; however, that of paxilline, iberiotoxin, or dithiothreitol did reduce $I_{K(Ca)}$ raised by VP. Tolbutamide and TRAM-39 are blockers of ATP-sensitive K^+ (K_{ATP}) and intermediated-conductance Ca^{2+}-activated K^+ (IK_{Ca}) channels (Chen P. C. et al., 2018; Chen T. S. et al., 2018; Liu et al., 2019a), respectively, while paxilline and iberiotoxin could suppress the activity of large-conductance Ca^{2+}-activated K^+ (BK_{Ca}) channels, respectively. Dithiothreitol is recognized as a sulfhydryl reducing agent.

Inhibitory Effect of VP on Delayed-Rectifier K^+ Current ($I_{K(DR)}$) in GH_3Cells

We further studied whether, in addition to $I_{K(Ca)}$, another different types of K^+ currents [e.g., $I_{K(DR)}$] could be modified by

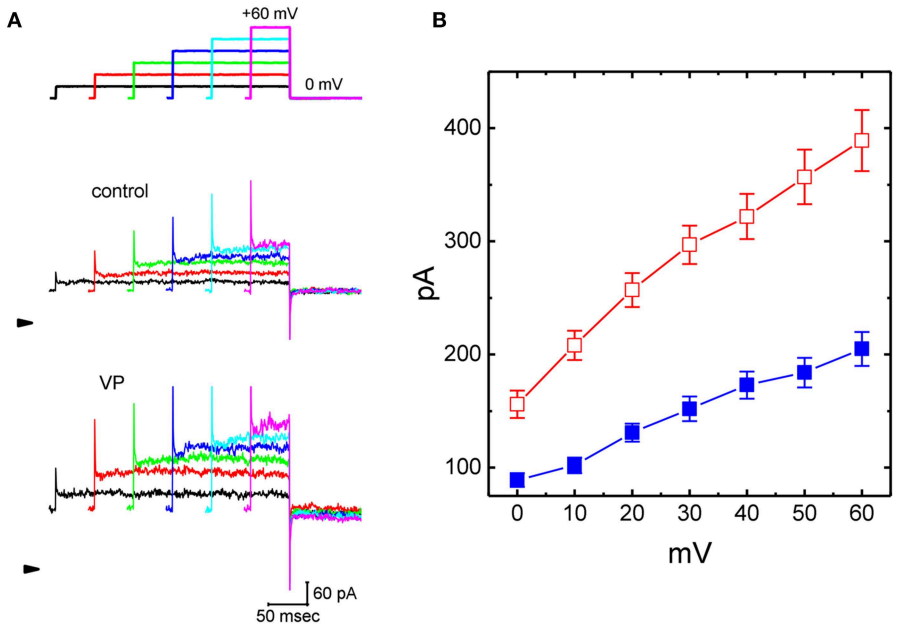

FIGURE 1 | Effects of verteporfin (VP) on Ca^{2+}-activated K^+ current ($I_{K(Ca)}$) measured from pituitary GH_3 cells. In these experiments, cells were bathed in normal Tyrode's solution containing 1.8 mM $CaCl_2$, and the recording pipette was filled with K^+-containing solution. The examined cell was voltage clamped at 0 mV to inactivate most of other types of voltage-gated K^+ currents, and a series of the voltage steps ranging between 0 and +60 mV [indicated in the uppermost part of **(A)**] was delivered. **(A)** Representative $I_{K(Ca)}$ traces taken in the absence (upper) and presence (lower) of 3 μM VP. The arrowhead indicates the zero current level, and calibration bar in the bottom right corner refers to both panels. **(B)** Averaged current-voltage (*I-V*) relationships of $I_{K(Ca)}$ measured from the control (■) and during cell exposure to 3 μM VP (□) (mean ± SEM; $n = 11$ for each point).

the presence of VP. In these experiments, cells were bathed in Ca^{2+}-free Tyrode's solution containing 1 μM TTX and 0.5 mM $CdCl_2$ and we filled the recording pipette by using K^+-containing solution. Addition of 3 μM VP was not found to modify $I_{K(DR)}$ amplitude significantly. However, as GH_3 cells were exposed to 10 μM VP, the $I_{K(DR)}$ amplitudes elicited in response to stepwise depolarizing voltages were progressively decreased (**Figures 3A,B**). **Figure 3B** illustrates averaged *I-V* relationships of $I_{K(DR)}$ measured at the end of each depolarizing pulse, as the results were obtained in the absence and presence of 10 μM VP. For example, as the examined cells were depolarized from −50 to +40 mV, addition of 10 μM VP diminished $I_{K(DR)}$ amplitude from 1,382 ± 145 to 1,114 ± 138 pA ($n = 13$, $P < 0.05$). After washout of the drug, current amplitude returned to 1,328 ± 141 pA ($n = 11$, $P < 0.05$). However, no modification of $I_{K(DR)}$ inactivation time course in response to membrane depolarization was demonstrated in the presence of 10 μM VP. Therefore, these results showed that VP at a concentration of 10 μM mildly suppressed the amplitude of $I_{K(DR)}$ in GH_3 cells.

Failure of VP to Modify M-Type K^+ Current ($I_{K(M)}$) Recorded From GH_3Cells

In addition to $I_{K(DR)}$, another type of K^+ current [i.e., $I_{K(M)}$] detected in GH_3 cells (Sankaranarayanan and Simasko, 1996; Stojilkovic et al., 2010; So et al., 2019) was further designed to evaluate whether the presence of VP has any modifications on this type of K^+ current. To amplify $I_{K(M)}$, we bathed cells in high-K^+ (145 mM), Ca^{2+}-free solution, the composition of which is described in **Materials and Methods**. In these experiments, the examined cell held in voltage clamp at −50 mV with a long-duration depolarizing step to −10 mV was able to generate a slowly activating K^+ inward current followed by a largely deactivating current, namely $I_{K(M)}$, as described previously (Sankaranarayanan and Simasko, 1996; Chen T. S. et al., 2018; Liu et al., 2019b; So et al., 2019). As illustrated in **Figure 4**, under our experimental conditions, we were unable to find out that the presence of 10 μM VP had any measurable effect on $I_{K(M)}$ amplitude [141 ± 19 pA [in the control] vs. 140 ± 18 pA [in the absence of 10 μM VP], $n = 11$, $P > 0.05$]. However, in continued presence of 10 μM VP, further application of 3 μM pioglitazone was effective at suppressing $I_{K(M)}$, as evidenced by the results showing that, in continued presence of 10 μM VP, further application of 10 μM pioglitazone substantially decreased $I_{K(M)}$ amplitude to 78 ± 12 pA ($n = 11$, $P < 0.05$). Therefore, the data prompted us to indicate that distinguishable from $I_{K(Ca)}$ or $I_{K(DR)}$, the $I_{K(M)}$ observed in GH_3 cells was relatively resistant to modification by VP, though it was potently suppressed by pioglitazone (Chen T. S. et al., 2018).

Effects of VP on the Activity of Bk_{ca} Channels in GH_3Cells

The results from our whole-cell experiments reflected that $I_{K(Ca)}$ described above could be K^+ flux through the large-conductance subtype of K_{Ca} channels, because VP-induced increase in $I_{K(Ca)}$ was effectively suppressed by iberiotoxin or paxilline, yet not by TRAM-39. Therefore, in attempts to ascertain how VP interacts pertinently with ion-channel activity to modify $I_{K(Ca)}$, the effects of VP on BK_{Ca}-channel activity was

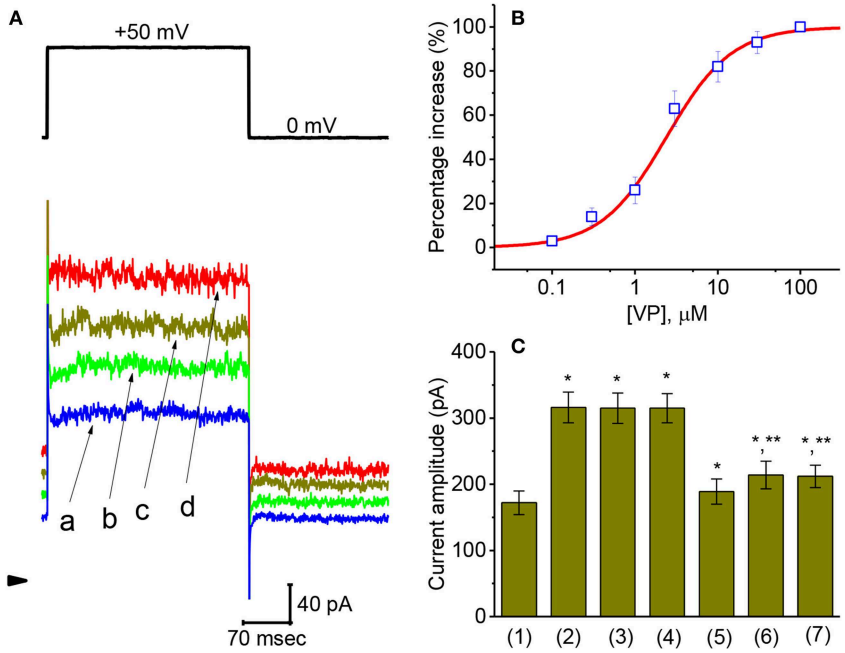

FIGURE 2 | Concentration-dependent effect of VP on $I_{K(Ca)}$ and the effects of different related compounds on VP-stimulated $I_{K(Ca)}$ in GH_3 cells. The experiments were conducted in cells bathed in normal Tyrode's solution and the depolarizing pulse from 0 to +50 mV [indicated in the upper part of **(A)**] was delivered to the cell examined. **(A)** Superimposed $I_{K(Ca)}$ taken during step depolarization. a: control; b:1 μM VP; c: 3 μM VP; d: 10 μM VP. Arrowhead is the zero-current level and calibration bar refers to all traces. **(B)** Concentration-dependent effect of VP on $I_{K(Ca)}$ amplitude [mean ± SEM; n = 10–14 for each point (□)]. The examined cell was depolarized from 0 to +50 mV and current amplitude at the end of each depolarizing step was measured. As cells were exposed to 100 μM VP, $I_{K(Ca)}$ amplitude was taken to be 100%, and those at different VP concentrations were then compared. The values for EC_{50} and the Hill coefficient were 2.4 μM and 1.1, respectively. Non-linear smooth line was least-squares fitted to a modified Hill function described in **Materials and Methods**. **(C)** Summary bar graph showing the effect of VP, VP plus tolbutamide, VP plus TRAM-39, VP plus paxilline, VP plus iberiotoxin, and VP plus dithiothreitol. Each bar showing $I_{K(Ca)}$ amplitude at the level of +60 mV indicates the mean ± SEM (n = 11–14). *Significantly different from control ($P < 0.05$) and **significantly different from VP (3 μM) alone group ($P < 0.05$).

also investigated in cell-attached or inside-out configuration. In cell-attached current recordings, cells were bathed in normal Tyrode's solution containing 1.8 mM $CaCl_2$, the activity of BK_{Ca} channels measured at +60 mV relative to the bath can be readily detected in these cells. In particular, when VP (3 μM) was applied to the bath medium, the probability of channel openness was drastically raised (**Figures 5A,B**). The open probability of BK_{Ca} channels maintained at +60 mV in the control was found to be 0.014 ± 0.004 (n = 13). One minute after addition of VP (3 μM) to the bath, the channel open probability was significantly increased to 0.024 ± 0.007 (n = 13, $P < 0.05$). The channel activity was reduced to 0.018 ± 0.005 (n = 12) after washout of the agent. However, the amplitude of single-channel currents remained unaltered in the presence of VP. The single-channel conductance of BK_{Ca} channels in control cells was 146 ± 8 pS (n = 12), a value that did not differ significantly from that (147 ± 13 pS, n = 12, $P > 0.05$) obtained in the presence of VP (3 μM). Moreover, in continued presence of 3 μM VP, further exposure to illumination with light intensity of 5.5 mW/cm^2 increased channel open probability further to 0.047 ± 0.011 (n = 11, $P < 0.01$). Subsequent addition of 1 μM paxilline reduced channel activity significantly (**Figure 5B**), as evidenced by a significant reduction in the channel open probability to 0.017 ± 0.005 (n = 11, $P < 0.05$).

Effect of VP, VP Plus GMQ, and VP PF573228 on BK_{Ca}-Channel Activity in GH_3 Cells

We also evaluated whether VP could exert any perturbation on BK_{Ca} channels in inside-out patch of the cell. Cells were immersed in high K^+ solution containing 1 μM Ca^{2+}, and the experiments were conducted in inside-out current recordings. As shown in **Figure 6**, when the excised patch was maintained at +60 mV, the addition of 3 μM VP to the intracellular leaflet of the inside-out patch did not modify the channel open probability. However, in continued presence of VP, further addition of either 2-guanidine-4-methylquinazoline (GMQ; 3 μM) or PF573228 (3 μM) was effective at raising the probability of BK_{Ca} channels. GMQ or PF573228 was previously reported to activate BK_{Ca} channels (So et al., 2011, 2018). The results thus showed the inability of VP to alter the probability of BK_{Ca}-channel openings recorded from the excised patch of GH_3 cells.

Suppressive Effect of VP on L-Type Ca^{2+} Current ($I_{Ca,L}$) in GH_3Cells

Whether VP exerts any perturbations on voltage-gated $I_{Ca,L}$ in these cells was further studied, because any modifications in $I_{Ca,L}$ magnitude can modify the level of intracellular Ca^{2+}, thereby influencing either the activity of BK_{Ca} channels or

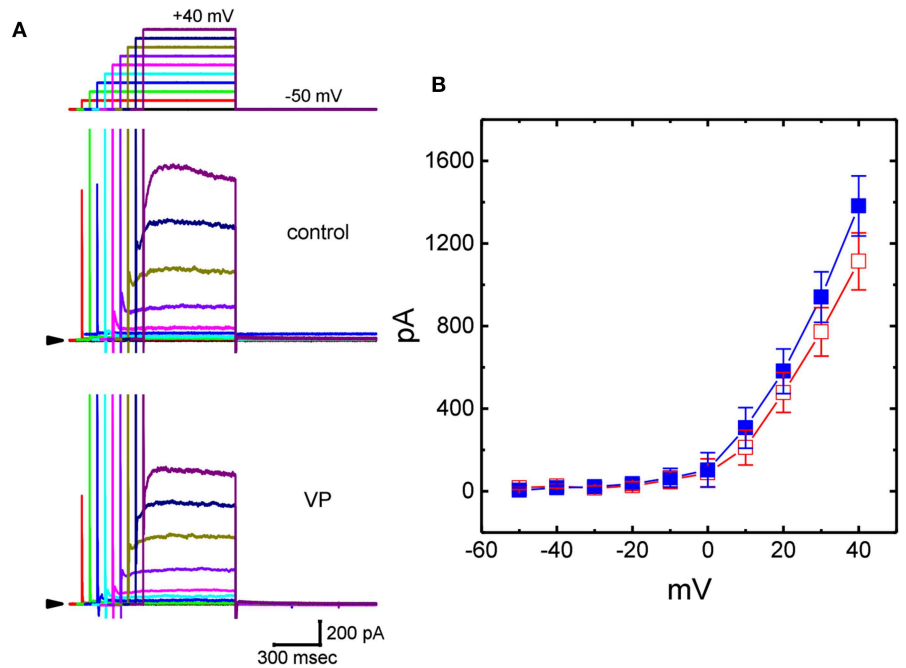

FIGURE 3 | Effects of VP on delayed-rectifier K^+ current ($I_{K(DR)}$) in GH_3 cells. In these experiments, we bathed cells in Ca^{2+}-free Tyrode's solution containing 1 μM tetrodotoxin (TTX), and whole-cell currents were recorded by filling the pipette with K^+-containing solution. The examined cell was held at −50 mV and a series of depolarizing steps ranging between −50 and +40 mV was applied [indicated in the uppermost part of **(A)**]. **(A)** Superimposed $I_{K(DR)}$ traces obtained during the control (upper) and cell exposure to 10 μM VP (lower). Arrowhead in each panel represents the zero-current level. **(B)** Averaged *I-V* relationships for $I_{K(DR)}$ obtained with or without the addition of 10 μM VP (mean ± SEM; $n = 13$ for each point). Current amplitudes were measured at the end of each depolarizing step. ■: control; □: in the presence of 10 μM VP.

$I_{K(Ca)}$ amplitude (Wu et al., 1998a,b, 2003; Stojilkovic et al., 2010). As cells were exposed to different VP concentrations the peak amplitude of $I_{Ca,L}$ elicited in response to single depolarizing step was progressively decreased (**Figures 7A,B**). The peak amplitude of $I_{Ca,L}$ by membrane depolarization was suppressed by nifedipine (3 μM) and enhanced by Bay K 8644 (3 μM) (data not shown). Moreover, the addition of 3 μM VP suppressed the peak amplitude of $I_{Ca,L}$ from 426 ± 22 to 267 ± 14 pA ($n = 12$, $P < 0.05$). Concomitant with this, the inactivation time constant of $I_{Ca,L}$ became slowed (**Figure 7C**). The value for the slow component of $I_{Ca,L}$ inactivation time constant ($\tau_{inact(s)}$) was prolonged to 63.7 ± 7.2 ms from a control value of 30.9 ± 5.6 ms ($n = 12$, $P < 0.05$). However, the fast component for the inactivation time constant of $I_{Ca,L}$ did not differ significantly between the absence and presence of 3 μM VP. The results indicate that the presence of VP is capable of altering the amplitude and inactivation time course of $I_{Ca,L}$ elicited in response to rapid membrane depolarization.

Stimulatory Effect of VP on Non-selective Cation Current (I_{NS}) in GH_3Cells

In another set of experiments, we tested whether VP has any effects on I_{NS}. The results showed that addition of VP (3 μM) did not have any effect on ion currents measured at the level of −50 mV. However, in continued presence of VP, as light illumination with intensity of 5.5 mW/cm^2 was further applied, an inward current was progressively induced as the examined cell was voltage-clamp held at the level of −50 mV (**Figure 7D**). Similar findings were observed in eight different GH_3 cells examined. As bathing solution was replaced with $NMDG^+$ solution, this current could still be induced in the presence of VP plus light exposure. However, chlorotoxin (1 μM), an inhibitor of Cl^- channels, did not have any effects on photosensitized VP-induced inward currents. Therefore, consistent with previous observations reported from frog heart cells (Tarr et al., 1994), the inward currents seen in these cells exhibited to be the non-selective, yet not Cl^- ion-specific, nature of the ionic conductance.

Inability of VP to Modify Voltage-Gated Na^+ Current (I_{Na})

Another important type of voltage-gated ionic current (i.e., I_{Na}) was also further examined to evaluate the possible modification of VP on this inward current. However, we were unable to detect any measurable change in the amplitude or gating of I_{Na} elicited by brief step depolarization (**Figure 8**). For example, the maximal peak amplitude of I_{Na} in the control was 2.52 ± 0.17 nA ($n = 12$), a value which did not differ significantly from that during cell exposure to 3 μM VP [2.52 ± 0.18 nA [$n = 12$, $P > 0.05$]]. In continued presence of 3 μM VP, subsequent addition of either A-803467 (3 μM) or A-887826 (3 μM) was potent in suppressing the peak I_{Na} in GH_3 cells (**Figure 8**); however, no modification

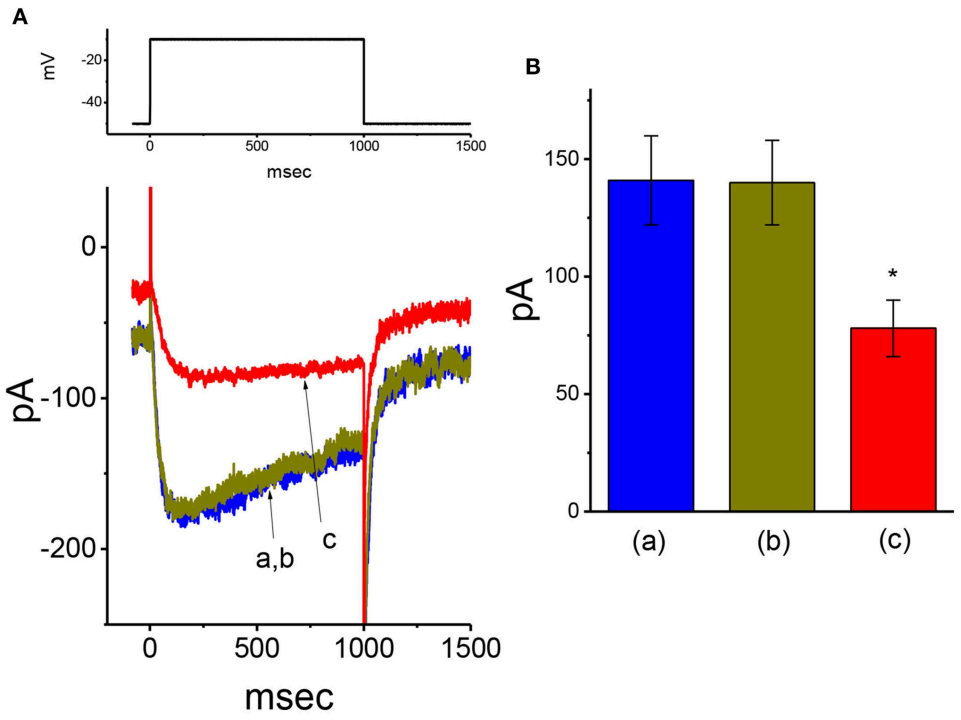

FIGURE 4 | Failure of VP to alter M-type K^+ current ($I_{K(M)}$) recorded from GH_3 cells. In these experiments, we bathed cells in high-K^+, Ca^{2+}-free solution, and filled the pipette by using K^+-containing solution. **(A)** Original $I_{K(M)}$ traces in response to long-lasting membrane depolarization from −50 to −10 mV. a: control; b: 10 μM VP; c: 10 μM VP plus 3 μM pioglitazone. The voltage protocol used is indicated in the upper part. **(B)** Summary bar graph showing the effect of VP and VP plus pioglitazone on $I_{K(M)}$ elicited by membrane depolarization (mean ± SEM; $n = 11$ for each bar). *Significantly different from control ($P < 0.05$).

in I_{Na} inactivation in the presence of these two agents was demonstrated. A-803467 or A-887826 was previously reported to inhibit $Na_V1.8$-encoded currents potently (Rush and Cummins, 2007; Zhang et al., 2010).

Effect of VP on Bk_{Ca}-Channel Activity in Human 13-06-MG Glioma Cells

VP has been recently reported to inhibit the proliferation of glioma cells (Al-Moujahed et al., 2017; Eales et al., 2018; Pellosi et al., 2019). In a final series of experiments, we therefore intended to investigate whether the presence of VP is also able to modulate ionic currents in another types of neoplastic cells (e.g., malignant glioma cells). As depicted in **Figures 9A,B**, in cell-attached measurements, the activity of BK_{Ca} channels in 13-06-MG glioma cells was robustly detected as described previously (Huang et al., 2015; Liu et al., 2015). Moreover, addition of VP to the bath increased the probability of BK_{Ca}-channel openings in these cells. For example, as the cells were maintained at +60 mV relative to the bath, the exposure to 3 μM VP significantly elevated the channel open probability from 0.018 ± 0.007 to 0.038 ± 0.011 ($n = 12$, $P < 0.05$). Therefore, similar to that of GH_3 cells described above, BK_{Ca}-channel activity existing in 13-06-MG cells was indeed found to be sensitive to stimulation by VP. Apart from the inhibition of YAP-TEAD complex, VP-induced inhibition of cell proliferation in glioma (Eskelin et al., 2008; Eales et al., 2018) could, to some extent, be linked to its stimulatory action on BK_{Ca}-channel activity.

DISCUSSION

The present investigation discloses important findings that VP produced a stimulatory effect on Ca^{2+}-activated K^+ current ($I_{K(Ca)}$) in pituitary GH_3 cells; however, it mildly depressed $I_{K(DR)}$ amplitude with no modification on I_{Na} or $I_{K(M)}$. The stimulatory effect on $I_{K(Ca)}$ caused by VP was presumably related to changes in the level of intracellular Ca^{2+} concentrations. The results showing that removal of extracellular Ca^{2+} suppressed VP-induced increase in $I_{K(Ca)}$ also suggest that extracellular Ca^{2+} and internal Ca^{2+} release both contribute to the increase in the amplitude of $I_{K(Ca)}$ in these cells.

The EC_{50} value for either VP-induced stimulation of $I_{K(Ca)}$ observed either in pituitary GH_3 cells or increase in BK_{Ca}-channel activity in 13-06-MG glioma cells was estimated to be 2.4 or 1.9 μM, respectively. These values are quite close to those that are either therapeutically achievable or required for the inhibitory actions on YAP-TEAD complex in different types of neoplastic cells (Faustino et al., 1997; Zhou et al., 2006; Feng et al., 2016; Gibault et al., 2016, 2017; Chen and Hu, 2017). As VP stimulated the $I_{K(Ca)}$ amplitude within a few minutes in GH_3 cells, it is therefore reasonable to elaborate that there is a conceivable link between the

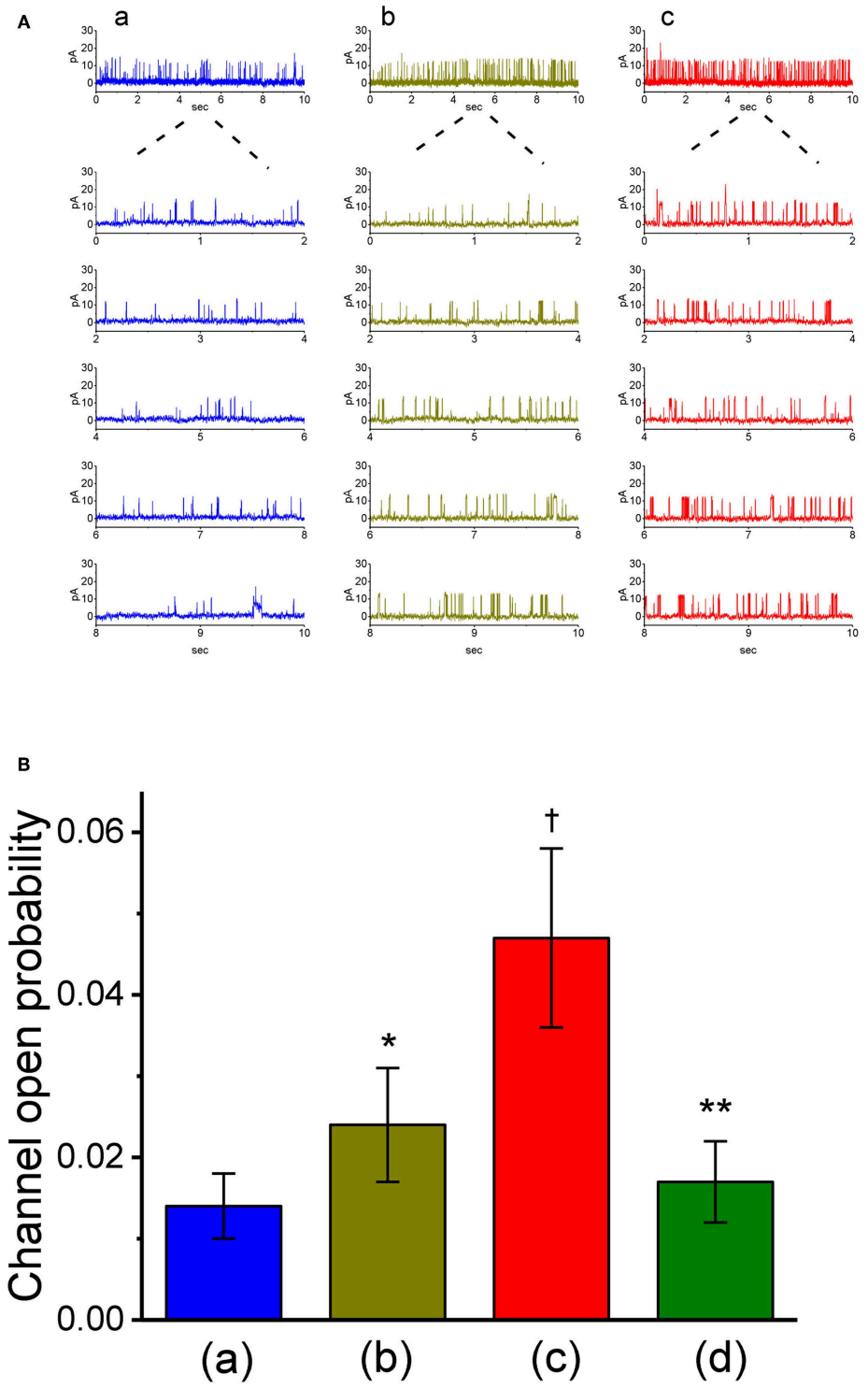

FIGURE 5 | Stimulatory effect of VP on the activity of large-conductance Ca^{2+}-activated K^+ (BK_{Ca}) channels measured from on-cell patch recordings of GH_3 cells. In these cell-attached current recordings, cells were bathed in normal Tyrode's solution containing 1.8 mM $CaCl_2$ and channel activity was measured by filling the pipette with K^+-containing solution. **(A)** BK_{Ca} channel activity measured at the holding potential of +60 mV relative to the bath. Panel a is control (i.e., in the absence of light and photosensitizer VP), while panels b and c were obtained in the presence of 3 μM VP and 3 μVP plus illumination with a light intensity of 5.5 mW/cm^2, respectively. The lower parts in each panel indicate the expanded traces recorded from the uppermost part. Note that channel opening causes an upward defection. **(B)** Summary bar graph showing the effects of VP and VP plus illumination on the probability of BK_{Ca} channels that would be open (mean ± SEM; $n = 11$–13 for each bar). *Significantly different from control ($P < 0.05$), †significantly different from control ($P < 0.01$), and **significantly different from VP (3 μM) plus illumination group ($P < 0.01$).

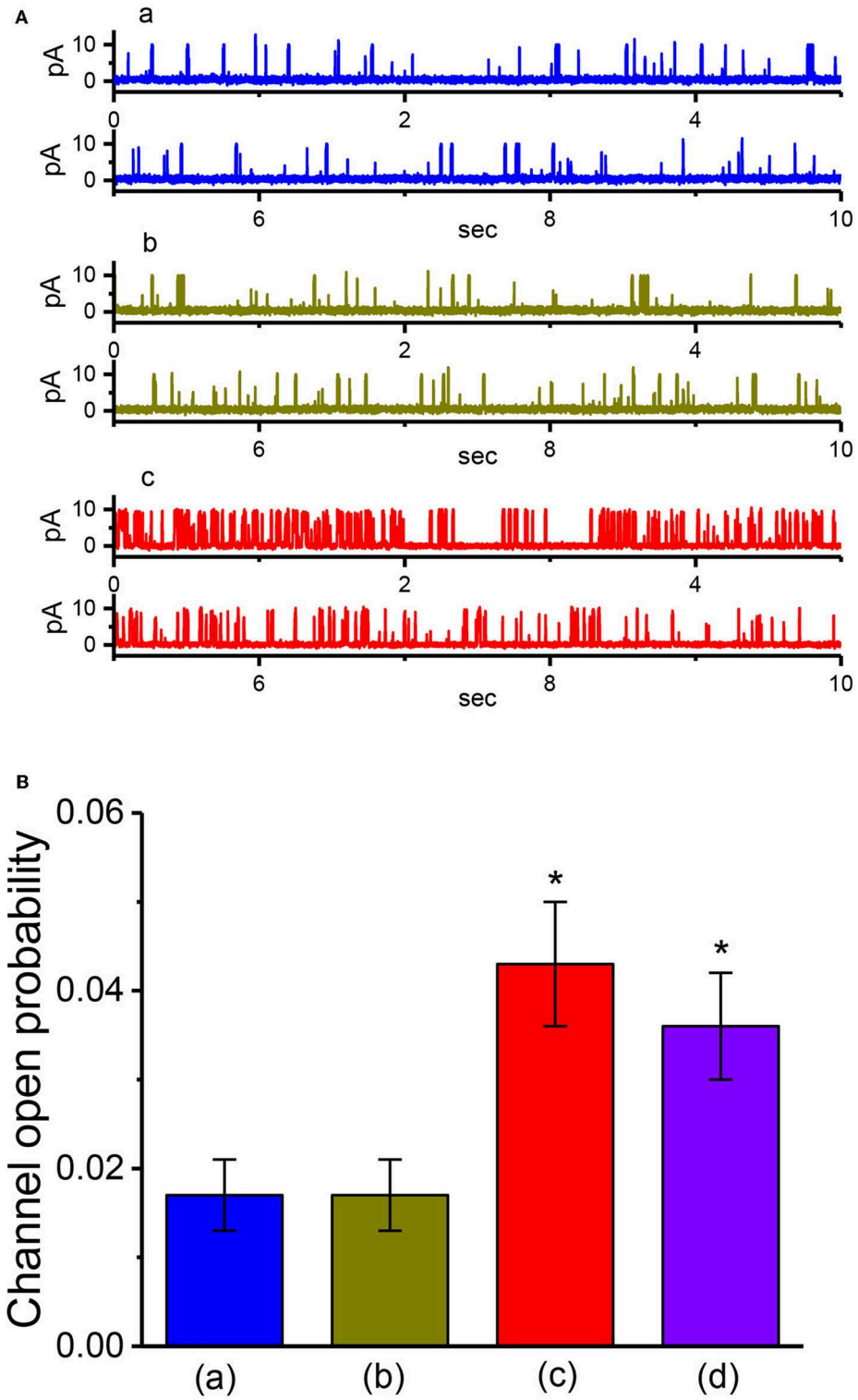

FIGURE 6 | The activity of BK_{Ca} channels produced by VP, VP plus GMQ, or VP plus PF573228 under inside-out current recordings. In these experiments, cells were bathed in high-K^+ solution which contained 1 μM Ca^{2+}, the excised patch was maintained at +60 mV, and tested compound was applied to the bath. **(A)** BK_{Ca}-channel current traces measured at +60 mV. a: control; b: 3 μM VP; c: 3 μM VP plus 3 μM GMQ. The open state of the channel is indicated by upward deflection. **(B)** Summary bar graph showing the effects of VP, VP plus GMQ, or VP plus PF573228 on the probability of BK_{Ca} channels that would be open (mean ± SEM; $n = 12$ for each bar). *Significantly different from control (i.e., in the absence of any agents; $P < 0.05$) and **significantly different from VP (3 μM) alone group ($P < 0.05$).

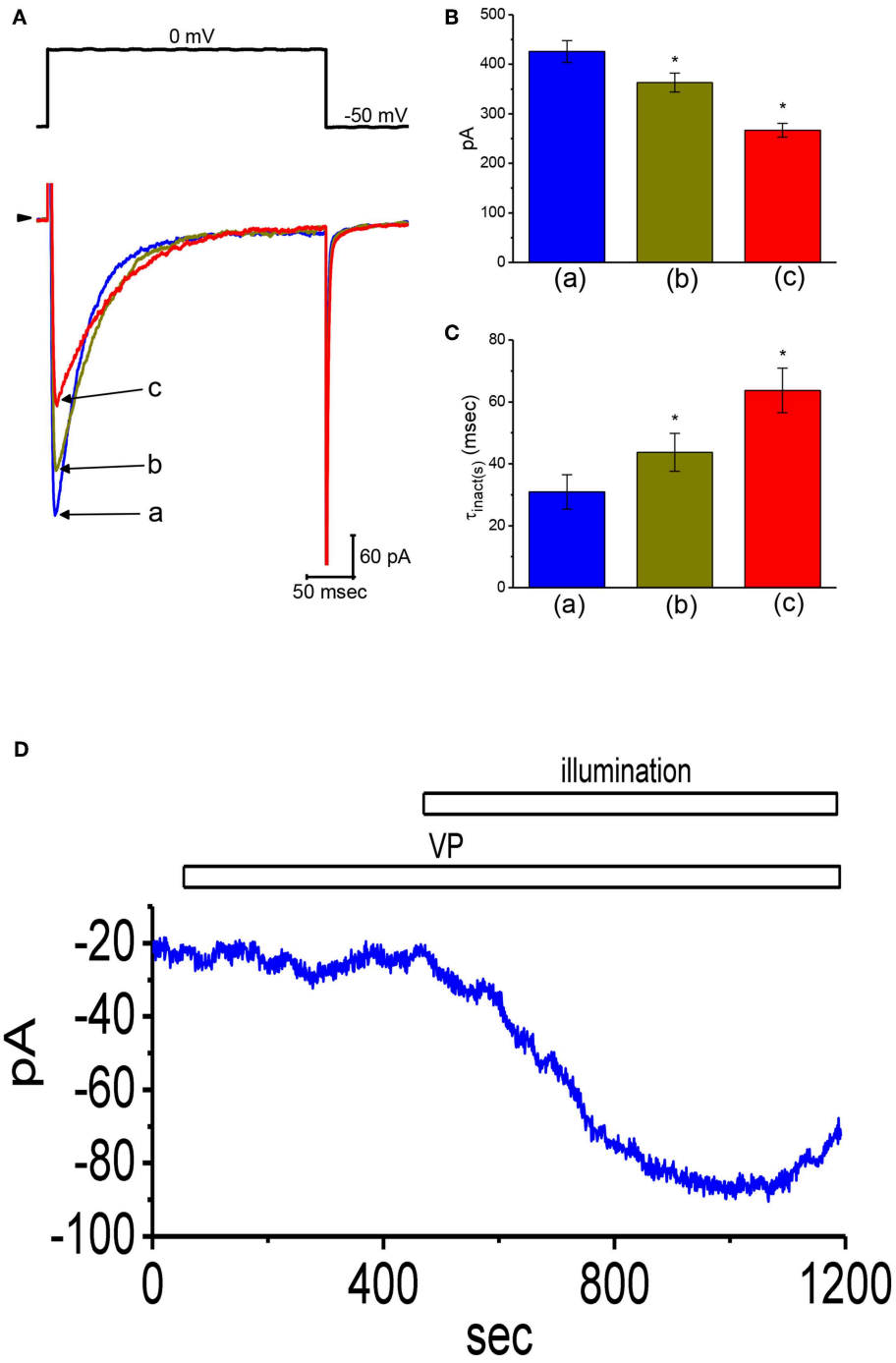

FIGURE 7 | Effects of VP on L-type Ca^{2+} current ($I_{Ca,L}$) and non-selective cation current (I_{NS}) in GH_3 cells. In this set of experiments, we bathed cells in normal Tyrode's solution containing 1.8 mM $CaCl_2$, 1 μM TTX, and 10 mM TEA, and the pipette used was filled with Cs^+-containing solution. **(A)** Original $I_{Ca,L}$ traces elicited by membrane depolarization from −50 to 0 mV [indicated in the upper part of **(A)**]. a: control; b: 1 μM VP; c: 3 μM VP. Panels **(B)** and **(C)** depict summarized bar graphs showing the effect of VP on the peak amplitude of $I_{Ca,L}$ and the slow component of inactivation time constant ($\tau_{inact(s)}$) for $I_{Ca,L}$, respectively (mean ± SEM; $n = 12$ for each bar). **(D)** Change in the amplitude of I_{NS} obtained in the presence of VP and VP plus illumination. The examined cell was held at the level of −50 mV. The horizontal bar indicates addition of 3 μM VP or illumination with light intensity of 5.5 mW/cm^2. *Significantly different from control ($P < 0.01$).

anti-neoplastic effects of this compound and its stimulatory actions on $I_{K(Ca)}$, before it passes through the membrane (Marks et al., 2000).

By using rose bengal, a natural polyphenolic compound known to be another type of photosensitizer, previous studies have demonstrated that this compound challenged with or

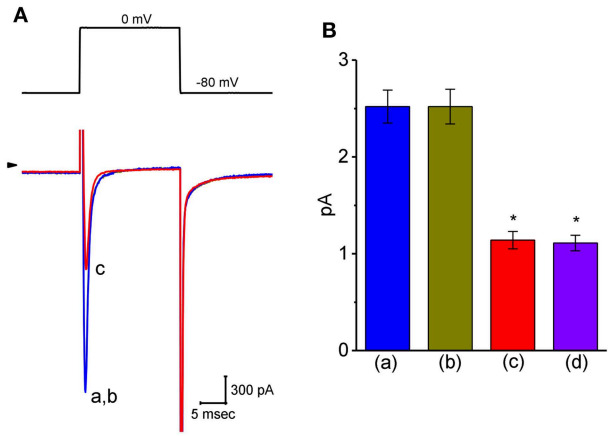

FIGURE 8 | Effect of VP on voltage-gated Na^+ current (I_{Na}) in GH_3 cells. The whole-cell current recordings made in this set of experiments were conducted in cells bathed in Ca^{2+}-free Tyrode's solution containing 10 mM TEA and 0.5 mM $CdCl_2$, and the recording pipette was filled with Cs^+-containing solution. **(A)** Original I_{Na} traces elicited by rapid membrane depolarization. The voltage protocol used is indicated in the upper part and arrowhead refers to the zero-current level. a: control; b: 3 μM VP; c: 3 μM VP plus 3 μM A-803467. **(B)** Summary bar graph of the effect of VP, VP plus A-803467, and VP plus A-887826 on the peak amplitude of I_{Na} (mean ± SEM; $n = 11$ for each bar). The peak I_{Na} amplitude was measured at the beginning of short depolarizing pulse from a holding potential of −80 mV. *Significantly different from control ($P < 0.05$).

without photosensitization was able to modify membrane ionic current in GH_3 cells along with mild damage on cell growth, although these cells were described to be relatively more resistant to photosensitized modification than other type of cells (Tarr et al., 1994; Valenzeno and Tarr, 1998, 2001). Similarly, findings from this study extended the observations and showed that VP was capable of stimulating $I_{K(Ca)}$ in a concentration-dependent manner in GH_3 cells. The illumination of VP could induce a non-selective cation current (Tarr et al., 1994), which appeared to be associated with the production of reactive oxygen species, and, in turn, increase the amplitude of $I_{K(Ca)}$ further in GH_3 cells (Valenzeno and Tarr, 1998; DeRosa and Crutchley, 2002). To what extent VP with or without illumination either modifies membrane potential or senses the photochemical modification remains to be further studied. It is also interesting to examine whether there are any other molecular target(s) which can regulate the VP-induced currents.

An earlier study has notably reported the capability of VP to dissipate mitochondrial inner transmembrane potential, hence decreasing the production of intracellular ATP (Belzacq et al., 2001). The pipette solution used in our whole-cell experiments contained 3 mM ATP; in particular, the amount of intracellular ATP is sufficient to fully suppress the activity of ATP-dependent K^+ (K_{ATP}) channels (Wu et al., 2000). Furthermore, VP-induced increase of outward currents observed in GH_3 cells was unable to be reversed by subsequent application of either tolbutamide, a blocker of K_{ATP} channels, or TRAM-39, an inhibitor of IK_{Ca} channels (Huang et al., 2015; Chen P. C. et al., 2018; Chen T. S. et al., 2018; Liu et al., 2019a). As such, VP-induced increase in K^+ outward currents conceivably is not associated with the activation of K_{ATP} or IK_{Ca} channels. Alternatively, in continued presence of VP, the ability of subsequent addition of dithiothreitol, a sulfhydryl reducing agent, to reverse VP-stimulated $I_{K(Ca)}$ seems to lend credence to suggest a possible link to VP-induced production of free oxygen species (DeRosa and Crutchley, 2002; Morishita et al., 2016; Baskaran et al., 2018; Eales et al., 2018; Kim et al., 2018).

In our cell-attached current recordings, addition of VP into the bath increased the activity of BK_{Ca} channels significantly with no clear change in the single-channel conductance. These results can be stated as meaning that VP-stimulated channel activity results largely from the availability of intracellular Ca^{2+}, despite inability of the VP molecules to act within the BK_{Ca}-channel's central pore. However, VP-mediated activation of BK_{Ca} channels found in GH_3 cells actually did not depend on increased availability of intracellular Ca^{2+}owing to elevated Ca^{2+} flux through voltage-gated Ca^{2+} channels, given the present results showing that VP effectively suppressed the amplitude of $I_{Ca,L}$ in GH_3 cells. Additionally, in inside-out current recordings, as VP was applied to the intracellular surface of the excised patch, little or no change in the activity of BK_{Ca} channels was demonstrated; however, subsequent addition of GMQ or PF573228, known to stimulate BK_{Ca} channels, was effective at raising the channel open probability (So et al., 2011, 2018). Notably, it has been also demonstrated that BK_{Ca} channels are functionally expressed in either retinal pigment epithelial cells, vascular endothelial cells, or amniotic fluid-derived stem cells (Li et al., 2000; Schmidt-Erfurth and Hasan, 2000; Sheu et al., 2005; Hua et al., 2014; Hu et al., 2015; Liu et al., 2015, 2018, 2019a,b). Taking this into account, to what extent VP-induced changes in BK_{Ca}-channel activity existing in these cells are intimately connected with its actions on sensory retina or pituitary adenoma during photodynamic therapy (Marks et al., 2000; Rahimipour et al., 2003; Rosenblatt et al., 2005; Hu et al., 2015; Nemes et al., 2016; Liu et al., 2018; Min et al., 2018; Iacono et al., 2019) remains to be imperatively investigated.

As being administrated, the VP molecules need to enter into cytosol or even nucleus, before being destined for having an interaction with YAP-TEAD complex (Brodowska et al., 2014; Feng et al., 2016; Gibault et al., 2016, 2017; Abe et al., 2018; Qin et al., 2019); hence, they must pass through surface membrane before entering the cell interior. From findings in this study, it is therefore tempting to speculate that the perturbations on membrane ion currents caused by VP would be required to precede its subsequent actions through suppression of YAP-TEAD complex. Moreover, another important determinants needed to be considered are the VP dose and the intensity of illumination, since the stimulatory effect of VP on $I_{K(Ca)}$ could be highly related to generation of reactive oxygen species (Morishita et al., 2016; Baskaran et al., 2018; Eales et al., 2018; Kim et al., 2018). The sensitization sites for the modification caused by the VP molecules are thought to be probably at an intramembranous location near the inner surface. Upon cell exposure to VP particularly along with long-term light exposure, the reactive oxygen species would be excessively produced, and resultant byproducts of oxidative metabolism can then interact

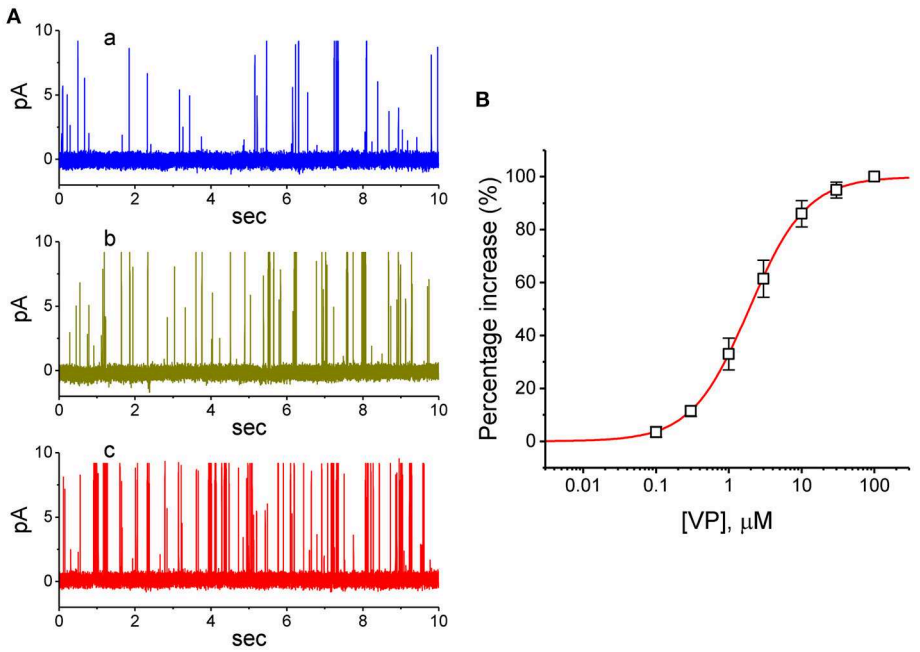

FIGURE 9 | Stimulatory effect of VP on BK_{Ca}-channel activity recorded from human 13-06-MG glioma cells. In this series of experiments, we bathed cells in normal Tyrode's solution and filled the recording pipette by using high K^+-containing solution. **(A)** Representative BK_{Ca}-channel currents taken under a holding potential of +60 mV relative to the bath. a: control; b: 1 μM VP; c: 3 μM VP. **(B)** Concentration-dependent relationship of VP effect on the probability of BK_{Ca}-channel openings in 13-06-MG cells (mean ± SEM; $n = 11$ for each point). The examined cell was held at +60 mV relative to the bath, and the channel open probability during the exposure to 100 μM VP was taken to be 100%. The smooth line represents the least-squares fit of the data points to the sigmoidal Hill equation as described in **Materials and Methods**. The values of EC_{50}, Hill coefficient, and maximal percentage increase of channel activity were estimated to be 1.9 μM, 1.1, and 100%, respectively.

with membrane phospholipids and proteins that constitute ion transport pathways such as BK_{Ca} channels. Lastly, It will be worthy of being investigated regarding to what extent VP-mediated modifications on membrane ion channels reported herein is closely linked to the inhibition of VAP-TEAD complex followed by changes in proliferation or differentiation of different types of neoplastic or stem cells, given that the fact that such photosensitizers as sensitized photochemical modification in an array of tumors, including pituitary tumors and gliomas, have been widely utilized (Marks et al., 2000; Brown et al., 2004; Solban et al., 2006; Triesscheijn et al., 2006; Cole et al., 2008; Brodowska et al., 2014; Valero et al., 2015; Morishita et al., 2016; Nemes et al., 2016; Chen and Hu, 2017; Baskaran et al., 2018; Liao et al., 2018; Mulder et al., 2018; Chen et al., 2019; Li et al., 2019; Pellosi et al., 2019; Qin et al., 2019; Zhang et al., 2019). Alternatively, the efficacy of VP in inhibiting YAP/TEAD interaction was currently noted to remain debated (Lui et al., 2019). Regardless of the detailed mechanism of VP actions, it is pertinent to point out that VP-induced modifications on membrane ion channels shown herein should not be ignored and is conceivably responsible for effecting its therapeutic or adverse actions (Marks et al., 2000; Abe et al., 2018; Min et al., 2018; Iacono et al., 2019 Isildak et al., 2019).

DATA AVAILABILITY

The raw data supporting the conclusions of this manuscript will be made available by the authors, without undue reservation, to any qualified researcher.

AUTHOR CONTRIBUTIONS

All authors listed have made a substantial, direct and intellectual contribution to the work, and approved it for publication.

ACKNOWLEDGMENTS

This study that led to the composition of this manuscript was supported in part by National Cheng Kung University (D106-35A13, D107-F2519, and NCKUH-10709001 to S-NW), Tainan City, Taiwan. The authors would like to acknowledge the technical assistance of Kaisen Lee for helping earlier work in this study. S-NW received a Talent Award for the Outstanding Researchers from Ministry of Education, Taiwan.

REFERENCES

Abe, T., Amaike, Y., Shizu, R., Takahashi, M., Kano, M., Hosaka, T., et al. (2018). Role of YAP activation in nuclear receptor CAR-mediated proliferation of mouse hepatocytes. *Toxicol. Sci.* 165, 408–419. doi: 10.1093/toxsci/kfy149

AlAmri, M., Kadri, H., Alderwick, L. J., Jeeves, M., and Mehellou, Y. (2018). The photosensitizing clinical agent verteporfin is an inhibitor of SPAK and OSR1 kinases. *Chembiochem* 4, 2072–2080. doi: 10.1002/cbic.201800272

Al-Moujahed, A., Brodowska, K., Stryjewski, T. P., Efstathiou, N. E., Vasilikos, I., Cichy, J., et al. (2017). Verteporfin inhibits growth of human glioma *in vitro* without light activation. *Sci. Rep.*7:7602. doi: 10.1038/s41598-017-07632-8

Baskaran, R., Lee, J., and Yang, S. G. (2018). Clinical development of photodynamic agents and therapeutic applications. *Biomater. Res.* 22:25. doi: 10.1186/s40824-018-0140-z

Belzacq, A. S., Jacotot, E., Vieira, H. L., Mistro, D., Granville, D. J., Xie, Z., et al. (2001). Apoptosis induction by the photosensitizer verteporfin: identification of mitochondrial adenine nucleotide translocator as a critical target. *Cancer Res.* 61, 1260–1264.

Brodowska, K., Al-Moujahad, A., Marmalidou, A., Meyer, Z. U., Horste, M., Cichy, J., et al. (2014). The clinically used photosensitizer verteporfin (VP) inhibits YAP-TEAD and human retinoblastoma cell growth *in vitro* without light activation. *Exp. Eye Res.* 124, 67–73. doi: 10.1016/j.exer.2014.04.011

Brown, S. B., Brown, E. A., and Walker, I. (2004). The present and further role of photodynamic therapy in cancer treatment. *Lancet Oncol.* 5, 497–508. doi: 10.1016/s1470-2045(04)01529-3

Chen, P. C., Ruan, J. S., and Wu, S. N. (2018). Evidence of decreased activity in intermediate-conductance calcium-activated potassium channels during retinoic acid-induced differentiation in motor neuron-like NSC-34 cells. *Cell. Physiol. Biochem.* 48, 2374–2388. doi: 10.1159/000492653

Chen, T. S., Lai, M. C., Hung, T. Y., Lin, K. M., Huang, C. W., and Wu, S. N. (2018). Pioglitazone, a PPAR-γ activator, stimulates BK_{Ca} but suppresses IK_M in hippocampal neurons. *Front. Pharmacol.* 9:977. doi: 10.3389/fphar.2018.00977

Chen, Y., and Hu, Y. (2017). Photodynamic therapy for an iris metastasis from pulmonary adenocarcinoma. *Photodiagn. Photodyn. Ther.* 20, 246–247. doi: 10.1016/j.pdpdt.2017.10.011

Chen, Y. A., Lu, C. Y., Cheng, T. Y., Pan, S. H., Chen, H. F., and Chang, N. S. (2019). WW domain-containing proteins YAP and TAZ in the Hippo pathway as key regulators in stemness maintenance, tissue homeostasis, and tumorigenesis. *Front. Oncol.* 9:60. doi: 10.3389/fonc.2019.00060

Cole, C. D., Liu, J. K., Sheng, X., Chin, S. S., Schmidt, M. H., Weiss, M. H., et al. (2008). Hypericin-mediated photodynamic therapy of pituitary tumors: preclinical study in a GH_4C_1 rat tumor model. *J. Neurooncol.* 87, 255–261. doi: 10.1007/s11060-007-9514-0

Deng, W., Chen, W., Clement, S., Guller, A., Zhao, Z., Engel, A., et al. (2018). Controlled gene and drug release from a liposomal delivery platform triggered by X-ray radiation. *Nat. Commun.* 9:2713. doi: 10.1038/s41467-018-05118-3

DeRosa, M. C., and Crutchley, R. J. (2002). Photosensitized singlet oxygen and its applications. *Coord. Chem. Rev.* 233-234, 351–371. doi: 10.1016/S0010-8545(02)00034-6

Eales, K. L., Wilkinson, E. A., Cruickshank, G., Tucker, J. H. R., and Tennant, D. A. (2018). Verteporfin selectively kills hypoxic glioma cells through iron-binding and increased production of reactive oxygen species. *Sci. Rep.* 8:14358. doi: 10.1038/s41598-018-32727-1

Eskelin, S., Tommila, P., Palosaari, T., and Kivelä, T. (2008). Photodynamic therapy with verteporfin to induce regression of aggressive retinal astrocytomas. *Acta Ophthalmol.* 86, 794–799. doi: 10.1111/j.1755-3768.2007.01151.x

Faustino, M. A., Neves, M. G., Vicente, M. G., Cavaleiro, J. A., Neumann, M., Brauer, H. D., et al. (1997). *Meso*-tetraphenylpoorphyrin dimer derivative as a potential photosensitizer in photodynamic therapy. *Photochem. Photobiol.* 66, 405–412.

Feng, J., Gou, J., Jia, J., Yi, T., Cui, T., and Li, Z. (2016). Verteporfin, a suppressor of YAP-TEAD complex, presents promising antitumor properties on ovarian cancer. *Onco. Targets Ther.* 9, 5371–5381. doi: 10.2147/OTT.S109979

Ghazai, B., Machacek, M., Shalaby, M. A., Novakova, V., Zimcik, P., and Makhseed, S. (2017). Phthalocyanines and tetrapyrazinoporphyrazines with two cationic donuts: high photodynamic activity as a result of rigid spatial arrangement of peripheral substituents. *J. Med. Chem.* 60, 6060–6076. doi: 10.1021/acs.jmedchem.7b00272

Gibault, F., Bailly, F., Corvaisier, M., Coevoet, M., Huet, G., Melnyk, P., et al. (2017). Molecular features of the YAP inhibitor verteporfin: synthesis of hexasubstituted dipyrrins as potential inhibitors of YAP/TAZ, the downstream effects of the Hippo Pathway. *ChemMedChem* 12, 954–961. doi: 10.1002/cmdc.201700063

Gibault, F., Corvaisier, M., Bailly, F., Huet, G., Melnyk, P., and Cotelle, P. (2016). Non-photoinduced biological properties of verteporfin. *Curr. Med. Chem.* 23, 1171–1184. doi: 10.2174/0929867323666160316125048

Hu, Y., Chen, Y., and Chen, L. (2015). Half-dosage and bolus injection photodynamic therapy for symptomatic circumscribed choroidal hemangioma: a case report. *Photodiagn. Photodyn. Ther.* 12, 526–529. doi: 10.1016/j.pdpdt.2015.05.005

Hua, R., Liu, L., Li, C., and Chen, L. (2014).Evaluation of the effects of photodynamic therapy on chronic central serous chorioretinopathy based on the mean choroidal thickness and the lumen area of abnormal choroidal vessels. *Photodiagn. Phododyn. Ther.* 11, 519–525. doi: 10.1016/j.pdpdt.2014.07.005

Huang, M. H., Huang, Y. M., and Wu, S. N. (2015). The inhibition by oxaliplatin, a platinum-based anti-neoplastic agent, of the activity of intermediate-conductance Ca^{2+}-activated K^+ channels in human glioma cells. *Cell. Physiol. Biochem.* 37, 1390–1406. doi: 10.1159/000430404

Iacono, P., Toto, L., Eliana, C., Varano, M., and Parravano, M. C. (2019). Pharmacotherapy of central serous chorioretinopathy: review of the current treatments. *Curr. Pharm. Des.* 24, 4864–4873. doi: 10.2174/1381612825666190123165914

Isildak, H., Schwartz, S. G., and Flynn, H. W. (2019). Pharmacotherapy of myopic choroidal neovascularization. *Curr. Pharm. Des.* 24, 4853–4859. doi: 10.2174/1381612825666190124102641

Kandoussi, I., Lakhlili, W., Taoufik, J., and Ibrahimi, A. (2017). Docking analysis of verteporfin with YAP WW domain. *Bioinformation* 13, 237–240. doi: 10.6026/97320630013237

Karacorlu, M., Karacorlu, S., and Ozdemir, H. (2004). Nonarteritic anterior ischemic optic neuropathy after photodynamic therapy for choroidal neovascularization. *Jpn. J. Ophthalmol.* 48, 424–426. doi: 10.1007/s10384-004-0078-7

Kim, T. W., Moon, J. W., and Yu, H. G. (2018). N-acetylcysteine protects against chorioretinal damage induced by photodynamic therapy for experimental choroidal neovascularization in a rat model. *Phtodiagn. Photodyn. Ther.* 23, 12–17. doi: 10.1016/j.pdpdt.2018.04.006

Konstantinou, E. K., Notomi, S., Kosmidou, C., Brodowska, K., Al-Moujahed, A., Nicolaou, F., et al. (2017). Verteporfin-induced formation of protein cross-linked oligomers and high molecular weight complexes is mediated by light and leads to cell toxicity. *Sci. Rep.* 7:46581. doi: 10.1038/srep46581

Li, H. F., Chen, S. A., and Wu, S. N. (2000). Evidence for the stimulatory effect of resveratrol on Ca^{2+}-activated K^+ current in vascular endothelial cells. *Cardiovasc. Res.* 45, 1035–1045. doi: 10.1016/S0008-6363(99)00397-1

Li, Y., Wang, S., Wei, X., Zhang, S., Song, Z., Chen, X., et al. (2019). Role of inhibitor of yes-associated protein 1 in triple-negative breast cancer with taxol-based chemoresistance. *Cancer Sci.* 110, 561–567. doi: 10.1111/cas.13888

Liao, T., Wei, W. J., Wen, D., Hu, J. Q., Wang, Y., Ma, B., et al. (2018). Verteporfin inhibits papillary thyroid cancer cells proliferation and cell cycle through ERK1/2 signaling pathway. *J. Cancer.* 9, 1329–1336. doi: 10.7150/jca.21915

Lin, J., Gu, Y., Du, R., Deng, M., Lu, Y., and Ding, Y. (2014). Detection of EGFR mutation in supernatant, cell pellets of pleural effusion and tumor tissues from non-small cell lung cancer patients by high resolution melting analysis and sequencing. *Int. J. Clin. Exp. Pathol.* 7, 8813–8822.

Lin, M. W., Yang, S. R., Huang, M. H., and Wu, S. N. (2004). Stimulatory actions of caffeic acid phenethyl ester, a known inhibitor of NF-κB activation, on Ca^{2+}-activated K^+ current in pituitary GH_3 cells. *J. Biol. Chem*. 279, 26885–26892. doi: 10.1074/jbc.M400356200

Liu, C. C., Huang, Y. M., Wu, S. N., and Sze, C. I. (2015). Correlation of mesenchymal differentiation and ion-channel activity in radiation-induced resistant human glioblastoma cell line. *FASEB J.* 29:1. Available online at: https://www.fasebj.org/doi/abs/10.1096/fasebj.29.1_supplement.844.17

Liu, L., Hu, C., Chen, L., and Hu, Y. (2018). Photodynamic therapy for symptomatic circumscribed choroidal hemangioma in 22 Chinese patients: a retrospective study. *Photodiagn. Photodyn. Ther.* 24, 372–376. doi: 10.1016/j.pdpdt.2018.10.019

Liu, Y. W., Fang, Y. H., Su, C. T., Hwang, S. M., Liu, P. Y., and Wu, S. N. (2019a). The biochemical and electrophysiological profiles of amniotic fluid-derived stem cells following Wnt signaling modulation cardiac differentiation. *Cell Death Discov*. 5:59. doi: 10.1038/s41420-019-0143-0

Liu, Y. Y., Hsiao, H. T., Wang, J. C., Liu, Y. C., and Wu, S. N. (2019b). Parecoxib, a selective blocker of cyclooxygenase-2, directly inhibits neuronal delayed-rectifier K^+ current, M-type K^+ current and Na^+ current. *Eur. J. Pharmacol.* 844, 95–101. doi: 10.1016/j.ejphar.2018.12.005

Lui, J. W., Xiao, S., Ogomori, K., Hammarstedt, J. E., Little, E. C., and Lang, D. (2019). The efficacy of verteporfin as a therapeutic option in pre-clinical models of melanoma. *J. Cancer*. 10, 1–10. doi: 10.7150/jca.27472

Marks, P. V., Belchetz, P. E., Saxena, A., Igbaseimokumo, U., Thomson, S., Nelson, M., et al. (2000). Effect of photodynamic therapy on recurrent pituitary adenomas: clinical phase I/II trial-an early report. *Br. J. Neurosurg.* 14, 317–325. doi: 10.1080/026886900417298

Min, J. Y., Lv, Y., Mao, L., Gong, Y. Y., Gu, Q., and Wei, F. (2018). A rodent model of anterior ischemic optic neuropathy (AION) based on laser photoactivation of verteporfin. *BMC Ophthalmol.* 18:304. doi: 10.1186/s12886-018-0937-5

Morishita, T., Hayakawa, F., Sugimoto, K., Iwase, M., Yamamoto, H., Hirano, D., et al. (2016). The photosensitizer verteporfin has light-independent anti-leukemic activity for Ph-positive acute lymphoblastic leukemia and synergistically works with dasatinib. *Oncotarget* 7, 56241–56252. doi: 10.18632/oncotarget.11025

Mulder, C. L., Eijkenboom, L. L., Beerendonk, C. C. M., Braat, D. D. M., and Peek, R. (2018). Enhancing the safety of ovarian cortex autotransplantation: cancer cells are purged completely from human ovarian tissue fragments by pharmacological inhibition of YAP/TAZ oncoproteins. *Hum. Reprod.* 34, 506–518. doi: 10.1093/humrep/dey384

Nemes, A., Fortmann, T., Poeschke, S., Greve, B., Prevedello, D., Santacroce, A., et al. (2016). 5-ALA fluorescence in native pituitary adenoma cell lines: resection control and basis for photodynamic therapy (PDT)? *PLoS ONE* 11:e0161364. doi: 10.1371/journal.pone.0161364

Pellosi, D. S., Paula, L. B., de Melo, M. T., and Tedesco, A. C. (2019). Targeted and synergic glioblastoma treatment: multifunctional nanoparticle delivering verteporfin as adjuvant therapy for temozolomide chemotherapy. *Mol. Pharm.* 16, 1009–1024. doi: 10.1021/acs.molpharmaceut.8b01001

Qin, X., Li, J., Sun, J., Liu, L., Chen, D., and Liu, Y. (2019). Low shear stress induces ERK nuclear localization and YAP activation to control the proliferation of breast cancer cells. *Biochem. Biophys. Res. Commun.* 510, 219–223. doi: 10.1016/j.bbrc.2019.01.065

Rahimipour, S., Ben-Aroya, N., Ziv, K., Chen, A., Fridkin, M., and Koch, Y. (2003). Receptor-mediated targeting of a photosensitizer by its conjugation to gonadotropin-releasing hormone analogues. *J. Med. Chem*. 46, 3965–3974. doi: 10.1021/jm020535y

Renno, R. Z., Terada, Y., Haddadin, M. J., Michaud, N. A., Gragoudas, E. S., and Miller, J. W. (2004). Selective photodynamic therapy by targeted verteporfin delivery to experimental choroidal neovascularization mediated by a homing peptide to vascular endothelial growth factor receptor-2. *Arch. Ophthalmol.* 122, 1002–1011. doi: 10.1001/archopht.122.7.1002

Rosenblatt, B. J., Shah, G. K., and Blinder, K. (2005). Photodynamic therapy with verteporfin for pericapillary choroidal neovascularization. Retina 25, 33–37.

Rush, A. M., and Cummins, T. R. (2007). Painful research: identification of a small-molecule inhibitor that selectively targets $Na_V1.8$ sodium channels. *Mol. Interv.* 7, 192–195. doi: 10.1124/mi.7.4.4

Sankaranarayanan, S., and Simasko, S. M. (1996). Characterization of an M-like current modulated by thyrotropin-releasing hormone in normal rat lactotrophs. *J. Neurosci.* 16, 1668–1678.

Schmidt-Erfurth, U., and Hasan, T. (2000). Mechanisms of action of photodynamic therapy with verteporfin for the treatment of age-related macular degeneration. *Surv. Ophthalmol.* 45, 195–214. doi: 10.1016/S0039-6257(00)00158-2

Sheu, S. J., Wu, S. N., and Hu, D. N. (2005). Stretch-stimulated activity of large conductance calcium-activated potassium channels in human retinal pigment epithelial cells. *J. Ocul. Pharmacol. Ther.* 21, 429–435. doi: 10.1089/jop.2005.21.429

So, E. C., Foo, N. P., Ko, S. Y., and Wu, S. N. (2019). Bisoprolol, known to be a selective β_1-receptor antagonist, differentially but directly suppresses $I_{K(M)}$ and $I_{K(erg)}$ in pituitary cells and hippocampal neurons. *Int. J. Mol. Sci.* 20:657. doi: 10.3390/ijms20030657

So, E. C., Wang, Y., Yang, L. Q., So, K. H., Lo, Y. C., and Wu, S. N. (2018). Multiple regulatory actions of 2-guanidine-4-methylquinazoline (GMQ), an agonist of acid-sensing ion channel type-3, on ionic currents in pituitary GH_3 cells and in olfactory sensory (Rolf B1.T) neurons. *Biochem. Pharmacol.* 151, 79–88. doi: 10.1016/j.bcp.2018.02.027

So, E. C., Wu, K. C., Liang, C. H., Chen, J. Y., and Wu, S. N. (2011). Evidence for activation of BK_{Ca} channels by a known inhibitor of focal adhesion kinase, PF573228. *Life Sci.* 89, 691–701. doi: 10.1016/j.lfs.2011.08.013

Solban, N., Rizvi, I., and Hasan, T. (2006). Targeted photodynamic therapy. *Lasers Surg. Med.* 38, 522–531. doi: 10.1002/lsm.20345

Stojilkovic, S. S., Tabak, J., and Bertram, R. (2010). Ion channels and signaling in the pituitary gland. *Endoc. Rev.* 31, 845–915. doi: 10.1210/er.2010-0005

Tarr, M., Arriaga, E., Goertz, K. K., and Valenzeno, D. P. (1994). Properties of cardiac I_{leak} induced by photosensitizer-generated reactive oxygen. *Free Radic. Biol. Med.* 16, 477–484.

Tekrony, A. D., Kelly, N. M., Fage, B. A., and Cramb, D. T. (2011). Photobleaching kinetics of verteporfin and lemuteporfin in cells and optically trapped multilamellar vesicles using two-photon excitation. *Photochem. Photobiol.* 87, 853–861. doi: 10.1111/j.1751-1097.2011.00933.x

Triesscheijn, M., Baas, P., Schellens, J. H., and Stewart, F. A. (2006). Photodynamic therapy in oncology. *Oncologist* 11, 1034–1044. doi: 10.1634/theoncologist.11-9-1034

Valenzeno, D. P., and Tarr, M. (1998). GH_3 cells, ionic currents and cell killing: photomodification sensitized by Rose Bengal. *Photochem. Photobiol.* 68, 519–526.

Valenzeno, D. P., and Tarr, M. (2001). Calcium as a modulator of photosensitized killing of H9c2 cardiac cells. Phtochem. Photobiol. 74, 605–610. doi: 10.1562/0031-8655(2001)074<0605:caamop>2.0.co;2

Valero, V. III., Pawlik, T. M., and Anders, R. A. (2015). Emerging role of Hpo signaling and YAP in hepatocellular carcinoma. *J. Hepatocell Carcinoma* 2, 69–78. doi: 10.2147/JHC.S48505

Wu, S. N., Chern, J. H., Shen, S., Chen, H. H., Hsu, Y. T., Lee, C. C., et al. (2017). Stimulatory actions of a novel thiourea derivative on large-conductance, calcium-activated potassium channels. *J. Cell. Physiol.* 232, 3409–3421. doi: 10.1002/jcp.25788

Wu, S. N., Chiang, H. T., Shen, A. Y., and Lo, Y. K. (2003). Differential effects of quercetin, a natural polyphenolic flavonoid on L-type calcium current in pituitary tumor (GH_3) cells and neuronal NG108-15 cells. *J. Cell. Physiol.* 195, 298–308. doi: 10.1002/jcp.10244

Wu, S. N., Li, H. F., and Chiang, H. T. (2000). Characterization of ATP-sensitive potassium channels functionally expressed in pituitary GH_3 cells. *J. Membr. Biol.* 178, 205–214. doi: 10.1007/s002320010028

Wu, S. N., Li, H. F., and Jan, C. R. (1998a). Regulation of Ca^{2+}-activated nonselective cationic currents in rat pituitary GH_3 cells: involvement in L-type Ca^{2+} current. *Brain Res.* 812, 133–141. doi: 10.1016/s0006-8993(98)00964-0

Wu, S. N., Li, H. F., Jan, C. R., Chen, I. J., and Lo, Y. C. (1998b). Selective block by glyceryl nonivamide of inwardly rectifying K^+ current in rat anterior

pituitary GH_3 cells. *Life Sci.* 63, PL281–PL288. doi: 10.1016/s0024-3205(98)00447-0

Zhang, Q., Guo, Y., Yu, H., Tang, Y., Yuan, Y., Jiang, Y., et al. (2019). Receptor activity-modifying protein 1 regulates the phenotypic expression of BMSCs via the Hippo/Yap pathway. *J. Cell. Physiol.* 234, 13969–13976. doi: 10.1002/jcp.28082

Zhang, X. F., Shieh, C. C., Chapman, M. L., Matulenko, M. A., Hakeem, A. H., Atkinson, R. N., et al. (2010). A-887826 is a structurally novel, potent and voltage-dependent $Na_V1.8$ sodium channel blocker that attenuates neuropathic tactile allodynia in rats. *Neuropharmacology* 59, 201–207. doi: 10.1016/j.neuropharm.2010.05.009

Zhou, X., Chen, B., Hoopes, P. J., Hasan, T., and Pogue, B. W. (2006). Tumor vascular area correlates with photosensitizer uptake: analysis of verteporfin microvascular delivery in the Dunning rat prostate tumor. *Photochem. Photobiol.* 82, 1348–1357. doi: 10.1562/2006-03-25-ra-858

Conflict of Interest Statement: The authors declare that the research was conducted in the absence of any commercial or financial relationships that could be construed as a potential conflict of interest.

frontiers in Chemistry

ORIGINAL RESEARCH
published: 25 February 2020
doi: 10.3389/fchem.2020.00100

Lithium-Ion Transport in Nanocrystalline Spinel-Type $Li[In_xLi_y]Br_4$ as Seen by Conductivity Spectroscopy and NMR

Maria Gombotz[1]*, *Daniel Rettenwander*[1] and *H. Martin R. Wilkening*[1,2]*

[1] Institute for Chemistry and Technology of Materials, Technical University of Graz, Graz, Austria, [2] ALISTORE-European Research Institute, CNRS FR3104, Hub de l'Energie, Amiens, France

Currently, a variety of solid Li^+ conductors are being discussed that could potentially serve as electrolytes in all-solid-state Li-ion batteries and batteries using metallic Li as the anode. Besides oxides, sulfides and thioposphates, and also halogenides, such as Li_3YBr_6, belong to the group of such promising materials. Here, we report on the mechanosynthesis of ternary, nanocrystalline (defect-rich) $Li[In_xLi_y]Br_4$, which crystallizes with a spinel structure. We took advantage of a soft mechanochemical synthesis route that overcomes the limitations of classical solid-state routes, which usually require high temperatures to prepare the product. X-ray powder diffraction, combined with Rietveld analysis, was used to collect initial information about the crystal structure; it turned out that the lithium indium bromide prepared adopts cubic symmetry ($Fd\bar{3}m$). The overall and electronic conductivity were examined via broadband conductivity spectroscopy and electrical polarization measurements. While electric modulus spectroscopy yielded information on long-range ion transport, ^7Li nuclear magnetic resonance (NMR) spin-lattice relaxation measurements revealed rapid, localized ionic hopping processes in the ternary bromide. Finally, we studied the influence of thermal treatment on overall conductivity, as the indium bromide might find applications in cells that are operated at high temperatures (330 K and above).

Keywords: lithium halogenides, all-solid-state batteries, ceramic electrolytes, diffusion, ionic conductivity, impedance spectroscopy, solid-state NMR

OPEN ACCESS

Edited by:
Neeraj Sharma,
University of New South Wales, Australia

Reviewed by:
Luke O'Dell,
Deakin University, Australia
Xifei Li,
Xi'an University of Technology, China

***Correspondence:**
Maria Gombotz
gombotz@tugraz.at
H. Martin R. Wilkening
wilkening@tugraz.at

Specialty section:
This article was submitted to Electrochemistry, a section of the journal Frontiers in Chemistry

Received: *20 November 2019*
Accepted: *03 February 2020*
Published: *25 February 2020*

Citation:
Gombotz M, Rettenwander D and Wilkening HMR (2020) Lithium-Ion Transport in Nanocrystalline Spinel-Type $Li[In_xLi_y]Br_4$ as Seen by Conductivity Spectroscopy and NMR. Front. Chem. 8:100. doi: 10.3389/fchem.2020.00100

1. INTRODUCTION

Next-generation energy storage systems, which rely on lithium-based batteries, need to be improved in terms of energy density and safety. One possibility for developing powerful batteries is to replace the flammable F-containing liquid electrolytes usually used by ceramic electrolytes (Goodenough, 2013; Bachman et al., 2016; Janek and Zeier, 2016; Zhang et al., 2018). The thermal runaway of such batteries is expected to shift significantly toward higher temperatures.

Suitable ceramics need to show very high ionic conductivities and a sufficiently high electrochemical stability. To achieve high energy densities, the use of Li metal as anode material is necessary. Li metal has already been used as anode material (Wenzel et al., 2016) in the early stages of Li-battery research. However, stability issues, the lack of suitable (liquid) electrolytes (Bruce et al., 2008), and the formation of dendrites (Porz et al., 2017) prevented the commercialization of

such systems. The discovery of highly conducting ceramics has changed this path of development. Of course, many studies have revealed that the Li|electrolyte interface suffers from contact issues (Cheng et al., 2014; Yu et al., 2017; Zhang et al., 2017). These interface issues are closely related to the formation of resistive interfacial phases (Richards et al., 2016). Controlling or preventing their formation is still a problem that needs to be overcome for the majority of ceramics currently discussed as solid electrolytes.

Presently, a range of Li-bearing oxides (Murugan et al., 2007; Buschmann et al., 2011; Thangadurai et al., 2014; Stanje et al., 2017; Uitz et al., 2017), sulfides (Kamaya et al., 2011; Wang et al., 2015; Dietrich et al., 2017), hydrides (Maekawa et al., 2009; Matsuo and Orimo, 2011; Kim et al., 2019), and thiophosphates (Deiseroth et al., 2008; Hanghofer et al., 2019) are being investigated with respect to ionic conductivity, stability and interfacial properties. Besides these classes of materials, halides (Lutz et al., 1990; Marx and Mayer, 1996; Gupta et al., 1997) are also regarded as up-and-coming materials to be employed as solid electrolytes. For instance, mixtures of Li^+ ion conductors with lithium salts, e.g., Li_2S mixed with LiBr, as well as compounds like $LiI_{1-x}Br_x$, which were already being studied in the 80s (Mercier et al., 1985; Schoch et al., 1986), show increased ionic conductivity as compared to the binary halides. The latter, particularly if we consider LiI and LiF, represent extremely poor ionic conductors. Regarding ternary Li-bearing halides with Y or In, compounds like Li_3YBr_6 or Li_3YCl_6 have entered the spotlight of research (Asano et al., 2018). Recently, the performance of a 3.5 V cell with either Li_3YBr_6 or Li_3YCl_6 as electrolyte has been investigated. First-principle analysis confirmed such compounds to have high ionic conductivity as well as relatively broad electrochemical stability. For example, a stability window of 0.59–3.15 V has been reported for Li_3YBr_6 (Wang et al., 2019). Because of this encouraging result, it is worth looking at this interesting class of materials and studying related compounds.

Here, we synthesized a cubic form of defect-rich $Li[In_xLi_y]Br_4$ in a nanocrystalline form. $LiInBr_4$ has been mentioned in the literature in a study carried out by Yamada et al. (2006). The authors speculated whether $LiInBr_4$ should be described by $(Li)_{8b}[In\square]_{16d}Br_4$ or by $(\square)_{8b}[InLi]_{16d}Br_4$, where 8*b* and 16*d* represent the tetrahedral and octahedral voids formed by the Br anion lattice. Preliminary studies also reported on coarse-grained Li_3InX_6 (X = Cl, Br) (Tomita et al., 2008, 2014; Li et al., 2019). In the present case, classical solid-state synthesis routes resulted in samples with a large amount of side phases, so we decided to take advantage of a mechanochemical synthesis approach to prepare $Li[In_xLi_y]Br_4$, which we characterized, apart from X-ray diffraction, also by high-resolution ^6Li and ^{79}Br magic angle spinning (MAS) nuclear magnetic resonance (NMR). Preliminary Rietveld analysis of the corresponding X-ray powder pattern revealed that nano-$Li[In_xLi_y]Br_4$ most likely crystallizes with cubic symmetry; roughly speaking the stoichiometry of the sample is best described by $Li[In_{0.62}Li_{1.38}]Br_{3.92}$. We used variable-temperature broadband conductivity and electrical modulus spectroscopy to measure its ionic transport properties. To understand the results from conductivity spectroscopy, we estimated site energies and diffusive barriers with the help of the bond valence energy landscape (BVEL) methodology developed by Chen et al. (2019). Here, at 293 K, the so-called direct current (dc) total ionic conductivity, σ_{dc}, is given by 4.9×10^{-6} S cm^{-1}. Of course, as a higher conductivity is needed for cells operated at room temperature, the ternary bromide might be a suitable electrolyte for cells that are cycled at $T > 330$ K. Furthermore, we characterized our sample in terms of temperature stability, electronic conductivity, and Li self-diffusion. The latter was investigated by means of ^7Li NMR line shape and spin-lattice relaxation measurements (Kuhn et al., 2011; Wilkening and Heitjans, 2012; Pecher et al., 2017; Stanje et al., 2017; Uitz et al., 2017; Dawson et al., 2018; Martin et al., 2019). Interestingly, ^7Li NMR points to rapid localized ion-hopping processes in the nanocrystalline form of the ternary indium bromide.

2. MATERIALS AND METHODS

2.1. Mechanochemical Synthesis of Nanocrystalline $Li[In_xLi_y]Br_4$

Mechanochemical synthesis was carried out in ZrO_2 beakers with a volume of 45 ml and using milling balls made of the same material with a diameter of 5 mm. The beakers were loaded with LiBr (99.999%, Sigma Aldrich) and $InBr_3$ (99.99%, Alfa Aesar) at a ratio of 3:1. Synthesis was carried out using a high-energy planetary mill Fritsch Pulverisette 7 premium line at a milling speed of 600 rpm. The total milling time was 10 h, whereas after each milling duration of 15 min, the beakers were allowed to cool down and to rest for 15 min. Loading as well as emptying of the beakers was strictly carried out in an argon-filled glovebox (H_2O, $O_2 < 0.5$ ppm), as both the starting materials and the product are highly hygroscopic.

2.2. X-Ray Powder Diffraction

X-ray powder diffraction (XRPD) was carried out on a Bruker D8 Advance diffractometer [Bragg Brentano geometry, CuKα radiation (1.5406 Å)]. Between 10 and 100° 2θ data points were collected for 1 s and with a stepsize of 0.02° 2θ. The measurements, at ambient temperature, had to be performed with a sample holder designed for air-sensitive materials; here, the samples were protected from any moisture by a Kapton® foil. For reasonable background correction, we performed a reference measurement, that is, a blank run using the empty sample holder and the Kapton® foil only. X-PertHighScorePlus software (PANalytical) was used to analyze the pattern according to the method introduced by Rietveld.

2.3. Conductivity and Electric Modulus Spectroscopy

The overall conductivity of site-disordered $Li[In_xLi_y]Br_4$ was investigated by broadband conductivity spectroscopy. Small amounts of the powdered sample were pressed into cylindrical pellets (5 mm in diameter) by applying a uniaxial pressure of 0.8 GPa. The pellets were equipped with ion-blocking electrodes (Pt, 100 nm in thickness) by sputtering (Leica, EM SCD050). Finally, the pellets were put in an air-tight sample holder. All preparation steps were carried out inside an Ar-filled glovebox (H_2O, $O_2 < 0.1$ ppm). Alternating current (ac) impedance data

were recorded with a Novocontrol Concept 80 spectrometer in combination with an active BDS 1200 cell and a ZGS interface (Novocontrol). A QUATRO cryosystem was employed to precisely control and monitor the temperature via Pt100 thermocouples. Here, we varied the temperature T from −40 to 100 °C. The frequency range covered for each isothermal measurement was 10^{-2}–10^{7} Hz.

2.4. Polarization Measurements to Estimate the Electronic Conductivity

The as-prepared nanocrystalline $Li[In_xLi_y]Br_4$ was pressed into a cylindrical pellet (d = 8 mm, h = 1.51 mm) under uniaxial pressure (0.3 GPa). Pt electrodes were applied on both sides via sputtering. Due to its hygroscopic character, the pellet with this electrode sandwich configuration was mounted in an air-tight Swagelok-type cell. We prepared the pellet and the cell in a glovebox (O_2, H_2O < 0.1 ppm) and subsequently placed the cell in a drying oven at 60°C. The cell was then connected to a Parstat MC potentiostat (Princeton Applied Research), which is equipped with a low-current option. We applied a constant voltage U of 300 mV and measured the change of current $I(t)$ over time.

2.5. ^{6}Li and ^{79}Br MAS NMR

High-resolution ^{6}Li and ^{79}Br magic angle spinning (MAS) NMR spectra were acquired with a 500 MHz Bruker Avance III spectrometer connected to a 11.7 T cryomagnet (Bruker Biospin, Ultrashield 500 WB plus). This magnetic field corresponds to resonance frequencies of 73.58 MHz for ^{6}Li and 125.27 MHz for ^{79}Br, respectively. The powder sample was stuffed into 2.5 mm ZrO_2 rotors designed for the MAS probehead used (Bruker). The spinning speed was set to 25 kHz; spectra were recorded at a bearing gas temperature of 303 K (frame cooling: 35% target gas flow, target gas flow: 400 L h^{-1}). ^{6}Li MAS NMR spectra were recorded at selected temperatures viz. at 253, 273, and 303 K. We used single-pulse excitation and converted the free induction decays (FIDs) into spectra by Fourier transformation. LiBr served as reference material (0 ppm) to determine chemical shifts δ_{iso}.

2.6. Static ^{7}Li NMR Spectroscopy

^{7}Li NMR longitudinal spin-lattice relaxation (SLR) rates ($1/T_1$) were recorded on a Bruker Avance III spectrometer with a nominal magnetic field of 7.05 T. This field corresponds to a ^{7}Li Larmor frequency of 116.59 MHz. A home-built NMR probe was used to record the static NMR signal in a temperature range from −40 to 100°C. Diffusion-induced SLR rates in the laboratory frame of reference were recorded by using a saturation recovery pulse, which includes a set of ten 90° pulses, destroying longitudinal magnetization M_z, and delay times t_d, after which the magnetization was detected with a single 90° pulse. The resulting transients $M_z(t_d)$ were analyzed with stretched exponentials to determine $1/T_1$. The spin-lock NMR technique was used to acquire SLR_ϱ rates in the so-called rotating frame of reference. We used a spin-locking frequency to record ^{7}Li NMR diffusion-induced rates $1/T_{1\varrho}$ at a locking field that corresponds to $\omega_1/2\pi$ = 20 kHz. For the static ^{7}Li NMR experiments, the sample was fire-sealed under vacuum in a glass (Duran®) ampoule with a diameter of 5 mm and a length of ∼3 cm.

3. RESULTS AND DISCUSSION

3.1. X-Ray Diffraction and Diffusion Pathways

The crystal structure of nanocrystalline $Li[In_xLi_y]Br_4$ was first characterized using XRPD. We used an airtight sample holder to record the diffraction pattern at ambient temperature; the pattern is shown in **Figure 1**. It perfectly agrees with that presented by Yamada et al. (2006). Our pattern reveals relatively broad reflections, which points to a sample with either low crystallinity or very small crystallites. According to the Scherrer equation (Scherrer, 1918; Heitjans et al., 2007), the mean crystallite size $\langle d \rangle$ is in the order of 17(5) nm if we use the reflections (448), (226), and (004) to estimate $\langle d \rangle$. These reflections correspond to the structure model estimated via Rietveld analysis with information derived from the bond valence energy landscape (BVEL) methodology developed by Chen et al. (2019). For our BVEL estimation, we used the structure model of Li_2MnBr_4. Despite the low crystallinity and the Kapton tape used to avoid degradation of the sample in air, we were able to propose a structure model (see **Table 1**), which summarizes the results from Rietveld refinement.

Indexing of all Bragg peaks is possible with the space group $Fd\bar{3}m$ (no. 227). Only a small amount of an unidentified extra phase is present. In addition, we cannot exclude that small amounts of amorphous LiBr or $InBr_3$, being invisible for X-ray diffraction, are present. Because of the low scattering factor of Li, its exact assignment to crystallographic positions is difficult if not impossible for powder samples. In order to obtain an initial guess for the refinement, we calculated site energies and diffusive barriers based on the BVEL methodology (see above) (Chen et al., 2019). Although the values calculated have unclear physical meaning, they can be used to estimate cation pathways and site preferences. It turned out that the Li ions prefer to occupy the sites 16*d* (octahedral site) and 8*b* (tetrahedral site). By using this information from BVEL calculations, we were able to estimate the Li site occupancies at the Wyckoff positions 16*d* (Li2) and 8*b* (Li1) via Rietveld refinement. The site occupancies are best described by 1.38(11) per formula unit (pfu) and 1.00(32) pfu, respectively. For In, placed at 16*d*, thus sharing the same site with Li2, and Br (32*e*), we obtained 0.62(11) pfu and 3.92(9) pfu, respectively. Finally, this yields the composition $Li_{8b}[In_{0.62}Li_{1.38}]_{16d}Br_{3.92}$, with Li-In positional disorder on 16*d*. Indium is in the oxidation state +3.

This inverse spinel-type structure displays a 3D framework consisting of edge-sharing $InBr_6$ octahedra (see inset in **Figure 1A**). Each 16*d* site shares faces with two tetrahedral 6*b* sites, whereby each 8*b* site shares common faces with four 16*d* sites. This polyhedra connection forms a 3D diffusion pathway, as described by the calculated isosurface of the Li BVEL map (see **Figure 1B**). The corresponding activation energy of this pathway turned out to be ∼0.5 eV. This value is in good

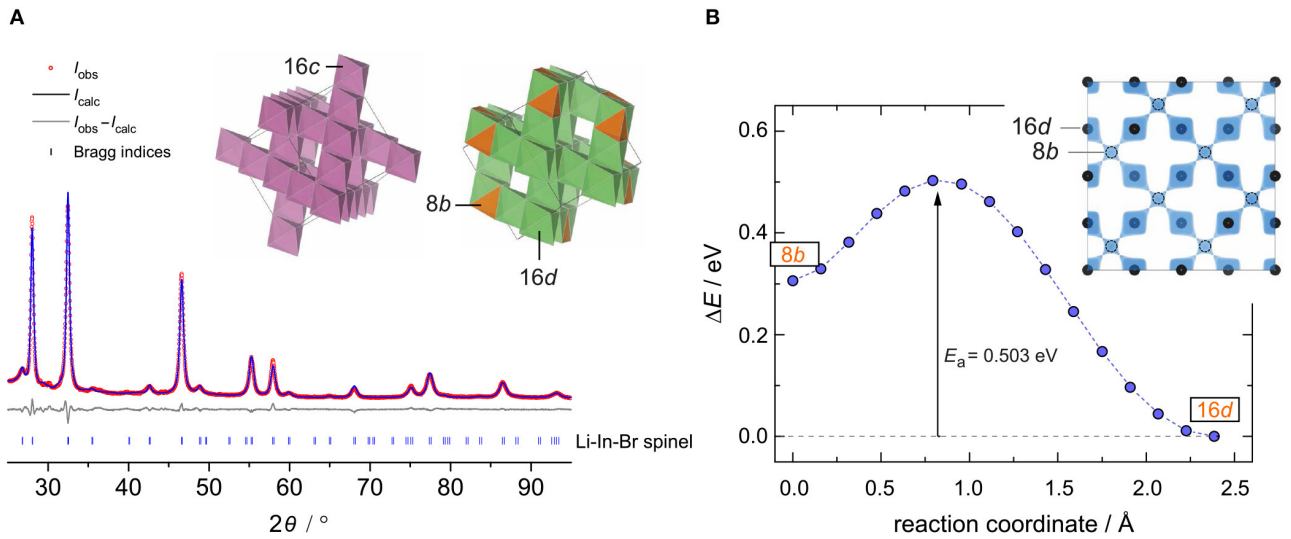

FIGURE 1 | (A) The observed (obs) XRPD pattern as well as the calculated and difference patterns (obs-calc) of the Rietveld refinement for the intended compound $Li[In_xLi_y]Br_4$. Vertical lines below the profile mark the positions of the possible Bragg reflections of spinel-type $Li[In_xLi_y]Br_4$ with its site disorder. Inset: framework formed by $InBr_6$ octahedra, and the Li-ion sublattice composed of tetrahedral and octahedral sites. **(B)** An energetically favored Li^+ diffusion pathway as estimated via the BVEL method; this pathway directly links the two crystallographically positions 16*d* and 8*b*. The corresponding iso-surface is shown in the inset.

TABLE 1 | X-ray diffraction data of $Li[In_xLi_y]Br_4$ with positional disorder on the 16*d* site as determined through Rietveld refinement; space group: $Fd\bar{3}m$ (no. 227); Z = 8; lattice parameters: $a = b = c$ = 11.026141(86) Å; R factors: R_{exp} = 1.78, R_{wp} = 4.54, R_p = 3.53; goodness of fit (GoF) = 2.56.

	Site	*x/a*	*y/b*	*z/c*	U_{iso}[a]	Occ.[b]
Li1	8*b*	1/8	5/8	1/8	4.60(31)	1.00(32)
Li2	16*d*	1/2	1/2	1/2	1.51(13)	0.69(11)
In	16*d*	1/2	1/2	1/2	1.51(13)	0.310(11)
Br	32*e*	0.25328(10)	0.25328(10)	0.25328(10)	1.316(51)	0.98(9)

[a] × 100 [Å^2], [b] occupation factor; 1.0 denotes full occupation of the site.
U_{iso} and Occ. were at first refined iteratively and finally simultaneously, leading to no change.
The occupation number of Li1 was set to 1, leading to an improved refinement. As Li2 and In share the 16d position, the occupation number of both together was constrained to 1.

agreement with that extracted from conductivity spectroscopy (vide infra).

3.2. Conductivity Measurements and Electrical Modulus

To characterize long-range ionic transport in $Li[In_xLi_y]Br_4$, we measured conductivity isotherms over a relatively broad frequency range (10^{-2}–10^7 Hz). **Figure 2A** shows the isotherms, that is, the real part, σ' of the complex conductivity $\hat{\sigma}$ plotted as a function of frequency ν. The isotherms reveal three characteristic regions that are universally found (Funke et al., 2005; Dunst et al., 2014). At high temperatures and low ν, the ions pile up at the ion-blocking electrode. This charge accumulation causes the effect of electrode polarization, which is not seen at low temperatures, as ionic conductivity sharply decreases with decreasing temperature. At sufficiently high frequencies, electrode polarization passes into the so-called direct current conductivity plateau, which is characterized by σ_{dc}, which we identify as the conductivity value that characterizes long-range ion transport. The same value could be extracted from complex plane representations of the impedance $\hat{Z}$; σ_{dc} refers to the intercept of the location curve with the abscissa of the corresponding Nyquist plot.

With decreasing temperature, we recognize that the dc-plateau of the isotherms shifts toward lower frequencies; simultaneously, at higher frequencies, it passes into a frequency-dependent dispersive regime. At the very low temperatures, the dispersive parts reveal a negligible temperature dependence, which indicates the beginning of the so-called nearly constant loss (NCL) regime (Dyre et al., 2009; Dunst et al., 2016). The latter is often ascribed to caged-like jump processes. While successful ion displacements govern the dc regime, the non-NCL disperse part is sensitive to unsuccessful jumps, including localized motions but also forward-backward jumps. In many cases, $\sigma'(\nu)$ in the dispersive regime can be approximated with Jonscher's power law $\sigma' \propto \nu^{\kappa}$. κ usually takes values ranging from 0.6 to 0.9 if ionic transport occurs in three dimensions. 1D and 2D ionic transport might result in lower values (Sidebottom, 2009). Here, we found $\kappa \approx 0.6$ (253 K), pointing to 3D ionic transport (see **Figure 2A**), as expected from the BVEL estimation (*vide supra*).

σ_{dc} values were directly read off from the distinct dc-plateaus of **Figure 2A**. $\sigma_{dc}T$, plotted vs. $1000/T$, is shown in **Figure 2B**. The linear behavior seen for the 1. run, which corresponds to the heating run, points to Arrhenius behavior according to $\sigma_{dc}T = \sigma_0 \exp(E_a/(k_BT))$. Here, k_B denotes Boltzmann's constant and σ_0 represents the Arrhenius pre-factor. The activation energy E_a turned out to be 0.58(2) eV. Above 313 K, a kink is seen and, at higher T than 313 K, the activation energy reduces to 0.42(3) eV.

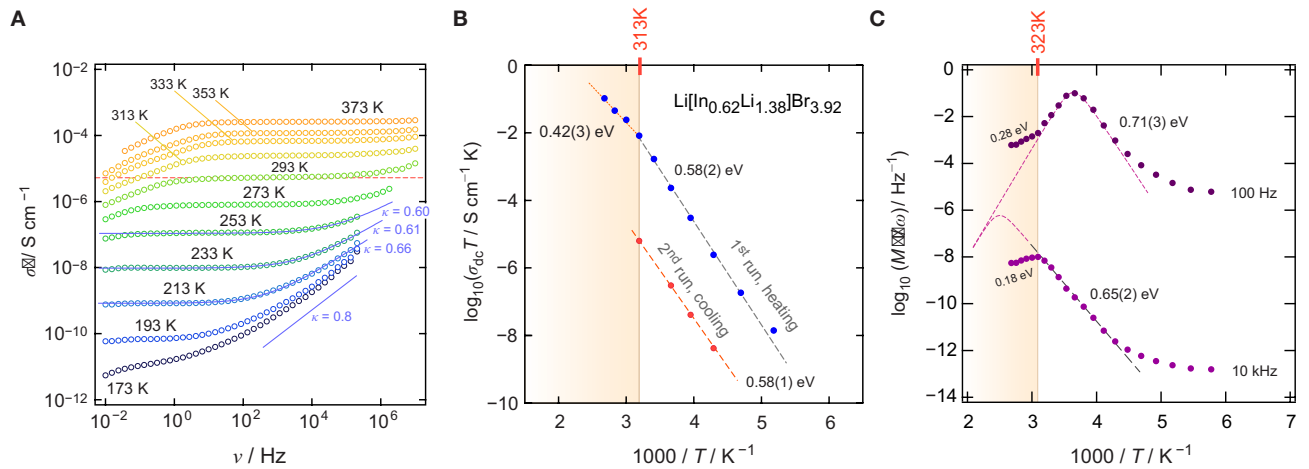

FIGURE 2 | (A) Conductivity isotherms $\sigma'(\nu)$ of $Li[In_xLi_y]Br_4$; isotherms were recorded at temperatures ranging from 173 to 373 K in steps of 20 K (1. run, heating). **(B)** Arrhenius plot to illustrate the temperature dependence of $\sigma_{dc}T$ for both the 1. run (heating) and the 2. run (cooling). **(C)** Real part of the complex resistivity ρ' expressed as M''/ν as a function of the inverse temperature $1/T$ and recorded for a fixed frequency of either $\nu = 10$ *kHz* or $\nu = 100$ Hz.

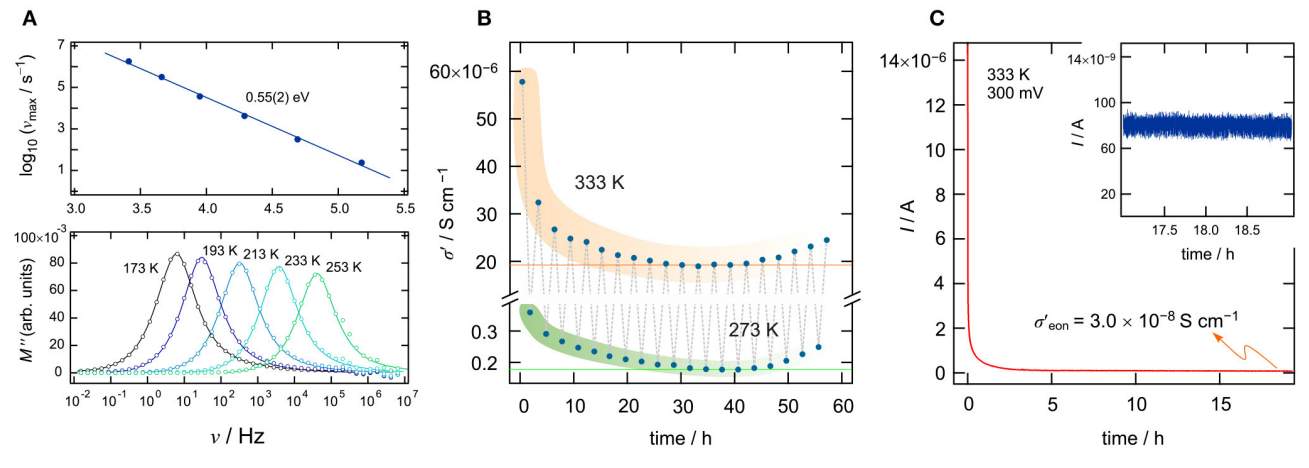

FIGURE 3 | (A) The upper graph shows the Arrhenius behavior of the characteristic frequencies ν_{max} at which the M'' peaks appear. Frequency dependence of the imaginary part of the complex part of the modulus as a function of frequency (ν). **(B)** Longtime measurement of σ_{dc} of $Li[In_xLi_y]Br_4$ over a time period of 58 h; we cycled the temperature in the sample chamber between 273 and 333 K. **(C)** Potentiostatic polarization curve ($U = 300$ *mV*) of $Li[In_xLi_y]Br_4$ sandwiched between two Pt electrodes. The $I(t)$ curve was recorded at $T = 333$ K. After $t = 18$ h, a final current of $I_{final} = 8 \times 10^{-8}$ A has been reached (see also inset), which leads to an electrical conductivity of $\sigma_{eon} = 3 \times 10^{-8}$ S cm^{-1}.

$E_a \approx 0.58$ eV (193–313 K) agrees nicely with the value estimated from BVEL (0.5 eV, see above).

The origin of the change of E_a at 313 K remains so far unknown; it was also observed by Yamada et al. (2006). If no phase transition takes place in $Li[In_xLi_y]Br_4$, one might assume that an order-disorder transition could cause this kink in the Arrhenius line. Such a transition has also been observed for Li_2MnBr_4 and Li_2MgBr_4 but at higher temperatures (Schmidt and Lutz, 1984). In addition, above 313 K, grain growth may already start, which is accompanied by the healing of, for example, point defects. It is well-known than the ionic self-diffusivity in poorly conducting materials can be drastically increased by the introduction of defects, either through mechanical treatment or through radiation (Stathopoulos and Pells, 1983; Ishimaru et al., 2003). Hence, at temperatures above 313 K, the material continuously changes and transforms into a more ordered structure. As expected, the conductivity values recorded during the 2. run, that is, the cooling run (313 K → 233 K), turn out to be lower by ∼3 orders of magnitude as compared to that governing the 1. run.

To investigate ionic transport further by means of electric modulus formalism (Hanghofer et al., 2019), we recorded the quantity M''/ν (see also **Figure 2C**) as a function of temperature and for constant frequency ($\nu = 100$ Hz and $\nu = 10$ kHz, 173 K $\leq T \leq$ 373 K). It turned out that, beginning from very low T, the quantity M''/ν obeys a weaker-than-activated temperature

behavior, in agreement with NCL-type electrical relaxation processes. Above 250 K, we recognize a strong increase with the inverse temperature. From the linear behavior observed, we extracted activation energies of 0.65(2) eV (10 kHz) and 0.71(3) eV (100 Hz). The increase seen if we compare these values to that found by σ_{dc} [0.58(2) eV] indicates that the number of charge carries seems to depend on temperature. Again, above 313 K, and independent of frequency ν, we observe a drastic change in $M''/\nu(1/T)$. The corresponding apparent activation energy of ∼0.18 eV (and 0.28 eV, see **Figure 2**) is much smaller than that seen in conductivity spectroscopy. We attribute this kink and the associated decrease in E_a to changes in morphology and the defect chemistry of the bromide. Finally, we looked directly at the temperature dependence of the electric modulus $M''(\nu)$; the corresponding modulus peaks are shown in the lower part of **Figure 3A**. The Arrhenius behavior of the characteristic frequencies ν_{max} at which the M'' peaks appear is displayed in **Figure 3A**. The linear fit points to an activation energy of 0.55 eV, which is smaller than that seen by σ_{dc}. The lower activation energy again points to a T-dependent charge carrier concentration N^{-1} that increases with temperature. As σ_{dc} is directly proportional to the charge carrier mobility mu_q, the charge of the moving species q and N^{-1}, ν_{max}, being a characteristic electrical relaxation frequency, increases slightly less with T than σ_{dc}.

At 293 K, we obtain an ionic conductivity of $\sigma_{dc} = 4.9 \times 10^{-6}\,S\,cm^{-1}$; this value is far below values needed for ceramic electrolytes in all-solid-state batteries. Thus, the current material is expected to be used in systems operated at higher T. For this reason, we studied the temperature stability of the ionic conductivity of the defect spinel over a time period of 58 h between 273 and 333 K. Moreover, as a sharp decrease in ionic conductivity was observed during the cooling run, we were interested in finding out which final conductivity value will be reached after annealing the sample for many hours at 333 K, which is just slightly above the kink seen in **Figure 2**. Hence, we kept the sample at 333 K for 1 h and then measured $\sigma'(\nu)$. The time needed to record the isotherm was 23 min. After that, we decreased the temperature in the sample chamber to 273 K, waited 1 h, and measured another isotherm $\sigma'(\nu)$; this cycle was repeated several times (see **Figure 3B**). For both the measurements at 333 K and at 273 K, we see the same trend. The conductivity decreases and reaches an almost constant value of $\sigma_{dc} = 2 \times 10^{-5}\,S\,cm^{-1}$ at 333 K. The corresponding conductivity at 273 K is two orders of magnitude lower as compared to that measured at 333 K. The reason for the slight increase in conductivity with increasing cycle number is still unknown.

Apart from overall conductivity and thermal stability, the ability of a material to conduct electrons is of significant importance when it comes to its application (Han et al., 2019). Ideally, the electronic conductivity should be orders of magnitude lower than the ionic contribution to the overall conductivity. Only electronically insulting ceramics will prevent soft shorts or the formation of detrimental Li dendrites. Here, we used a symmetric Pt | $Li[In_xLi_y]Br_4$ | Pt cell to monitor the evolution of current $I(t)$ at a constant voltage $U = 300$ mV. The final current of such a polarization measurement (Breuer et al., 2018a; Gombotz et al., 2019) will give the upper limit of the electronic conductivity σ_{eon}. The curve shown in **Figure 3C** refers to 333 K and reaches a steady state of I after 18 h. The final current ($I_{final} = I(18\,h)$) can be used to estimate σ_{eon} according to $\sigma_{eon} = I_{final}/U \cdot d/(r^2\pi)$, d denotes the thickness of the pellet and r refers to its diameter. For σ_{eon} we obtain $\sigma_{eon} = 3 \times 10^{-8}\,S\,cm^{-1}$ at 333 K, which is a factor of 10^3 smaller than the overall conductivity at this temperature ($\sigma_{dc} \approx 6 \times 10^{-5}\,S\,cm^{-1}$). For battery applications, even smaller values for σ_{eon} would be desirable ($\sigma_{dc}/\sigma_{eon} > 10^6$) and, thus, great care has to be taken when In-containing ceramics play a role as solid electrolytes. As an example, for oxide electrolytes, values of σ_{eon} in the order of $10^{-8}\,S\,cm^{-1}$ have been reported to trigger Li dendrite formation in all-solid-state batteries (Han et al., 2019). Li dendrites constitute a major safety problem, as they initiate short circuits and, thus, thermal runaways.

3.3. ^{7}Li NMR Spin-Lattice Relaxation and Line Shapes

To study solely ion dynamics in $Li[In_xLi_y]Br_4$, we took advantage of ^{7}Li NMR SLR measurements. In general, NMR spectroscopy is a contactless method and does not require any post-preparation steps, such as the application of conducting electrodes. As it is mainly sensitive to bulk ion dynamics, any interfering effects of ion-blocking grain-boundary regions are absent. Of course, the latter holds only for single crystals or polycrystalline materials with crystallites that show diameters in the μm range. For nanocrystalline samples, the ions residing in the large volume fraction of interfacial regions can be, simultaneously with those in the bulk regions, visualized by NMR (Wilkening et al., 2003; Breuer et al., 2018b). Here, we recorded diffusion-induced ^{7}Li SLR rates, in both the laboratory and rotating frame of reference, as a function of the inverse temperature (233–393 K) (Heitjans et al., 2005). The magnetization transients were analyzed in terms of stretched exponential functions (Stanje et al., 2017). The stretching exponents $\gamma_{1(\varrho)}$ are given in the upper graph of **Figure 4A**; the corresponding rates are shown in the Arrhenius diagram below.

Interestingly, the SLR NMR rates $1/T_1$ of nano-$Li[In_xLi_y]Br_4$ reveal only a slight dependence on reciprocal temperature. We recognize shallow maxima at ca. 333 K and ca. 260 K. Usually, if purely induced by diffusion, the rate $1/T_1(1/T)$ passes through a rate peak whose flanks contain the activation energy. For 3D uncorrelated motion, a symmetric peak is expected (Bloembergen et al., 1948); correlated motion, which originates from structural disorder and/or Coulomb interactions, often produces an asymmetric peak with a lower slope in the limit $\omega_0\tau \gg 1$, that is, on the low-T side of the peak. The same asymmetry is obtained for ionic diffusion in an irregularly shaped potential landscape, with short-range motions being different from long-range ionic transport. In the limit $\omega_0\tau \gg 1$, the flank contains a mean activation energy that characterizes short-range diffusion, i.e., localized site-to-site hopping processes. In the limit $\omega_0\tau \ll 1$, that is, the high-T side of the peak, the slope of the flank contains an average activation energy that might be identified with that sensed by σ_{dc}. Here, the shallow peaks

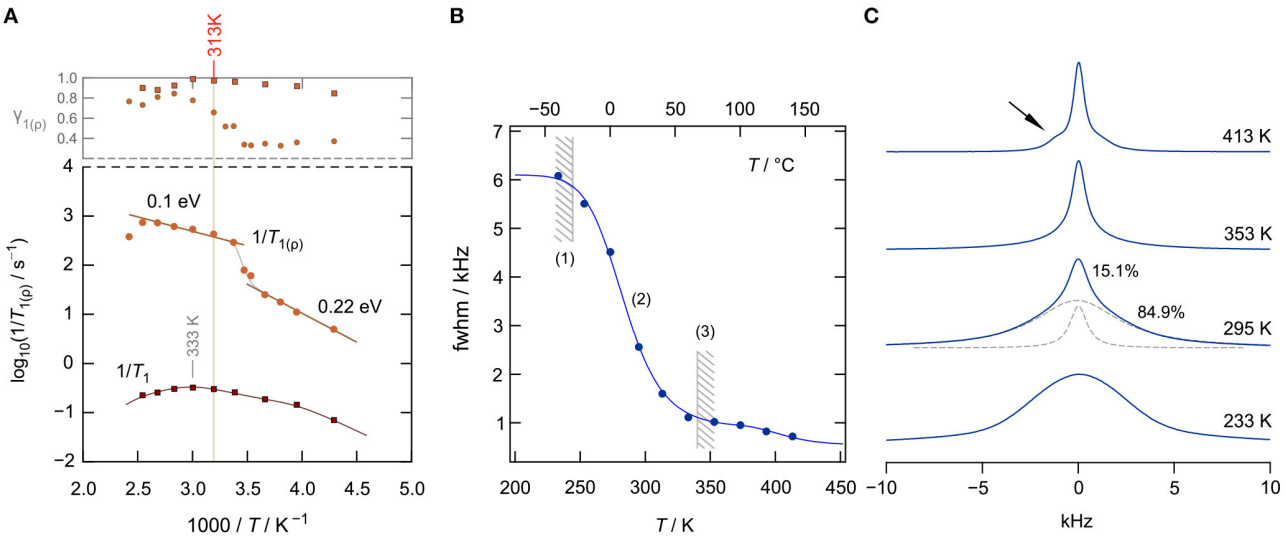

FIGURE 4 | (A) ^{7}Li NMR spin lattice relaxation (SLR) rates $1/T_{1(\varrho)}$ (116.59 MHz) of nanocrystalline, cubic-Li[In_xLi_y]Br_4 as a function of inverse temperature measured (233–393 K). The upper graph shows the $\gamma_{1(\varrho)}$ values used to approximate the magnetization transients. **(B)** ^{7}Li NMR line width (fwhm = full width at half maximum, total fwhm from net spectrum) as a function of temperature; regime (1) denotes the rigid lattice, (2) refers to the motional narrowing regime, and (3) represents the regime of extreme narrowing. The solid line (up to 353 K) represents a fit according to the model Abragam, yielding an activation energy of ~0.25 eV. **(C)** Change of the shape of the ^{7}Li NMR spectra with temperature (233, 295, 353, and 413 K). The spectrum at 295 K has been deconvoluted with a sum of a Gaussian and a Lorentzian function (see dashed lines). Motional narrowing is almost completed at $T = 353$ K.

are characterized by very small values of $E_a \approx 0.1$ eV. Thus, they seem to sample localized ionic motions, which could also originate from Li spins in the interfacial regions (Wilkening et al., 2003; Breuer et al., 2018b) of nanocrystalline Li[In_xLi_y]Br_4. Note that at above 313 K, the Arrhenius line of $\sigma_{dc}T$ reveals a kink. Thus, care has to be taken if we want to interpret the rates $1/T_1$ recorded at $T > 313$ K; they might be affected by irreversible change in the nanostructured sample, which produces only an apparent rate peak.

To study ^{7}Li NMR SLR behavior at temperatures well below 313 K, we recorded spin-lock NMR rates $1/T_\varrho$ in the rotating frame of reference. These rates sense, *per se*, slower ion dynamics as, formally, the Larmor frequency in the MHz range is replaced by a value in the kHz range. Here, we used a locking B_1 field that corresponds to a spin-lock frequency of 20 kHz. The rates obtained are also included in **Figure 4A**. At low T, they follow an activation energy of 0.22 eV, which we attribute to the elementary hopping barrier in site-disordered Li[In_xLi_y]Br_4, also including jump processes in the interfacial regions of the sample. If considering the crystal structure of spinel-type Li[In_xLi_y]Br_4, $1/T_\varrho$ seems to sense (local) hopping between the sites 16*d* and 8*b*. At higher temperatures, the rate shows a sharp increase, passing into a region that is activated with an activation energy of only 0.1 eV. Again, irreversible changes in the heat-sensitive sample seem to be responsible for the anomalous behavior appearing at elevated T.

Alternatively, Li ion dynamics in the ternary indium bromide were studied by recording ^{7}Li NMR spectra; selected spectra are displayed in **Figure 4C**). At low T, that is, the so-called rigid-lattice regime, Li^+ motions are too slow to effectively average dipole-dipole interactions. Thus, the line can be well-described with a broad Gaussian. With increasing T, we clearly see the onset of motional line narrowing. This narrowing process proceeds in a heterogeneous way, i.e., a narrow line appears on top of the broad one. At $T = 295$ K, the area under the narrow line amounts to about 15%, showing that only a fraction of the available Li spins participate in rapid ion exchange. As for other nanocrystalline ceramics, one might attribute this fraction to those spins residing in the structurally disordered interfacial regions (Wilkening et al., 2003; Breuer et al., 2018b) of nanocrystalline Li[In_xLi_y]Br_4. At elevated T, the whole line is affected by motional narrowing. The regime of extreme narrowing is reached at 350 K.

At even higher temperatures, intensities next to the central line appear (see arrow in **Figure 4C**), which we attribute to quadrupole satellites. Likely, grain growth and healing of defects ensure the formation of an ordered phase. In nanocrystalline or amorphous ceramics, satellite intensities are usually smeared out and only appear as a broad foot. Distinct singularities, referring to spin-transitions between the Zeeman levels characterized by $m_I = \pm 1/2$ and $m = \pm 3/2$, are seen in samples with a high degree of crystallinity. Here, σ_{dc} of the annealed sample is, however, much lower than σ_{dc} of the as-prepared, mechanosynthesized sample (see **Figure 2B**). The full narrowing curve of the ^{7}Li NMR central transition is shown in **Figure 4B**. The solid line shows a fit with the model introduced by Abragam (1961) to parameterize the curve; the activation energy turned out to be 0.25 eV, in agreement with the value seen by spin-lock NMR. Details on analyzing NMR line widths with the Abragam formula are given elsewhere (Wilkening et al., 2002). Interestingly, at higher T, a second step in the motional

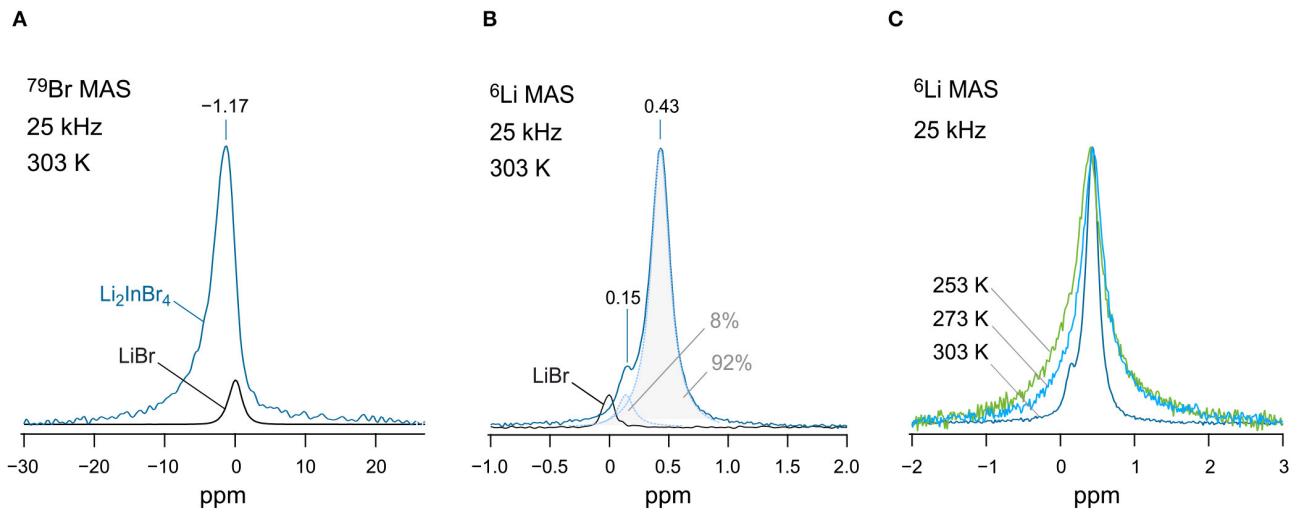

FIGURE 5 | (A) ^{79}Br MAS NMR spectra (125.27 MHz) of nano-Li[In_xLi_y]Br_4 and pure LiBr for comparison. Spectra were recorded at 303 K. LiBr served as a primary reference for both the ^{79}Br MAS NMR and ^{6}Li MAS NMR spectra, see **(B)**. **(B)** ^{6}Li MAS NMR spectra (73.58 MHz) of the nanocrystalline sample; the signal of pure LiBr is shown for comparison. The overall signal of Li[In_xLi_y]Br_4 is composed of two lines appearing at 0.43 and 0.15 ppm. The total NMR signal was deconvoluted with the help of two Lorentzian functions to estimate the area under the signal with low intensity (8%). **(C)** Variable-temperature ^{6}Li MAS NMR spectra (73.58 MHz) recorded at 253, 273, and 303 K. Dipolar interactions cause line broadening at low temperatures.

narrowing curve is seen, which is in line with the deviations seen by σ_{dc} measurements and by the analysis of M''/ν data (see above).

Finally, we checked whether it is possible to distinguish any magnetically inequivalent Li sites by ^{6}Li high-resolution (MAS) NMR. For this purpose, we recorded variable-temperature ^{6}Li NMR spectra (**Figures 5B,C**). Note that the quadrupole moment of the ^{6}Li nucleus is a factor of 50 smaller than that of the ^{7}Li one. Thus, any interfering second-order quadrupole interactions, which are not averaged under ordinary MAS conditions, are almost eliminated, leading to a higher resolution of ^{6}Li NMR spectra. At 253 and 273 K, we detected only a single ^{6}Li line at $\delta_{iso} = 0.43$ ppm. We used LiBr (0 ppm) as a primary reference of the spectra. At 303 K, however, increasing dipole-dipole averaging originating from motional narrowing, which adds up to the elimination of dipolar broadening by MAS, reveals a second line at $\delta_{iso} = 0.15$ ppm. At first glance, we would simply assign this additional line to LiBr. The area under the line with low intensity amounts to ∼8% if we convolute the total signal with a sum of two Lorentzian functions. Interestingly, the line at 0.15 ppm does not match the isotropic shift of LiBr exactly. Furthermore, ^{79}Br MAS NMR gives no strong evidence for LiBr being indeed detectable by NMR (see **Figure 5A**). The signal with low intensity might be attributed to the unidentified phase seen in XRD. Possibly, the presence of In-doped LiBr could serve as an explanation of the signal.

4. CONCLUSION

We successfully synthesized nanocrystalline Li[In_xLi_y]Br_4 directly via a one-pot mechanochemical route. The nanostructured sample was characterized by X-ray powder diffraction and ^{6}Li, ^{79}Br MAS NMR. Li[In_xLi_y]Br_4 needs to be described by a spinel structure with positional disorder on the 16*d* site. Via the bond valence energy landscape methodology, we estimated site energies and a hopping barrier between the Li sites 16*d* and 8*b*. Broadband conductivity helped us to measure long-range ion transport that is characterized by an activation energy of 0.61 eV. Electric modulus data pointed to barriers as high as 0.71 eV if analyzed at 100 Hz. Most likely because of the non-stoichiometry of the sample, a relatively high electronic conductivity in the order of 10^{-8} S cm^{-1} has been found, which is a factor of 10^3 lower than the room-temperature ionic conductivity. Local barriers were probed by diffusion-induced ^{7}Li NMR SLR measurements. In particular, spin-lock NMR yielded an activation energy of 0.22 eV, which either characterizes local (forward-backward) Li jumps between 16*d* and 8*b* or motional events of the Li ions in the interfacial regions. As σ_{dc} is rather low at room temperature, Li[In_xLi_y]Br_4 seems to be a candidate for high-temperature battery cells.

DATA AVAILABILITY STATEMENT

The raw data supporting the conclusions of this article will be made available by the authors, without undue reservation, to any qualified researcher.

AUTHOR CONTRIBUTIONS

MG: synthesis of the material via the mechanochemical synthesis route, characterization, evaluation and interpretation of the data, and writing. DR: rietveld refinement, Li pathway calculations, and data interpretation. HW: supervision, conceptualization,

data interpretation, and writing. All authors contributed to the manuscript revision, read, and approved the submitted version.

FUNDING

This work was supported by TU Graz Open Access Publishing Fund.

ACKNOWLEDGMENTS

We thank Prof. Günther J. Redhammer (Salzburg) for helpful discussion regarding the interpretation and analysis of our preliminary XRPD data. We thank our colleagues at the ICTM (TU Graz) for fruitful discussions.

REFERENCES

Abragam, A. (1961). *The Principles of Nuclear Magnetism*. Oxford: Clarendon.

Asano, T., Sakai, A., Ouchi, S., Sakaida, M., Miyazaki, A., and Hasegawa, S. (2018). Solid halide electrolytes with high lithium-ion conductivity for application in 4 V class bulk-type all-solid-state batteries. *Adv. Mater.* 30:1803075. doi: 10.1002/adma.201803075

Bachman, J. C., Muy, S., Grimaud, A., Chang, H.-H., Pour, N., Lux, S. F., et al. (2016). Inorganic solid-state electrolytes for lithium batteries: mechanisms and properties governing ion conduction. *Chem. Rev.* 116, 140–162. doi: 10.1021/acs.chemrev.5b00563

Bloembergen, N., Purcell, E. M., and Pound, R. V. (1948). Relaxation effects in nuclear magnetic resonance absorption. *Phys. Rev.* 73, 679–712.

Breuer, S., Gombotz, M., Pregartner, V., Hanzu, I., and Wilkening, M. (2018a). Heterogeneous f anion transport, local dynamics and electrochemical stability of nanocrystalline $La_{1-x}Ba_xF_{3-x}$. *Energy Storage Mater.* 16, 481–491. doi: 10.1016/j.ensm.2018.10.010

Breuer, S., Uitz, M., and Wilkening, H. M. R. (2018b). Rapid Li ion dynamics in the interfacial regions of nanocrystalline solids. *J. Phys. Chem. Lett.* 9, 2093–2097. doi: 10.1021/acs.jpclett.8b00418

Bruce, P. G., Scrosati, B., and Tarascon, J.-M. (2008). Nanomaterials for rechargeable lithium batteries. *Angew. Chem. Int. Ed.* 47, 2930–2946. doi: 10.1002/anie.200702505

Buschmann, H., Döelle, J., Berendts, S., Kuhn, A., Bottke, P., Wilkening, M., et al. (2011). Structure and dynamics of the fast lithium ion conductor $Li_7La_3Zr_2O_{12}$. *Phys. Chem. Chem. Phys.* 13, 19378–19392. doi: 10.1039/c1cp2 2108f

Chen, H., Wong, L. L., and Adams, S. (2019). *SoftBV*—a software tool for screening the materials genome of inorganic fast ion conductors. *Acta Cryst. B* 75, 18–33. doi: 10.1107/S2052520618015718

Cheng, L., Crumlin, E. J., Chen, W., Qiao, R., Hou, H., Franz Lux, S., et al. (2014). The origin of high electrolyte–electrode interfacial resistances in lithium cells containing garnet type solid electrolytes. *Phys. Chem. Chem. Phys.* 16, 18294–18300. doi: 10.1039/c4cp02921f

Dawson, J. A., Attari, T. S., Chen, H., Emge, S. P., Johnston, K. E., and Islam, M. S. (2018). Elucidating lithium-ion and proton dynamics in anti-perovskite solid electrolytes. *Energy Environ. Sci.* 11, 2993–3002. doi: 10.1039/C8EE00779A

Deiseroth, H.-J., Kong, S.-T., Eckert, H., Vannahme, J., Reiner, C., Zaiss, T., et al. (2008). Li_6PS_5X: a class of crystalline li-rich solids with an unusually high Li^+ mobility. *Angew. Chem. Int. Ed.* 47, 755–758. doi: 10.1002/anie.200703900

Dietrich, C., Weber, D. A., Sedlmaier, S. J., Indris, S., Culver, S. P., Walter, D., et al. (2017). Lithium ion conductivity in Li_2S-P_2S_5 glasses—building units and local structure evolution during the crystallization of superionic conductors Li_3PS_4, $Li_7P_3S_{11}$ and $Li_4P_2S_7$. *J. Mater. Chem. A* 5, 18111–18119. doi: 10.1039/C7TA06067J

Dunst, A., Epp, V., Hanzu, I., Freunberger, S. A., and Wilkening, M. (2014). Short-range Li diffusion vs. long-range ionic conduction in nanocrystalline lithium peroxide Li_2O_2—the discharge product in lithium-air batteries. *Energy Environ. Sci.* 7, 2739–2752. doi: 10.1039/C4EE00496E

Dunst, A., Sternad, M., and Wilkening, M. (2016). Overall conductivity and NCl-type relaxation behavior in nanocrystalline sodium peroxide Na_2O_2—consequences for Na-oxygen batteries. *Mater. Sci. Eng. B* 211, 85–93. doi: 10.1016/j.mseb.2016.06.002

Dyre, J. C., Maass, P., Roling, B., and Sidebottom, D. L. (2009). Fundamental questions relating to ion conduction in disordered solids. *Rep. Prog. Phys.* 72:046501. doi: 10.1088/0034-4885/72/4/046501

Funke, K., Cramer, C., and Wilmer, D. (2005). "Concept of mismatch and relaxation for self-diffusion and conduction in ionic materials with disordered structures," in *Diffusion in Condensed Matter-Methods, Materials, Models, 2nd Edn*, eds P. Heitjans and J. Kärger (Berlin: Springer), 857–893.

Gombotz, M., Lunghammer, S., Breuer, S., Hanzu, I., Preishuber-Pflügl, F., and Wilkening, H. M. R. (2019). Spatial confinement–rapid 2D F^- diffusion in micro- and nanocrystalline $RbSn_2F_5$. *Phys. Chem. Chem. Phys.* 21:1872. doi: 10.1039/C8CP07206J

Goodenough, J. B. (2013). Evolution of strategies for modern rechargeable batteries. *Acc. Chem. Res.* 46, 1053–1061. doi: 10.1021/ar2002705

Gupta, H. C., Zwinscher, J., and Lutz, H. D. (1997). Lattice dynamical calculations of deficient NaCl superstructure-type Li_2CoCl_4 and Li_2MnBr_4. *J.Phys. Chem. Solids* 58, 173–175. doi: 10.1016/S0022-3697(96)00082-0

Han, F., Westover, A., Yue, J., Fan, X., Wang, F., Chi, M., et al. (2019). High electronic conductivity as the origin of lithium dendrite formation within solid electrolytes. *Nat. Energy* 4, 187–196. doi: 10.1038/s41560-018-0312-z

Hanghofer, I., Brinek, M., Eisbacher, S. L., Bitschnau, B., Volck, M., Hennige, V., et al. (2019). Substitutional disorder: structure and ion dynamics of the argyrodites Li_6PS_5Cl, Li_6PS_5Br and Li_6PS_5I. *Phys. Chem. Chem. Phys.* 21, 8489–8507. doi: 10.1039/c9cp00664h

Heitjans, P., Masoud, M., Feldhoff, A., and Wilkening, M. (2007). NMR and impedance studies of nanocrystalline and amorphous ion conductors: lithium niobate as a model system. *Faraday Discuss.* 134, 67–82. doi: 10.1039/b602887j

Heitjans, P., Schirmer, A., and Indris, S. (2005). *Diffusion in Condensed Matter—Methods, Materials, Models. 2nd Edn.* Chapter 9. Berlin: Springer, 369–415.

Ishimaru, M., Bae, I.-T., and Hirotsu, Y. (2003). Electron-beam-induced amorphization in SiC. *Phys. Rev. B* 68:144102. doi: 10.1103/PhysRevB.68.144102

Janek, J., and Zeier, W. G. (2016). A solid future for battery development. *Nat. Energy* 1:16141. doi: 10.1038/nenergy.2016.141

Kamaya, N., Homma, K., Yamakawa, Y., Hirayama, M., Kanno, R., Yonemura, M., et al. (2011). A lithium superionic conductor. *Nat. Mater.* 10, 682–686. doi: 10.1038/nmat3066

Kim, S., Oguchi, H., Toyama, N., Sato, T., Takagi, S., Otomo, T., et al. (2019). A complex hydride lithium superionic conductor for high-energy-density all-solid-state lithium metal batteries. *Nat. Commun.* 10:1081. doi: 10.1038/s41467-019-09061-9

Kuhn, A., Narayanan, S., Spencer, L., Goward, G., Thangadurai, V., and Wilkening, M. (2011). Li self-diffusion in garnet-type $Li_7La_3Zr_2O_{12}$ as probed directly by diffusion-induced ^{7}Li spin-lattice relaxation nmr spectroscopy. *Phys. Rev. B* 83:094302. doi: 10.1103/PhysRevB.83.094302

Li, X., Liang, J., Chen, N., Luo, J., Adair, K. R., Wang, C., et al. (2019). Water-mediated synthesis of a superionic halide solid electrolyte. *Angew. Chem. Int. Ed.* 131, 16579–16584. doi: 10.1002/ange.201909805

Lutz, H., Cockcroft, J., Kuske, P., and Schneider, M. (1990). Polymorphism of the fast ionic conductor Li_2MnBr_4 - neutron diffraction and differential scanning calorimetry. *Mat. Res. Bull.* 25, 451–456.

Maekawa, H., Matsuo, M., Takamura, H., Ando, M., Noda, Y., Karahashi, T., et al. (2009). Halide-stabilized $LiBH_4$, a room-temperature lithium fast-ion conductor. *J. Am. Chem. Soc.* 131, 894–895. doi: 10.1021/ja807392k

Martin, D. Z. C., Haworth, A. R., Schmidt, W. L., Baker, P. J., Boston, R., Johnston, K. E., et al. (2019). Evaluating lithium diffusion mechanisms in the complex spinel $Li_2NiGe_3O_8$. *Phys. Chem. Chem. Phys.* 21, 23111–23118. doi: 10.1039/c9cp02907a

Marx, R., and Mayer, H. M. (1996). Darstellung und lithiumteilstruktur von lithiumnnitridtribromid, Li_6NBr_3 und lithiumnitridtriiodid, Li_6NI_3/preparation and lithium sublattice of lithium nitride

trihalides, Li_6NHal_3 (Hal = Br, I). *Z. Naturforsch.* 51b, 525–530. doi: 10.1515/znb-1996-0415

Matsuo, M., and Orimo, S.-I. (2011). Lithium fast-ionic conduction in complex hydrides: review and prospects. *Adv. Energy Mater.* 1, 161–172. doi: 10.1002/aenm.201000012

Mercier, R., Tachez, M., Malugani, J., and Robert, G. (1985). Effect of homovalent (I^- - Br^-) ion substitution on the ionic conductivity of $LiI_{1-x}Br_x$ systems. *Solid State Ion.* 15, 109–112.

Murugan, R., Thangadurai, V., and Weppner, W. (2007). Fast lithium ion conduction in garnet-type $Li_7La_3Zr_2O_{12}$. *Angew. Chem. Int. Ed.* 46, 7778–7781. doi: 10.1002/anie.200701144

Pecher, O., Carretero-González, J., Griffith, K. J., and Grey, C. P. (2017). Materials' methods: NMR in battery research. *Chem. Mater.* 29, 213–242. doi: 10.1021/acs.chemmater.6b03183

Porz, L., Swamy, T., Sheldon, B. W., Rettenwander, D., Froemling, T., Thaman, H. L., et al. (2017). Mechanism of lithium metal penetration through inorganic solid electrolytes. *Adv. Energy Mater.* 7:1701003. doi: 10.1002/aenm.201701003

Richards, W. D., Miara, L. J., Wang, Y., Kim, J. C., and Ceder, G. (2016). Interface stability in solid-state batteries. *Chem. Mater.* 28, 266–273. doi: 10.1021/acs.chemmater.5b04082

Scherrer, P. (1918). Bestimmung der Größe und der inneren Struktur von Kolloidteilchen mittels Röntgenstrahlen. *Göttin. Nachrich.* 2:98.

Schmidt, W., and Lutz, H. D. (1984). Fast ionic conductivity and dielectric properties of the lithium halide spinels Li_2MnCl_4, Li_2CdCl_4, Li_2MnBr_4 and Li_2CdBr_4. *Ber. Bunsenges. Phys. Chem.* 88, 720–723.

Schoch, B., Hartmann, E., and Weppner, W. (1986). New fast solid lithium ion conductors at low and imtermediate temperatures. *Solid State Ion* 18–19, 529–533.

Sidebottom, D. L. (2009). Understanding ion motion in disordered solids from impedance spectroscopy scaling. *Rev. Mod. Phys.* 81, 999–1014. doi: 10.1103/RevModPhys.81.999

Stanje, B., Rettenwander, D., Breuer, S., Uitz, M., Berendts, S., Lerch, M., et al. (2017). Solid electrolytes: extremely fast charge carriers in garnet-type $Li_6La_3ZrTaO_{12}$ single crystals. *Ann. Phys.* 529:1700140. doi: 10.1002/andp.201700140

Stathopoulos, A. Y., and Pells, G. P. (1983). Damage in the cation sublattice of γ-Al_2O_3 irradiated in an HVEM. *Phil. Mag. A* 47, 381–394.

Thangadurai, V., Narayanan, S., and Pinzaru, D. (2014). Garnet-type solid-state fast Li ion conductors for Li batteries: critical review. *Chem. Soc. Rev.* 43, 4714–4727. doi: 10.1039/c4cs00020j

Tomita, Y., Matsushita, H., Kobayashi, K., Maeda, Y., and Yamada, K. (2008). Substitution effect of ionic conductivity in lithium ion conductor, $Li_3InBr_{6-x}Cl_x$. *Solid State Ion* 179, 867–870. doi: 10.1016/j.ssi.2008.02.012

Tomita, Y., Yamada, K., Ohki, H., and Okuda, T. (2014). Structure and dynamics of Li_3InBr_6 and $NaInBr_4$ by means of nuclear magnetic resonance. *Z. Naturf. A* 53, 466–472. doi: 10.1515/zna-1998-6-730

Uitz, M., Epp, V., Bottke, P., and Wilkening, M. (2017). Ion dynamics in solid electrolytes for lithium batteries. *J. Electroceram.* 38, 142–156. doi: 10.1007/s10832-017-0071-4

Wang, S., Bai, Q., Nolan, A. M., Liu, Y., Gong, S., Sun, Q., et al. (2019). Lithium chlorides and bromides as promising solid-state chemistries for fast ion conductors with good electrochemical stability. *Angew. Chem. Int. Ed.* 131, 8123–8127. doi: 10.1002/ange.201901938

Wang, Y., Richards, W. D., Ong, S. P., Miara, L. J., Kim, J. C., Mo, Y., et al. (2015). Design principles for solid-state lithium superionic conductors. *Nat. Mater.* 14, 1026–1031. doi: 10.1038/nmat4369

Wenzel, S., Randau, S., Leichtweiss, T., Weber, D. A., Sann, J., Zeier, W. G., et al. (2016). Direct observation of the interfacial instability of the fast ionic conductor $Li_{10}GeP_2S_{12}$ at the lithium metal anode. *Chem. Mater.* 28, 2400–2407. doi: 10.1021/acs.chemmater.6b00610

Wilkening, M., Bork, D., Indris, S., and Heitjans, P. (2002). Diffusion in amorphous $LiNbO_3$ studied by ^{7}Li NMR – comparison with the nano- and microcrystalline material. *Phys. Chem. Chem. Phys.* 4, 3246–3251. doi: 10.1039/b201193j

Wilkening, M., and Heitjans, P. (2012). From micro to macro: access to long-range Li^+ diffusion parameters in solids via microscopic ^{6,7}Li spin-alignment echo nmr spectroscopy. *ChemPhysChem* 13, 53–65. doi: 10.1002/cphc.201100580

Wilkening, M., Indris, S., and Heitjans, P. (2003). Heterogeneous lithium diffusion in nanocrystalline Li_2O:Al_2O_3 composites. *Phys. Chem. Chem. Phys.* 5, 2225–2231. doi: 10.1039/B300908D

Yamada, K., Kumano, K., and Okuda, T. (2006). Lithium superionic conductors Li_3InBr_6 and $LiInBr_4$ studied by ^{7}Li and ^{115}In NMR. *Solid State Ion* 177, 1691–1695. doi: 10.1016/j.ssi.2006.06.026

Yu, C., Ganapathy, S., Eck, E. R. H. V., Wang, H., Basak, S., Li, Z., et al. (2017). Accessing the bottleneck in all-solid state batteries, lithium-ion transport over the solid-electrolyte-electrode interface. *Nat. Commun.* 8:1086. doi: 10.1038/s41467-017-01187-y

Zhang, W., Schroeder, D., Arlt, T., Manke, I., Koerver, R., Pinedo, R., et al. (2017). (Electro)chemical expansion during cycling: monitoring the pressure changes in operating solid-state lithium batteries. *J. Mater. Chem. A* 5, 9929–9936. doi: 10.1039/C7TA02730C

Zhang, Z., Shao, Y., Lotsch, B., Hu, Y.-S., Li, H., Janek, J., et al. (2018). New horizons for inorganic solid state ion conductors. *Energy Environ. Sci.* 11, 1945–1976. doi: 10.1039/C8EE01053F

Conflict of Interest: The authors declare that the research was conducted in the absence of any commercial or financial relationships that could be construed as a potential conflict of interest.

frontiers in Chemistry

REVIEW
published: 04 September 2020
doi: 10.3389/fchem.2020.00821

Regulating the Performance of Lithium-Ion Battery Focus on the Electrode-Electrolyte Interface

Dongni Zhao[1] *and Shiyou Li*[1,2]*

[1] College of Petrochemical Technology, Lanzhou University of Technology, Lanzhou, China, [2] Gansu Engineering Laboratory of Electrolyte Material for Lithium-Ion Battery, Lanzhou, China

The development of lithium-ion battery (LIB) has gone through nearly 40 year of research. The solid electrolyte interface film in LIBs is one of most vital research topics, its behavior affects the cycle life and safety of LIBs significantly. Progress in understanding the interfacial layer on the negative and positive electrodes in LIBs has been the focus of considerable research in the past few decades, but there remains a number of problem to be understood at the fundamental level, and there is still a great deal of controversy regarding the composition and formation mechanism of the interfacial film. In this article, we summarize recent research conducted on the interfacial film in LIBs, including the film formation mechanism, the composition, and stability of the interfacial film on the positive electrodes (in both diluted and high-concentration electrolytes). And the methodologies and advanced techniques implemented for the characterization of the interfacial film. Finally, we put forward some of the future development direction for the interfacial film and urgent problems that need to be solved.

Keywords: interfacial film, CEI film, advanced characterization, lithium-ion battery, mechanism

OPEN ACCESS

Edited by:
Wenping Sun,
Zhejiang University, China

Reviewed by:
Yuesheng Wang,
Hydro-Québec's Research Institute, IREQ, Canada
Xifei Li,
Xi'an University of Technology, China

***Correspondence:**
Shiyou Li
lishiyoulw@163.com

Specialty section:
This article was submitted to Electrochemistry, a section of the journal Frontiers in Chemistry

Received: *16 February 2020*
Accepted: *04 August 2020*
Published: *04 September 2020*

Citation:
Zhao D and Li S (2020) Regulating the Performance of Lithium-Ion Battery Focus on the Electrode-Electrolyte Interface. Front. Chem. 8:821. doi: 10.3389/fchem.2020.00821

INTRODUCTION

In recent years, the demands on lithium-ion batteries has increased, due to their applicability in hybrid and electric vehicles. The requirements for such application manifest in the a cycle life and safety features needed for the successful application of the device. The operational mechanism for the lithium-ion battery works through the movement of electric charge through an external circuit to balance the shuttle movement of lithium-ions in the main structures of the cathode and anode of the device (Mizushima et al., 1980; Yazami and Touzain, 1983; Goodenough and Kim, 2010; Goodenough, 2018; Han et al., 2019). The positive and negative electrodes are kept apart by a separator to avoid short circuiting, and are surrounded with an aprotic non-aqueous electrolyte. When the anodic operating voltage of the cell is close to 0 V, elemental lithium is stored; when the cathodic voltage of the cell exceeds 3 V, lithium-ion is stored (Hightower et al., 2000; Lu et al., 2011; Suo et al., 2012; Zheng et al., 2013). The reaction of the aprotic electrolyte on the electrode is thermodynamically unstable. Therefore, understanding the active electrochemical and chemical reactions on the electrode-electrolyte interface is the key to the development of a stable, high-efficiency lithium-ion battery. These reactions occuring on the electrode will affect the composition, the microstructure, and the properties of the interfacial film, while the nature of the interfacial film will determine the coulombic efficiency, cycle life, and operational safety during the operational life of the battery.

Cyclic carbonate-based electrolytes are widely used in lithium-ion batteries, such as ethylene carbonate (EC), and they go through reduction or oxidation reactions on the surface of negative or positive electrodes, to form the well-known electrode-electrolyte interface film (EEI). The EEI is permeable to lithium-ions in the electrolyte but not conductive to the electrons on the electrode, and its formation can impede the continuation of the reduction and oxidation of the electrolyte, and the irreversible consumption of lithium-ions during cycling. However, the formation of a non-uniform EEI film may result in uneven lithium deposition and cause the formation of lithium dendrites, which in turn leads to internal short circuiting and failure in the battery. The interface film formed on the positive electrode is incomprehensible in composition and properties compared to that forming on the negative electrode (Verma et al., 2010; Xing et al., 2011; Leung, 2013; Gallego et al., 2014). The study of the cathode electrode interface (called as CEI film) film is the key to reducing the activity between the electrolyte and positive electrode material, which will affect the life and safety of the battery, because the exothermic reaction between the positive electrode material and the flammable electrolyte generates a large amount of heat and cause thermal runaway.

Although many advanced researches have been made in studying the properties of interfacial films in LIBs, and many advanced equipment and technologies are continuously being used to investigate and characterize their nature and composition, many aspects of the properties of interfacial films remain in need of further exploration. For example, the film formation mechanism and the role of composition in the behavior of the interfacial film and performance of the battery have not been thoroughly studied. **Figure 1** gives a schematic diagram of the research structure of the positive electrode interface film for lithium-ion batteries.

This article summarizes the progress of research related to CEI films in LIBs positive electrode in the past decade. Firstly, the thermodynamic factors of the redox reaction on the positive and negative electrodes are reviewed and discussed to understand the basic principles behind them. Then, the formation mechanism, composition, and stability of the interfacial film on the positive electrode are mainly discussed. Finally, the main characterization methods of the interfacial film are summarized, and the opportunities and techniques that can be used to obtain further insight on the formation mechanism and the composition of the interfacial film, as well as the correlation between the properties of the interfacial film and battery performance, are also put forward and discussed.

EFFECT OF THERMODYNAMIC FACTORS ON THE FORMATION OF INTERFACIAL FILMS

Goodenough et al. described the relationship between the Fermi level of the positive and negative electrodes in a lithium-ion battery as well as the solvent and electrolyte HOMO (highest occupied molecular orbital) and LUMO (lowest unoccupied molecular orbital) in the electrolyte (shown in **Figure 2**) (Borodin et al., 2013; Goodenough, 2018). The difference between the Fermi energies of the electrodes and the HOMO and LUMO energy levels of the electrolyte controls the thermodynamics and the driving forces behind the formation of the electrode surface interfacial film (Goodenough and Kim, 2010). When the LUMO level of the organic solvent or electrolyte lithium salt is lower than the Fermi level of the negative electrode, electrons will be injected into the LUMO orbit by that driving force, causing the electrolyte component to be reduced; when the HOMO level is higher than Fermi energy level of the positive electrode, electrons are driven into the positive electrode, causing the solvent or lithium salt to be oxidized. The solvent or lithium salt is reduced or oxidized at the surface of the electrode during charging, and a portion of the resulting substance that is insoluble in the electrolyte will be deposited on the surface of the negative electrode or the positive electrode (Goodenough and Kim, 2010). These substances can conduct lithium-ions transferred from the electrolyte due to the presence of lithium-ions, but at the same time they are insulating to electrons from the electrode, which prevents the electrode from further reacting with the electrolyte. We will give below a detailed review of the dynamic driving force behind the formation of the interfacial film, in relation to the instability of the electrolyte on the electrode surface.

Storage Electrode Potential of Lithium

The electrode potential of lithium metal corresponds to the average electron energy level at the top of its valence band (electron transfer energy level or redox electron energy of materials). The difference in electrochemical potential between the positive and negative electrodes gives the thermodynamic battery voltage change, the kinetic effects come from the battery assembly, current rates, electrode configuration, and electrolyte not from their standard redox potential. The most common negatively charged sheets of metallic lithium and graphite store lithium at 0 and ∼0.1 V, respectively, and their Fermi level is above the estimated LUMO level of the electrolyte (**Figure 3A**; Zhang et al., 2001). Therefore, there is a driving force on the surfaces of these negative electrodes to promote the electrochemical reduction of the electrolyte. The surface of the electrode is passivated by the stable, electronically insulating, lithium-ion-conducting surface film formed on the interface, thereby preventing the electrode surface from coming into direct contact with the aprotic electrolyte.

The potential of lithium transition metal compounds such as oxides, sulfides, and phosphates (**Figures 3A,B**) is lower than the reduction potential of the aprotic electrolyte, and their electrochemical potentials are largely determined by the redox energy of the transition metal ion (Yazami and Touzain, 1983; Xu et al., 1999; Egashira et al., 2001). On the other hand, by replacing the M-O skeleton in $LiMO_2$ (M refers to metal element) with the inductive effect of M-O-P, the redox energy of the transition metal ion may be further reduced (i.e., the lithium intercalation potential is further increased, **Figure 3A**) (Zhou et al., 2004; Wolfenstine and Allen, 2005; Leung, 2013). There is closer energy level between oxidation potential of high voltage energy storage materials and HOMO level of electrolyte. Examples include materials such as $Li_{1-x}Mn_{1.5}Ni_{0.5}O_4$ (Ni^{4+}/Ni^{2+} at 4.7 V),

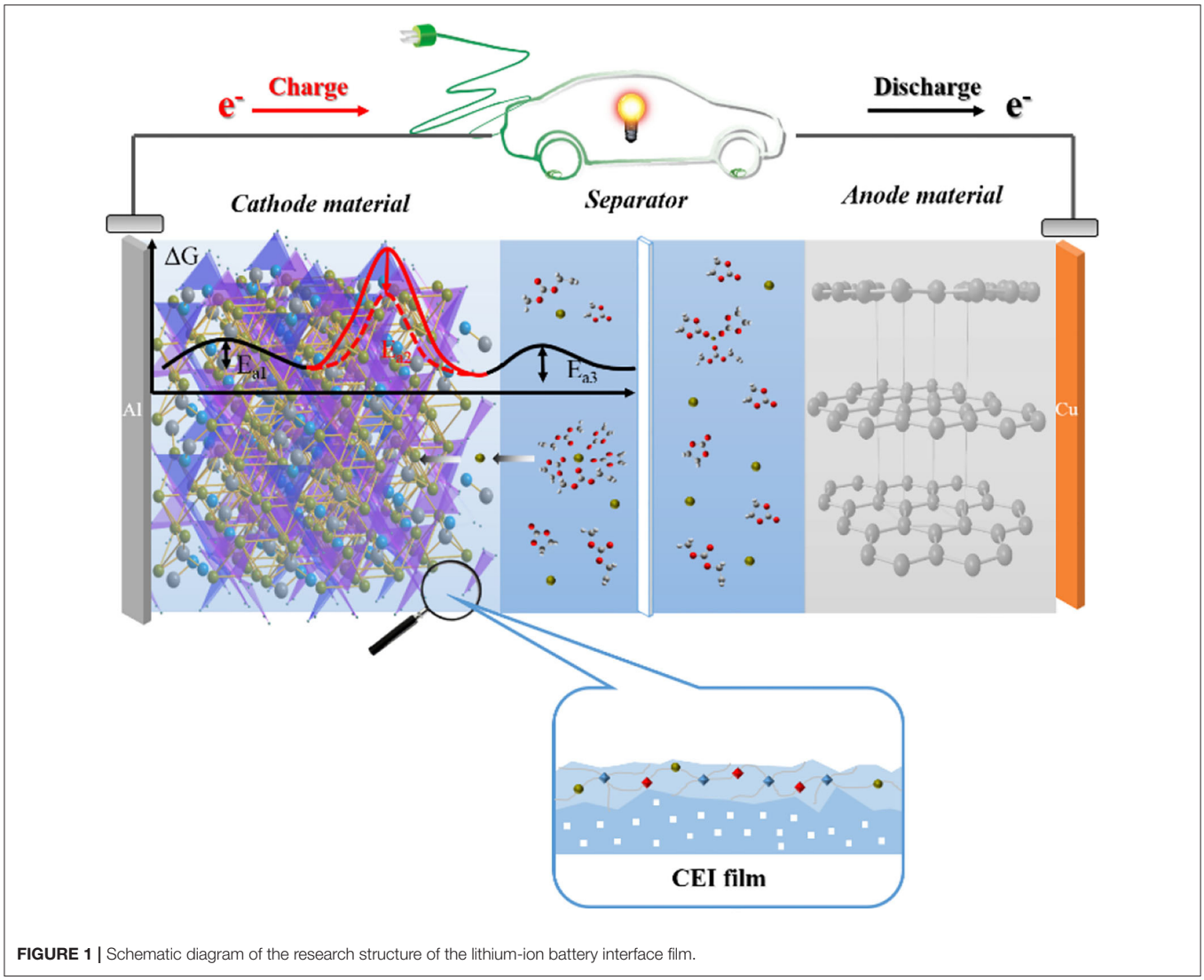

FIGURE 1 | Schematic diagram of the research structure of the lithium-ion battery interface film.

$Li_{1-x}NiPO_4$ ($Ni^{3+/2+}$ at 5.2 V) and even $Li_{1-x}CoO_2$ (x <0.7, voltage above 4.5 V), which are shown in **Figure 3A**, and have the thermodynamic driving force for the oxidation of the electrolyte on the electrode surface (Wolfenstine and Allen, 2005; Ménétrier et al., 2008). Recent research has focused on some new lithium storage material, including high-capacity layered composites or solid solutions such as $yLi_{2-x}MnO_3\bullet(1-y)\ Li_{1-x}MO_2$ (M = Ni, Co, Mn) (Thackeray et al., 2007; Croy et al., 2013), lithium-rich material such as $Li_{1+y}M_{1-y}O_2$ (Koga et al., 2012; Ates et al., 2015) and Li_2MO_3 (M = Ru, Mn, Ti, Sn) (Ménétrier et al., 2008; Sathiya et al., 2015). In addition to the use of transition metal ion redox to store lithium, the redox reactions of oxyanions are also used compared to $LiCoO_2$ has a real capacity of 140 mAh g^{-1}, with more than 230 mAh g^{-1} of reversible capacity, where the electron energy in the d orbital of the transition metal drops below that in the p orbital of the oxygen anion (Thackeray et al., 2007; Koga et al., 2012; Croy et al., 2013). The redox reaction of these oxide anions may cause the production of higher active species such as the peroxide ion O_2^{2-}-, molecular oxygen, and superoxide compounds (O_2^- is produced by the reduction of O_2 at voltages below ~3 V), that will chemically react with an aprotic electrolyte to form a surface film (Xu et al., 2011).

Estimation of the Electrolyte LUMO/HOMO Energy Levels

The first adiabatic electron transfer and the nature of electrolyte itself can be used to estimate the HOMO/LUMO levels of electrolyte. The solvent molecules and Li^+ solvation or anion solvation complexes are used to describe the oxidation and reduction processes of pure solvents and solvated lithium salts, respectively (Xing et al., 2011; Leung, 2013). The reduction potential (relative to the LUMO energy levels) is obtained by density functional theory (DFT) calculations with adding a continuous pole model (Vollmer et al., 2004; Leung, 2013). For example, the carbonate solvents EC, PC, and DMC, which are commonly used in lithium-ion batteries, are found to have LUMO energy close to the Li^+/Li pair (shown in **Figure 4A**; Vollmer et al., 2004; Leung, 2013). Through calculation, it was

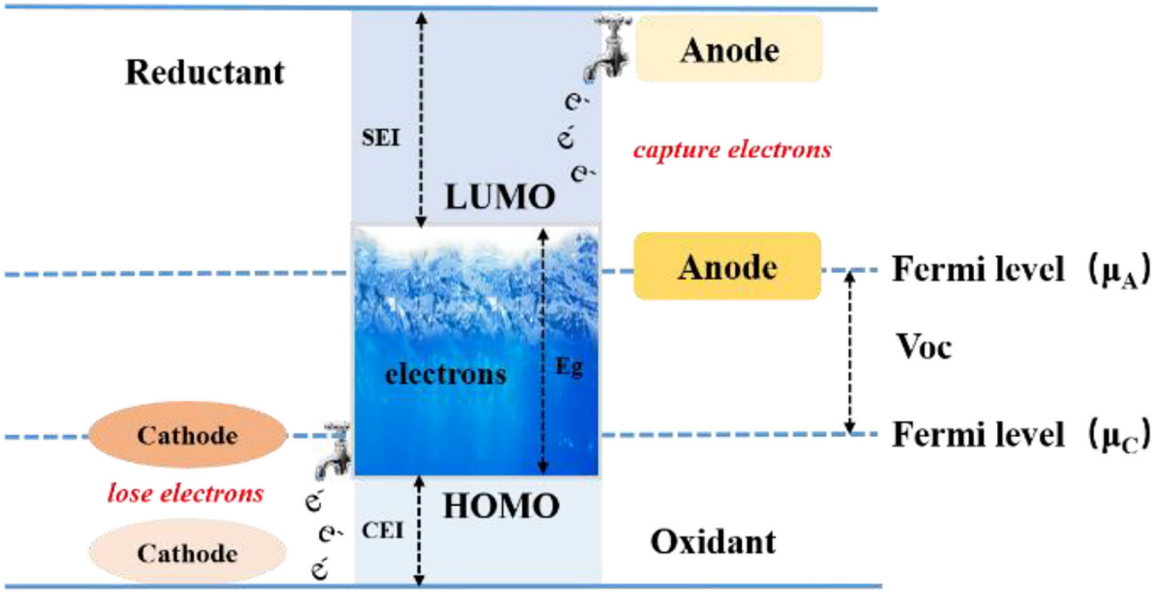

FIGURE 2 | Schematic drawing formation mechanism of SEI (Goodenough and Kim, 2010).

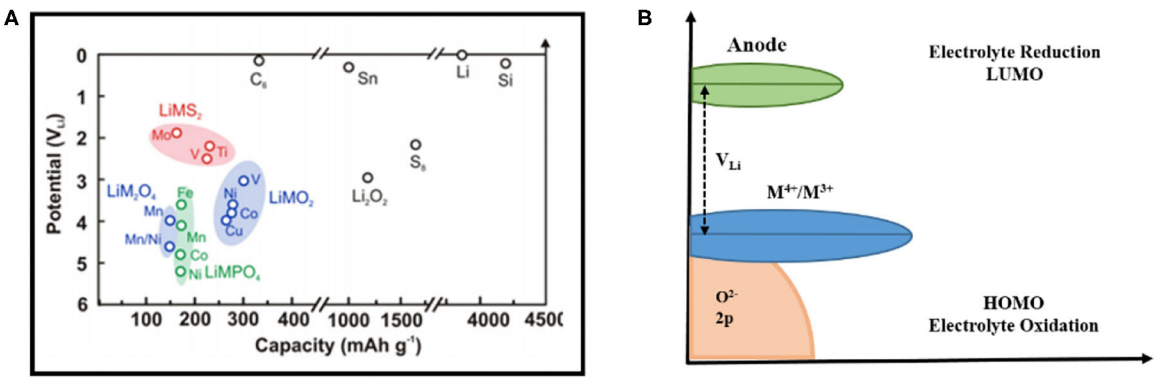

FIGURE 3 | (A) Comparison of potential and theoretical capacity of several lithium-ion battery lithium storage cathode materials (Zhang et al., 2001); **(B)** The difference between the HOMO/LUMO orbital energy level of the electrolyte and the Fermi level of the electrode material controls the thermodynamics and driving force of interface film growth (Goodenough and Kim, 2010).

found that several homologs of pure carbonate solvents such as PC, EC, and DMC, are not particularly large in their LUMO values, which indicates that the number of carbon chains has a small effect on the LUMO value of carbonate groups. The main reason is related to the electron transfer occurring mainly in the carbonate group (shown in **Figure 4B**). When lithium-ions are included in the calculation, the calculated LUMO energy level will be reduced by ∼0.5 eV relative to the pure solvent, and the stability will therefore decrease, and the reduction reaction will occur on the lithium or graphite anode (**Figure 4A**). In addition to the influence of lithium-ions on the solvent LUMO level, the role of lithium salt anions such as PF_6^-, ClO_4^-, and BF_4^- should also be considered, which requires further computational studies.

The calculated HOMO energy level of the pure-carbonate solvent is lower than the Fermi level of the cathode material, and its oxidation potential is close to 7 V (Zhang et al., 2001). When the anion of the salt is added to the solvent, the calculated HOMO level of the electrolyte is increased by ∼1.5 eV (the potential is about 5.5 V), which reduces the thermal stability of the electrolyte relative to the electrochemical oxidation reaction, and then proton transfer between anions causes the oxidation of the electrolyte (Xing et al., 2011). The thermal stability of the electrolyte decreases in the order of PF_6^- >BF_4^- >ClO_4^-, and the complexation of PF_6^- with the solvent is the most resistant to oxidation (**Figure 4A**).

Although DFT calculations predict that the electrolyte solvent is not easily oxidized when the potential is lower than ∼5.5 V,

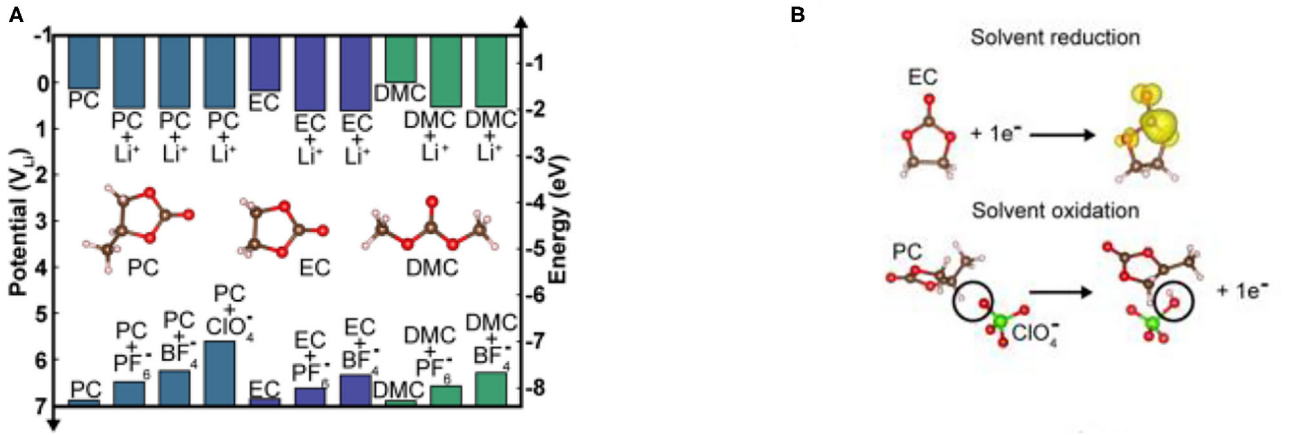

FIGURE 4 | (A) Calculated reduction and oxidation energy levels of common solvents and solvated salts for Li-ion battery. **(B)** Reaction formulae used for calculating redox levels under ideal conditions (Gauthier et al., 2015) (reproduced from ref. 5 with permission from Springer Nature, copyright 2016).

carbonate-based electrolytes can be electrochemically oxidized in the range of 4.5–6.5 V according to reported experimental results (Xu et al., 1999; Egashira et al., 2001). Tests on the catalytic activation of different electrodes show that these contradictions may be caused by the presence of impurities leading to the change in the redox potential during the experiment, and to the inaccuracies associated with DFT calculations. The data reported in **Figure 4A** shows the clear trend of using the calculated HOMO/LUMO energy levels of the solvent molecules to judge the electrochemical stability window of electrolyte, and ignoring the interaction between the solvent and the electrode surface.

In addition to the electrochemical reduction and oxidation of the electrolyte described in **Figures 4A,B**, the electrolyte may decompose through other chemical reactions, and may compete with these electrochemical reactions simultaneously, which will affect the composition of the interfacial film formed on the electrode (Endo et al., 1998). We will introduce next in this article the influence of the electrochemical and chemical reactions of different positive electrodes on the composition and structure of the interfacial film, and how the electrode composition and decomposition affect them.

MECHANISM OF FILM FORMATION ON THE CATHODE SURFACE (INCLUDING DILUTE AND CONCENTRATED SOLUTION)

Mechanism of Positive Film Formation in Dilute Solution Electrolyte

There is no thermodynamic driving force for the electrochemical oxidation of the electrolyte on most traditional positive electrode materials (**Figure 4A**). There are currently three generally accepted mechanisms that describe the formation of the CEI film on the positive electrode (Li et al., 2008; Kempaiah et al., 2019; Gründer and Lucas, 2020):

(1) The drift mechanism, which considers the solid-electrolyte interface (SEI) film on the surface of the positive electrode to form through the reduction of the organic electrolyte on the negative electrode that is saturated with the electrolyte, and then diffused and deposited on the surface of the positive electrode material (Aurbach, 2000; Ostrovskii et al., 2001);

(2) The nucleophilic reaction mechanism, according to which electrophilic solvent molecules (such as EC or DMC) in the organic electrolyte are formed by a nucleophilic reaction with the negatively charged positive electrode materials or the interfacial film forms when the solvent reacts with the electrode, then the insoluble products from that reaction are deposited on the surface of the electrode (Wang et al., 2004a);

(3) The spontaneous reaction mechanism that relates the interfacial layer to the products from the reaction between electrolyte and positive electrode (Wang et al., 2004b; Wang and Chen, 2005).

Battery cycling under high voltage and high temperature will exacerbate the formation process of the interfacial film. Research on the positive electrode interfacial film is still in the development stage, and plenty of studies found that the film covering the surface of the positive electrode material is also incomplete, which caused by the continuous decomposition of the CEI film. There are three reasons to investigate the film formation on the positive electrode (Dupre et al., 2009): (1) the driving force of film formation. Compared with the negative electrode, the driving force for the positive electrode film formation is not easy to study. This is because of the structure of the negative electrode. Taking graphite as an example, the fragile structure of graphite is supported by weak Van der Waals forces, which allows its structure to easily co-embed and dissolve in the solvent, often leading to the failure of the battery. The coulombic forces and covalent bonds constituting the positive electrode material result in robust structure that is not particularly sensitive to the co-embedding of solvents; (2) the complex chemical composition on the surface of the cathode material makes it difficult to identify the electrochemical oxidation reaction of the electrolyte. The surface of most cathode materials originally has a film of Li_2CO_3 that is formed on the transition metal oxide, then

subsequently reacts with the acid electrolyte to introduce new substances (Wang et al., 2003; Würsig et al., 2005; He et al., 2008; Dupre et al., 2009). Although quite a few of the products of these spontaneous reactions are interfacially mixed with the products of subsequent reactions, the irreversible electrochemical reaction and the phase change on the surface of the cathode will occur during the initial charging cycle, making the final interface different in chemical composition and morphology; (3) more importantly, the operation voltage of most cathode materials does not tend to be excessively higher than the limit of the oxidation potential of the electrolytic solution. Unlike with the negative electrode, the decomposition of the electrolytic solution at the positive electrode is not inevitable. However, with "5 V" positive electrode materials such as $LiNi_{0.5}Mn_{1.5}O_4$ (4.6 V vs. Li^+/Li) or $LiCoPO_4$ (4.8 V vs. Li^+/Li), the thermodynamic stability of the surface potential of the positive electrode becomes more positive compared to that of the components of the organic electrolyte, which Fermi level of the material is higher than the HOMO level of the electrolyte.

In general, the film on the surface of the positive electrode undergoes at least three processes: (1) a natural surface film forms during the electrode manufacturing process; (2) the natural surface film goes through a spontaneous chemical reaction when exposed to the electrolyte; (3) the products of steps (1) and (2) go through electrochemical rearrangement during the initial charging process.

Thomas et al. was the first to show the presence of an interfacial film on the surface of the cathode material, and their work was followed by a large number of studies that tried to characterize the structure of the film and speculate its origin (Thomas et al., 1985). The interfacial film on the positive electrode usually consists of chemical species surprisingly similar to the products of the decomposition of solvents and salts, similarly to the case of the products found on the negative electrode. The interfacial film on the positive electrode is mainly derived from the electrochemical chemically nucleophilic attack reaction on the electrode surface. Using *in situ* Fourier-transform infrared spectroscopy (FTIR), Wang et al. demonstrated the presence of carboxylate groups (O-C = O) on the surface of $Li_{1-x}CoO_2$ under cycling (Laudadio et al., 2019), while recently the oxidation of carbonate solvent on the surface of $LiNi_xMnyCo_{1-x-y}O_2$ has also been developed by the *in situ* FTIR (Zhang et al., 2020). The use of lithium-rich layered compounds such as $0.5Li_{2-x}MnO_3$ $0.5Li_{1-x}Co_{0.33}Ni_{0.33}Mn_{0.33}O_2$ or $Li_{1.2-x}Co_{0.13}Ni_{0.13}Mn_{0.54}O_2$ as reported in numerous recent studies, will give rise to the further oxidation of the electrolyte by reaction with the O_2 released during the charging process, and generate inorganic carbonates Li_2CO_3 (Yabuuchi et al., 2011). The use of *in-situ* monitoring techniques for probing the changes occurring on the surface of the cathode, like the use of *in-situ* synchronous XPS and XAS on $Li_{1-x}Mn_{1.5}Ni_{0.5}O_4$ neutron reflectometer and $LiCoO_2$ or $Li_{1-x}Ni_{0.2}Co_{0.7}Mn_{0.1}O_2$ (Browning et al., 2014; Yamamoto et al., 2014; Cherkashinin et al., 2015), offers the potential to provide new insight on the process of formation of the interfacial films on the surface of the positive electrode material, without any interference from the effect of the conductive agent and the binder. Also, the interface film of high-nickel ternary material $LiNi_{0.8}Co_{0.1}Mn_{0.1}O_2$ is also a recent research content (Hirbod and Xifei, 2019).

Mechanism of CEI Film Formation in High-Concentration Electrolyte

The mechanism of film-forming in high-concentration electrolytes is quite different from that of traditional diluted solution systems. The SEI film in high-concentration electrolytes is derived entirely from the anions, and the choice of anions will therefore directly determine the chemical properties of the interfacial film. Recently, and by defining the structure of ionic solvation, Borodin et al. temporarily divided all electrolytes into three different categories, instead of defining a limited concentration limit (Borodin et al., 2020). As shown in **Figure 5**, these categories are: (1) "salt-in-solvent" electrolyte, in which the number of solvent molecules is higher than that required for first-order solvation of all cations; (2) "salt-solvated" electrolyte, in which the number of solvent molecules is just enough to complete the main cations solvent layer, so most dissociated salts usually form stoichiometric solvates; (3) "solvent-in-salt" electrolyte, which is a super-concentrated electrolyte. These three categories provide a new idea for us to elucidate the formation mechanism of the interfacial film in high-concentration electrolytes. Although conventional electrolytes with molarity of 1.0 M belong to the "solvent-in-salt" category (Xu, 2014; Borodin et al., 2020), the latter two categories cover ultra-concentrated electrolytes, of which "salt solvation" is also commonly referred to as "solvated ionic liquid" to highlight its relationship with room temperature ionic liquids (RTIL), because of the lower proportion of "free" solvents. The main limitation on obtaining super-concentrated electrolytes is obviously the solubility of the salt in a given solvent, which is related to the melting point, disorder, and crystallization kinetics of the solvate, and can produce crystallinity and voids at salt concentrations. The special properties of the positive electrode surface brought about by the high concentration of an electrolyte are often apparent in the interfacial electrochemical behavior.

Among the "extraordinary" properties of concentrated electrolytes, there are reactions that may qualify as new interfacial chemical reactions different from those occurring in dilute solutions. This new interface has been recognized as the key to allow the electrochemical performance to reach extreme voltages. Examples on such electrolytes include ultra-concentrated ethers, sulfones, sulfites, nitriles, and water, which form a protective interfacial layer on the electrode material and allow the material to exhibit reversibility at high potentials (Xu, 2004; von Wald Cresce et al., 2012). All these new interfacial layers have the characteristics of the anions rather than those of the solvent molecules. Unlike dilute solutions, the interfacial chemical reaction is mainly the oxidative decomposition of solvent molecules. That new interfacial chemistry that relies on anions rather than solvent molecules, has lifted many of the traditional restrictions on electrolyte design, the most obvious of which being ethylene carbonate (EC), which is not an option in the manufacturing of any modern lithium-ion battery. The lack of

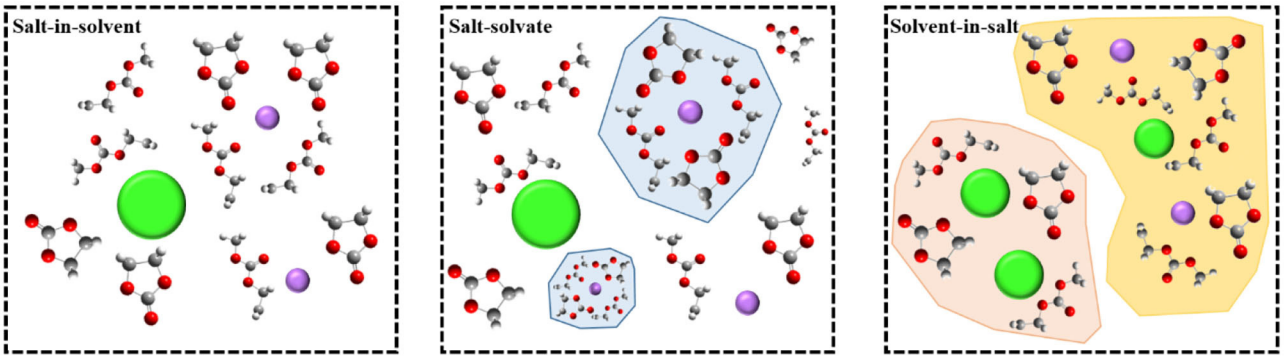

FIGURE 5 | Schematic diagram of electrolytes classified by concentration (Borodin et al., 2020).

solvent is mainly due to its key role in film formation on the surface of graphite negative electrodes (Xu, 2004; von Wald Cresce et al., 2012).

Although there is a correlation between the solvated shell of lithium-ion and the hypothetical transition state of the lithium ion-solvent co-embedded at the graphite interface, predicting the interfacial chemical reactions remains a challenge (von Wald Cresce et al., 2012). In general cases, it can be reasonably assumed that when an electrode potential reaches the threshold value of the decomposition potential of the electrolyte component, that is, when the interfacial chemical reaction begins, there may already be an interfacial structure existing in the so-called internal Helmholtz layer. This self-assembly of electrolyte components is enriched in some components and absent in others, and should be the intermediate parent entity that determines the final interface. Therefore, understanding the chemical composition and structural properties of an interface can open the door for predicting interfacial electrochemical reactions (Borodin et al., 2017; Suo et al., 2017; Vatamanu and Borodin, 2017; Yang et al., 2017, 2019; McEldrew et al., 2018). The same process occurs on the surface of the positive electrode. Molecular dynamics simulations show that the anion concentration in the inner layer of Helmholtz increases when the electrode is positively polarized (Vatamanu et al., 2012). When the electrolyte is based on a mixed solvent, such as the typical formulation of a commercial lithium-ion battery, and regardless of whether it is a negative electrode or a positive electrode, the preferential coordination of EC increases its chance of participating in the formation of SEI and CEI compared to DMC or other linear carbonates. When the salt concentration is ∼1.0 M, both solvents and anions are observed in the internal Helmholtz layer near the surface of the positive electrode, but the super-concentrated electrolyte or ionic liquid will completely build up in the internal Helmholtz layer and disperse all the solvents molecules, causing them to cover the surface of the positive electrode, and preventing the possibility of their oxidation (McOwen et al., 2014; Borodin et al., 2017; Vatamanu and Borodin, 2017; McEldrew et al., 2018). The anionic structure plays a key role in determining whether or not adsorption occurs preferentially. For example, molecular dynamics simulations (Vatamanu and Borodin, 2017) found that TFSI has a greater advantage than trifluoromethanesulfonate (OTf) during positive electrode polarization, and this result was confirmed using infrared spectroscopy of the electrode surface.

We now present future research directions in this area and address their significance as follows:

(1) The formation mechanism of the SEI is in need of in-depth exploration. The majority of literature attributed the preferential reduction of the anion to the decrease in LUMO energy level due to the complexation of the anion with Li^+ (**Figure 6**). This proposal represents an important aspect in linking micro-coordination states with electrochemical reactions. Moreover, the equilibrium potential and the solubility of the SEI substance cannot be ignored (Sodeyama et al., 2014; Yamada et al., 2014). The equilibrium reaction potential of the negative electrode (and the positive electrode) is also shifted upwards according to the Nernst equation, because of the increase in lithium-ion activity in the high-concentration electrolyte, which may change the path of the main electrochemical reaction. Also, it is not easy to dissolve the components of the SEI film, because there are fewer free solvent molecules in the high-concentration electrolytic solution (Sodeyama et al., 2014). To tackle the microscopic aspects of the latter, a hybrid Monte Carlo-molecular dynamics approach may be a powerful tool, as recently described in the SEI film formation process. In addition, the modification of electrolyte additives is also an aspect worth studying (Takenaka et al., 2018).
(2) Multi-layering is an aspect that should be used to standardize SEI film. Although there are many characterization methods, there is no analysis capable of *in situ* characterization of SEI film (Wang et al., 2016; Yamada et al., 2016).
(3) The most challenging task would be to correlate the chemical composition of SEI membranes with their functions (Qian et al., 2015; Wang et al., 2018a).

RESEARCH METHODS AND ADVANCED CHARACTERIZATION FOR CEI FILM

The characterization of the interfacial film is very challenging due to many reasons (Chu et al., 2019): First, the reaction

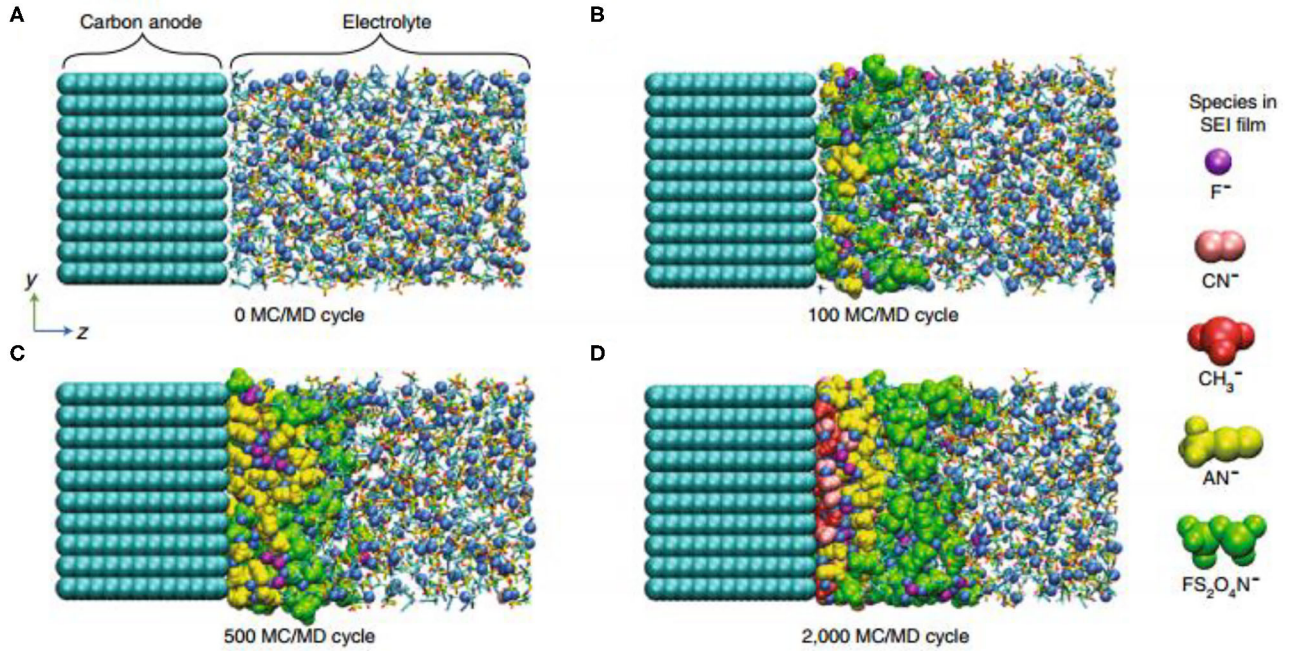

FIGURE 6 | Molecular dynamics simulation of interfacial film formation in high-concentration electrolytes (5 M LiFSA/AN) by the mixed Monte Carlo/molecular dynamics (MC/MD) method: **(A)** Activation process (0 MC/MD cycle). **(B)** Preferential reduction of FSA^- to from green $FS_2O_4N^-$ anions (100 MC/MD cycle). **(C)** Sequential reduction of AN at the FSA^--poor surface (500 MC/MD cycle). **(D)** Final equilibrium state to form a stable SEI (2,000 MC/MD cycle) (Takenaka et al., 2018) (reproduced with permission from ACS The Journal of Physical Chemistry C, copyright 2018).

of SEI formation is accompanied by lithium-ion insertion and is affected by many factors, including the composition of the electrolyte and the charge and discharge conditions. This means that the chemical composition and structure of the SEI film are complicated. In addition, the thinner SEI is buried between the two electrodes of the battery, and becomes unstable and "non-living" when taken out of the volatile electrolyte in a lithium-ion battery. Since the physical properties of the interfacial film cannot be observed *in situ*, characterizing and understanding the correlation between the interfacial film and battery performance has become extremely important, but remains a challenge to tackle. Moreover, the lack of basic research means that a large number of efforts follow a process of continuous trial and error to study the regulatory role of the interfacial film. In order to optimize the battery's performance, the ideal interfacial film should be thin (to reduce the consumption of active lithium-ions and lower the impedance of the lithium-ion transport process), dense (to better block the electrons), and have a uniform morphology and structure (for uniform lithium-ion transport) and mechanical flexibility (to cushion the volume expansion of the active material).

In addition to some of the traditional characterization methods, recent years have brought along advances and new characterization methods that provided great help for the interpretation of the interfacial film mechanisms with high spatial resolution close to the chemical structural units, and a state close to "effective" interfacial film (Liu et al., 2014; Zhang et al., 2014; Huang et al., 2018). For example, the mechanical curve of the atomic force microscopy is used to test the mechanical elasticity and structure of the interfacial film with nanometer-level resolution, and the non-porous near-field scanning optical microscopy (aNSOM) also uses the AFM tip that is in contact with the surface of the probed material (Ayache et al., 2015a,b). Optical probes for high-resolution spectroscopy and imaging measurements have been used to map the chemical composition of the interfacial film. In addition, secondary time-of-flight ion mass spectrometry (ToF-SIMS) is also used as a detection technique (Zhu et al., 2015; Yuan et al., 2017). Moreover, cryo-STEM, which was originally designed to protect aqueous biological samples from damage, has been introduced since 2017 to study the chemical composition and structure of the interfacial film, and allowed researchers to obtain many exciting results. We will present in the following section some of the novel testing technologies used in the recent years, and mainly discuss their development and some of the progress made in their application for the characterization of surface CEI films (Alvarado et al., 2018; Li et al., 2018a; Zachman et al., 2018).

Depth Profiling Using *in-situ* TOF-SIMS

The application of SIMS for situ in measurements in lithium-ion battery research is still a challenge, due to the high volatility of non-aqueous liquid electrolytes. In order to solve this problem, Zhu et al. designed an *in situ* battery to explore the lithium insertion and extraction process on the copper foil in $LiPF_6$/(EC + DMC) electrolyte (**Figure 7A**; Zhu et al., 2015). In a different study, Li et al. used TOF-SIMS to study the role of the conductive

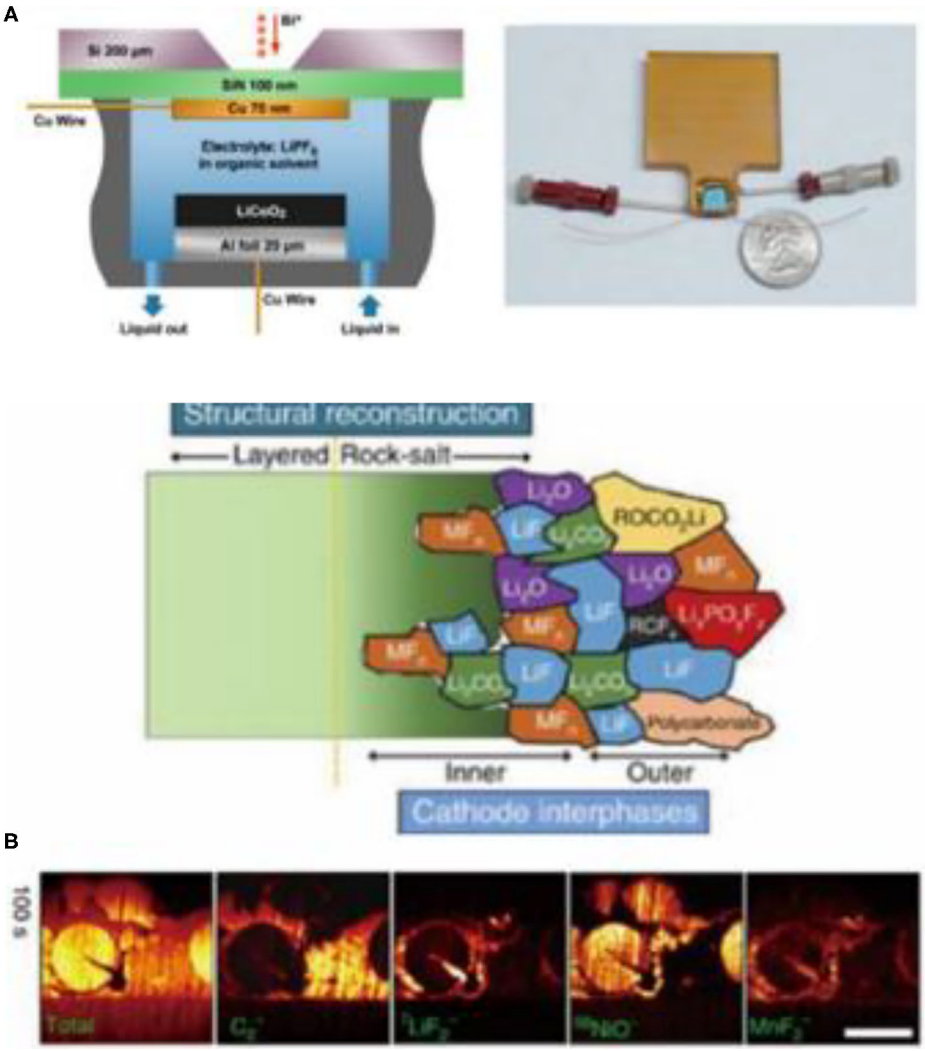

FIGURE 7 | (A) Schematic diagram of a device embedded with positive and negative electrodes in liquid battery (left) and picture of the actual device (right) (Zhu et al., 2015) **(B)** Schematic diagram of the composition of the CEI film on the positive electrode surface and the TOF-SIMS ion sputtering distribution at the material interface (Yuan et al., 2017) (reproduced with permission from ACS Nano Letters, copyright 2015).

additive in the formation of CEI films and the performance of full cells with nickel-rich layered oxide positive electrodes ($LiNi_{0.7}Co_{0.15}Mn_{0.15}O_2$) (Yuan et al., 2017). Area-sensitive SIMS indicated that CEI was originally formed on the conductive carbon additives without electrochemical bias, and that it could passivate the positive electrode particles through the exchange of surface substances (**Figure 7B**).

Recently, Xu et al. propose new research using molecular eye technology to draw SEI chemical and structural dynamic map. With molecular eye technology, scientists can more accurately understand the inner workings of batteries and find out why they tend to catch fire. According to foreign media reports, researchers from the US Army Combat Capabilities Development Command's Army Research Laboratory and the US Department of Energy's Pacific Northwest National Laboratory explore how a chemical reaction occurs when two key parts of a battery come into contact, and form a key part of the battery, commonly known as a SEI film (Zhou et al., 2020).

Scientists at the Environmental Molecular Sciences Laboratory and the Pacific Northwest National Laboratory have developed *in-situ* liquid secondary ion mass spectrometry. In collaboration with Army scientists, they used this technology to study how electrode-electrolyte interface chemistry works at the molecular level when the battery is charged for the first hour. By monitoring the formation of SEI and its chemical changes, a picture of the chemical reactions that occurred are drawm, and combining molecular dynamics simulation methods, their work revealed something that could only have been speculated before (Zhou et al., 2020).

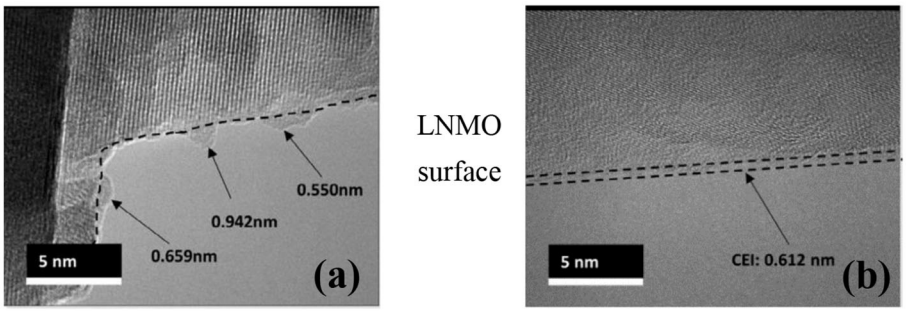

FIGURE 8 | (a) Cryo-TEM images of LNMO particle CEIs after discharging for 50 cycles with 1.2 M $LiPF_6$/(EC + EMC, 3:7) and **(b)** 3 M LiFSI-SL (Alvarado et al., 2018).

Detection of Spatially Resolved SEI Chemical Structures Using Nano-Infrared Spectroscopy

Usually, FTIR and Raman vibrational spectroscopy are used to analyze the composition and spatial distribution of the SEI film, but their spatial resolution is usually limited by the beam size, which is mainly in the order of decimeters. However, it is well-known that the composition of the interfacial film at the nanoscale is highly uneven. Therefore, chemical analysis results obtained for SEI film by FTIR are only based on the average value of the light emitting area. In order to solve this problem, researchers in recent years have invented a method of infrared spectrum imaging at nanometer-scale spatial resolution. Through three different methods, including infrared non-aperture near field scanning optical microscopy (IR-aNSOM) (Wickramasinghe and Williams, 1994; Centrone, 2015; Muller et al., 2015), light-induced resonance (PTIR) (Dazzi and Prater, 2017), and light-induced force microscopy (PiFM) (Liu et al., 2018). Because of the unique capabilities of these high-resolution chemical imaging methods, new insight can be gained in the study of interfacial films.

In aNSOM, a beam of light is fixed on a metal AFM probe placed close to the sample surface to allow the light intensity to be greatly enhanced at the probe tip due to local surface plasmon resonance. The scattered signal is modulated by the local dielectric properties of the sample to be measured and collected from the far field, where different compounds absorb the infrared spectrum, thereby producing image contrast in the IR-aNSOM as the AFM probe scans the entire surface. Based on this, Ayache et al. (2015b) pioneered the application of IR-aNSOM in SEI research on Sn and HOPG electrodes. In their first study, the HOPG electrode was selected from OCP (∼2.9 V) to 0.8 V (in Li ion embedded graphite) in 1.0M $LiPF_6$ dissolved in EC / DEC (weight ratio of 1:2) Samples taken from the electrolyte at 1.66, 1.36, and 0.9V were used for IR-aNSOM measurement of the (002) surface. As a result, these researchers reported that the morphological image of the sample discharged to 1.6 V showed that the 200 nm SEI layer was composed of loosely packed particles, while the multi-wavelength near-field IR absorption image showed a large contrast, indicating that SEI has a relatively high The thick inner and outer particle layers, as well as the two layers, have unique but uniform composition.

These characterization methods are widely used for characterizing SEI films on the surface of negative electrode. Considering that the positive electrode interface film is thin, it may not be particularly widely used. In the future, research on the positive electrode interfacial films can also be used to characterize the composition and dynamic characteristics of interfacial films by analogy.

Original Structure of Interfacial Films Characterized by Cryo-TEM

Although traditional transmission electron microscopy (TEM) can obtain atomic-level structural images of the material, it is still not ideal for the characterization of interfacial films, because these films are chemically active and sensitive to electron beam radiation. Therefore, many studies on interfacial films obtained from traditional TEM are now limited to the decimeter level because detailed crystal structure cannot be probed. However, recent studies have used cryo-electron microscopy to study the interfacial film at the atomic level, maintaining the original structure by freezing samples in liquid nitrogen (Li et al., 2017, 2018a,b; Alvarado et al., 2018; Wang et al., 2018b). In the field of characterization of high-voltage electrolytes for lithium-ion batteries, Alvarado et al. used cryo-electron microscopy (cryo-STEM) to retain the structure of the CEI film of the $LiNi_{0.5}Mn_{1.5}O_4$ cathode and avoid disturbance to the electron transfer (Alvarado et al., 2018). The technique probes obvious changes in thickness and uniformity, while the CEI film of the electrolyte system under study remains thin and uniform (**Figure 8**). Recently, Huang used Cryo-STEM to study the spatial distribution of SEI components such as LiF and Li_2O in the SEI of the Li metal anode. Cryo-STEM EELS confirmed that the dense SEI connected with the negative electrode material does not contain LiF (William et al., 2020).

Analysis of Mechanical Elasticity of SEI Films by AFM Mechanical Curves

In addition to being an electronic insulator and ion conductor, the SEI/CEI layer also needs to have sufficient mechanical flexibility and excellent hardness to adapt to the changes in the electrode volume during charge and discharge cycles, especially for conversion reactions with large volume expansion, as with alloy anodes and some cathode materials. A fragile SEI/CEI film

will break during the volume expansion of the electrode and cause the formation of a new interface film, which will result in lower coulombic efficiency and rapid capacity decay. Although many instruments are used to detect the chemical composition and morphology of the interfacial film, the characterization of its mechanical properties is still relatively unaddressed. To solve this problem, AFM-based mechanical instruments, local strain forces, or "nano surveys" measurements were proposed as the only suitable equipment (Chu et al., 2019). Liao et al. (2018) used AFM to characterize the roughness of the CEI film formed by the LiDFBOP additive in graphite-$LiNi_{0.5}Co_{0.2}Mn_{0.3}O_2$ system. The results showed that the CEI film formed by LiDFBOP on the positive electrode $LiNi_{0.5}Co_{0.2}Mn_{0.3}O_2$ was more uniform than that in transition electrolyte system without additive. This also provides a basis for LiDFBOP to adjust the positive electrode interface mechanism, and thereby improve the electrochemical performance of the system.

OUTLOOK

In this article, we reviewed the studies that addressed the composition and properties of the interfacial film on the positive electrode of lithium-ion batteries over the past decade. It can be seen from various studies that researchers have been paying increasing attention to the investigation of the CEI membranes, and obtaining informative results that will guide the research on the anode decay mechanism and the design and optimization of electrolyte formulation. The interfacial film can be seen as a phenomenon associated with the reaction between the electrolyte and the electrode material, it can also be used as a bridge toward studying the reaction mechanism. It is necessary to balance the relation between the loss of irreversible capacity and the repair during the formation of the CEI film, and whether the consumed lithium-ions can be added to the deteriorated performance with time.

The use of advanced characterization methods enables us to explore the key to the film formation mechanism. The application of some of the most advanced characterization methods reviewed in this article is not very extensive, and these characterization methods suffer from few problems that require consideration by future researchers. First, there is a need for the development of proper *in situ* characterization protocols for the battery. Second, multiple detection technologies may need to be combined to achieve the characterization of multiple properties of the interface. Finally, proper methodologies are needed to perform the characterization of the positive electrode interfacial film while the electrode is paired with the negative electrode in a full cell, to study the film formation kinetics of the entire process.

Our current research on the interface films is largely traceable to the study of composite electrodes containing conductive agents and binders. This will affect the formation of interfacial films, and lead to misunderstandings of its composition. On the other hand, the simultaneous observation of the same decomposition products on the negative and positive electrodes is more confusing, because different reactions will be involved on each side of the electrode. In order to avoid these complications, it is necessary to study the surface mode of the electrode, such as oxidized microspheres and films, which will help study the activity between the electrolyte and the surface of the individual material. Another obstacle is the lack of information on the kinetic properties of the surface film formed at the interface. The implementation of *in-situ* technologies such as *in-situ* XPS, XAS, and surface-enhanced Raman spectroscopy, may draw a clear portrait of the surface structural features that are well-defined in the working environment. An example is seen in the recent use of high-voltage X-ray photoelectron spectroscopy to study the latest advances in interface films on silicon electrodes.

Overall, researchers around the world have invested considerable effort into the research of interfacial film, and more work is expected in this field in the future. The secret of the relation between the interfacial film and the device electrochemical performance is being gradually unveiled with the expansion of research and the advancement of characterization methods.

AUTHOR CONTRIBUTIONS

DZ: conceptualization, methodology, and writing–original draft. SL: writing–review & editing, funding acquisition, and project administration. All authors contributed to the article and approved the submitted version.

FUNDING

This work was supported by the Natural Science Foundation of China (Grant Nos. 51962019 and 21766017), Major Science and Technology Project of Gansu Province (18ZD2FA012), and Lanzhou University of Technology Hongliu first-class discipline construction program.

REFERENCES

Alvarado, J., Schroeder, M. A., Zhang, M., Borodin, O., Gobrogge, E., Olguin, M., et al. (2018). A carbonate-free, sulfone-based electrolyte for high-voltage Li-ion batteries. *Mater. Today* 21, 341–353. doi: 10.1016/j.mattod.2018.02.005

Ates, M. N., Mukerjee, S., and Abraham, K. M. (2015). A search for the optimum lithium rich layered metal oxide cathode material for Li-ion batteries. *J. Electrochem. Soc.* 162, A1236–A1245. doi: 10.1149/2.0481507jes

Aurbach, D. (2000). Review of selected electrode–solution interactions which determine the performance of Li and Li ion batteries. *J. Power Sources* 89, 206–218. doi: 10.1016/S0378-7753(00)00431-6

Ayache, M., Jang, D., Syzdek, J., and Kostecki, R. (2015a). Near-field IR nanoscale imaging of the solid electrolyte interphase on a HOPG electrode. *J. Electrochem. Soc.* 162, A7078–A7082. doi: 10.1149/2.0101513jes

Ayache, M., Lux, S. F., and Kostecki, R. (2015b). IR near-field study of the solid electrolyte interphase on a tin electrode. *J. Phys. Chem. Lett.* 6, 1126–1129. doi: 10.1021/acs.jpclett.5b00263

Borodin, O., Behl, W., and Joe, T. T. (2013). Oxidative stability and initial decomposition reactions of carbonate, sulfone, and alkyl phosphate-based electrolytes. *J. Phys. Chem. C* 117, 8661–8682. doi: 10.1021/jp400527c

Borodin, O., Ren, X., Vatamanu, J., Cresce, A. V., Knap, J., and Xu, K. (2017). Modeling insight into battery electrolyte electrochemical stability and interfacial structure. *Acc. Chem. Res.* 50, 2886–2894. doi: 10.1021/acs.accounts.7b00486

Borodin, O., Self, J., Persson, K. A., Wang, C., and Xu, K. (2020). Uncharted waters: super-concentrated electrolytes. *Joule* 4, 69–100. doi: 10.1016/j.joule.2019.12.007

Browning, J. F., Baggetto, L., Jungjohann, K. L., Wang, Y., Tenhaeff, W. E., Keum, J. K., et al. (2014). *In situ* determination of the liquid/solid interface thickness and composition for the Li ion cathode $LiMn_{1.5}Ni_{0.5}O_4$. *ACS Appl. Mater. Interfaces* 6, 18569–18576. doi: 10.1021/am5032055

Centrone, A. (2015). Infrared imaging and spectroscopy beyond the diffraction limit. *Annu. Rev. Anal. Chem.* 8, 101–126. doi: 10.1146/annurev-anchem-071114-040435

Cherkashinin, G., Motzko, M., Schulz, N., Spath, T., and Jaegermann, W. (2015). Electron spectroscopy study of Li[Ni, Co, Mn]O_2/electrolyte interface: electronic structure, interface composition, and device implications. *Chem. Mater.* 27, 2875–2887. doi: 10.1021/cm5047534

Chu, Y., Shen, Y., Guo, F., Zhao, X., Dong, Q., Zhang, Q., et al. (2019). Advanced characterizations of solid electrolyte interphases in lithium-ion batteries. *Electrochem. Energy Rev.* 3, 187–219. doi: 10.1007/s41918-019-00058-y

Croy, J. R., Gallagher, K. G., Balasubramanian, M., Chen, Z., Ren, Y., Kim, D., et al. (2013). Examining hysteresis in composite $xLi_2MnO_3\bullet(1–x)$ $LiMO_2$ cathode structures. *J. Phys. Chem. C* 117, 6525–6536. doi: 10.1021/jp312658q

Dazzi, A., and Prater, C. B. (2017). AFM-IR: technology and applications in nanoscale infrared spectroscopy and chemical imaging. *Chem. Rev.* 117, 5146–5173. doi: 10.1021/acs.chemrev.6b00448

Dupre, N., Martin, J.-F., Oliveri, J. M., Soudan, P., Guyomard, D., Yamada, A., et al. (2009). Aging of the $LiNi_{1/2}Mn_{1/2}O_2$ positive electrode interface in electrolyte. *J. Electrochem. Soc.* 156, C180–C185. doi: 10.1149/1.3098494

Egashira, M., Takahashi, H., Okada, S., and Yamaki, J. (2001). Measurement of the electrochemical oxidation of organic electrolytes used in lithium batteries by microelectrode. *J. Power Sources* 92, 267–271. doi: 10.1016/S0378-7753(00)00553-X

Endo, E., Ata, M., Tanaka, K., and Sekai, K. (1998). Electron spin resonance study of the electrochemical reduction of electrolyte solutions for lithium secondary batteries. *J. Electrochem. Soc.* 145, 3757–3764. doi: 10.1149/1.1838870

Gallego, N. C., Contescu, C. I., Meyer, H. M., Howe, J. Y., Meisner, R. A., Payzant, E. A., et al. (2014). Advanced surface and microstructural characterization of natural graphite anodes for lithium ion batteries. *Carbon N. Y.* 72, 393–401. doi: 10.1016/j.carbon.2014.02.031

Gauthier, M., Carney, T. J., Grimaud, A., Giordano, L., Pour, N., Chang, H., et al. (2015). Electrode–electrolyte interface in Li-ion batteries: current understanding and new insights. *J. Phys. Chem. Lett.* 6, 4653–4672. doi: 10.1021/acs.jpclett.5b01727

Goodenough, J. B. (2018). How we made the Li-ion rechargeable battery. *Nat. Electron.* 1, 204–204. doi: 10.1038/s41928-018-0048-6

Goodenough, J. B., and Kim, Y. (2010). Challenges for rechargeable Li batteries. *Chem. Mater.* 22, 587–603. doi: 10.1021/cm901452z

Gründer, Y., and Lucas, C. A. (2020). Potential-induced structural deformation at electrode surfaces. *Curr. Opin. Electrochem.* 19, 168–174. doi: 10.1016/j.coelec.2019.12.009

Han, X., Lu, L., Zheng, Y., Feng, X., Li, Z., Li, J., et al. (2019). A review on the key issues of the lithium ion battery degradation among the whole life cycle. *ETransportation* 1:100005. doi: 10.1016/j.etran.2019.100005

He, P., Zhang, X., Wang, Y., Cheng, L., and Xia, Y. (2008). Lithium-ion intercalation behavior of $LiFePO_4$ in aqueous and nonaqueous electrolyte solutions. *J. Electrochem. Soc.* 155, A144–A150. doi: 10.1149/1.2815609

Hightower, A., Ahn, C. C., Fultz, B., and Rez, P. (2000). Electron energy-loss spectrometry on lithiated graphite. *Appl. Phys. Lett.* 77, 238–240. doi: 10.1063/1.126936

Hirbod, M. K. S., and Xifei, L. (2019). Controllable cathode–electrolyte interface of $Li[Ni_{0.8}Co_{0.1}Mn_{0.1}]O_2$ for lithium ion batteries: a review. *Adv. Energy Mater.* 9, 1901597–1901628. doi: 10.1002/aenm.201901597

Huang, S., Cheong, L.-Z., Wang, D., and Shen, C. (2018). Thermal stability of solid electrolyte interphase of lithium-ion batteries. *Appl. Surf. Sci.* 454, 61–67. doi: 10.1016/j.apsusc.2018.05.136

Kempaiah, R., Vasudevamurthy, G., and Subramanian, A. (2019). Scanning probe microscopy based characterization of battery materials, interfaces, and processes. *Nano Energy* 65:103925. doi: 10.1016/j.nanoen.2019.103925

Koga, H., Croguennec, L., Mannessiez, P., Menetrier, M., Weill, F., Bourgeois, L., et al. (2012). $Li_{1.20}Mn_{0.54}Co_{0.13}Ni_{0.13}O_2$ with different particle sizes as attractive positive electrode materials for lithium-ion batteries: insights into their structure. *J. Phys. Chem. C* 116, 13497–13506. doi: 10.1021/jp301879x

Laudadio, E. D., Ilani-Kashkouli, P., Green, C. M., Kabengi, N., and Hamers, R. J. (2019). Interaction of phosphate with lithium cobalt oxide nanoparticles: a combined spectroscopic and calorimetric study. *Langmuir* 35, 16640–16649. doi: 10.1021/acs.langmuir.9b02708

Leung, K. (2013). Two-electron reduction of ethylene carbonate: A quantum chemistry re-examination of mechanisms. *Chem. Phys. Lett.* 568–569, 1–8. doi: 10.1016/j.cplett.2012.08.022

Li, H., Wang, Z., Huang, X., and Chen, L. (2008). Size effect and surface/interface issues in lithium ion batteries. *Physics* 37, 416–420.

Li, Y., Huang, W., Li, Y., Pei, A., Boyle, D., and Cui, Y. (2018a). Correlating structure and function of battery interphases at atomic resolution using cryoelectron microscopy. *Joule* 2, 2167–2177. doi: 10.1016/j.joule.2018.08.004

Li, Y., Li, Y., and Cui, Y. (2018b). Catalyst: how cryo-EM shapes the development of next-generation batteries. *Chem* 4, 2250–2252. doi: 10.1016/j.chempr.2018.09.007

Li, Y., Li, Y., Pei, A., Yan, K., Sun, Y., Wu, C., et al. (2017). Atomic structure of sensitive battery materials and interfaces revealed by cryo–electron microscopy. *Science* 358, 506–510. doi: 10.1126/science.aam6014

Liao, B., Li, H., Xu, M., Xing, L., Liao, Y., Ren, X., et al. (2018). Designing low impedance interface films simultaneously on anode and cathode for high energy batteries. *Adv. Energy Mater.* 8:1800802. doi: 10.1002/aenm.201800802

Liu, J., Park, S., Nowak, D., Tian, M., Wu, Y., Long, H., et al. (2018). Near-field characterization of graphene plasmons by photo-induced force microscopy. *Laser Photonics Rev.* 12:1800040. doi: 10.1002/lpor.201800040

Liu, X.-R., Deng, X., Liu, R., Yan, H., Guo, Y., Wang, D., et al. (2014). Single nanowire electrode electrochemistry of silicon anode by *in situ* atomic force microscopy: solid electrolyte interphase growth and mechanical properties. *ACS Appl. Mater. Interfaces* 6, 20317–20323. doi: 10.1021/am505847s

Lu, X., Jian, Z., Fang, Z., Gu, L., Hu, Y., Chen, W., et al. (2011). Atomic-scale investigation on lithium storage mechanism in $TiNb_2O_7$. *Energy Environ. Sci.* 4, 2638–2644. doi: 10.1039/c0ee00808g

McEldrew, M., Goodwin, Z. A., Kornyshev, A. A., and Bazant, M. Z. (2018). Theory of the double layer in water-in-salt electrolytes. *J. Phys. Chem. Lett.* 9, 5840–5846. doi: 10.1021/acs.jpclett.8b02543

McOwen, D. W., Seo, D. M., Borodin, O., Vatamanu, J., Boyle, P. D., and Henderson, W. A. (2014). Concentrated electrolytes: decrypting electrolyte properties and reassessing Al corrosion mechanisms. *Energy Environ. Sci.* 7, 416–426. doi: 10.1039/C3EE42351D

Ménétrier, M., Carlier, D., Blangero, M., and Delmas, C. (2008). On "really" stoichiometric $LiCoO_2$. *Electrochem. Solid State Lett.* 11:A179. doi: 10.1149/1.2968953

Mizushima, K., Jones, P. C., and Goodenough, J. B. (1980). Li_xCoO_2 ($0<x<-1$): a new cathode material for batteries of high energy density. *Mater. Res. Bull.* 15, 783–789. doi: 10.1016/0025-5408(80)90012-4

Muller, E. A., Pollard, B., and Raschke, M. B. (2015). Infrared chemical nano-imaging: accessing structure, coupling, and dynamics on molecular length scales. *J. Phys. Chem. Lett.* 6, 1275–1284. doi: 10.1021/acs.jpclett.5b00108

Ostrovskii, D., Ronci, F., and Jacobsson, P. (2001). Reactivity of lithium battery electrode materials toward non-aqueous electrolytes: spontaneous reactions at the electrode–electrolyte interface investigated by FTIR. *J. Power Sources* 103, 10–17. doi: 10.1016/S0378-7753(01)00815-1

Qian, J., Henderson, W. A., Xu, W., Bhattacharya, P., Engelhard, M. H., Borodin, O., et al. (2015). High rate and stable cycling of lithium metal anode. *Nat. Commun.* 6:6362. doi: 10.1038/ncomms7362

Sathiya, M., Abakumov, A. M., Foix, D., Rousse, G., Ramesha, K., Saubanere, M., et al. (2015). Origin of voltage decay in high-capacity layered oxide electrodes. *Nat. Mater.* 14, 230–238. doi: 10.1038/nmat4137

Sodeyama, K., Yamada, Y., Aikawa, K., Yamada, A., and Tateyama, Y. (2014). Sacrificial anion reduction mechanism for electrochemical stability improvement in highly concentrated Li-salt electrolyte. *J. Phys. Chem. C* 118, 14091–14097. doi: 10.1021/jp501178n

Suo, L., Han, W., Lu, X., Gu, L., Hu, Y., Li, H., et al. (2012). Highly ordered staging structural interface between $LiFePO_4$ and $FePO_4$. *Phys. Chem. Chem. Phys.* 14, 5363–5367. doi: 10.1039/c2cp40610a

Suo, L., Oh, D., Lin, Y., Zhuo, Z., Borodin, O., Gao, T., et al. (2017). How solid-electrolyte interphase forms in aqueous electrolytes. *J. Am. Chem. Soc.* 139, 18670–18680. doi: 10.1021/jacs.7b10688

Takenaka, N., Fujie, T., Bouibes, A., Yamada, Y., Yamada, A., and Naganka, M. (2018). Microscopic formation mechanism of solid electrolyte interphase film in lithium-ion batteries with highly concentrated electrolyte. *J. Phys. Chem. C* 122, 2564–2571. doi: 10.1021/acs.jpcc.7b11650

Thackeray, M. M., Kang, S.-H., Johnson, C. S., Vaughey, J. T.,Benedek, R., and Hackney, S. A. (2007). Li_2MnO_3-stabilized $LiMO_2$ (M= Mn, Ni, Co) electrodes for lithium-ion batteries. *J. Mater. Chem.* 17, 3112–3125. doi: 10.1039/b702425h

Thomas, M., Bruce, P., and Goodenough, J. B. (1985). AC impedance analysis of polycrystalline insertion electrodes: application to $Li_{1-x}CoO_2$. *J. Electrochem. Soc.* 132:1521–1528. doi: 10.1149/1.2114158

Vatamanu, J., and Borodin, O. (2017). Ramifications of water-in-salt interfacial structure at charged electrodes for electrolyte electrochemical stability. *J. Phys. Chem. Lett.* 8, 4362–4367. doi: 10.1021/acs.jpclett.7b01879

Vatamanu, J., Borodin, O., and Smith, G. D. (2012). Molecular dynamics simulation studies of the structure of a mixed carbonate/$LiPF_6$ electrolyte near graphite surface as a function of electrode potential. *J. Phys. Chem. C* 116, 1114–1121. doi: 10.1021/jp2101539

Verma, P., Maire, P., and Novak, P. (2010). A review of the features and analyses of the solid electrolyte interphase in Li-ion batteries. *Electrochim. Acta* 55, 6332–6341. doi: 10.1016/j.electacta.2010.05.072

Vollmer, J. M., Curtiss, L. A., Vissers, D. R., and Amine, K. (2004). Reduction mechanisms of ethylene, propylene, and vinylethylene carbonates a quantum chemical study. *J. Electrochem. Soc.* 151, A178–A183. doi: 10.1149/1.1633765

von Wald Cresce, A., Borodin, O., and Xu, K. (2012). Correlating Li^+ solvation sheath structure with interphasial chemistry on graphite. *J. Phys. Chem. C* 116, 26111–26117. doi: 10.1021/jp303610t

Wang, J., Yamada, Y., Sodeyama, K., Chiang, C. H., Tateyama, Y., and Yamada, A. (2016). Superconcentrated electrolytes for a high-voltage lithium-ion battery. *Nat. Commun.* 7:12032 doi: 10.1038/ncomms12032

Wang, J., Yamada, Y., Sodeyama, K., Watanabe, E., Takada, K., Tateyama, Y., et al. (2018a). Fire-extinguishing organic electrolytes for safe batteries. *Nat. Energy* 3, 22–29. doi: 10.1038/s41560-017-0033-8

Wang, X., Li, Y., and Meng, Y. S. (2018b). Cryogenic electron microscopy for characterizing and diagnosing batteries. *Joule* 2, 2225–2234. doi: 10.1016/j.joule.2018.10.005

Wang, Z., and Chen, L. (2005). Solvent storage-induced structural degradation of $LiCoO_2$ for lithium ion batteries. *J. Power Sources* 146, 254–258. doi: 10.1016/j.jpowsour.2005.03.041

Wang, Z., Dong, H., Chen, L., Mo, Y., and Huang, X. (2004b). Understanding mechanism of improved electrochemical performance of surface modified $LiCoO_2$. *Solid State Ionics* 175, 239–242. doi: 10.1016/j.ssi.2004.09.043

Wang, Z., Huang, X., and Chen, J. (2004a). Characterization of spontaneous reactions of $LiCoO_2$ with electrolyte solvent for lithium-ion batteries. *J. Electrochem. Soc.* 151, A1641–A1652. doi: 10.1149/1.1793651

Wang, Z., Huang, X., and Chen, L. (2003). Performance improvement of surface-modified $LiCoO_2$ cathode materials: an infrared absorption and X-ray photoelectron spectroscopic investigation. *J. Electrochem. Soc.* 150, A199–A208. doi: 10.1149/1.1532326

Wickramasinghe, H. K., and Williams, C. C. (1994). Apertureless near-field optical microscope. *Appl. Phys. Lett.* 65, 1623–1625. doi: 10.1063/1.112931

William, H., Hansen, W., Boyle, D., Li, Y., and Cui, Y. (2020). Resolving nanoscopic and mesoscopic heterogeneity of fluorinated species in battery solid-electrolyte interphases by cryogenic electron microscopy. *ACS Energy Lett.* 5, 1128–1135. doi: 10.1021/acsenergylett.0c00194

Wolfenstine, J., and Allen, J. (2005). Ni^{3+}/Ni^{2+} redox potential in $LiNiPO_4$. *J. Power Sources* 142, 389–390. doi: 10.1016/j.jpowsour.2004.11.024

Würsig, A., Buqa, H., Holzapfel, M., Krumeich, F., and Novak, P. (2005). Film formation at positive electrodes in lithium-ion batteries. *Electrochem. Solid-State Lett.* 8, A34–A37. doi: 10.1149/1.1836114

Xing, L., Borodin, O., Smith, G., and Li, W. (2011). Density functional theory study of the role of anions on the oxidative decomposition reaction of propylene carbonate. *J. Phys. Chem. A* 115, 13896–13905. doi: 10.1021/jp206153n

Xu, K. (2004). Nonaqueous liquid electrolytes for lithium-based rechargeable batteries. *Chem. Rev.* 104, 4303–4418. doi: 10.1021/cr030203g

Xu, K. (2014). Electrolytes and interphases in Li-ion batteries and beyond. *Chem. Rev.* 114, 11503–11618. doi: 10.1021/cr500003w

Xu, K., Ding, S. P., and Jow, T. R. (1999). Toward reliable values of electrochemical stability limits for electrolytes. *J. Electrochem. Soc.* 146, 4172–4178. doi: 10.1149/1.1392609

Xu, W., Viswanathan, V. V., Wang, D., Towne, S. A., Xiao, J., Nie, Z., et al. (2011). Investigation on the charging process of Li_2O_2-based air electrodes in Li–O_2 batteries with organic carbonate electrolytes. *J. Power Sources* 196, 3894–3899. doi: 10.1016/j.jpowsour.2010.12.065

Yabuuchi, N., Yoshii, K., Myund, S., Nakai, L., and Komaba, S. (2011). Detailed studies of a high-capacity electrode material for rechargeable batteries, Li_2MnO_3-$LiCo_{1/3}Ni_{1/3}Mn_{1/3}O_2$. *J. Am. Chem. Soc.* 133, 4404–4419. doi: 10.1021/ja108588y

Yamada, Y., Furukawa, K., Sodeyama, K., Kikuchi, K., Yaegashi, M., Tateyama, Y., et al. (2014). Unusual stability of acetonitrile-based superconcentrated electrolytes for fast-charging lithium-ion batteries. *J. Am. Chem. Soc.* 136, 5039–5046. doi: 10.1021/ja412807w

Yamada, Y., Usui, K., Sodeyama, K., Ko, S., Tateyama, Y., and Yamada, A. (2016). Hydrate-melt electrolytes for high-energy-density aqueous batteries. *Nat. Energy* 1:16129. doi: 10.1038/nenergy.2016.129

Yamamoto, K., Minato, T., Mori, S., Takamatsu, D., Orikasa, Y., Tanida, H., et al. (2014). Improved cyclic performance of lithium-ion batteries: an investigation of cathode/electrolyte interface via *in situ* total-reflection fluorescence X-ray absorption spectroscopy. *J. Phys. Chem. C* 118, 9538–9543. doi: 10.1021/jp5011132

Yang, C., Chen, J., Qing, T., Fan, X., Sun, W., Cresce, A., et al. (2017). 4.0 V aqueous Li-ion batteries. *Joule* 1, 122–132. doi: 10.1016/j.joule.2017.08.009

Yang, Y., Davies, D. M., Yin, Y., Borodin, O., Lee, J. Z., Fang, C., et al. (2019). High-efficiency lithium-metal anode enabled by liquefied gas electrolytes. *Joule* 3, 1986–2000. doi: 10.1016/j.joule.2019.06.008

Yazami, R., and Touzain, P. (1983). A reversible graphite-lithium negative electrode for electrochemical generators. *J. Power Sources* 9, 365–371. doi: 10.1016/0378-7753(83)87040-2

Yuan, Y., Amine, K., Lu, J., and Shahbazianyassar, R. (2017). Understanding materials challenges for rechargeable ion batteries with *in situ* transmission electron microscopy. *Nat. Commun.* 8:15806. doi: 10.1038/ncomms15806

Zachman, M. J., Tu, Z., Choudhury, S., Archer, L., and Kourkoutis, L. (2018). Cryo-STEM mapping of solid–liquid interfaces and dendrites in lithium-metal batteries. *Nature* 560, 345–349. doi: 10.1038/s41586-018-0397-3

Zhang, J., Yang, X., Wang, R., Dong, W., Lu, W., Wu, X., et al. (2014). Influences of additives on the formation of a solid electrolyte interphase on MnO electrode studied by atomic force microscopy and force spectroscopy. *J. Phys. Chem. C* 118, 20756–20762. doi: 10.1021/jp503953n

Zhang, X., Pugh, J. K., and Ross, P. N. (2001). Computation of thermodynamic oxidation potentials of organic solvents using density functional theory. *J. Electrochem. Soc.* 148, E183–E188. doi: 10.1149/1.1362546

Zhang, Y., Katayama, Y., Tatara, R., Giordano, L., Yu, Y., Fraggedakis, D., et al. (2020). Revealing electrolyte oxidation via carbonate dehydrogenation on Ni-based oxides in Li-ion batteries by *in situ* fourier transform infrared spectroscopy. *Energy Environ. Sci.* 13, 183–199. doi: 10.1039/C9EE02543J

Zheng, H., Gao, J., Wang, S., and Li, H. (2013). Fundamental scientific aspects of lithium batteries (VI)–Ionic transport in solids. *Energy Storage Sci. Technol.* 2, 620–635. doi: 10.3969/j.issn.2095-4239.2013.06.010

Zhou, F., Cococcioni, M., Kang, K., and Ceder, G. (2004). The Li intercalation potential of $LiMPO_4$ and $LiMSiO_4$ olivines with M= Fe, Mn, Co, Ni. *Electrochem. Commun*. 6, 1144–1148. doi: 10.1016/j.elecom.2004.09.007

Zhou, Y., Su, M., Yu, X., Zhang, Y., Wang, J., Ren, X., et al. (2020). Real-time mass spectrometric characterization of the solid–electrolyte interphase of a lithium-ion battery. *Nat. Nanotechnol*. 15, 224–230. doi: 10.1038/s41565-019-0618-4

Zhu, Z., Zhou, Y., Yan, P., Vemuri, R. S., Xu, W., Zhao, R., et al. (2015). *In situ* mass spectrometric determination of molecular structural evolution at the solid electrolyte interphase in lithium-ion batteries. *Nano Lett*. 15, 6170–6176. doi: 10.1021/acs.nanolett.5b02479

Conflict of Interest: The authors declare that the research was conducted in the absence of any commercial or financial relationships that could be construed as a potential conflict of interest.

frontiers in Chemistry

ORIGINAL RESEARCH
published: 14 October 2020
doi: 10.3389/fchem.2020.00771

Effect of Pulse Current and Pre-annealing on Thermal Extrusion of Cu in Through-Silicon via (TSV)

Youjung Kim[1], Sanghyun Jin[2], Kimoon Park[3], Jinhyun Lee[1], Jae-Hong Lim[4] and Bongyoung Yoo[1,2,3]**

[1] Department of Materials Science and Chemical Engineering, Hanyang University, Ansan, South Korea, [2] Department of Material Engineering, Hanyang University, Ansan, South Korea, [3] Department of Advanced Material Science Engineering, Hanyang University, Ansan, South Korea, [4] Department of Materials Science and Engineering, Gachon University, Seongnam-Si, South Korea

Thermal stress induced by annealing the Cu filling of through-silicon vias (TSVs) requires further investigation as it can inhibit the performance of semiconductor devices. This study reports the filling behavior of TSVs prepared using direct current and pulse current Cu electrodeposition with and without pre-annealing. The thermal extrusion of Cu inside the TSVs was studied by observing the extrusion behavior after annealing and the changes in grain orientation using scanning electron microscopy and electron backscatter diffraction. The bottom-up filling ratio achieved by the direct current approach decreased because the current was used both to fill the TSV and to grow bump defects on the top surface of the wafer. In contrast, pulse current electrodeposition yielded an improved TSV bottom-up filling ratio and no bump defects, which is attributable to strong suppression and thin diffusion layer. Moreover, Cu deposited with a pulse current exhibited lesser thermal extrusion, which was attributed to the formation of nanotwins and a change in the grain orientation from random to (101). Based on the results, thermal extrusion of the total area of the TSVs could be obtained by pulse current electrodeposition with pre-annealing.

Keywords: through-silicon-via (TSV), pulse current, pre-annealing, thermal extrusion, seed layer

OPEN ACCESS

Edited by:
Cheng Zhong,
Tianjin University, China

Reviewed by:
Fei Qin,
Beijing University of Technology, China
Yangting Sun,
Fudan University, China
Yao Yang,
University of Alberta, Canada

****Correspondence:***
Jae-Hong Lim
limjh@gachon.ac.kr
Bongyoung Yoo
byyoo@hanyang.ac.kr

Specialty section:
This article was submitted to Electrochemistry, a section of the journal Frontiers in Chemistry

Received: *23 May 2020*
Accepted: *24 July 2020*
Published: *14 October 2020*

Citation:
Kim Y, Jin S, Park K, Lee J, Lim J-H and Yoo B (2020) Effect of Pulse Current and Pre-annealing on Thermal Extrusion of Cu in Through-Silicon via (TSV). Front. Chem. 8:771. doi: 10.3389/fchem.2020.00771

INTRODUCTION

The through-silicon via (TSV) is an important technology for connecting dies in 3D interconnects to overcome the physical and economic limitations associated with wiring and enhance the performance of semiconductor devices (Beica et al., 2008; Motoyoshi, 2009; Cao et al., 2013; Pan et al., 2018). In general, Cu with its high electrical conductivity is used to fill TSVs by deposition methods, such as chemical vapor deposition, physical vapor deposition, and electrodeposition. Among these, electrodeposition is a simple and efficient approach for the cost-effective production of void-free fillings (El-Giar et al., 2000).

After TSV filling, Cu is typically subjected to high-temperature processes such as annealing to stabilize its microstructure (Yang et al., 2011). However, annealing induces thermal stress, which can cause reliability problems such as degraded device performance in keep-out zone and thermal extrusion of Cu (De Wolf et al., 2011; Heryanto et al., 2012; Ryu et al., 2012; Guo et al., 2013). A keep-out zone, or keep-away zone, is an area where the transistor is affected by thermal stress from the mismatched coefficients of thermal

expansion between Si (2.3 ppm/°C) and Cu (16.7 ppm/°C); this stress can decrease the carrier mobility and device performance (Selvanayagam et al., 2009; De Wolf et al., 2011; Farooq et al., 2011; Heryanto et al., 2012; Ryu et al., 2012). Cu extruded from the surface of the Si wafer by annealing can destroy the insulating layer or interconnection layer. The stress distribution of a TSV affects the size and performance of the chip because the TSV is larger than the transistor (Chen et al., 2012). In addition, when a TSV, which connects chips and chips, is arranged in multiple arrays, the higher TSV density can cause greater effects from thermal stress during annealing. Therefore, as the dimensions of TSVs continue to decrease, TSV thermal stress becomes a more important issue.

Nanotwins, which can be formed with a pulse current, change the microstructure of Cu and enhance its mechanical properties (Liao et al., 2013; Seo et al., 2014). Lu et al. succeeded in forming nanotwin Cu using a pulse current with a high current density at a low temperature (Lu et al., 2004). Xu et al. formed nanotwin Cu thin films using a pulse current and measured the stress of Cu using an *in situ* measurement system; they found that the nanotwin structure formed due to stress changes induced by repeated pulse on-time and off-time cycles (Xu et al., 2007, 2009). These previous studies reported the relationship between nanotwins and enhanced mechanical properties of Cu thin films. However, there have been no studies on the properties of Cu inside TSVs fabricated by pulse current electrodeposition. In addition, Jing et al. performed a reliability assessment of Cu extrusions in TSVs with controlled annealing conditions including pre-chemical-mechanical polishing (CMP) (Jing et al., 2015). The effect of pre-CMP was also studied by De Wol et al. who showed that the pre-CMP time and temperature after sintering reduced the Cu extrusion (De Wolf et al., 2011). Jing et al. also measured silicon stress and Cu extrusion with different annealing temperatures and pre-annealing by simulation and micro-Raman microscopy (Jing et al., 2014). However, the effect of both electrodeposition conditions and the employment of a pre-annealing process on the crystal structure and mechanical process of Cu in TSVs has not yet been reported.

Chen et al. investigated the effects of small grain size on reducing extrusion and suggested higher current density, higher additive concentration, and optimized annealing temperature ramp rate could control grain size and reduce extrusion (Chen et al., 2016, 2017). The microstructure of grain size was also observed by An et al., who proposed diffusion creep rate model of TSV-Cu (An et al., 2018). The creep deformation caused Cu extrusion through the diffusion of grain boundaries. In addition, Si anisotropy and Cu plasticity on interface cracking has been found to affect extrusion (Dai et al., 2019).

High mechanical strength and electrochemical behaviors are essential characteristics for Cu in TSV to improve the performance of devices. In this study, a nanotwin structure was formed by pulse current to enhance the properties of electrodeposited Cu. In addition, the influence of plating and annealing conditions on the crystal and mechanical properties of Cu in TSVs and changes in the thermal extrusion behaviors were investigated. TSVs were filled with Cu by direct current and pulse current electrodeposition for different processing times as well as with and without pre-annealing. The mechanical properties, morphologies, and thermal extrusion behaviors were measured experimentally, and via filling mechanisms for direct and pulse current deposition were proposed.

Abbreviations: TSV, through-silicon via; EBSD, electron backscatter diffraction; pre-CMP, pre-chemical–mechanical polishing.

MATERIALS AND METHODS

The electrolytes for Cu TSV filling were prepared by dissolving 1 M $CuSO_4$ (Yakuri Pure Chemicals, 99.5%, Japan) and 1.9 mM HCl (Daejung Chemicals & Metals, 60%, Korea) in deionized water. The pH of the electrolytes was adjusted to 0.5 using H_2SO_4 (Junsei Chemical, 95%, Japan). For void-free TSV filling, 100 ppm of suppressor (CuSupH-1, Hangaram Chemistry Co., Korea) was added. All of the Cu filling experiments were conducted without agitation in a 100-mL electrochemical cell with a typical three-electrode system consisting of a Pt-coated Ti plate and Ag/AgCl electrode (Thermo Fisher Scientific, USA) as the counter and reference electrode, respectively. A via-patterned Si wafer with an aspect ratio of 12 (diameter: 5 μm, depth: 60 μm) and SiO_2/Ta barrier layer/Cu seed layer were utilized as the working electrode. The Cu TSV filling was performed with direct current and pulse current deposition at current densities of 1, 3, 5, and 10 mA/cm^2 at room temperature using a potentiostat/galvanostat (Princeton Applied Research, VersaSTAT4, AMETEK, Inc., USA) after a diffusion time of 60 s. The filling shapes of the direct current and pulse current are shown in **Figures 1A,B**. The pulse current comprised various factors, such as peak current density (i_{peak}), on-time (t_{on}), and off-time (t_{off}). The average current density (i_{avg}) of the pulse current was calculated by the following equation:

$$i_{avg} = \frac{i_{peak} \times t_{on}}{t_{on} + t_{off}}. \quad (1)$$

In our previous study, the high peak current density and short on-time of the pulse current were optimized with a high frequency of the pulse current. For pulse current deposition, the average current density was controlled by the off-time, and the peak current and on-time were fixed at 450 mA/cm^2 and 2 μs, respectively.

After the Cu filling, the samples were molded with epoxy resin and polished using a polishing machine (SSAUL BESTECH, BESTPOL P362, Korea) to analyze the filling behavior in the TSVs. The cross-sections of the Cu-filled TSVs were observed using optical microscopy (Hirox, KH-7700, Japan). In addition, the Cu films electrodeposited with both direct current and pulse current on nonpattern wafers with a Ti layer were used for tensile stress–strain testing. The Cu film of 10 μm was electrodeposited with an applied current time of 226 min. The tensile strength of the deposited Cu was measured by a universal testing machine (UTM, INSTRON, model 3343, USA).

To investigate the effects of Cu thermal extrusion in the TSV, the TSVs were fully filled and mechanically polished to expose the top surface of the via using a polishing machine. **Figure 2** shows

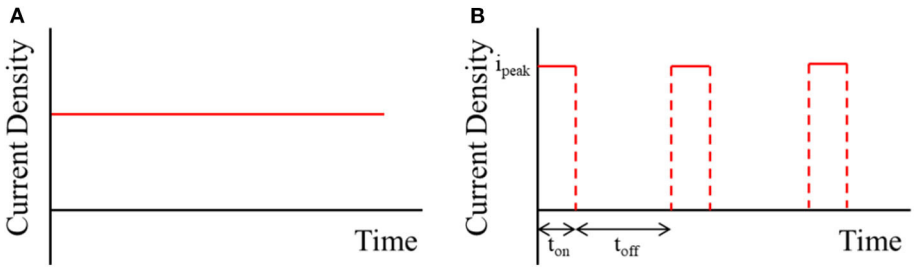

FIGURE 1 | The schematic diagram (current vs. time) of **(A)** direct current and **(B)** pulse current.

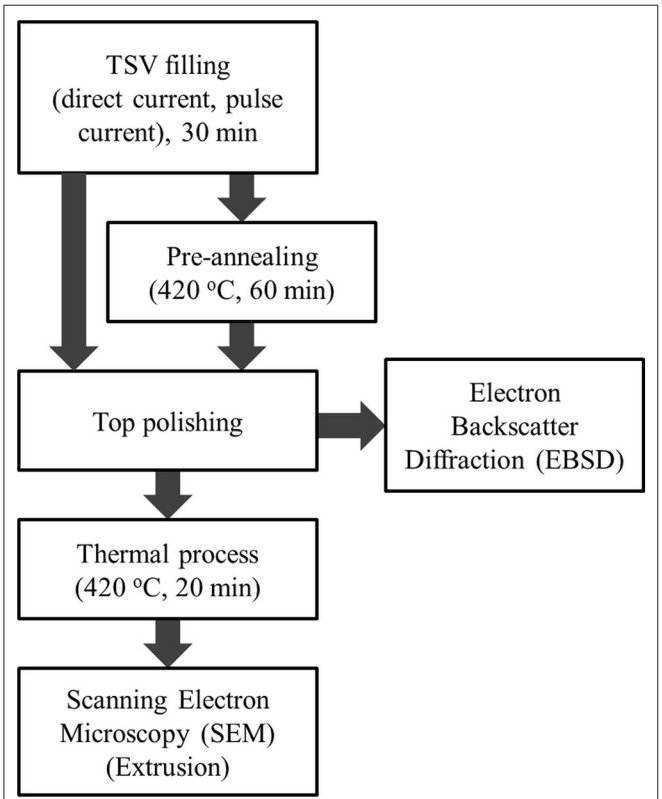

FIGURE 2 | Process flow of thermal annealing.

the experimental procedure. The prepared samples were pre-annealed and annealed at 420°C for 60 and 20 min, respectively, using rapid thermal annealing under an N_2 atmosphere after TSV filling. The ramp-up and ramp-down rate were set as 84°C/min and 7°C/min, respectively. The distributions of Cu grain orientation angles in the TSVs depending on current type (direct or pulse) and the use of pre-annealing were observed by electron backscatter diffraction (EBSD, TESCAN, MIRA3) after top polishing. Annealing was performed after top polishing under an atmosphere of 95% Ar and 5% H_2 to prevent oxidation. The thermally extruded top surfaces of the TSVs were observed by field emission scanning electron microscopy (FE-SEM, TESCAN, model MIRA3) for the selected current types (direct and pulse) and with and without pre-annealing.

RESULTS AND DISCUSSION

TSV Filling Using Pulse Current

The cross-sectional optical images of Cu-filled TSVs deposited for duration of 10 min with direct and pulse currents are shown in **Figure 3**. In pulse current electrodeposition, the on-time and frequency are critical factors for TSV filling. The effect of on-time on TSV filling was investigated in our previous study (Jin et al., 2013). In that study, on-time and frequency affected the coulombic current density and dissolution rate, and the fastest void-free bottom-up filling was achieved with an on-time of 2 μs. Therefore, for pulse current electrodeposition, the peak current density and on-time were fixed at 450 mA/cm^2 and 2 μs, respectively. The TSV filling ratio using a direct current decreased with increasing average current density because of the current lost to the additional growth of bump defects on the surface (**Supplementary Figure 1**). The filling ratio was calculated as the height of the filled Cu relative to the depth of the TSV. Electrodeposition using direct and pulse currents had the highest filling ratios without bump defects at 1 and 3 mA/cm^2, respectively (number of bump defects shown in **Supplementary Figure 1**). During direct current electrodeposition, the suppressor on the top surface of the wafer desorbed, and thus bump defects formed in the suppressor desorbed region. Bottom-up filling did not begin with 5 or 10 mA/cm^2 because many bump defects formed. In contrast, the suppressor is re-supplied during the off-time using a pulse current. Therefore, the filling ratio for pulse current electrodeposition was higher than that of direct current deposition because the top surface of the wafer was strongly suppressed and thus the current was only used for TSV filling instead of defect formation. However, the supply of suppressor in the TSV was not sufficient for deposition above an average current density of 5 mA/cm^2 due to the short off-time. In addition, the suppressor easily desorbed from the sidewall of the TSV under very high current densities using pulse current electrodeposition, resulting in a pinch-off effect at the sidewall and a void because of the much higher current density and lower suppressor concentration (Song et al., 2012; Wheeler et al., 2013; Yang et al., 2013; Wang et al., 2016, 2018; Xiao et al., 2017).

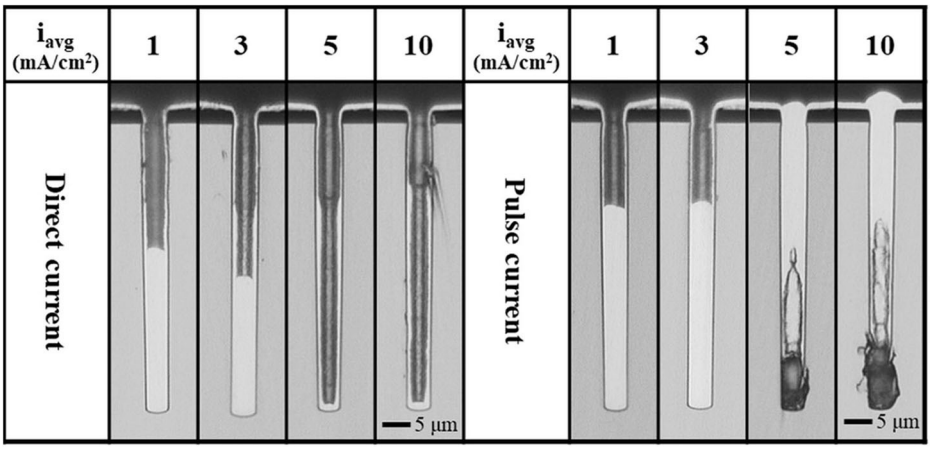

FIGURE 3 | Cross-sectional images of Cu-filled TSVs deposited by direct current and pulse current for 10 min.

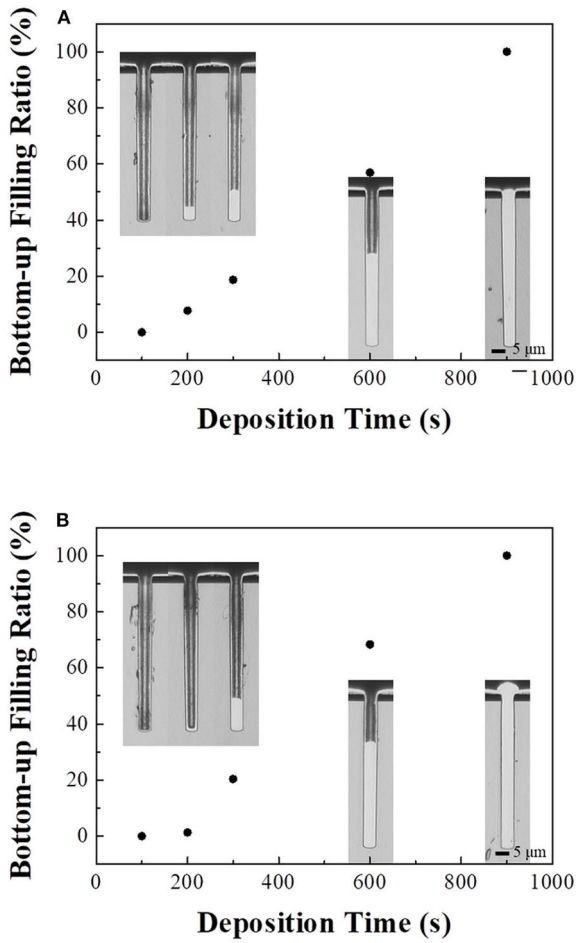

FIGURE 4 | Cross-sectional images of Cu-filled TSVs and their bottom-up filling ratios depending on deposition time. **(A)** Direct current (1 mA/cm^2), **(B)** pulse current (3 mA/cm^2).

Cross-sectional images and bottom-up filling ratios until filling completion acquired with the best defect-free conditions (1 and 3 mA/cm^2 for direct and pulse currents, respectively) for each deposition time are shown in **Figure 4**, with the results for direct current electrodeposition in **Figure 4A**. The initial filling using direct current electrodeposition reached completion in less than 200 s, and the filling ratio linearly increased because the current was effectively used for TSV filling. In addition, the linear slope of the filling ratio with respect to deposition time from the start might indicate a constant thickness of the diffusion layer of cupric ions and a sufficient ion supply. However, it may be difficult for the cupric ions to diffuse into the via for a TSV with a high-aspect ratio (Gambino et al., 2015; Lee and Chen, 2018). In addition, as shown in **Figure 4B**, the bottom-up filling ratio using pulse current electrodeposition was lower than that using a direct current at the initial stage due to re-adsorption of the suppressor during the off-time. The adsorbed suppressor could interrupt the initial bottom-up filling; the bottom-up filling then began after the breakdown of the suppressor on the bottom of the via (Wheeler et al., 2013; Yang et al., 2013). However, the slope of the pulse current filling ratio with respect to deposition time becomes linear and steeper than that of the direct current from 200 s onward, indicating a shorter diffusion layer and higher filling ratio. The diffusion layer using a pulse current was reduced because of the supply of cupric ions provided during the off-time (Chandrasekar and Pushpavanam, 2008).

The proposed TSV filling mechanisms for direct current and pulse current electrodeposition are shown in **Figure 5**. The concentrations of cupric ions and suppressor decrease gradually toward the bottom of the via before electrodeposition. **Figure 5A** shows the filling mechanism using a direct current. The suppressor at the bottom of the TSV easily desorbs by breaking down, and the TSV filling begins from the bottom when the current is initially applied. The filling ratio remains constant over time because of the sufficient diffusion of cupric ions to the

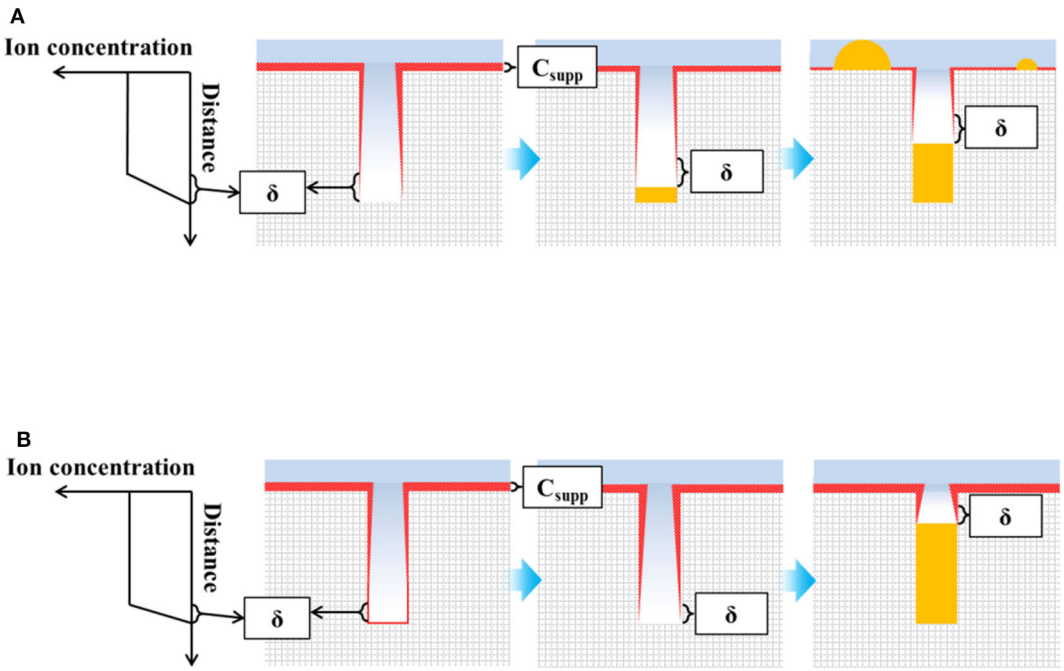

FIGURE 5 | Schematic of suppressor and ion concentration for TSV filling and filling mechanisms with a **(A)** direct current and **(B)** pulse current (δ is the diffusion layer; the thickness of C_{supp} indicates the suppressor concentration).

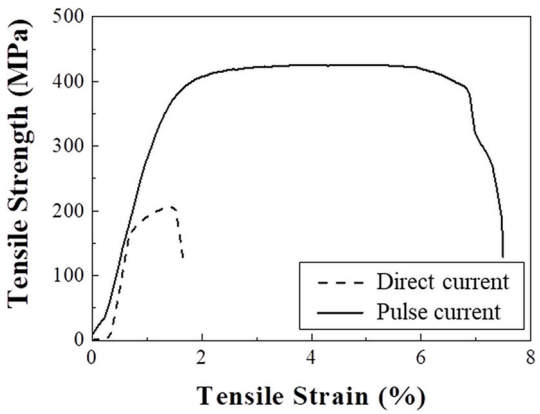

FIGURE 6 | Tensile stress–strain curves of samples electrodeposited with a direct current and a pulse current.

TSV. However, the suppressor on the wafer surface also desorbs, resulting in bump defects and thus a lower filling ratio. However, the sufficient supply of cupric ions and suppressor using pulse current electrodeposition results in a shorter diffusion layer of cupric ions and increased adsorption of the suppressor, as shown in **Figure 5B**. Therefore, bottom-up filling does not begin by adsorption of the suppressor on the via bottom. Instead, TSV filling starts after desorption of the suppressor on the bottom of the TSV with a higher filling ratio due to the short diffusion layer. In addition, unlike direct current deposition, pulse current deposition does not form bump defects on the surface because the suppressor is re-adsorbed during the off-time. In other words, the high filling ratio using pulse current deposition was attributed to the shorter diffusion layer and lack of bump defect formation.

Mechanical Properties Using Pulse Current

In addition to increasing the TSV filling ratio, pulse current deposition also forms a nanotwin structure. In our previous work, a high density of nanoscale twins was observed under pulse current conditions (Jin et al., 2013). In addition, the thermal extrusion behavior, which is related to mechanical strength, decreased with nanotwin structures. Lu et al. similarly concluded that nanotwins could increase mechanical strength (Lu et al., 2004). Therefore, stress–strain curves were measured to investigate the mechanical strength of Cu plated with direct and pulse currents. **Figure 6** shows the stress–strain curves of samples electrodeposited with a direct current and a pulse current with an. Stress–strain curves consist of elastic and plastic regions (Sharir et al., 2008). In the elastic region, which has a linear slope before the yield strength, only elastic (reversible) deformation occurs, whereas non-reversible (permanent) deformation begins to occur in the plastic region located between the yield strength and fracture point. Therefore, the yield strength can indicate the maximum allowable strength before plastic deformation occurs (Yonenaga, 2005). The 0.2% offset strength, which is defined as the stress that results in a strain of 0.2%, was measured for engineering evaluation instead of yield strength (Albrecht et al., 2017). The Cu formed by a direct current had a 0.2% offset strength of 186 MPa, which resulted in plastic deformation at a low strain energy, while the Cu formed by a pulse current had a higher 0.2% offset strength of 372 MPa, allowing it to deform elastically without plastic deformation

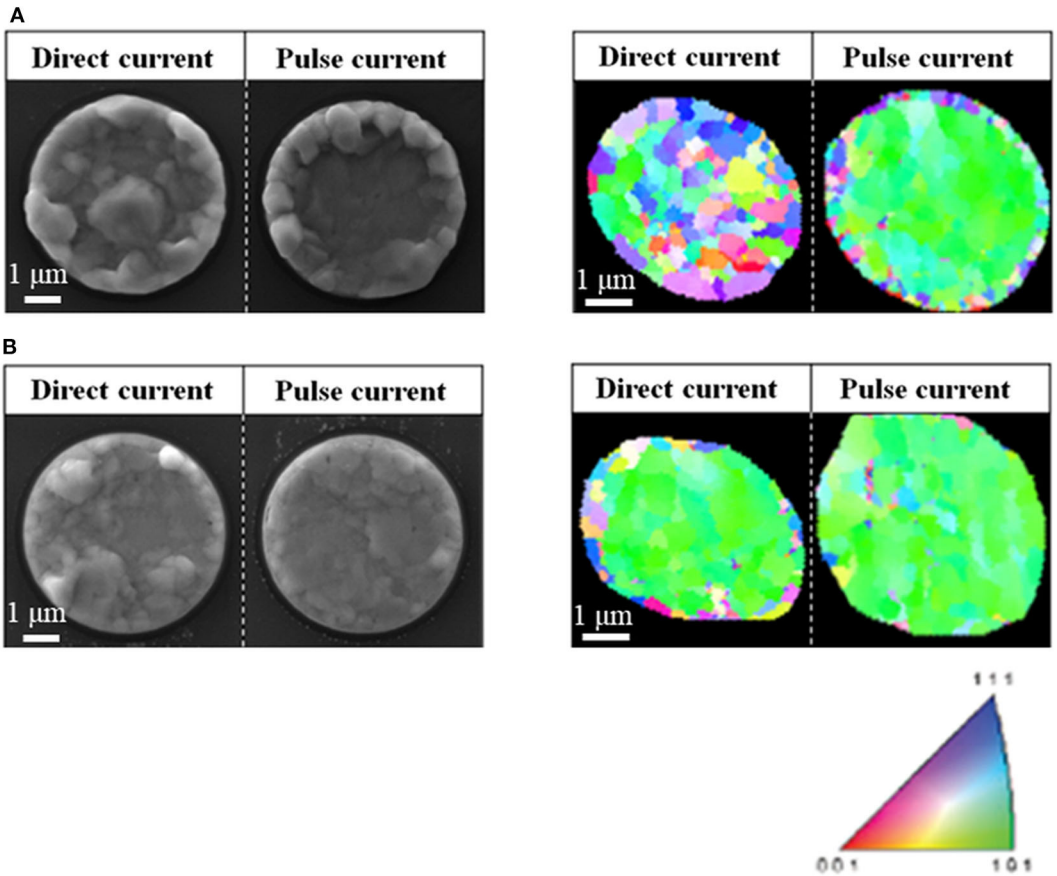

FIGURE 7 | Thermal extrusion behaviors and grain orientations (EBSD analysis) of TSVs depending on current type (direct current 1 mA/cm^2, pulse current 3 mA/cm^2) **(A)** before and **(B)** after pre-annealing.

at a higher strain energy. The higher offset strength was due to the nanotwin boundaries interrupting the migration of dislocations (Lu et al., 2004; Jin et al., 2013). Grain boundaries also block the migration of electrons, resulting in a high electrical resistance. However, nanotwin boundaries block the migration of dislocations without disturbing the transport of electrons. Therefore, the twin boundaries formed by a pulse current can increase the mechanical strength of Cu without sacrificing electrical conductivity.

Thermal Extrusion of TSV Using Pulse Current and Pre-annealing

The thermal extrusion behaviors and EBSD analysis of TSVs prepared with direct current and pulse current plating are illustrated in **Figure 7A**. The thermal extrusion behavior was observed after annealing at 420°C for 20 min in an N_2 gas atmosphere. The Cu electrodeposited using direct current inside the TSV was severely expanded after annealing, which is attributed to plastic deformation from thermal stress exceeding the yield strength (Heryanto et al., 2012). In contrast, thermal extrusion occurred to a lesser extent in the Cu deposited with a pulse current, which is attributed to the Cu nanotwins allowing only for elastic deformation during annealing. However, the Cu at the edge of the TSV severely expanded even with the use of a pulse current. The proportion of the extruded area among the total TSV area for each direct current and pulse current condition was 71.9 and 47.7%, respectively. EBSD analysis was used to investigate the grain orientation before thermal extrusion. The Cu plated with a direct current had a random orientation, resulting in thermal extrusion throughout, whereas the Cu plated with a pulse current had a (101) orientation except at the TSV edge, resulting in more thermal extrusion at the edge. Thermal extrusion seems to be affected by not only nanotwins but also preferred orientation. The random crystal orientation at the edge might be attributable to the Cu seed layer formed by physical vapor deposition. Thus, further methods such as an additional annealing process are necessary to improve the crystal orientation and minimize thermal extrusion. The thermal extrusion behaviors and EBSD analysis of TSVs prepared with a direct current and pulse current after an additional pre-annealing treatment are shown in **Figure 7B**. Pre-annealing was carried out at 420°C for 60 min in an N_2 gas atmosphere. After pre-annealing, the proportion of the extruded area among the total TSV decreased from 71.9 to 47.0% under the direct current condition and from 47.7 to 23.7% under the pulse current condition. The pre-annealing also changed the grain orientation at the center of the Cu plated by a direct current to the (101) orientation and grain orientation at the edge of the Cu plated by

a pulse current to the (101) orientation as determined by EBSD. **Supplementary Figure 2** shows that the dominant preferred orientation of both the direct current and pulse current Cu samples was further improved toward the (101) orientation after pre-annealing. Therefore, it is important to note that controlling the density of nanotwin boundaries and the grain orientation could improve the mechanical properties of TSVs and reduce the extent of thermal extrusion.

CONCLUSIONS

The filling behaviors and thermal extrusion of the high-aspect ratio Cu in TSV using pulse current with pre-annealing were much improved. In summary, The pulse current plating formed less bump defect on the surface, which indicates low current loss high filling efficiency than direct current one because the cupric ion and suppressor were supplied during off-time. In addition, mechanical properties of Cu electrodeposited using pulse current were improved. The tensile strength of Cu electrodeposited with pulse current was 425 MPa, which was higher than one of direct current (206 MPa). The higher tensile strength and more (101) preferred orientation of Cu using pulse current much reduced thermal extrusion.

DATA AVAILABILITY STATEMENT

The original contributions presented in the study are included in the article/**Supplementary Material**, further inquiries can be directed to the corresponding author/s.

AUTHOR CONTRIBUTIONS

The concept for this study was designed by BY, SJ, and J-HL. BY and SJ designed the experiment. YK, SJ, and JL performed experiments on electrodeposition and KP helped in stress test. SJ and YK performed experiments on EBSD and analyzed EBSD data. All authors helped to write the manuscript.

FUNDING

This study was supported by the MOTIE (Ministry of Trade, Industry, & Energy (Grant No. 10067804) and KSRC (Korea Semiconductor Research Consortium) support program for the development of the future semiconductor device, Basic Science Research Program (Grant No. 2015R1A5A1037548) and the Global Frontier Hybrid Interface Materials (GFHIM) project (Grant No. 2013M3A6B1078870) through the National Research Foundation of Korea (NRF) funded by the Ministry of Science, ICT & Future Planning and the Technology Innovation Program (20005011, Development of Materials and Process Technology for highly luminance micro display with 2000 PPI resolution) funded by the Ministry of Trade, Industry, & Energy (MOTIE, Korea).

SUPPLEMENTARY MATERIAL

The Supplementary Material for this article can be found online at: https://www.frontiersin.org/articles/10.3389/fchem.2020.00771/full#supplementary-material

REFERENCES

Albrecht, J., Weissbach, M., Auersperg, J., and Rzepka, S. (2017). "Method for assessing the delamination risk in BEoL stacks around copper TSV applying nanoindentation and finite element simulation," in *2017 IEEE 19th Electronics Packaging Technology Conference (EPTC)* (Singapore: IEEE), 1–6.

An, T., Qin, F., Chen, S., and Chen, P. (2018). The effect of the diffusion creep behavior on the TSV-Cu protrusion morphology during annealing. *J. Mater. Sci. Mater Electron.* 29, 16305–16316. doi: 10.1007/s10854-018-9720-x

Beica, R., Sharbono, C., and Ritzdorf, T. (2008). "Through silicon via copper electrodeposition for 3D integration," in *2008 58th Electronic Components and Technology Conference* (Lake Buena Vista, FL), 577–583.

Cao, H., Hang, T., Ling, H., and Li, M. (2013). Behaviors of chloride ions in methanesulfonic acid bath for copper electrodeposition of through-silicon-via. *J. Electrochem. Soc.* 160, D146–D149. doi: 10.1149/2.052304jes

Chandrasekar, M. S., and Pushpavanam, M. (2008). Pulse and pulse reverse plating—conceptual, advantages and applications. *Electrochim. Acta* 53, 3313–3322. doi: 10.1016/j.electacta.2007.11.054

Chen, S., An, T., Qin, F., and Chen, P. (2017). Microstructure evolution and protrusion of electroplated Cu-filled through-silicon vias subjected to thermal cyclic loading. *J. Electron. Mater.* 46, 5916–5932. doi: 10.1007/s11664-017-5577-7

Chen, S., Qin, F., An, T., Chen, P., Xie, B., and Shi, X. (2016). Protrusion of electroplated copper filled in through silicon vias during annealing process. *Microelectron. Reliab.* 63, 183–193. doi: 10.1016/j.microrel.2016.04.005

Chen, S., Thijs, S., Linten, D., Scholz, M., Hellings, G., and Groeseneken, G. (2012). "ESD protection devices placed inside keep-out zone (KOZ) of through silicon via (TSV) in 3D stacked integrated circuits," in *Electrical Overstress/Electrostatic Discharge Symposium Proceedings 2012*, (Tucson, AZ), 1–8.

Dai, Y., Zhang, M., Qin, F., Chen, P., and An, T. (2019). Effect of silicon anisotropy on interfacial fracture for three dimensional through-silicon-via (TSV) under thermal loading. *Eng. Fract. Mech.* 209, 274–300. doi: 10.1016/j.engfracmech.2019.01.030

De Wolf, I., Croes, K., Varela Pedreira, O., Labie, R., Redolfi, A., Van De Peer, M., et al. (2011). Cu pumping in TSVs: effect of pre-CMP thermal budget. *Microelectron. Reliab.* 51, 1856–1859. doi: 10.1016/j.microrel.2011.06.003

El-Giar, E. M., Said, R. A., Bridges, G. E., and Thomson, D. J. (2000). Localized electrochemical deposition of copper microstructures. *J. Electrochem. Soc.* 147:586. doi: 10.1149/1.1393237

Farooq, M. G., Graves-Abe, T. L., Landers, W. F., Kothandaraman, C., Himmel, B. A., Andry, P. S., et al. (2011). "3D copper TSV integration, testing and reliability," in *2011 International Electron Devices Meeting* (Washington, DC: IEEE).

Gambino, J. P., Adderly, S. A., and Knickerbocker, J. U. (2015). An overview of through-silicon-via technology and manufacturing challenges. *Microelectron. Eng.* 135, 73–106. doi: 10.1016/j.mee.2014.10.019

Guo, W., Moroz, V., Van der Plas, G., Choi, M., Redolfi, A., Smith, L., et al. (2013). "Copper through silicon via induced keep out zone for 10nm node bulk FinFET CMOS technology," in *2013 IEEE International Electron Devices Meeting* (Washington, DC: IEEE).

Heryanto, A., Putra, W. N., Trigg, A., Gao, S., Kwon, W. S., Che, F. X., et al. (2012). Effect of copper TSV annealing on via protrusion for TSV wafer fabrication. *J. Electron. Mater.* 41, 2533–2542. doi: 10.1007/s11664-012-2117-3

Jin, S., Wang, G., and Yoo, B. (2013). Through-silicon-via (TSV) filling by electrodeposition of Cu with pulse current at ultra-short duty cycle. *J. Electrochem. Soc.* 160, D3300–D3305. doi: 10.1149/2.050312jes

Jing, X., He, H., Ji, L., Xu, C., Xue, K., Su, M., et al. (2014). "Effect of thermal annealing on TSV Cu protrusion and local stress," in *2014 IEEE 64th Electronic Components and Technology Conference (ECTC)* (Lake Buena Vista, FL: IEEE), 1116–1121.

Jing, X., Lee, U., Xu, C., Niu, Z., Hao, H., Bae, J., et al. (2015). "Effect of pre-CMP annealing on TSV pumping in thermal budget and reliability test," in *2015 IEEE 22nd International Symposium on the Physical and Failure Analysis of Integrated Circuits* (Hsinchu: IEEE), 45–47.

Lee, H., and Chen, C.-M. (2018). Impurity effects in electroplated-copper solder joints. *Metals* 8:388. doi: 10.3390/met8060388

Liao, C.-N., Lu, Y.-C., and Xu, D. (2013). Modulation of crystallographic texture and twinning structure of Cu nanowires by electrodeposition. *J. Electrochem. Soc*. 160, D207–D211. doi: 10.1149/2.046306jes

Lu, L., Shen, Y., Chen, X., Qian, L., and Lu, K. (2004). Ultrahigh strength and high electrical conductivity in copper. *Science*. 304, 422–426. doi: 10.1126/science.1092905

Motoyoshi, M. (2009). Through-silicon via (TSV). *P. IEEE* 97, 43–48. doi: 10.1109/JPROC.2008.2007462

Pan, H., Zhang, Y., Li, M., and Gao, L. (2018). "Effect of pretreatment on copper filling of high aspect ratio through-silicon via (TSV)," in *2018 19th International Conference on Electronic Packaging Technology (ICEPT)* (Shanghai: IEEE), 672–675. doi: 10.1109/ICEPT.2018.8480652

Ryu, S., Lu, K., Jiang, T., Im, J., Huang, R., and Ho, P.S. (2012). Effect of thermal stresses on carrier mobility and keep-out zone around through-silicon vias for 3-D integration. *IEEE Trans. Device and Mater. Reliab.* 12, 255–262. doi: 10.1109/TDMR.2012.2194784

Selvanayagam, C. S., Lau, J. H., Zhang, X., Seah, S. K. W., Vaidyanathan, K., and Chai, T. C. (2009). Nonlinear thermal stress/strain analyses of copper filled TSV (through silicon via) and their flip-chip microbumps. *IEEE Trans. Adv. Packag.* 32, 720–728. doi: 10.1109/TADVP.2009.2021661

Seo, S., Jin, S., Wang, G., and Yoo, B. (2014). The effect of copper dissolution in acidic electrolyte on the formation of nanotwin in pulse electrodeposited copper. *J. Electrochem. Soc*. 161, D425–D428. doi: 10.1149/2.032140 9jes

Sharir, A., Barak, M. M., and Shahar, R. (2008). Whole bone mechanics and mechanical testing. *Vet. J.* 177, 8–17. doi: 10.1016/j.tvjl.2007.09.012

Song, C., Wu, H., Jing, X., Dai, F., Yu, D., and Wan, L. (2012). "Numerical simulation and experimental verification of copper plating with different additives for through silicon vias," in *2012 4th Electronic System-Integration Technology Conference* (IEEE), 1–6. doi: 10.1109/ESTC.2012.65 42054

Wang, F., Zhao, Z., Nie, N., Wang, F., and Zhu, W. (2018). Effect of via depth on the TSV filling process for different current densities. *J. Micromech. Microeng.* 28:045004. doi: 10.1088/1361-6439/aaaa40

Wang, Y., Zhu, W., Li, X., and Wang, F. (2016). Parameters analysis of TSV filling models of distinct chemical behaviours of additives. *Electrochim. Acta* 221, 70–79. doi: 10.1016/j.electacta.2016.09.144

Wheeler, D., Moffat, T. P., and Josell, D. (2013). Spatial-temporal modeling of extreme bottom-up filling of through-silicon-vias. *J. Electrochem. Soc*. 160, D3260–D3265. doi: 10.1149/2.040312jes

Xiao, H., He, H., Ren, X., Zeng, P., and Wang, F. (2017). Numerical modeling and experimental verification of copper electrodeposition for through silicon via (TSV) with additives. *Microelectron. Eng.* 170, 54–58. doi: 10.1016/j.mee.2016.12.030

Xu, D., Kwan, W. L., Chen, K., Zhang, X., Ozolinš, V., and Tu, K. N. (2007). Nanotwin formation in copper thin films by stress/strain relaxation in pulse electrodeposition. *Appl. Phys. Lett*. 91:254105. doi: 10.1063/1.2825412

Xu, D., Sriram, V., Ozolins, V., Yang, J.-M., Tu, K. N., Stafford, G. R., et al. (2009). In situ measurements of stress evolution for nanotwin formation during pulse electrodeposition of copper. *J. Appl. Phys*. 105:023521. doi: 10.1063/1.3068191

Yang, C. C., Witt, C., Wang, P. C., Edelstein, D., and Rosenberg, R. (2011). Stress control during thermal annealing of copper interconnects. *Appl. Phys. Lett*. 98:051911. doi: 10.1063/1.3551627

Yang, L., Radisic, A., Deconinck, J., and Vereecken, P. M. (2013). Modeling the bottom-up filling of through-silicon vias through suppressor adsorption/desorption mechanism. *J. Electrochem. Soc*. 160, D3051–D3056. doi: 10.1149/2.010312jes

Yonenaga, I. (2005). Hardness, yield strength, and dislocation velocity in elemental and compound semiconductors. *Mater. Trans.* 46, 1979–1985. doi: 10.2320/matertrans.46.1979

Conflict of Interest: The authors declare that the research was conducted in the absence of any commercial or financial relationships that could be construed as a potential conflict of interest.

frontiers in Chemistry

ORIGINAL RESEARCH
published: 08 December 2020
doi: 10.3389/fchem.2020.581653

Template-Sacrificing Synthesis of Ni-Co Layered Double Hydroxides Polyhedron as Advanced Anode for Lithium Ions Battery

Youjun Lu[1]*, *Yingjie Du*[2] and *Haibo Li*[2]*

[1] School of Materials Science and Engineering, North Minzu University, Yinchuan, China, [2] Ningxia Key Laboratory of Photovoltaic Materials, Ningxia University, Yinchuan, China

The novel hollowed Ni-Co layered double hydroxide polyhedron (H-(Ni, Co)-LDHP) is synthesized via a template-sacrificing approach using ZIF-67 as template. The morphology, crystallinity, porous texture, and chemical state of H-(Ni, Co)-LDHP are examined. It demonstrates that the H-(Ni, Co)-LDHP not only provides rich redox sites but also promotes the kinetics due to presence of numerous rational channels. As a result, the H-(Ni, Co)-LDHP manifests the desirable lithium ions storage performance when employed as anode. This study paves a new way for preparing hollowed nanostructure toward advanced electrochemical applications.

Keywords: energy storage, layered double hydroxides, polyhedron, electrochemistry, anode

OPEN ACCESS

Edited by:
Cheng Zhong,
Tianjin University, China

Reviewed by:
Kangning Zhao,
École Polytechnique Fédérale de Lausanne, Switzerland
Xifei Li,
Xi'an University of Technology, China

***Correspondence:**
Youjun Lu
youjunlu518@hotmail.com
Haibo Li
lihaibo@nxu.edu.cn

Specialty section:
This article was submitted to Electrochemistry, a section of the journal Frontiers in Chemistry

Received: *10 July 2020*
Accepted: *30 October 2020*
Published: *08 December 2020*

Citation:
Lu Y, Du Y and Li H (2020) Template-Sacrificing Synthesis of Ni-Co Layered Double Hydroxides Polyhedron as Advanced Anode for Lithium Ions Battery. Front. Chem. 8:581653. doi: 10.3389/fchem.2020.581653

INTRODUCTION

Currently, the environmental tolerance is priority to the development of new energy storage devices which are of great significance to our daily life (He et al., 2018). Among all candidates, lithium ion batteries (LIBs) are considered to be the suitable one due to many advantages such as high energy density, high specific capacity, and long lifetime (Li et al., 2019).

Layered double hydroxides (LDHs) are hydrotalcite-like compounds. The general formula of LDH can be expressed as $[M^{2+}_{1-x}M^{3+}_{x}(OH)_2]\ [A^{n-}]_{x/n}\cdot zH_2O$ (Chen et al., 2013) where M^{2+} generally indicates the Mg^{2+}, Zn^{2+}, Ni^{2+}, and Cu^{2+}, and M^{3+} represents the Al^{3+}, Ga^{3+}, Fe^{3+}, and Mn^{3+}. Moreover, the LDH often exhibits the laminated structure which is composed of exchangeable interlayer anions and positively charged host layers (Wang and O'Hare, 2012). In the past few years, the LDHs have been widely applied in many fields, such as catalysis, photoelectricity, and bioengineering (Zand et al., 2019). Owing to the presence of abundant active sites and layered structure, the expected redox reaction incorporated short diffusion lengths of ions and electrons are affiliated with LDH, making it a potential anode for LIBs. However, the poor conductivity and serious aggregation of LDH nanosheets restricts its lithium storage performance (Xuan et al., 2019). Based on many cases, one of the effective strategies is to modify LDHs with rational carbon materials coatings enabling the improved conductivity and expected electrochemical properties, such as aerogel, graphene nanosheets, and carbon nanotubes (Gao et al., 2011; Yang et al., 2013; Song et al., 2017).

Metal organic frameworks (MOFs) representing a class of unique 3D carbon materials are synthesized via linking metal ions with organic molecules. As a result, the MOFs have superior advantages of well-defined porosity, controllable particle size, and tunable electronic structure. Most significantly, MOF have been extensively proposed and developed as sacrificing template for

the synthesis of LDH@C nanocomposites for electrochemical applications since it is able to derive the desirable transition metal oxides and sufficient specific surface area (Furukawa et al., 2013; Gao et al., 2019).

In this work, we developed a facile strategy to prepare hollowed Ni-Co layered double hydroxide polyhedron [H-(Ni, Co)-LDHP]. The typical ZIF-67 was synthesized initially and then employed as sacrificing template and Co source to couple with nickel ions, forming polyhedron-like Ni-Co LDH with hollowed nanostructure. The hollowed structures have shown significant advantages of huge specific surface area and excellent mass permeability enabling to create plenty of active sites and promote charge transfer during the charge/discharge process and further enhance the electrochemical performance. The structure, crystallinity, porous texture, and chemical state are examined using transmission electron microscopy (TEM), high-resolution TEM (HRTEM), X-ray diffraction (XRD), nitrogen adsorption-desorption, and X-ray photoelectron spectrum (XPS). Moreover, the electrochemical performances of H-(Ni, Co)-LDHP have been explored by applying H-(Ni, Co)-LDHP as anode for LIBs.

EXPERIMENTAL

Preparation of H-(Ni, Co)-LDHP

Firstly, 30 mmol of $Co(NO_3)_26H_2O$ and 120 mmol of dimethylimidazole were dissolved in 400 ml mixed solution consisting of methanol and absolute ethanol in a volume ratio of 1:1. After stirring for 5 min, the mixed solution was placed for 24 h, and then the purple precipitates which are ZIF-67 nanoparticles were collected. Subsequently, 120 mg of ZIF-67 powders and 400 mg $Ni(NO_3)_26H_2O$ were dissolved in 100 ml absolute ethanol, which was then subjected to ultrasonic bath for 90 min. The ultrasonic power was 120 W. Finally, the green H-(Ni, Co)-LDHP powders were obtained via centrifugation and washed three times using absolute ethanol.

Electrochemical Tests

The cyclic voltammetry (CV) curves and electrochemical impedance spectroscopy (EIS) within the frequency range from 0.1 to 10 000 Hz were carried out on electrochemical workstation (Princeton PARSTAT 3000-DX, USA). The galvanostatic charging/discharging curves (GCD) were measured on Land battery test system (CT2001A, China). All tests were performed under a CR2032 coins-type cell which was assembled in a glove box filled with argon gas. Regarding the cell, the lithium metal foil and Celgard membrane were employed as counter electrode and separator, respectively. The active materials, acetylene carbon black and polyvinylidene fluoride (PVDF), were dissolved in N-methylpyrrolidinone (NMP) in a mass ratio of 8:1:1 to fabricate electrode, and the average mass loading of anode is 10 mg. Besides, 1 M $LiPF_6$ in ethylene carbonate (EC), propylene carbonate (PC), and Dimethyl Carbonate (DEC) (1:1:1 V/V/V) was employed as the electrolyte. In general, the volume of electrolyte is set as 1.2 ml.

RESULTS AND DISCUSSION

Figures 1a,b show the scanning electron microscope (SEM, Hitachi SU5000, Japan) and transmission electron microscopy (TEM, Hitachi HT7700, Japan) images of H-(Ni, Co)-LDHP, respectively. Through employing ZIF-67 as sacrificing template, the irregular Ni-Co LDH hollow polyhedral nanocages were obtained. Roughly, the average geometrical size of H-(Ni, Co)-LDHP is 500 nm. Beyond that, the fine structure of H-(Ni, Co)-LDHP is explored by high-resolution TEM (HRTEM, FEI TalosF200s, USA). In **Figure 1c**, the H-(Ni, Co)-LDHP is assembled by a large number of nanosheets. It is proposed that the multistage structure is beneficial to increase the specific surface area (SSA) and expose as much as active cites for the diffusion of electrolyte ions, which promote the reaction kinetics and thus contribute to high LIBs' performance. Further, the distinct lattice fringe spacing of 0.26 nm corresponding to the (009) crystal plane of NiCo-LDHs is verified from the inset of **Figure 1c**, indicating the good crystallinity of LDHs. **Figure 1d** is the combined elemental mapping image of H-(Ni, Co)-LDHP, suggesting the even distribution of C, Co, Ni, and O. According to the respective atomic fraction of C, Co, and Ni, the content of carbon is thereby obtained as 3.45%. Further, the element mapping reveals that LDH nanosheets uniformly disperse on ZIF-67, suggesting that the ZIF-67 as sacrificing template effectively inhibits the agglomeration of LDH and improves the specific surface area. The mechanism of MOF-derived hollow structure can be briefly stated as follows: ion exchange initiates the interchange of cation/anions during the synthesis of MOF-directed hollowed structures. When excess $Ni(NO_3)_2$ and ZIF-67 are dissolved in absolute ethanol, the hydrolysis of Ni^{2+} ions would etch the surface of ZIF-67. Meanwhile, Co^{2+} released from ZIF-67 is partially oxidized by O_2 and NO^{3-} ions (Hu et al., 2015; Xu et al., 2018b). Afterwards, the Co^{2+} and Ni^{2+} consume large amount of hydroxide ions to co-precipitate around the ZIF-67 polyhedron forming an LDH layer. Besides, the continuous ultrasonic vibration and outflow of Co^{2+} ions empty ZIF-67 polyhedron, leading to the formation of hollowed Ni-Co layered double hydroxide polyhedron.

Figure 2A exhibits the X-ray diffraction (XRD, Rigaku Smart Lab, Japan) pattern of H-(Ni, Co)-LDHP and ZIF-67 precursor. The XRD pattern of ZIF-67 corresponds to previous report very well (Kong et al., 2018). Regarding H-(Ni, Co)-LDHP, the peaks located at 11.6, 23.8, 33.7, and 60.4° are ascribed to (003), (006), (009), and (110) crystal plane of hydrotalcite-like NiCo-LDH (Jiang et al., 2013). **Figure 2B** illustrates the Fourier transform infrared spectroscopy spectrum (FTIR PerkinElmer S2, USA) of H-(Ni, Co)-LDHP. The broad band emerging at 3,450 cm^{-1} is associated to O-H stretching mode of hydrogen-bonded hydroxyl, and the unimpressive bands presenting at 1,636 and 2,970 m^{-1} are assigned to the water molecules in the interlayer and adsorbed on the sample (Hu et al., 2019). Further, the intense band focusing at 1,386 cm^{-1} is ascribed to the N-O vibration mode of NO^{3-} (Xu et al., 2018a). Besides, the successive band in the low wavenumber ranging from 500 to 1,000 cm^{-1} are identified as the stretching vibrations of M-O-H (M represents Ni or Co) (Tang et al., 2015). The component

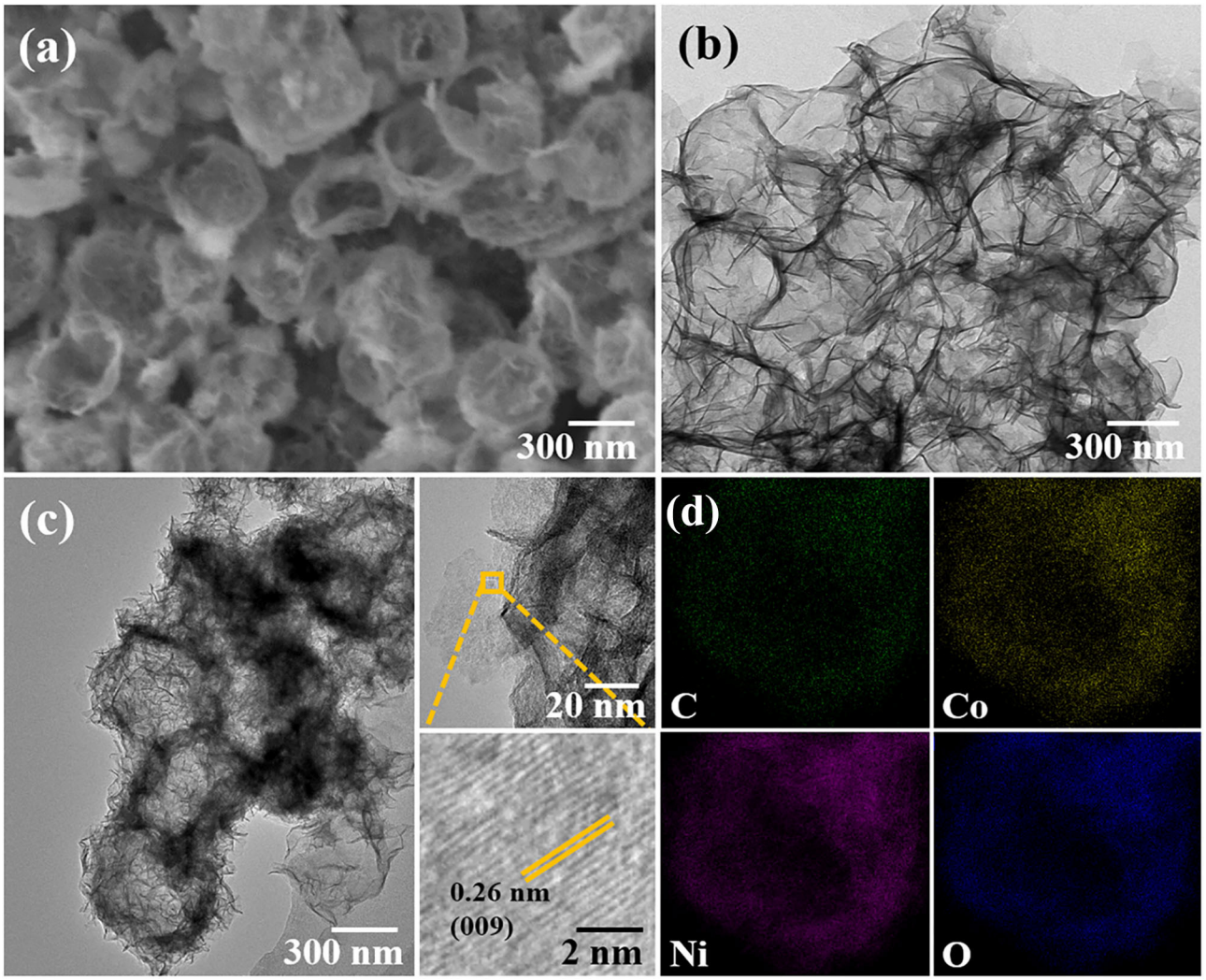

FIGURE 1 | SEM **(a)** and TEM **(b)** image of H-(Ni, Co)-LDHP, **(c)** HRTEM images, and **(d)** element mapping image of H-(Ni, Co)-LDHP.

elements and chemical states of H-(Ni, Co)-LDHP were detected by X-ray photoelectron spectrum (XPS, Thermo Fischer DXR, USA). The full XPS survey spectrum shown in **Figure 2C** verifies the existence of C, N, O, Co, and Ni. **Figure 2D** draws the Ni 2p spectrum of H-(Ni, Co)-LDHP. Two dominant peaks showing at 855.8 and 873.5 eV with spin-energy separation of 17.7 eV indicate the presence of Ni^{2+}, together with two satellite peaks located at 861 and 879.7 eV, respectively (Lee et al., 2018). In terms of the high-resolution spectra of Co 2p (**Figure 2E**), two peaks emerging at 781.2 and 796.5 eV are resulted from Co^{3+}, while the binding energy corresponds to 783 and 798.2 eV conforming the appearance of Co^{2+} (Su et al., 2019). The pore texture and SSA of sample were investigated by nitrogen adsorption-desorption system (JW-BK200, CHN). As implied in **Figure 2F**, it manifests distinct hysteresis loop which signifies the imbalance of adsorption-desorption process due to the hollow structure of H-(Ni, Co)-LDHP. Note that the SSA of H-(Ni, Co)-LDHP is 60.65 m^2/g which is superior to traditional NiCo-LDHs nanosheets in previous reports, originating from the unique nanostructure (Qian et al., 2019). Meanwhile, the pore size distribution curve extracted from the inset of **Figure 2F** demonstrates that the dominant pore size is 3 nm, which is favorable for penetrating Li^+, resulting in high kinetics.

Figure 3A shows the first, second, and third GCD profiles of H-(Ni, Co)-LDHP anode at current density of 100 mA/g. In the first circle, the initial discharge capacity is 928.3 mAh/g, and the reversible charge capacity is 630.8 mAh/g, illustrating that the coulumbic efficiency (CE) is 68%. The inferior CE can be attributed to the formation of steady solid electrolyte interphase (SEI) film. The obvious discharge plateau appears from 0.6 to 1.2 V which is in accordance with the characteristic peaks from CV curves. The cyclic performance and CE are exhibited in **Figure 3B**. As it is shown, the discharge capacity

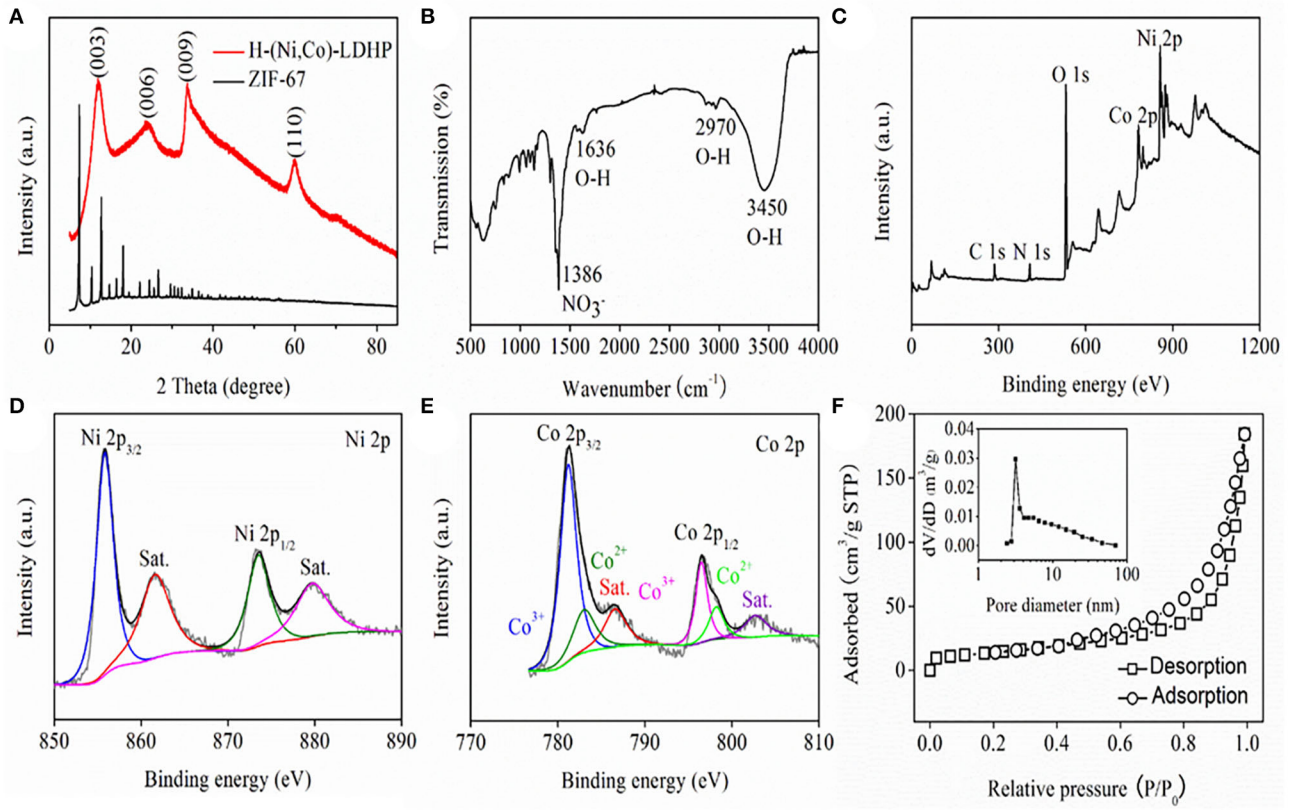

FIGURE 2 | (A) XRD pattern, **(B)** FTIR spectrum, **(C)** XPS survey spectrum, **(D)** high-resolution Ni 2p spectrum, **(E)** high-resolution Co 2p spectrum, and **(F)** Nitrogen adsorption-desorption isotherm and pore size distribution curve of H-(Ni, Co)-LDHP.

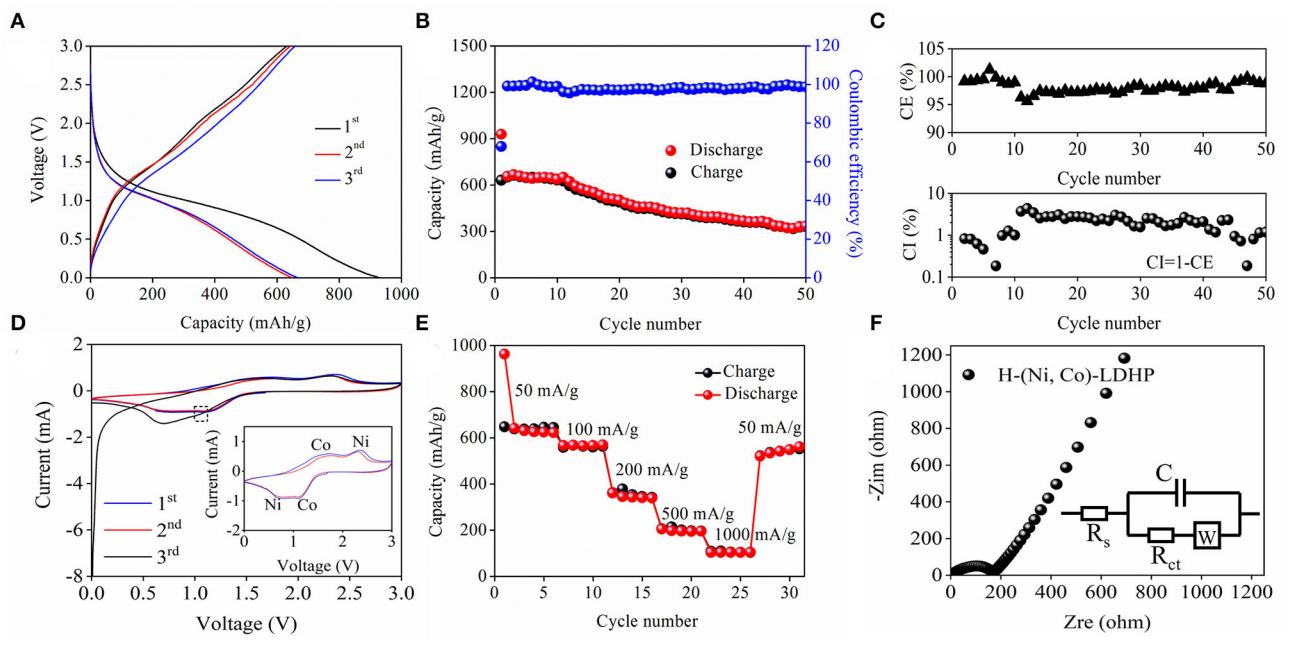

FIGURE 3 | (A) GCD curves of H-(Ni, Co)-LDHP at current density of 100 mA/g, **(B)** cycling performance and Columbic efficiency, **(C)** enlarged Columbic efficiency curve, **(D)** CV curves, **(E)** rate capability, and **(F)** Nyquist plots of the H-(Ni, Co)-LDHP.

decreased from 928.3 to 335.4 mAh/g after 50 cycles at current density of 100 mA/g, suggesting 36.1% capacitance retention. In terms of the CE, the initial value increased from 68 to 98% after subsequent cycle and then became stable. Besides the SEI film, the unexpected CE should be ascribed to the crack of H-(Ni, Co)-LDHP associated with the porous hollowed microstructure and low carbon content. Furthermore, there is obvious downtrend in CE after undergoing several times cycles in **Figure 3C**. Actually, the frequently insertion and de-insertion of Li^+ damages the nanoarchitecture of H-(Ni, Co)-LDHP, leading to serious collapse. As a result, the fresh SEI is generated on the surface of cracked H-(Ni, Co)-LDHP, which continuously consumes electrolyte and transferable Li^+, causing the fact that the CE only maintains at 98%. On the other hand, the coulombic inefficiency (CI) is equal to 1-CE, which is helpful to evaluate the lithiation reversibility of H-(Ni, Co)-LDHP. In **Figure 3C**, the fluctuant CI curve again verifies the formation of unstable SEI layer and continuous capacity attenuation of H-(Ni, Co)-LDHP anode. **Figure 3D** draws the CV curves of H-(Ni, Co)-LDHP anode at scan rate of 0.1 mV/s with the potential range from 0 to 3 V. In the first curve, a deflected anodic peak at 1.03 V is assigned to the formation of SEI film. In the subsequent curves, the cathodic peaks at 0.63 V can be ascribed to conversion of Ni^{2+} to Ni^0, and anodic peak at 2.32 V is attributed to oxidation of Ni^0 to Ni^{2+}. Meanwhile, the reduction peak at 1.13 V and oxidation peak at 1.73 V represent the redox reactions of ionic Co^{2+} and Co^0. **Figure 3E** exhibits the rate capability of H-(Ni, Co)-LDHP anode. When the current density is set as 50, 100, 200, 500, and 1,000 mA/g, the discharge capacity stabilizes at 641.6, 566, 361, 204.8, and 103.6 mAh/g, respectively. Significantly, it is found that the specific capacity reached 520.4 mAh/g when the current density returned to 1,000 mA/g from 50 mA/g. **Figure 3F** demonstrate the Nyquist plots of H-(Ni, Co)-LDHP, and equivalent circuit (insert). In simulation, the R_s and R_{ct} represent the resistance of Li^+ passing through the SEI and charge transfer process, respectively. The Warburg resistance (W) is on behalf of the diffusion rate of Li^+ in the electrolyte. Originating from the fitting, the R_s and R_{ct} can be calculated, which are 5.66 and 170.7 Ω, respectively. Such low value indicates the superior reaction kinetics and preferable electron transport characteristics.

CONCLUSION

In summary, the H-(Ni, Co)-LDHP has been synthesized by a rational template-sacrificing approach. Benefiting from the abundant active sites and convenient diffusion path of charge transfer, the H-(Ni, Co)-LDHP anode exhibited delivered high specific capacity (928.3 mAh/g at 100 mA/g). Thus, this work provides a new method to design hollow LDH nanocages for high specific capacity LIBs.

DATA AVAILABILITY STATEMENT

The original contributions generated for the study are included in the article/supplementary material, further inquiries can be directed to the corresponding author/s.

AUTHOR CONTRIBUTIONS

YL, HL, and YD analyzed the data and wrote the manuscript. All authors contributed to the article and approved the submitted version.

FUNDING

This work was supported by project of Ningxia key R&D plan (2018BEE03013, 2018YBZD0625, and 2019BFH02021).

REFERENCES

Chen, H., Hu, L. F., Chen, M., Yan, Y., and Wu, L. M. (2013). Nickel-Cobalt layered double hydroxide nanosheets for high-performance supercapacitor electrode materials. *Adv. Funct. Mater.* 24, 934–942. doi: 10.1002/adfm.201301747

Furukawa, H., Cordova, K. E., O'Keeffe, M., and Yaghi, O. M. (2013). The chemistry and application of metal-organic frameworks. *Science* 131, 1230444–1230456. doi: 10.1126/science.1230444

Gao, H. W., Zang, J. B., Liu, X. X., Wang, Y. H., Tian, P. F., Tian, S. Y., et al. (2019). Ruthenium and cobalt bimetal encapsulated in nitrogen-doped carbon material derived of ZIF-67 as enhanced hydrogen evolution electrocatalyst. *Appl. Surf. Sci.* 494, 101–110. doi: 10.1016/j.apsusc.2019.07.181

Gao, Z., Wang, J., Li, Z. S., Yang, W. L., Wang, B., Hou, M. J., et al. (2011). Graphene nanosheet/Ni^{2+}/Al^{3+} layered double-hydroxide composite as a novel electrode for a supercapacitor. *Chem. Mater.* 23, 3509–3516. doi: 10.1021/cm200975x

He, J., Wei, Y. Q., Hu, L. T., Li, H. Q., and Zhai, T. Y. (2018). Aqueous binder enhanced high-performance GeP_5 anode for lithium-ion batteries. *Front. Chem.* 6:21. doi: 10.3389/fchem.2018.00021

Hu, H., Guan, B. Y., Xia, B. Y., and Lou, X. W. (2015). Designed formation of Co_3O_4/$NiCo_2O_4$ double-shelled nanocages with enhanced pseudocapacitive and electrocatalytic properties. *J. Am. Chem. Soc.* 137, 5590–5595. doi: 10.1021/jacs.5b02465

Hu, H. J., Liu, J. Y., Xu, Z. H., Zhang, L. Y., Cheng, B., and Ho, W. K. (2019). Hierarchical porous Ni/Co-LDH hollow dodecahedron with excellent adsorption property for congo red and Cr(VI) ions. *Appl. Surf. Sci.* 478, 981–990. doi: 10.1016/j.apsusc.2019.02.008

Jiang, Z., Li, Z. P., Qin, Z. H., Sun, H. Y., Jiao, X. L., and Chen, D. R. (2013). LDH nanocages synthesized with MOF templates and their high performance as supercapacitors. *Nanoscale* 5, 11770–11775. doi: 10.1039/c3nr03829g

Kong, W. P., Li, J., Chen, Y., Ren, Y. Q., Guo, Y. H., Niu, S. L., et al. (2018). ZIF-67-derived hollow nanocages with layered double oxides shell as high-efficiency catalysts for CO oxidation. *Appl. Surf. Sci.* 437, 161–168. doi: 10.1016/j.apsusc.2017.12.158

Lee, I., Jeong, G. H., An, S., Kim, S. W., and Yoon, S. H. (2018). Facile synthesis of 3D MnNi-layered double hydroxides (LDH)/graphene composites from directly graphites for pseudocapacitor and their electrochemical analysis. *Appl. Surf. Sci.* 429, 196–202. doi: 10.1016/j.apsusc.2017.06.259

Li, Y. F., Li, Q. H., and Tan, Z. C. (2019). A review of electrospun nanofiber-based separators for rechargeable lithium-ion batteries. *J. Power Sources* 443, 227262–227264. doi: 10.1016/j.jpowsour.2019.227262

Qian, X., Wu, W. M., Zhuang, J. H., Niu, Y. D., Huang, J., and Hou, L. X. (2019). CoMoSx@Ni-CoMoSx double-shelled cage-in-cage hollow polyhedron as enhanced Pt-free catalytic material for high-efficiency dye-sensitized solar cell. *J. Power Sources* 417, 21–28. doi: 10.1016/j.jpowsour.2019.02.008

Song, Y. J., Li, H., Yang, L., Bai, D. X., Zhang, F. Z., and Xu, S. L. (2017). Solid-solution sulfides derived from tunable layered double hydroxide precursors/graphene aerogel for pseudocapacitors and sodium-ion batteries. *ACS Appl. Mater. Inter.* 9, 42742–42750. doi: 10.1021/acsami.7b13622

Su, W., Wu, F., Fang, L., Hu, J., Liu, L. L., Guan, T., et al. (2019). NiCo-LDH nanowires@ nanosheets core-shell structure grown on carbon fiber cloth for high performance flexible supercapacitor electrode. *J. Alloys Compd*. 799, 15–25. doi: 10.1016/j.jallcom.2019.05.305

Tang, Y. F., Liu, Y. Y., Yu, S. X., Guo, W. C., Mu, S. C., Wang, H. C., et al. (2015). Template-free hydrothermal synthesis of nickel cobalt hydroxide nanoflowers with high performance for asymmetric supercapacitor. *Electrochim. Acta* 161, 279–289. doi: 10.1016/j.electacta.2015.02.095

Wang, Q., and O'Hare, D. (2012). Recent advances in the synthesis and application of layered double hydroxide (LDH) nanosheets. *Chem. Rev*. 112, 4124–4155. doi: 10.1021/cr200434v

Xu, H. J., Cao, J., Shan, C. F., Wang, B. K., Xi, P. X., Liu, W. S., et al. (2018a). MOF-derived hollow CoS decorated with CeO_x nanoparticles for boosting oxygen evolution reaction electrocatalysis. *Angew. Chem*. 130, 8790–8794. doi: 10.1002/ange.201804673

Xu, L. P., Ding, Y. S., Chen, C. H., Zhao, L. L., Rimkus, C., Joesten, R., et al. (2018b). 3D flowerlike α-nickel hydroxide with enhanced electrochemical activity synthesized by microwave-assisted hydrothermal method. *Chem. Mater*. 20, 308–316. doi: 10.1021/cm702207w

Xuan, X. Y., Qian, M., Han, L., Wan, L. J., Li, Y. Q., Lu, T., et al. (2019). *In-situ* growth of hollow NiCo layered double hydroxide on carbon substrate for flexible supercapacitor. *Electrochim. Acta* 321, 134710–134713. doi: 10.1016/j.electacta.2019.134710

Yang, W. L., Gao, Z., Wang, J., Ma, J., Zhang, M. L., and Liu, L. H. (2013). Solvothermal one-step synthesis of Ni–Al layered double hydroxide/carbon nanotube/reduced graphene oxide sheet ternary nanocomposite with ultrahigh capacitance for supercapacitors. *ACS Appl. Mater. Inter*. 5, 5443–5454. doi: 10.1021/am4003843

Zand, Z., Salimi, P., Mohammadi, M. R., Bagheri, R., Chernev, P., Song, Z. L., et al. (2019). Nickel-Vanadium layered double hydroxide under water-oxidation reaction: new findings and challenges. *ACS Sustain. Chem. Eng*. 7, 17252–17262. doi: 10.1021/acssuschemeng.9b03971

Conflict of Interest: The authors declare that the research was conducted in the absence of any commercial or financial relationships that could be construed as a potential conflict of interest.

frontiers in Chemistry

REVIEW
published: 17 December 2020
doi: 10.3389/fchem.2020.607504

Carbon Anode Materials for Rechargeable Alkali Metal Ion Batteries and *in-situ* Characterization Techniques

Ruida Ding[1†], *Yalan Huang*[2,3†], *Guangxing Li*[1], *Qin Liao*[1], *Tao Wei*[1], *Yu Liu*[1], *Yanjie Huang*[1] *and Hao He*[1*]

[1] College of Materials Science and Engineering, Changsha University of Science & Technology, Changsha, China, [2] Department of Physics, City University of Hong Kong, Hong Kong, China, [3] Shenzhen Research Institute, City University of Hong Kong, Shenzhen, China

Lithium-ion batteries (LIBs), used for energy supply and storage equipment, have been widely applied in consumer electronics, electric vehicles, and energy storage systems. However, the urgent demand for high energy density batteries and the shortage of lithium resources is driving scientists to develop high-performance materials and find alternatives. Low-volume expansion carbon material is the ideal choice of anode material. However, the low specific capacity has gradually become the shortcoming for the development of LIBs and thus developing new carbon material with high specific capacity is urgently needed. In addition, developing alternatives of LIBs, such as sodium ion batteries and potassium-ion batteries, also puts forward demands for new types of carbon materials. As is well-known, the design of high-performance electrodes requires a deep understanding on the working mechanism and the structural evolution of active materials. On this issue, *ex-situ* techniques have been widely applied to investigate the electrode materials under special working conditions, and provide a lot of information. Unfortunately, these observed phenomena are difficult to reflect the reaction under real working conditions and some important short-lived intermediate products cannot be captured, leading to an incomplete understanding of the working mechanism. *In-situ* techniques can observe the changes of active materials in operando during the charge/discharge processes, providing the concrete process of solid electrolyte formation, ions intercalation mechanism, structural evolutions, etc. Herein, this review aims to provide an overview on the characters of carbon materials in alkali ion batteries and the role of *in-situ* techniques in developing carbon materials.

Keywords: ion batteries, carbon anode materials, *in-situ* techniques, solid electrolyte interface, ions intercalation, structural evolution

OPEN ACCESS

Edited by:
Ge Li,
University of Alberta, Canada

Reviewed by:
Matthew Li,
University of Waterloo, Canada
Zhenyu Xing,
South China Normal University, China
Lei Han,
Hunan University, China

***Correspondence:**
Hao He
hehao0520@gmail.com

[†] *These authors have contributed equally to this work*

Specialty section:
This article was submitted to Electrochemistry, a section of the journal Frontiers in Chemistry

Received: *18 September 2020*
Accepted: *17 November 2020*
Published: *17 December 2020*

Citation:
Ding R, Huang Y, Li G, Liao Q, Wei T, Liu Y, Huang Y and He H (2020) Carbon Anode Materials for Rechargeable Alkali Metal Ion Batteries and in-situ Characterization Techniques. Front. Chem. 8:607504. doi: 10.3389/fchem.2020.607504

INTRODUCTION

The energy crisis and severe environmental issues have driven scientists to develop efficient energy conversion solutions to utilize renewable energy and reduce emissions (Armand and Tarascon, 2008; Winter et al., 2018). Although traditional lead-acid batteries play an irreplaceable role in society, they are insufficient to meet the requirement of energy density for electronic devices and

electric vehicles. Therefore, it is urgent to develop a more efficient and lighter energy storage system. A high energy density Li-based battery (e.g., Li-$LiTiS_2$ cell), developed in the 1970s, was not successfully commercialized due to the safety issue of Li metal as the anode electrode (Whittingham, 1976). With the development of cathode materials and electrolyte systems (Armand and Touzain, 1977; Armand et al., 1979; Mizushima et al., 1981; Yazami and Touzain, 1983), anode materials with a stable and reversible ion intercalation/deintercalation property is urgently needed to form a full ion battery. In 1985, Yoshino et al. developed a full lithium ion battery (LIB) with $LiCoO_2$ as cathode, carbon material as anode and $LiPF_6$/ethylene carbonate (EC)/propylene carbonate (PC) as electrolyte, respectively. This battery is further commercialized by SONY in 1991 (Yoshino et al., 1987; Yoshino, 2012) and "a reachargeable world was created at this time" (The Nobel Prize in Chemistry, 2019).

With the large-scale promotion of lithium-ion batteries, lithium resources have gradually become one of the most concerning issues. Sodium and potassium, showing similar properties to lithium but with much higher reserves, are considered to be alternatives for lithium (Hou et al., 2017; Pramudita et al., 2017). Since sodium-ion batteries (SIBs) and potassium-ion batteries (KIBs) can learn from the technology and materials for LIBs, they are most expected in rechargeable batteries.

Developing anode materials with a high specific capacity plays an important role in enhancing the energy density of alkali ion batteries (LIBs) (Lee et al., 2016). The alloy and conversion type anode materials (e g., Si) showed high specific capacity, however it is still far away from practical applications due to the huge volume expansion (Sun et al., 2016; Yun Zhao et al., 2019). In contrast, carbon materials, showing excellent electrical conductivity and cycle stability, are considered the most promising anode materials for ion batteries. Therefore, it is of importance to further develop stable carbon materials with a high specific capacity to increase battery energy density (Li et al., 2019). The main limitation for SIBs and KIBs is to develop stable anode materials with high specific capacity that can be intercalated with ions reversibly, since the larger radiuses of sodium and potassium cause the hardness for the intercalations. Therefore, the behavior and mechanism of ion intercalation still need further investigation.

In ion batteries, carbon material undergoes three reaction processes in ion batteries: (1) SEI film formation, (2) structural evolution during ion insertion/extraction and (3) performance degradation. In early days, *ex-situ* characterization techniques have been applied and provided a lot of information on the morphology, structure, and composition, and these work play an important role in understanding the working mechanism of active materials in ion batteries. However, it is also found that the *ex-situ* techniques cannot capture the intermediate products and phenomenon during working under high charge/discharge rates. Different from the *ex-situ* techniques, the *in-situ* characterization techniques monitor the signal of active materials in ion batteries under working conditions, providing time-resolved information on solid electrolyte formation, ions insertion/extraction and structural evolutions, etc. (Harks et al., 2015; Yang et al., 2016; Yuan et al., 2017; Zhu et al., 2019). This operando information is of great significance in developing new electrode materials and improving the performance of batteries.

This review aims to highlight the recent developments and discoveries on carbon materials for alkali ion batteries and provide an overview on employing *in-situ* techniques in the understanding the working mechanism. In detail, carbon materials as well as their reaction mechanism in alkali metal ions batteries are elaborately expounded, followed with a presentation about the *in-situ* techniques on the investigation of SEI formation, ion insertion/extraction mechanism, degradation mechanism, etc. Subsequently, a summary on the current progress toward *in-situ* techniques is presented as well as the key issues concerning the challenges and perspectives prospect, which give constructive suggestions on the research focus and direction for developing better carbon anode materials.

CARBON MATERIALS AS ANODES FOR ION BATTERIES

For anode materials in ion batteries, carbon-based materials, silicon-based materials, tin-based materials, and metal oxides have been developed. And after several years of development, carbon materials have become the most successful anode materials. There are usually three types of orbital hybridization for C atoms in carbon materials, e.g., sp, sp2, and sp3. Generally, carbon materials based on sp or sp3 hybrid orbitals, e.g., polyacetylene, hydrocarbons, are difficult materials with which to form a regular structure allowing the insertion/extraction of guest ion, thus they are rarely used as anode materials for ion batteries. The carbon material with sp2 hybridization takes a planar sheet of carbon atoms in a honeycomb structure as a basic unit, and is formed by a stack of these basic units in an ordered or disordered manner (Wu et al., 2003). These three orbital hybrid carbon atoms form a large amount of carbon materials with diverse structures which can be characterized by X-ray diffraction (XRD), Raman, Transmission electron microscopy (TEM), Nitrogen sorption measurements, etc. (Xing et al., 2017b), and these diverse structures ensure their application in energy storage and conversion (Xing et al., 2015, 2016, 2017a). This structure information is generally characterized by Alkali metal ions, such as lithium, sodium, and potassium, and can reversibly intercalate into these materials. This section will focus on these carbon materials.

Types of Carbon Anode Materials

Graphite

Graphite, one of the most widely used anode materials in commercial LIBs, delivers a capacity of 372 mA h g^{-1} which corresponds to the formation of LiC_6 (Hou et al., 2017). Due to the high initial coulombic efficiency (CE), low volume expansion, rich natural resources and the ability to form graphite intercalation compounds (GICs), graphite is also widely applied as an anode material in potassium ion batteries (PIBs) and other alkaline metal ion batteries, such as Rb and Cs

ion battery (Dresselhaus and Dresselhaus, 2002). As is well-known, the structure of graphite is a unique layered structure with hexagonal stacking (AAA), Bernal stacking (ABA), or rhombohedral stacking (ABC), as shown in **Figures 1A–C** (Bao et al., 2017). The structure features a strong covalent bond within the graphene layers with a weak bond through van der Waals interactions in the vertical direction, resulting in an interlayer spacing of 3.35 Å which is capable of guest ions insertion/extraction. This structure ensures that alkali metal ions can be inserted into graphite to form metallized graphite. Generally, the layered structure of graphite will not be destroyed during the ion insertion/extraction, which ensures its long-term cycle performance in ion batteries. Conversely, anodes based on alloys or conversion reactions exhibit severe volume changes during cycling, which can easily lead to electrode material failures. Therefore, due to the high stability and long cycle life, it is reasonable to use graphite as the preferred anode based on intercalation chemistry.

For LIBs, graphite is one of the most widely used anode materials. Due to its good electrical conductivity, high crystallinity, and good layered structure, lithium ions can be reversibly inserted or extracted, and a theoretical specific capacity of 370 $mAhg^{-1}$ and an efficiency above 90% are delivered. The intercalation reaction of lithium in graphite occurs at 0–0.25 V (vs. Li/Li+), which makes graphite an anode that can be matched with a variety of positive electrode materials to form a battery with high voltage. Similar to lithium, potassium ions also undergo reversible intercalation/extraction reactions in graphite, resulting in a reversible specific capacity of 273 $mAhg^{-1}$ (Jian et al., 2015).

Different from LIBs and potassium ion batteries (PIBs), graphite is considered to be difficult to apply as an anode for sodium ions batteries (SIBs). The reason leading to this issue is attributed to the fact that the insertion mechanisms of different alkali ions into graphite are different, so the electrochemical behavior of graphite electrodes in LIBs, SIBs, and PIBs varies a lot. Unfortunately, the fundamental origin of the difference is still not clear due to the complexity of the system and the difficulty of quantifying ion intercalation (Winter et al., 2018). To explore the cause of the undesirable Na^+ storage properties of graphite, the mechanism of Na^+ insertion into graphite has been investigated by theoretical studies. According to the calculations of density functional theory (DFT), it was found that the local binding of a Na ion to a single layer of graphene was quite unstable by ≈0.5 eV (E_i) compared with those for other alkali metals (AMs). This E_i was in accordance with the formation energy (E_f) reported for AM-GICs (Nobuhara et al., 2013; Okamoto, 2014; Wang et al., 2014; Liu et al., 2016; Yoon et al., 2017) (SM 50), which revealed that the repulsive local interactions between graphite layers and Na^+ ions dominantly destabilized the Na-GICs, consequently leading to poor sodium storage capacities in graphite anodes. The poor performance of graphite anodes on sodium storage has been preliminarily revealed through the theoretical calculation, however, there is still a lack of experimental evidence. Investigation of sodium ions intercalation behavior in graphite by multiple *in-situ* techniques is of great significance, and the results will provide guidance for developing new carbon anode materials for SIBs.

Carbon Nanotube (CNT)

As one of the carbon allotropes, carbon nanotubes (CNTs) have been approved to be an additive or substitute in LIBs anode owing to the chemical stability, large surface area, robust mechanical properties, and high electrical conductivity (Thess et al., 1996; Gu et al., 2015; Liew et al., 2015). The structure of CNTs presents as one-dimensional cylindrical tubule of graphite sheets, including multi-walled (MWCNTs), double-walled (DWCNTs), and single-walled (SWCNTs) tubes (**Figure 1D**). This tubular structure contributes to the mitigation of structural integrity degradation resulting from the significant volume change during charge/discharge process. In addition, CNTs possess superb conductivity ($\sim 10^6$ S m^{-1}), high rigidity (Young's modulus of the order of 1 TPa), low density and high tensile strength (60 GPa) (Thess et al., 1996; Treacy and Ebbesen, 1996; Lier et al., 2000; Yu et al., 2000). In LIBs, SWCNTs display a reversible capacity ranging from 300 to 600 $mAhg^{-1}$, significantly higher than that of graphite (372 $mAhg^{-1}$), making them a competitive lithium storage material (Meunier et al., 2002; Yang et al., 2008).

Generally, the reversible capacity can reach up to 1,000 $mAhg^{-1}$ via mechanical and chemical treatments. To achieve this purpose, one of the typical ways is to synthesize hybrid composites with CNT as a key component. For example, Su and his co-workers demonstrated a lightweight CNT paper as a freestanding framework to accommodate Li metal in a mass fraction of 80.7 wt% (Sun et al., 2018). The highly conductive CNT network effectively inhibited the formation of Li dendrites so that the anode afforded a favorable coulombic efficiency of over 97.5%. Additionally, owing to the robust and expandable nature of the CNT paper beyond other 3D scaffolds, the Li/CNT anodes exhibited areal and gravimetric capacities of 10 mA h cm^{-2} and 2,830 mA h g^{-1}. The Li utilization after 1,000 cycles at a current density of 10 mA cm^{-2} remained 90.9%. Inserting the substitutional heteroatoms in the graphitic layers is another way to optimize the properties of CNTs in ion batteries. Due to their similar sizes, N and B are the most preferred heteroelements to replace C atoms. A novel aligned N-doped core-sheath carbon nanotube (N-CNT) film has been synthesized by Pan et al., and a high capacity of 390 mAh g^{-1} and retention of 97% after 200 cycles at a rate of 4C were delivered in LIBs (Pan et al., 2016). It is found that nitrogen-doped graphene shells could facilitate the insertion of lithium ions.

Nonetheless, the capacity of CNTs are partially irreversible in LIBs since a fraction of the inserted lithium during the first charge process is consumed in formation of SEI. Another problem for CNT-based anodes is the lack of voltage plateau during discharging process. The broad changes in voltage make its utilization difficult in most electronics which require a stable voltage source. In fact, all the disadvantages of CNT are related to morphology. Therefore, *in situ* characterization methods, such as *in-situ* TEM, Raman, FTIR, etc., are needed to conduct multi-scale observation on CNT anode materials to figure out the relationship between their structure and properties. This information is of important guiding significance

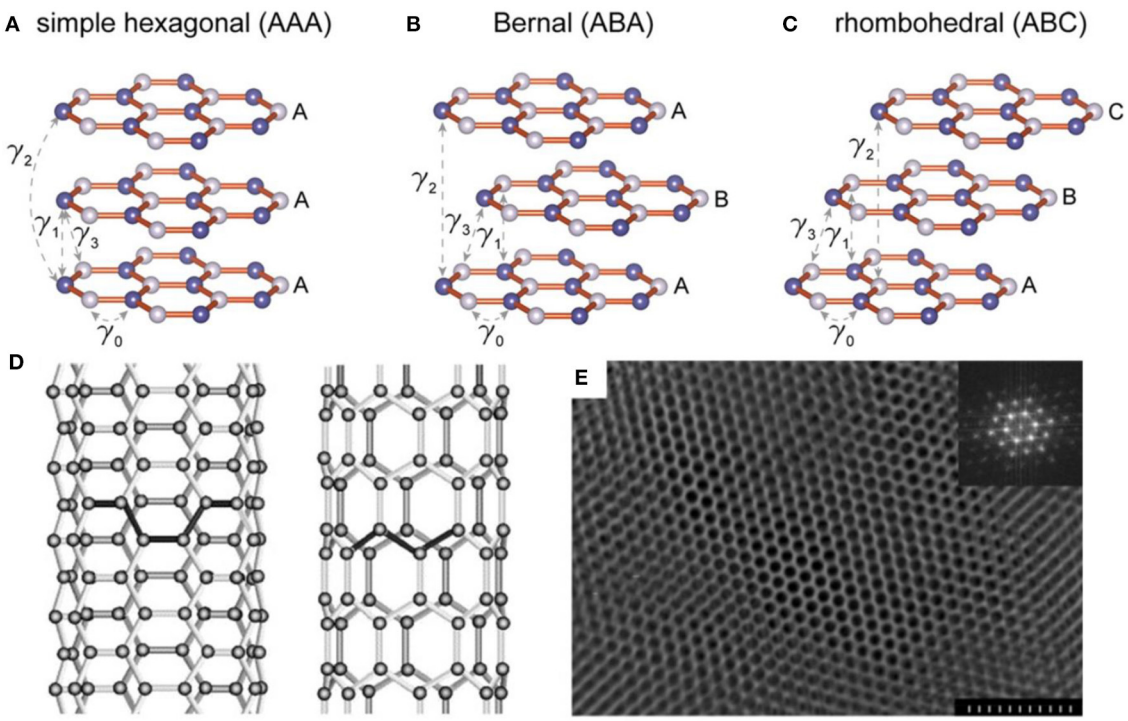

FIGURE 1 | Three types of stackings for layered graphene and the corresponding calculated electronic structures. **(A)** Schematic drawings of simple hexagonal (AAA), **(B)** Bernal (ABA), and **(C)** rhombohedral (ABC) stackings (Bao et al., 2017). **(D)** Illustrations of the atomic structure of (left) an armchair and (right) a zig-zag single-walled nanotube (Thostenson et al., 2001). **(E)** Electron microscopy image of the highly ordered mesoporous carbon structure. In the inset, a Fourier transform (FT) of the image shows a pattern with multiple reflections, which are characteristic of a highly ordered hexagonal array. The scale bar is 300 nm (Liang et al., 2004).

for the researchers to develop new synthesis methods and novel carbon nanotubes.

Amorphous Carbon Materials

Amorphous carbon materials, including soft carbon materials and hard carbon materials, are short of long-range ordered structure in plane and ordered stacked structures of graphite. Generally, the amorphous carbon materials are comprised of voids, distorted graphene nanosheets, and randomly distributed graphitized micro-domains, so they prefer to remain in the amorphous structure and restrain the development of graphitic structure.

Soft carbon, including petroleum coke, needle coke, carbon microspheres, etc., can be transformed into graphite after heat treatment at a temperature above 2,000°C. Due to the small crystal grain size and large interplanar spacing, soft carbon materials show a faster lithium ion diffusion coefficiency and a more stable charge/discharge platform during lithiation/delithiation.

In contrast, hard carbon maintains a disordered structure permanently regardless of the temperature (Bommier and Ji, 2015). This is mainly due to the formation of three-dimensional crosslinking via sp3 hybridization at the early stage of carbonization, which hinders the parallel growth of the graphite surface. Generally, hard carbon is prepared by pyrolysis of polymers such as resin and organic polymer. The pore structure and good electrolyte compatibility of hard carbon ensure it to be a potential storage material for AM ions. Unfortunately, hard carbon materials show a large irreversible capacity decay during the first charge-discharge.

The interlayer spacing for d002 is 3.4–3.6 and 3.7 Å for soft carbons and hard carbons, respectively, which is bigger than that of graphite (3.35 Å) (Saurel et al., 2018). Therefore, amorphous carbon materials, especially hard carbon materials, are excellent anode materials for AM-ion batteries due to their being kinetically favorable for the transportation of ion and electron. Many micro/nanostructured hard carbon materials have been exploited as anode materials for LIBs, such as hollow nanostructured carbon materials (Cao et al., 2012; Tang et al., 2012), porous carbon materials (Yan et al., 2014; Hou et al., 2015), carbon fibers (Bai et al., 2015; Zhu et al., 2015), carbon nanosheets (Ding et al., 2013; Wang et al., 2013; Yang et al., 2015), etc. In addition to being directly used as electrode materials, these carbon materials can be prepared as compounds by heteroatomic doping, loading with metal oxides, etc. to enhance their electrochemical performances. For instance, Zheng et al. reported an anode material obtained by coating the lithium metal on a monolayer of interconnected amorphous hollow carbon nanospheres, which showed excellent performance in LIBs (Zheng et al., 2014). Due to the protection of carbon materials, lithium dendrites did not form up and thus the composite displayed a high Coulombic efficiency of ∼99% after

more than 150 cycles. Yang et al. synthesized N-doped hollow carbon nanospheres with an optimized shell thickness of 20 nm and N dopant concentrations of 16.6 at %. This anode material delivered a specific capacity of 2,053 mA h g^{-1} at 100 mA g^{-1} and a superior cycling stability of 879 mA h g^{-1} at 5 A g^{-1} after 1,000 cycles (Yang et al., 2017).

Although hard carbon materials are widely used as electrode materials in ion batteries, the *in situ* characterization on them is still rarely reported since the structure changes of amorphous structures are difficult to capture by multiple detection techniques. This is one of the major challenges in developing hard carbon as anode material for ion batteries.

Mesoporous Carbon Materials

Compared with block carbon materials, porous carbon materials deliver a significant enhancement in power density and energy density and they have attracted wide attention regarding their employment as electrode materials of energy storage devices. Porous carbon materials display many advantages, such as high surface area, numerous active sites for lithium ions adsorption and storage and pore sizes ranging from nanometers to microns. **Figure 1E** shows the electron microscopy image of the highly ordered mesoporous carbon structure. These typical morphological features enable porous carbon materials, continuous electron conduction pathways, high-speed ion migration channels, large electrolyte/electrode interface, strain relaxation during the charge/discharge process and high electrical conductivity and thus an enhanced energy storage performance (Hu et al., 2007; Woo et al., 2007; Cheng et al., 2008; Mao et al., 2012). In fact, carbon materials with different pore sizes demonstrate different performances. Microporous carbons (pore size < 2 nm) show greater capacity than conventional graphite. However, they are subject to high irreversibility during lithium insertion/extraction due to their increased solid electrolyte interface (SEI) area and/or the interactions of lithium ions with carbon surface functional groups (Kim et al., 2013). In contrast, mesoporous carbon materials deliver a better capacity reversibility in LIBs.

These high specific surface area carbon materials are usually synthesized by the template method, typically involving the establishment of a sacrificial porous silicon template, followed by impregnation and subsequent carbonization of proper carbon precursors to form a carbon/template composite, and then removing the silicon template to obtain a highly porous carbon. Kim et al. successfully synthesized hollow core-mesoporous shell carbon (HCMSC) with hierarchical nanoarchitecture, and this anode material exhibited a ultra-high Li storage capacity of 1,000 mAh g^{-1} and excellent cycling performance in LIBs (Kim et al., 2011). These improved performances are mainly attributed to the unique structural characteristics, such as large surface area (2,418 m^2 g^{-1}) and mesopore volume of the HCMSC, which facilitated fast mass transport. An ultra-thick mesoporous carbon with a thickness up to 850 μm and an areal mass of 55 mg cm^{-2} was firstly demonstrated by Shen and his co-workers. This mesoporous carbon showed a high specific capacity of 270 mA h g^{-1} and a high areal capacity of 13.6 mA h cm^{-2} in sodium ion half cells, which were significantly higher than those of the state-of-the-art sodium batteries (Shen et al., 2016).

In recent years, the Li storage capacity of porous carbon materials has been further promoted by means of composite with metals or metal oxides or doped with heterogeneous ions (Jahel et al., 2015; Liu H. et al., 2015; Wang et al., 2015; Zhang et al., 2015). For instance, Jahel et al. designed a SnO_2/C composite with ultra small SnO_2 particles (∼2.0 nm) homogeneously confined in the micro/mesoporous pores of porous carbon to accommodate the volume changes upon lithiation/delithiation. The as-prepared composite delivered a high initial reversible charge capacity of 916 mAh g^{-1} and an reversible capacity retention of 79% after a long cycling life (≈2,000 cycles) (Jahel et al., 2014).

It is well-known that the high specific surface area of carbon material leads to the initial coulombic efficiency of <40% and the changes of the structure and volume during the cycling have great influence on the performance. These issues are the greatest resistance to further applying porous carbon materials in ion batteries. So far, there are few systematic studies on the influence of the porous nanostructure on these phenomena, especially the dynamic evolution of the structure during long-term cycle. Therefore, the introduction of *in-situ* characterization is of great significance to the development of porous carbon materials.

Biomass Derived Carbon Materials

Producing carbon materials from biomass materials is theoretically feasible since most biomass materials are mainly composed of C, H and O elements. Additionally, biomass materials are renewable, abundant, and environmentally friendly resources, the application of these sustainable materials is quite attractive (Wang et al., 2017). Experimental results show that, in general, biomaterials typically release some small molecules (e.g., CH_4, CO, H_2) during the pyrolysis process, and then convert to amorphous carbon through the crosslinking and partial aromatic ordering process. In the past few years, biomass materials have developed rapidly. A large amount of biomass materials, such as carbohydrates, lignin, chitin, cellulose, proteins, etc., have been prepared as carbon materials and used as electrode materials for energy storage devices. Carbon nanoparticles were prepared by Gaddam et al. through a flame deposition method with coconut oil as carbon sources, and delivered capacities of 277 and 741 mA h g^{-1} in sodium and lithium ion batteries, respectively (Gaddam et al., 2016). Porous hard carbon materials were synthesized by Hong et al. through a simple pyrolysis of H_3PO_4-treated pomelo peels at 700°C in N_2 (Hong et al., 2014). The as-prepared carbon material displayed a 3D connected porous structure and a large specific surface area of 1,272 m^2 g^{-1}. This porous structure ensures a good cycling stability and rate capability. In a sodium ion battery, it delivered a capacity of 181 mA h g^{-1} at 200 mA g^{-1} and the capacity retained 71 mA h g^{-1} at 5 A g^{-1} after 220 cycles.

The biomass-derived carbon shows broad application prospects, and one of the challenges in this field is to develop controllable methods to adjust the functionality of carbon. At present, establishing the relationship between the structure and properties of biomass-derived carbon to guide the improvement of material characteristics (including morphology, porosity, and

surface chemistry properties), and achieving the controllable preparation of materials are of great significance for the development of biomass carbon materials.

In addition to the above carbon materials, some new types of carbon materials with special structure are synthesized and applied as anode for ion batteries. Xing et al. synthesized polynanocrystalline graphite via chemical vapor deposition on a nanoporous graphenic carbon as an epitaxial template. This new carbon shows a structure of essentially hollow to a certain extent with randomly arranged nanosized graphite building blocks, which is different to most low-dimensional nanocrystalline carbon materials. This novel structure with disorder at nanometric scales but strict order at atomic scales enables substantially superior long-term cycling life and capacity retention for K-ion storage than that of graphite (Xing et al., 2017c).

Reaction Process and Mechanism of Carbon Anode Materials in Ions Batteries

Ions Storage Mechanism

For lithium-ion batteries, there are usually three storage mechanisms for lithium ions: (i) Li-alloy reaction mechanism, (ii) conversion reaction mechanism that involves the Li oxides (Li_2O) formation/decomposition as well as the reduction/oxidation of anode material, and (iii) insertion/extraction reaction mechanism that involves the insertion/extraction of Li into/from the lattice of the carbon material (Ji et al., 2011). The former two are usually employed by metal oxides or metals, and the last one is employed by carbonaceous materials such as graphite and CNTs. In order to figure out the mechanism of lithium intercalation into graphite, numerous studies have been conducted (Zanini et al., 1978; Dahn, 1991; Ohzuku et al., 1993). After lithium is intercalated into graphite, lithium atoms will occupy the sites between two adjacent graphene planes, and are associated with a hexagonal C ring in a plane, thus avoiding the nearest neighbor occupation (maximum composition LiC_6) (Winter et al., 1998). Theoretical studies revealed that the structure of graphite after lithiation fully changes to AA stacking, and the interplanar distance is enlarged from 3.35 Å for $x = 0$ in Li_xC_6 to 3.70 Å for $x = 1$ (Boehm and Banerjee, 1992; Song et al., 1996). Shi et al. show that both hexagonal and rhombohedral graphite phases are capable of reversible lithium intercalation with little difference in the insertion capability (Shi, 1996; Shi et al., 1997). In fact, the insertion of lithium into graphite conducts through a stage mechanism in which different phases occur sequentially as stage 4, stage 3, stage 2 and stage 1 corresponding to LiC_{36}, LiC_{24}, LiC_{12}, LiC_6, respectively. The stage mechanism may be attributed to the distinct repulsion of adjacent Li layers which is in competition with lateral interactions, local reactions, and configurational entropy contributions. In charge/discharge curves, different potential plateaus are characteristic of the staging phenomenon, which is also confirmed by the advanced characterization technology such as XRD and Raman spectroscopy.

The AM ion storage mechanism of hard carbon is quite different from the aforementioned carbon materials. The curves of the lithiation/delithiation process is composed of a slopy line in the high potential region and a plateau in the low potential region. To date, there are different opinions on the AM ion storage mechanism in hard carbon anodes. One thinks it is the insertion-absorbtion mechanism, in which the capacity in the slope area mainly results from the insertion/extraction of Li^+/Na^+ into/from carbon layers while the capacity in the plateau area is attributed to the adsorption/deposition of Li^+/Na^+ in the micropores. For the first time, Stevens and Dahn compared the behaviors of lithium and sodium insertion in hard carbon materials and demonstrated that a similar AM insertion mechanism were followed in both cases (Stevens and Dahn, 2000a). They proposed a "house of cards" model for the carbon structure in which random stacking of multiple layers (2 to 3 layers) creates nanoscale porosity. It is considered that the slope potential profile was attributed to the insertion of lithium or sodium into parallel or nearly parallel layers. Both the interlayer metal content and the random arrangement between parallel slices would affect the lithiation potential. The plateaus at low potential were believed to be attributed to a process analogous to adsorption of metal ions in the nanopores. This process resulted in a potential that was close to the chemical potential of the metal itself, and thus produced an electric potential close to 0 V. Afterwards, *in situ* X-ray scattering was carried out to study the storage of sodium/lithium in hard carbon, proving that both lithium and sodium can be inserted into the interlayer of hard carbon and absorbed in the nanopores. Unfortunately, there are still some experimental phenomena that cannot be fully explained.

In contrast, an absorption-insertion mechanism was proposed, in which the capacity in the slope region was considered to be the absorption of Li^+/Na^+ on the surface sites of carbon materials (e.g., functional groups, defective sites and active sites) while the capacity in the plateau region derived from the insertion/extraction of Li^+/Na^+. In 2012, Cao et al. investigated the sodium and lithium storage mechanisms in hollow carbon nanowires (HCNWs) and demonstrated that the electrochemical behaviors of HCNWs in SIBs and LIBs are distinctly different (Cao et al., 2012). The sodium storage behavior in HCNWs at the low-potential zone is similar with lithium storage behavior in graphite, corresponding to the intercalation/deintercalation of metal ions into/from graphite interlayers. However, in high-potential area, the electrochemical reaction was believed to be due to the charge transfer on the graphite surface. The theoretical calculation, based on the equilibrium of attractive van der Waals interactions among carbon layers and the repulsion interactions between Na^+/Li^+ and carbon material, was also conducted to investigate the Na^+/Li^+ insertion/extraction mechanism for HCNW anodes. The calculation showed that the interplanar equilibrium distances for NaC_6 and LiC_6 were 0.45 and 0.37 nm while the energy costs for Li^+ and Na^+ insertion were 0.03 and 0.12 eV, respectively. Due to the high energy cost, sodium intercalation into graphite is difficult, however, when the interlayer distance of graphite increased up to 0.37 nm, it could be achieved by overcoming the energy barrier, and this is consistent with the experimental results.

Solid Electrolyte Interphase

Solid electrolyte interphase (SEI), a protective layer on the surface of carbon anode, is formed by electrolyte decomposition during the first charge/discharge process. For LIBs, many performances, e.g., the irreversible charge loss, rate capability, cycling performance, graphite anode spalling and the battery safety, are related to the quality of SEI. Generally, the electrolyte of LIBs is thermodynamically unstable at a relatively low or high potential. Thus, there is a reduction process of solvents and salts on the surface of carbon materials, resulting in a deposition of organic/inorganic decomposition to form an SEI membrane. The potential for SEI formation is not a fixed value, generally ranging from 0.5 to 2 V (Ein-Eli et al., 1994; Aurbach et al., 1997; Stevens and Dahn, 2000a; Edström et al., 2006; Bryngelsson et al., 2007; Kang et al., 2008) SEI is mainly formed during the first few cycles and its quality depends on many indicators, such as the additives in the electrolyte, cycling rate, temperature and so on (Ein-Eli et al., 1994; Liebenow et al., 1995). It is desirable that the LIBs are sold to users after a good SEI film has been formed since a well-grown SEI interface would ensure that the dynamic stability of the battery can be improved, and the dynamic stability of electrolyte promoted, thereby ensuring good circulation ability (Aurbach, 2000). The SEI interface also prevents co-insertion of solvents into graphite interlayers, and thereby preventing the exfoliation of graphite anode.

In fact, SEI is a complex layer, and its composition is still not completely determined. At present, it is generally considered to be composed of inorganic components (degradation products of salts in electrolyte) which displays as a dense layer near carbin and organic components (partially or completely reduced products of solvents) which displays as a porous organic or polymer layer (Edström et al., 2006). Additionally, it is difficult to accurately measure the thickness of the SEI since some components are partially soluble in the electrolyte. The thickness of SEI is generally considered to range from a few Angstroms to tens of Angstroms or hundreds of Angstroms. The composition and thickness of the SEI is also considered to be constantly changing during cycling. For example, it may be partially dissolved in the electrolyte [e.g. dimethyl carbonate (DMC)], and the thickness would be larger at low potentials and smaller at high potentials (Winter, 2009).

The parameters of the SEI, such as composition, thickness, shape, and compactness, show significant impact on battery performance. For instance, the irreversible charge loss in the first cycle occurs owing to solvent reduction and the SEI formation (Zaghib et al., 2000). The harmful process (e.g., self-discharge) during the cycle depends mainly on the ability of SEI to passivate the active material, and affects the capacity decay behavior (Yazami and Reynier, 2002). Moreover, the dissolution and transformation of SEI membrane during the cycle also affect the battery performance and stability (Novák et al., 2000). It is also noted that SEI is temperature-sensitive, and thus the performance at high/low temperatures is limited (Churikov, 2001). Most importantly, SEI also has a huge influence on the safety of batteries. Therefore, it is of great significance to understand the properties and behaviors of SEI for the development of better batteries (Park et al., 2009). Unfortunately, the information about SEI is still limited due to the lack of effective characterization techniques.

Degradation Mechanism

As mentioned above, a layer of SEI film composed of inorganic and organic substances is formed on the surface of the carbon anode during the first few cycles. And this SEI interface is beneficial to the stability of both carbon anode and organic electrolyte. When lithium ions are intercalated into graphite, the anode potential is very low, which is close to the standard electrode potentials. At such a low potential, the solvent of the electrolyte (e.g., ethylene carbonate) is highly active and could react with lithium to rapidly produce precipitate on the surface of graphite anode (Smith et al., 2012). As the cycle number increases, the thickness of the formed SEI interface increases due to the continued decomposition reaction (Lee and Pyun, 2002; Bodenes et al., 2012). More importantly, the SEI interface retards the kinetics of lithium ions intercalation into carbon anode and is unstable due to the reduplicative expansion and contraction of graphite during lithium insertion and extraction (Li et al., 2001; Aurbach et al., 2006). This reaction leads to the growth of the SEI interface and eventually causes the graphite particles to detach from the current collector. During cycling of LIBs, the formation of this surface membrane is the main cause of lithium ion loss (Broussely et al., 2001). The SEI interlayer also leads to an increase in the charge transfer resistance and blockage of carbon anode, resulting an increase in irreversible capacity (Abraham et al., 2007; Yamada et al., 2008; Moss et al., 2010).

On the other hand, large mechanical strain in graphite would be generated during cycling at high C-rate and high state of charge (SOC), leading to cracks and splits in graphite particles, and thus causing a decrease in orientation (Yuqin et al., 1997). It is reported that the orientation of graphite particles affects the reversible capacity of anode, namely, less-oriented graphite particles display a lower reversible capacity (Shim and Striebel, 2004). This is due to the low orientation of particles, which brings difficulties in kinetics of lithium insertion and leads to the formation of new boundaries between particles through the irreversible interaction of lithium ions and electrolyte (Rhodes et al., 2011; Lai et al., 2012). Furthermore, the content of hexagons changes during cycling while the layered structure of graphite maintains unchanged, and this change substantially leads to the performance degradation (Andersson et al., 1999; Ridgway et al., 2012). Therefore, in order to ensure the stable performance, the content of rhombohedron/hexahedron is an important parameter for carbon anode.

There are several degradation mechanisms for carbon anode in LIBs which seriously affect the long-term cycle life. This degradation can be mitigated by adding various stabilizers, robust electrolytes, and temperature treatments. Thus, it is still necessary to further explore the relationship between the decay mechanism of carbon anodes and external factors, such as electrolytes, voltages, etc., so as to develop an improved stable anode which provides high energy density and good circulability under various operating conditions.

IN-SITU TECHNIQUES FOR CARBON MATERIALS

Structural characterization of electrode materials is extremely important for understanding the reaction mechanism of the battery during operation. In this regard, the "*ex-situ*" characterization can hardly capture the transient state of structures and the complex electrochemical process involving a series of reactions, thus cannot fully understand the relationship between structural evolution and performance changes of ions batteries. Besides, the *ex-situ* tests normally require the battery to be disassembled and the stripped electrode materials which may react with the trace H_2O, O_2, etc. in the glove box, causing irreversible damage, so the test results may not respond to the real state. Moreover, poor consistency is a concern when preparing electrodes at various states, so it is difficult to guarantee that the tested batteries are exactly the same. In addition, numerous batteries should be disassembled for a continuous test, which is really time consuming.

On the other hand, the "*in-situ*" means that the whole characterization is operandoly performed under real working condition, and thus real-resolved signals for electrode materials. The advantages of *in-situ* technique are as follows: (1) the operando evolution of dynamic structure changes under real working condition; (2) focus on the same location to ensure a good comparability among obtained results; (3) collect signals quickly to capture intermediate product information; (4) simple operation.

In this part, the *in-situ* techniques used to investigate carbon materials are summarized, including scanning probe microscopy (SPM), Raman spectra, Fourier transform infrared spectroscopy (FTIR), X-ray/neutron diffraction (XRD/ND), small-angle X-ray/neutron scattering, transmission electron microscope (TEM), and nuclear magnetic resonance spectroscopy (NMR).

In-situ SPM

SPM is an analytical technique for characterizing the real-space morphology of electrodes on the nanometer scale with minimal destruction. One of the most important advantages of SPM is that it can be conducted in a liquid environment to obtain operando information about the SEI film. The edge plane of graphite, which is fault-like, is the main research objective of SPM.

STM can visually observe the morphology changes of the graphite edge plane. Combining with atomic force microscope (AFM) which determines the change of the distance between graphite layers, STM can precisely speculate the growth mechanism of SEI film. It is found that SEI film growth mainly includes four stages: (1) HF reduction; (2) intercalation of solvated Li^+ into graphite; (3) electrolyte reduction on the surface of graphite; (4) enrichment of inorganic phases. The SEI film is initially triggered by electrochemical reaction at the defects and edge plane of graphite at 1.5 V due to the reduction of trace amount of HF to produce LiF particles. The inorganic particles are deposited in a ring-shaped and non-uniform form (Domi et al., 2011). Seidl et al. (2016) employed STM to monitor the SEI formation and found that structural damage began to appear on the graphite edge plane of the highly oriented pyrolytic graphite (HOPG) surface at above 1.0 V (**Figure 2A**). When the potential decreased to 0.9 V, the irreversible structural change became more pronounced. This phenomenon was further confirmed by AFM at voltage of 0.88 V, wherein the solvated was Li^+ inserted into the graphite layer and increased the layer space by 1.3 nm or higher (**Figure 2C**) (Liu T. et al., 2019). At 0.7 V, the graphite edge structure began to break down on a large scale, and the interface structure was more complicated (**Figure 2B**) (Seidl et al., 2016) since the reduction of solvated Li^+ produced gel precipitation at 0.74 V (**Figure 2C**). After this, the electrochemical process is accompanied by the formation of the inorganic layer to form a stable SEI film (Liu T. et al., 2019). The current findings provide a good understanding in the changes of the graphite edge plane during SEI formation, which offers guidance on the formation of a more uniform and stable SEI film.

The common electrolytes used in LIBs cannot guarantee the complete and uniform growth of SEI film, and the thickness of the formed SEI film varies at different locations. Specifically, the thickness of SEI film, measured by AFM, is about 10.4 nm after the first cycle (Xin et al., 2014), and increases by 3.4 nm for the second cycle, demonstrating the non-uniform growth of SEI film (Jeong et al., 2001). Commonly, solvated Li^+ ions intercalate into the graphite, and pass through the thinner SEI film, thus causing damage to the graphite structure (Jeong et al., 2001). Sometimes, solvated Li^+ would continuously intercalate into graphene layers, resulting in serious structural deterioration at the edge plane of graphite (Xin et al., 2014; Liu X. -R. et al., 2015). To promote uniform growth of SEI, proper electrolyte additives, e.g., vinyl ethylene carbonate, are added into electrolyte (Domi et al., 2012). It is obvious that *in-situ* observation of SEI growth is of great significance for optimizing SEI, and SPM has unparalleled advantages in this respect.

In-situ Raman Spectra and FTIR

Optical spectroscopy is an effective technique to identify materials and determine their structures, chemical compositions, and relative contents. Since the energy level of atoms, ions, and molecules varies in different materials, the energy levels of absorbing/emitting photons are also characteristic. For carbon materials, the optical spectroscopy is mainly based on Raman spectra and FTIR. The former focuses on structural changes in carbon materials (**Figure 3A**), and the latter is applicable to characterize molecular functional groups, which can be used in conjunction with Raman spectra.

Generally, carbon materials demonstrate three main peaks at 1,336, 1,580, and 2,670 cm^{-1} in Raman spectra, corresponding names are D, G, and 2D bands, respectively. D band, generally associated with the disordered materials, is applied to characterize graphite edge planes and internal defects. G peak normally shows the structural information for the graphite layer, such as the changes of C=C bond, electron cloud density, etc. 2D band is usually related to the number of graphene layers, and its changes are more complicated.

D band usually appears at a potential lower than 1.0–0.6 V during cycling of graphite/Li cells, which generally occurs with the generation of the SEI film, and D band disappears when the

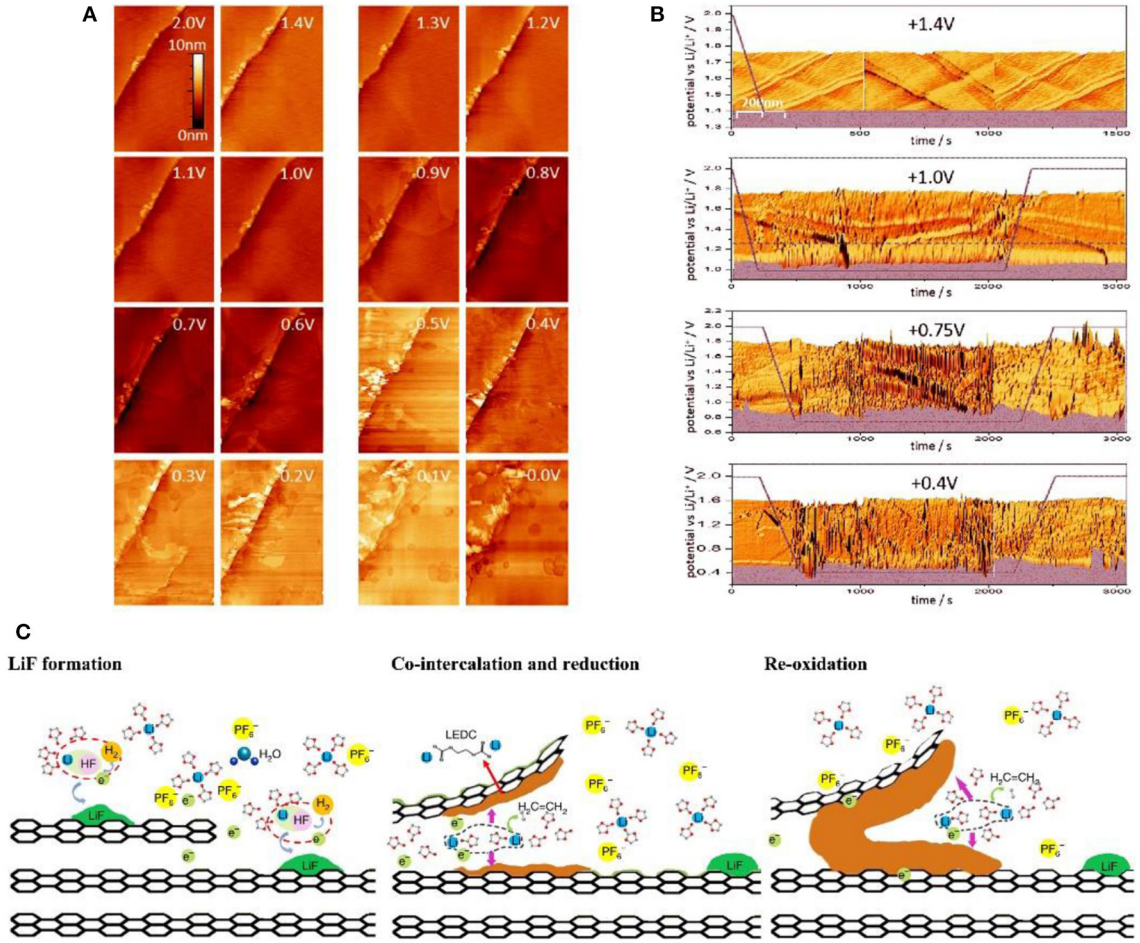

FIGURE 2 | (A) STM images of HOPG during delithiation process (Seidl et al., 2016). **(B)** *In-situ* real time STM images of HOPG (Seidl et al., 2016). **(C)** Schematic illustration of the interfacial formation chemistry during the very first lithiation (Liu T. et al., 2019).

SEI film becomes stable. It is difficult to observe the behavior of ion insertion into graphite through the changes of D band.

2D band existing below 0.15 V is mainly used to characterize the lithium intercalation mechanism. As ions intercalate into graphite, the graphite layer may bend and the electron cloud density between the graphite layers changes, resulting in a shift in 2D peak. Therefore, a reaction model for ions' insertion into graphite can be determined. For example, the 2D peak decreases from 2,681 to 2,611 cm^{-1} during the charging process, demonstrating that the graphite layer in the anode is bent after the ion insertion, corresponding with the Daumas–Hérold model (Sole et al., 2014).

The significant changes in the G band peak suggest the necessity of investigation on ion insertion mechanism (**Figures 3B,C**). In the absence of Li^+ insertion, i.e., 1.5–0.5 V, the value of the G band is around 1,582 cm^{-1}. With the beginning of lithium ion insertion into graphene layers, both the shoulder peak and the characteristic peak gradually raise up with the increase of the Li^+ content (**Figure 3C**). Simlar with voltage, the peak position of the G band shifts with the amount of inserted ions. The G band signal for single-layer graphene starts moving at 1.5 V and becomes stable at 0.5 V (**Figure 3B**), reflecting that the G band in Raman spectra is sensitive to the reactions in carbon materials. Therefore, it can be concluded that the capacity of single-layer graphene is not contributed to by the ion intercalated mechanism but by the reaction between graphene and ions or the adsorption mechanism of graphene (Pollak et al., 2010).

Reddy et al. investigated the working mechanism of sodium-ion batteries with hard carbon as an anode material. There are a large number of defects in hard carbon, which shows a strong D band peak. During the initial discharge process, the D band peak becomes weak, proving the adsorption and reaction mechanisms of Na storage. Afterwards, the G band peak shifts to a low-frequency region and becomes stable at 0.2 V. This also proves that the adsorption mechanism is the final stage of the capacity contribution in sodium storage (**Figures 3D,E**) (Anji Reddy et al., 2018).

It was found that K^+ were embedded in graphite without an initial dilution stage (Yoshino et al., 1987; Jian et al., 2015;

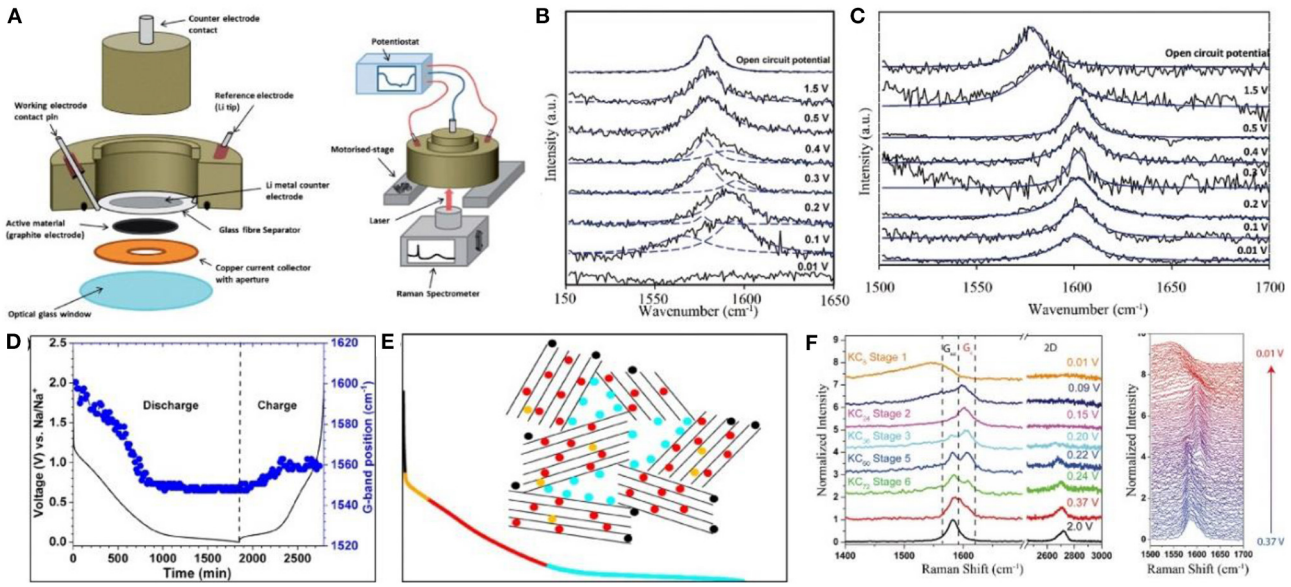

FIGURE 3 | (A) A schematic of the Raman cell assembly and in operation (Sole et al., 2014). **(B,C)** *In-situ* Raman spectra of the few-layer graphene and single layer graphene electrodes during electrochemical lithiation, respectively (Pollak et al., 2010). **(D)** Evolution of G-band position as a function of discharge and charge (Anji Reddy et al., 2018). **(E)** The discharge curve. The color code qualitatively represents different processes during discharge: Adsorption on surface sites (black), filling of defects in graphitic layers (orange), filling of the layers (red) and adsorption on nanopores (light blue) (Anji Reddy et al., 2018). **(F)** Selective Raman spectra taken at different states of charge and the waterfall plot of all Raman spectra taken between 0.37 and 0.01 V (Share et al., 2016).

Cohn et al., 2016) and no gradual peak shifting could be observed in Raman spectra. Pint et al. reported that the G band of graphene sheets moved to the high-frequency region of 1,589 cm^{-1} at 0.37 V for potassium ion batteries. At 0.15 V, only one peak at 1,589 cm^{-1} is identified. Subsequently, the peak began to evolve symmetrically and eventually generated a new peak. Therefore, three stages in K^+ insertion into the graphene layers were proposed, namely KC_{72}, KC_{24}, KC_8 (Share et al., 2016), and this mechanism is similar to Lithium intercalation into graphene sheets which was reported by Pollak et al. (2010) (**Figure 3F**).

By comparing graphene sheets with different layers, the failure mechanism can be predicted through the variation in tension of the single-layer material which is evaluated by the G band. Generally, failure of anode material is caused by structural changes, volume expansion, and damage to the SEI film, and Raman spectra has been proved to be an efficient technique for failure mechanism prediction (Zou et al., 2016).

FTIR, sensitive to polar groups, e.g., OH^-, C=O, COO^-, is a good technique to characterize changes of functional groups in carbon materials (Li et al., 2013). For example, *in-situ* FTIR can show the evolution of the groups in reduced graphene oxide (rGO) during the electrochemical process. The absorption strength of oxygen-containing groups is significantly weaker than that of pristine materials after the initial cycle, demonstrating that the capacity of rGO in the first cycle is mostly irreversible. The signal for the C=O group in the EC is clearly identified in the SEI film, proving that the EC molecule plays a great role in the SEI formation.

Fiber Evanescent Wave Spectroscopy, a cost-effective, real-time, non-destructive, and robust method to optically interrogate a harsh environment, is also designed as an *in-situ* characterization method for LIBs (Ghannoum et al., 2016). By quantitatively analyzing the reflectance of visible and infrared light (500–900 nm), a direct correlation between the state of charge and the measured reflectance is demonstrated for graphite anode in wavelengths ranging from 750 to 900 nm (near-infrared band). Based on this observation, a custom-designed Swagelok cell with etched optical fiber embedded between the graphite electrode and separator is assembled to measure the transmittance of graphite anode in the near-infrared band. This technique is expected to be developed as a unique inexpensive method to estimate the SOC of a LIB.

In-situ Diffractive Techniques (Neutrons/X-Rays)

XRD and neutron diffraction (ND) are the most important techniques to study material structure. The orientation and intensity of the diffraction in the spatial distribution are closely related to the crystal structure. However, since the principle of XRD is that the X-ray interacts with electrons, the obtained scattering intensity in XRD patterns is proportional to the atomic number of elements, and a low sensitivity to light elements such as Li and C is delivered. Fortunately, scattering intensity of ND originated from the interaction between neutrons and nuclei is non-linearly related to nuclei, therefore ND is particularly suitable for probing the atomic arrangements of lithium and carbon during lithium intercalation. Hence, XRD is applied to provide information on the reversibility of the Li^+ intercalation process through the structure changes of graphite while the ND is suitable for the determination of compositions of LiC_x.

Ion-intercalated graphite would induce a series of phase transitions as well as the volume change. The former has guiding significance for developing new electrode materials while the latter provides valuable information for practical applications (capacity decay and safety issue). Graphite is composed of multiple layers of graphene, and the intercalation mechanism at the beginning of ion intercalation, during which ions would be uniformly intercalated into each layer or into specific layers, is a remaining debate. Fortunately, combining *in-situ* XRD and ND, the structural evolution and lithium intercalation behavior can be well-characterized.

Dahn, Janek, and other groups demonstrated the phase diagram of Li_xC_6 and presented the single-phase and coexisting-phase region by *in-situ* XRD (**Figures 4A–C**) (Dahn, 1991; Schweidler et al., 2018). The phase region and the graphite volume expansion are interrelated: In stage 2 and stage 1, the volume of graphite remains constant and only the single-phase is observed. At the coexisting-phase region, graphite is in an indeterminate state and tends to be stable. In order to achieve stability under Li intercalation conditions, the graphene layers in graphite must be in the same chemical environment (Mathiesen et al., 2019). Therefore, there are only two possibilities: (1) lithium intercalates into each layer indiscriminately; (2) lithium intercalates into only one layer in every two layers, so that all graphenes are in the same chemical state (**Figure 4C**). In the dilute region, lithium inserts into the graphene interlayer, enlarging the spatial distance of the graphene layers, thus the volume expands in *c* axis. During the transition from stage 2 to stage 1, more space is needed for lithium storage and thus lithium intercalates into the unoccupied layers accompanied by further expansion in volume (**Figure 4D**). This mechanism can explain well why the battery is allowed to be discharged and charged to state of charge (SOC) 20 and 80%, respectively. The reasons are as follows: (1) It is necessary to retain certain lithium ions in graphite layer during discharge, ensuring the reversible lithium intercalation/deintercalation without destroying the graphite structure; (2) when charged to SOC of 100%, the risk of Li metal deposition on the surface of the negative electrode is greatly increased, resulting in safety issues; it is likely to cause the deposition of the Li metal in the negative electrode, which may cause serious safety issues; (3) when the battery is operated between SOC of 20–80%, the graphite experiences only a small volume expansion, which is beneficial to the stability of the battery.

For LIBs, NIBs, and PIBs with different electrolyte systems, *in-situ* XRD research is important to understand the battery operating mechanism. By collecting the signal of crystal phases, the structure changes of the electrode material during the charging/discharging process can be well-detected. For example, Kang et al. found that $[Na–ether]^+$ complexes would be reversibly intercalated into carbon materials and the intercalation of solvated Na^+ followed a stage process. After several intercalation/deimtercalation cycles, Na_xC_y a single phase of Na_xC_y is observed at Na/C ratio of 1/72 and the stage 1 compound is presented as a mixture with Na/C ratio from 1/28 to 1/21 (**Figure 4E**) (Kim et al., 2015).

Although some valuable phenomena have been observed, the structural evolution of Li^+ embedded in graphite is still not fully understood due to the weak scattering of X-rays by Li and C, especially at a low lithium content. In this regard, neutron diffraction, which shows a strong diffraction intensity for light elements, can be employed as a powerful supplementary tool to track the details of the intercalation/deintercalation process.

In the initial process of intercalation, the LiC_x intermediate phase is hardly confirmed by XRD due to the low content. Based on the hexagonal structure LiC_x, *c* lattice parameter of 10.42 Å is considered to be related to three layers of lithiated graphene (Pang et al., 2014). ND displays an identifiable scattering intensity even at a very small amount of LiC_x. Nanda et al. revealed the existence of LiC_{12} phase in the final stage of lithium insertion in a commercial battery, proving that full intercalation of graphite is prohibited under real working condition. More specifically, Pang et al. investigated a $LiNi_{1/3}Co_{1/3}Mn_{1/3}O_2$/graphite full cell with 91 mol% LiC_6 and 9 mol% LiC_{12} at an overcharge potential of 4.5 V (Pang et al., 2014). The detailed information of lithium intercalation/deintercalation and the transformation of LiC_x intermediate phase can be tracked through neutron diffraction. Bobrikov et al. studied the changes of graphite by ND. It is found that the initial increase in *d* space is resulted from the formation of $LiC_{\sim 27}$.Further Li^+ intercalation leads to the formation of LiC_{18} phase. From the phase of LiC_{18} to LiC_{12}, there is no obvious change in *d* space and it is considered to be due to the redistribution of lithium in the basal planes of graphite (**Figure 5A**). Based on the strong scattering data, one can illustrate the content of different LiC_x phases at different states of charge (**Figure 5B**) (Bobrikov et al., 2014).

Since XRD shows advantages in the determination of unit cell parameters while neutron diffraction is more sensitive to light elements, there are still certain differences between these two *in-situ* techniques in characterizing material structural changes. The structural changes of graphite anode during cycling were investigated through *in situ* neutron diffraction and *in situ* high energy synchrotron XRD by Sharma et al. (2010) and He et al. (2013), respectively. In both works, a two-phase region composed of the lithiated graphite phase and LiC_6 was identified. According to phase changes shown by neutron diffraction, it is inferred that Li may be trapped in the SEI layer results in minimal structural changes to the lithiated graphite anode across the constant cell voltage regions of the electrochemical cycle. In the *in situ* XRD work, the relationship between the variation of d-spacing and the lithium content in graphite has been explored, and it is found that the dynamic mechanism of lithium intercalation into graphite may deviate from the traditional stage mechanism at a higher rate. It is noted that XRD shows more advantages than neutron diffraction for Na and K ions with larger atomic numbers.

Small-angle neutron scattering (SANS) is a technique to study the internal mesoscale structure of materials by elastic neutron scattering. Due to its high sensitivity to light elements, the lithium inercalation/deintercalation process can be visually observed during charging/discharging. During lithium intercalation, the relationship between lithium intercalation and voltage can be deduced due to the different neutron absorption intensity of lithium and graphite (Zhou et al., 2016).

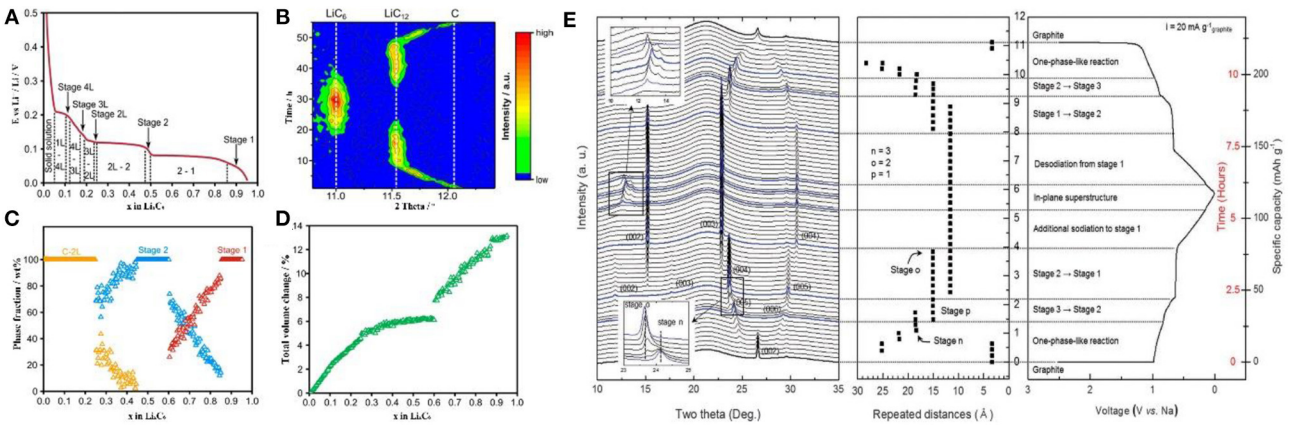

FIGURE 4 | (A) The different lithium intercalation stages and phase transition regimes in the second cycle. **(B)** Evolution of the 002 reflection (equivalent to 002 for LiC_{12} and 001 for LiC_6) during the second cycle. **(C)** Phase fraction, and **(D)** total volume change of graphite vs. lithium content (Schweidler et al., 2018). **(E)** In operando synchrotron X-ray diffraction analysis of the structural evolution of the ternary Na-ether-graphite system observed during electrochemical solvated-Na-ion intercalation and deintercalation into/out of graphite (Kim et al., 2015).

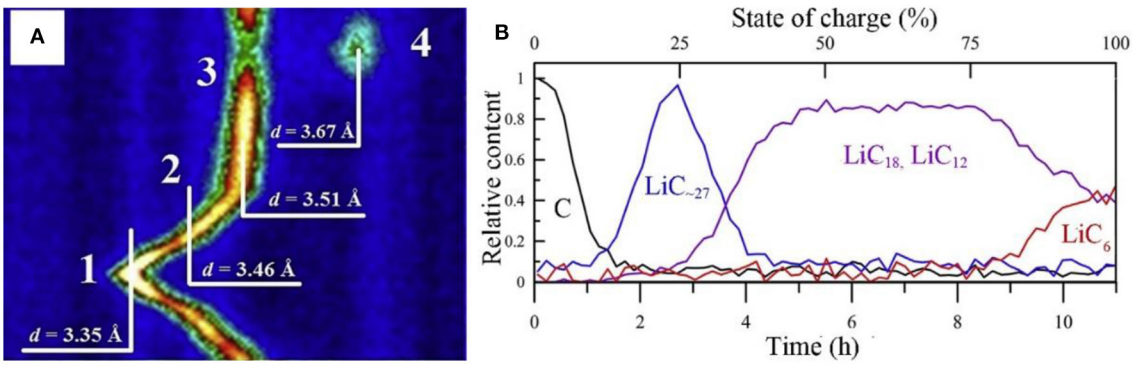

FIGURE 5 | (A) 2D diffraction pattern region characterizing structural processes in LFP-battery anode. Initial state of the anode graphite without lithium (1, d = 3.35 Å), and sequentially emerging phases $LiC_{\sim 27}$ (2, d = 3.46 Å), LiC_{18}, LiC_{12} (3, d = 3.51 Å), and LiC_6 (4, d = 3.67 Å) for battery. **(B)** Content of different LiC_x phases of battery in course of one charge cycle as a function of time (lower scale) or SOC (upper scale) recovered from relative changes in intensity of corresponding diffraction peaks (Bobrikov et al., 2014).

In-situ SAXS/SANS

When X-rays pass through a sample with nano-scale density inhomogeneities inside, the scattering phenomenon occurs within a small angle range ($2\theta \leq 5^{\circ}$) close to the original beam, which is called small-angle neutron scattering (SAXS) (**Figure 6A**). Since the signal is a statistical result of many scatterers affected by particle size, shape, dispersion, orientation, and electron density distribution, SAXS is an important method to study the submicroscopic internal structure of materials.

SAXS is a superior technique to study the changes of pore structure. Synchronous light source with high energy X-rays enables SAXS to *in-situly* characterize the porous carbons in lithium-ion batteries, such as the entry of electrolytes, chemical reactions in the pores and the changes of pores. Csencsits et al. investigated the lithium storage during the charging/discharging process through continuous SAXS and no evident structure change was observed, suggesting that the electrolyte does not enter the porous material and would not react with the inside material (Sandí, 1999).

Generally, porous carbon materials exhibit high specific capacity during ions storage and there is no clear explanation for this high capacity. In Dhan's work, no changes in the pore structure of porous carbon materials has been observed during sodium intercalation. Instead, when the cell is discharged close to 0 V, sodium begins to deposit in the micropores to form metallic sodium, which blocks the micropores. During the charging process, the metallic sodium migrates away and the pores are gradually released. This work proves that the metal deposition in carbon materials is reversible (Stevens and Dahn, 2000b).

The basic principle of SANS is similar to that of SAXS (**Figure 6B**), while SANS is sensitive to the light elements, such as H, O, Li, etc. (Bridges et al., 2012; Zhou et al., 2016). This advantage is beneficial in determining the components and position of light elements in materials. In particular,

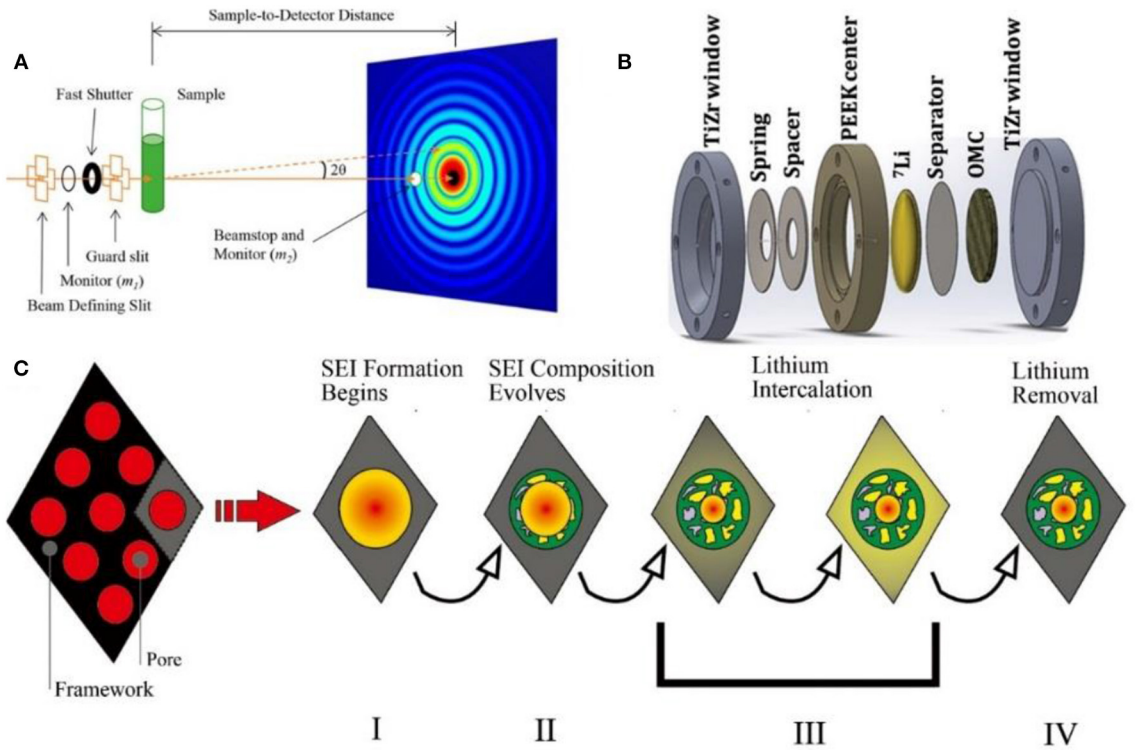

FIGURE 6 | (A) Schematic illustration of the various stages of the initial charge/discharge cycle for the non-deuterated cell (Li et al., 2016). **(B)** Schematic view of the operando SANS cell (Jafta et al., 2019). **(C)** Schematic illustration of the various stages of the initial charge/discharge cycle for the non-deuterated cell, including: Stage I (pore filling and surface adsorption of solvated lithium during discharge), Stage II (SEI formation), Stage III (lithium intercalation), and Stage IV (lithium removal during charging) (Bridges et al., 2012).

in-situ, SANS is suitable for observing the interface between the carbon materials and the electrolyte, as well as the structural changes of the bulk material. Therefore, SANS is applied to study the SEI growth, components and lithiation gradients in carbon materials.

SANS can observe the framework changes of hard carbon in different electrolyte systems. During the formation of SEI film in the first cycle, the graphite interlayer will be enlarged due to the intercalation of solvated lithium ions into graphite, causing an increase of about 5%. After the SEI film is well-grown, the volume changes during cycling would be <1% (Bridges et al., 2017). It is noted that SEI film growth occurs in all pores in a hard carbon framework (**Figure 6C**). Besides, the results show that SEI is composed of various lithium containing salt, such as Li_2CO_3 and/or $(CH_2OCO_2Li)_2$. As the charge/discharge cycle progresses, the content of the inorganic phase, such as Li_2O, LiOH, LiF, etc. gradually increases. It is also observed that the intercalation of lithium occurred at a lower potential which was the dominant scattering process (Bridges et al., 2012). Jafta et al. found that the SEI formation followed a similar mechanism in both diluted and high concentration electrolytes (Jafta et al., 2019). However, due to the high viscosity of the high concentration electrolyte, the filling of the micropores occurs only at a low potential. Moreover, the formed SEI film is thinner in high concentration electrolyte since the SEI is formed by the decomposition of Li salt instead of the organic solvents.

Imaging, phase changes of pores, and crystals, as well as the component detection are important techniques to understand the working mechanism of batteries. They also provide important reference for improving the consistency of industrial batteries and battery failure analysis.

In-situ TEM

TEM is the projection of an accelerated and concentrated electron beam onto a thin sample and the electron collides with atoms to change its direction, resulting in solid angle scattering. Since the scattering angle is related to the density and thickness of the sample, the images are formed with different brightness and darkness, and displayed on a imaging device after being enlarged (**Figure 7A**). The TEM images are very sensitive to the homogeneity and spatial change of the characterized samples. As all known, electrode materials are often accompanied by complex interface evolution, new phases formation, structures change, etc. during charge and discharge process. Therefore, *in-situ* TEM is emerging as a powerful tool in revealing the underlying reaction mechanisms between the intercalated ions and carbon host,

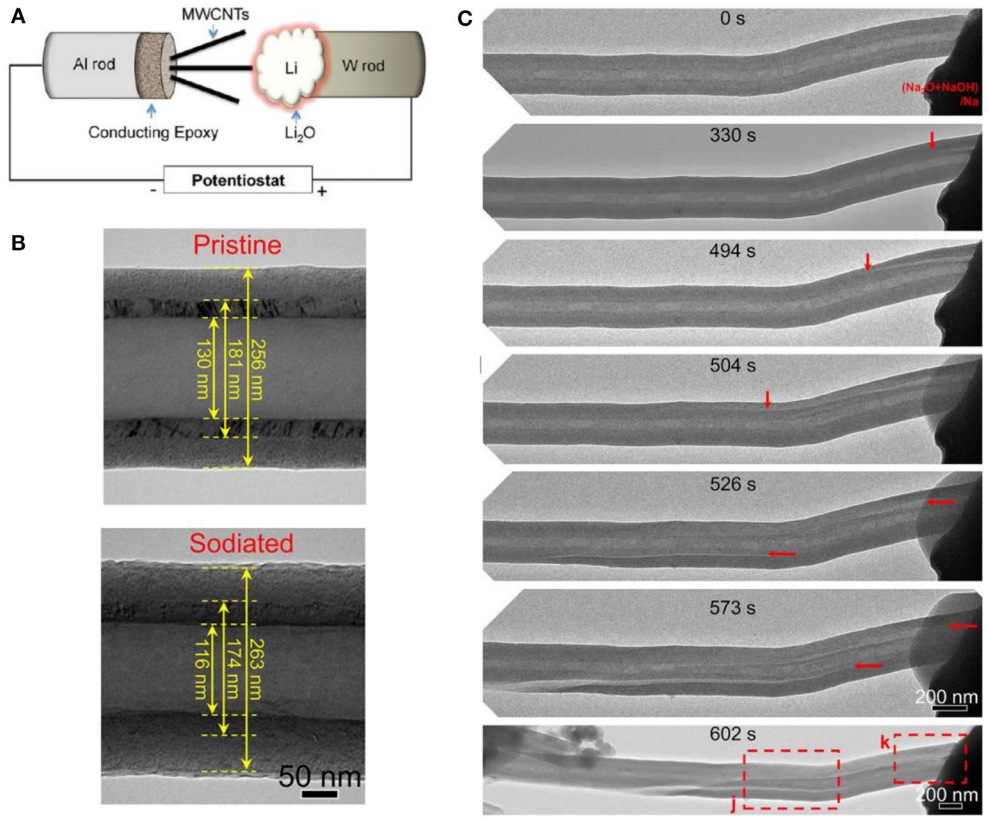

FIGURE 7 | (A) Schematic illustration of the *in-situ* TEM experimental setup. **(B)** Structure changes of a bilayer CNF during sodiation. **(C)** Sodiation-induced crack nucleation and propagation in a hollow bilayer CNF (Liu et al., 2014).

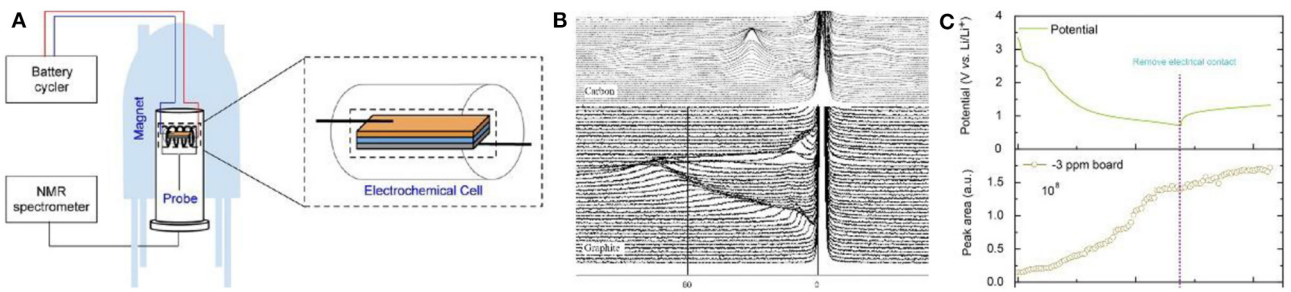

FIGURE 8 | (A) Schematic illustration of the *in-situ* NMR experimental setup. **(B)** *In-situ* ^{7}Li NMR during the first galvanostatic cycle: top picture, lithium in graphite; bottom picture, lithium in the carbon/carbon composite (Letellier et al., 2006). **(C)** Potential–time plot to demonstrate the potential evolution after remove the electrical contact from rGO cell (top); *In-situ* NMR peak area evolution of the −3 ppm board (bottom) (Tang et al., 2016).

observing the change of SEI film and microstructure during cycling (Wen et al., 2014).

One of the basic functions of *in-situ* TEM is to observe the change of layer spacing. After sodium intercalation, the graphite layer spacing increases from 0.38 to 0.40 nm (Wang et al., 2019). The size of the carbon nanotubes and few-layer graphene sheets increases from 3.4 to 3.6 Å, with a 5.9% diameter expansion (Liu et al., 2011). Due to its one-dimensional structure, it is much easier to characterize carbon fiber *in-situ* (**Figure 7B**).

TEM can also capture the information about the formation of new phases during the electrochemical process. During lithiation, a Li_2O layer would be formed in several layers on the surface of graphene nanoribbons. However, this formed Li_2O layer does not completely transform to freely migrating lithium ions during delithiation. As a result, part of Li_2O deposits as the component of SEI film (Liu et al., 2012). Direct observation of irreversible oxides, such as Na_2O, can be used to estimate the cause of battery capacity loss, especially in the materials with large specific surface

area or abundant hydroxyl groups (Liu et al., 2011; Wan et al., 2016).

rGO has a large specific surface area, multiple defects, and a complex ionization mechanism. Hu et al. studied the electrochemical behavior on rGO through *in-situ* TEM. At voltage between 2 and 0.15 V, Na^+ is mainly adsorbed on the surface of defects of rGO. Below 0.15 V, rGO begins to swell and sodium ions are inserted into the graphite layer (Wang et al., 2019). Besides, it is also occasionally observed that metallic sodium clusters with the sizes of 10 nm are deposited on the surface and defects of rGO, leading to a high reversible capacity. In half-cells, rGO shows a reversible specific capacity of up to 450 mAh g^{-1}. Due to the low volume expansion, rGO can cycle 750 cycles at high rate (Wan et al., 2016).

Generally, failure of carbon material is accompanied by instability of the material structure. After lithium intercalation, MWCNTs become brittle and the outer carbon structure begins to collapse when stretched (Liu et al., 2011). This collapse would lead to the growth of flaws in the SEI film. Subsequently, the collapse begins to spread along the axis. To provide mechanistic insights into the electrochemical reaction, microstructure evolution and mechanical degradation of carbon-based anodes during sodiation and potassiation, individual carbon nanofibers (CNFs) was studied by *in situ* TEM (**Figure 7C**) and this revealed that the mechanical degradation of CNFs takes place through the formation of longitudinal cracks near the c-C/d-C interface during sodiation and potassiation (Liu et al., 2014).

In addition to the volume change and material analysis, *in-situ* TEM also provides information on the rate and uniformity of ion transport in carbon materials (Shan et al., 2014).

In-situ NMR

NMR, which provides information about the number and type of chemical groups in the molecule, is an important technique to determine organic and inorganic compounds in battery at different states of charge (**Figure 8A**). In a single NMR spectrum, different lithium compounds, such as lithium salt in the electrolyte, lithium compounds in the SEI film and lithium intercalated into graphite, can be identified separately. And thus, the state of lithium during the charge/discharge process can be clearly observed by *in-situ* NMR (Gerald et al., 2001).

For NMR testing, both ^{6}Li and ^{7}Li can be used, however, ^{7}Li is more sensitive to discriminate in the spectrum. In a spectrum, lithium in SEI films and electrolyte exists in the 0 ppm while metallic Li is located at near 263 ppm. During the intercalation process of lithium into carbon materials, the peak for LiC_x gradually shifts from 0 ppm to the position for Li metal (Letellier et al., 2003). Letellier et al. did not observe independent phases in *in-situ* ^{7}Li NMR, indicating that the intercalation of lithium into graphite is relatively continuous, while LiC_x species at each stage can be distinguished (**Figure 8B**) (Stevens and Dahn, 2000b; Bridges et al., 2017).

SEI film plays an important role in carbon anode materials and its growth mechanism and composition are crucial to battery design. Loh et al. studied the lithium compounds in SEI and found that their content gradually increased during the first discharge process and then was basically stable in the following charge process (**Figure 8C**). It is worth noting that the changes during high self-discharge was also intuitively observed by *in-situ* NMR (Tang et al., 2016). Unfortunately, only the specific composition and formation of the SEI film on the carbon surface were investigated by NMR, the detailed mechanism was not discussed. Later, the surface of Si anode was analyzed through NMR C spectrum by Grey et al., confirming that NMR can be applied to speculate the specific decomposition mechanism of the electrolyte on the carbon surface as well as the influence of the electrolyte additive on the SEI film formation (Jin et al., 2017).

Different from a single technique, multiple techniques can provide more information to better reflect the internal structural changes. To promote better fundamental understanding of K^+ storage behavior in graphite, *in situ* Raman mapping and *in situ* X-ray diffraction (XRD) characterizations, in combination with density functional theory simulations are carried out to correlate the real-time electrochemical K^+ intercalation/deintercalation process with structure/component evolution. The experimental results, together with theoretical calculations, reveal that the reversible K ion intercalation into graphite follows a staging transition (Liu J. et al., 2019).

Summary of *in-situ* Techniques for Carbon Materials

So far, carbon-based materials are the most ideal and widely used anode materials for alkali ion batteries. With the increasing requirements on the performance of commercial batteries, such as energy density, operating temperature range and rapid charging/discharging, developing new carbon-based anode materials is one of the most concerned issues. Figuring out the ion diffusion behavior of the battery under real working conditions, and understanding the working mechanism of the active materials and the changes of the interface are of great significance for the designing new materials and improving battery performance. However, the mechanism of different carbon materials, the structural changes of the same material at different working conditions, the formation/transformation of chemical compounds are extremely complicated, and it is difficult to characterize them with conventional methods (**Figure 9**).

With *in-situ* technologies, changes of components and material structure in the battery can be characterized operandoly while the electrochemical reaction is proceeding. However, it is difficult to deduce the working mechanism based on the data obtained by a single characterization technique. In terms of the mechanism characterization of alkali metal ion batteries, SPM and TEM are suitable for observing the growth of SEI film on the surface of carbon materials, Raman spectroscopy can observe the changes of carbon materials during the formation of SEI film, FTIR, and NMR are used to determine the chemical composition of the SEI film, XRD and ND are applied to study intercalation/deintercalation behaviors of alkali ions into/from carbon materials, SAXS and SANS mainly observe the structural changes of microporous or mesoporous materials which are of great benefit to help understand the ions intercalation and the

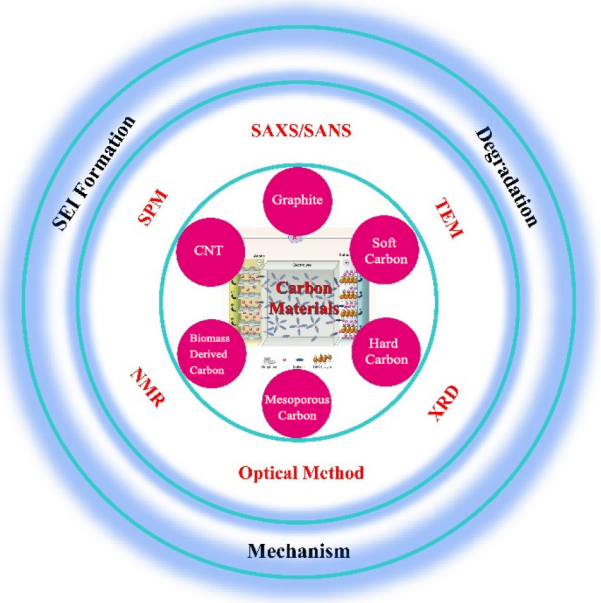

FIGURE 9 | Scheme of *in-situ* techniques for the studies of carbon anode in alkali metal ion batteries (Dunn et al., 2011).

SEI formation, and XRD, TEM, and SANS are often used in the study of material failure. By combining the observation of these characterization techniques, a true working mechanism of alkali metal ion batteries would be better understood and deduced.

SUMMARY AND PERSPECTIVES

In conclusion, the recent research on the understanding the working behavior of carbon materials in alkali ion batteries through *in-situ* techniques has been summarized. The ion intercalation mechanism, SEI formation and degradation of carbon materials in anode have been explored using *in-situ* techniques including SPM, optical spectroscopy, XRD, SAXS/SANS, TEM, and NMR. Nonetheless, except for graphite, other types of materials are just partially studied. Hence, more details of the different carbon materials need to be investigated in order to provide guidance for future material development. It is noted that there are many studies on graphite anodes and their mechanism is relatively clear. However, the mechanism for new carbon-based materials is still controversial. Research on these new carbon materials can provide guidance for the development of new carbon-based anode materials.

As the anode material for the ion batteries, the specific capacity of graphite is limited by the ion intercalation mechanism. To increase the specific capacity of carbon-based materials, it is necessary to introduce a different capacity contribution mechanism. However, the new mechanisms, such as defect adsorption and ions deposition, lead to lower initial Colombic efficiency and thus difficulty in practical application in commercial batteries. Therefore, improving the initial Colombic efficiency and stability of carbon materials is the basis for designing new materials. As is well-known, the adsorption of ions in the defect sites and the deposition in the pores can greatly increase the specific capacity of the carbon based anode materials. However, there are still a large number of phenomena that need to be determined clearly, such as the influence of different kinds of defects, contribution of pore size and distribution to capacity, as well as the exact reaction process. Addressing these issues is essential for the design of practically applicable high specific capacity anode materials.

Analysis and understanding of chemical reactions, degradation mechanisms and thermal failure mechanisms ion batteries play particularly important roles for the development of confidence electrode materials. The material structural transformation during the charge/discharge process, the redox process, the transformation of SEI formation, and other side reactions that occur in the battery can be monitored by *in-situ* techniques. However, most of these *in-situ* techniques suffer from poor penetration and small characterization depth, as a result, *in situ* devices with complex structures need to be specially designed. Therefore, the development of non-destructive *in situ* techniques to directly monitor the structural changes in commercial batteries is still urgently needed. In addition, a single *in situ* characterization only evaluates specific signals which makes it difficult to fully reflect the behaviors inside the battery. To fully understand the behavior of materials under working conditions, multiple *in situ* techniques are required. Therefore, evaluation of the internal behaviors via multi-techniques under the same working conditions is the focus of future.

In situ techniques exhibit unparalleled advantages in mechanism research and characterization of reaction behavior. With the application of more *in situ* techniques and the maturity of technology, more details about the real working behaviors in alkali metal ion batteries will be observed. And these new findings will enhance the understanding of alkali metal ion batteries and promote the development of new electrode materials.

AUTHOR CONTRIBUTIONS

RD and YalH collected the articles and wrote the first manuscript. GL and QL organized references and revised the manuscript. TW organized the figures. YanH and YL modified the format and revised the manuscript. HH revised the manuscript, approved the final version, and supervised the whole work. All authors contributed to revise the manuscript, approved the final version, and agreed to be accountable for all aspects of this work.

FUNDING

This review was partially sponsored by the Shenzhen Science and Technology Innovation Commission under grant JCYJ20180507181806316, the City University of Hong Kong (Project No. 9610399), and the Shenzhen Research Institute, City University of Hong Kong.

REFERENCES

Abraham, D. P., Knuth, J. L., Dees, D. W., Bloom, I., and Christophersen, J. P. (2007). Performance degradation of high-power lithium-ion cells—electrochemistry of harvested electrodes. *J. Power Sources* 170, 465–475. doi: 10.1016/j.jpowsour.2007.03.071

Andersson, A. M., Edström, K., and Thomas, J. O. (1999). Characterisation of the ambient and elevated temperature performance of a graphite electrode. *J. Power Sources* 81–82, 8–12. doi: 10.1016/S0378-7753(99)00185-8

Anji Reddy, M., Helen, M., Groß, A., Fichtner, M., and Euchner, H. (2018). Insight into sodium insertion and the storage mechanism in hard carbon. *ACS Energy Lett*. 3, 2851–2857. doi: 10.1021/acsenergylett.8b01761

Armand, M., and C. J. M., Duclot M, J. (1979). "Polyethers as solid electrolytes," in *Proceedings of the International Conference* on *Fast Ion Transport in Solids: Electrodes Electrolytes* (Lake Geneva, WI), 131–136.

Armand, M., and Tarascon, J. M. (2008). Building better batteries. *Nature* 451, 652–657. doi: 10.1038/451652a

Armand, M., and Touzain, P. (1977). Graphite intercalation compounds as cathode materials. *Mater. Sci. Eng.* 31, 319–329. doi: 10.1016/0025-5416(77)90052-0

Aurbach, D. (2000). Review of selected electrode–solution interactions which determine the performance of Li and Li ion batteries. *J. Power Sources* 89, 206–218. doi: 10.1016/S0378-7753(00)00431-6

Aurbach, D., Levi, M. D., Levi, E., and Schechter, A. (1997). Failure and stabilization mechanisms of graphite electrodes. *J. Phys. Chem. B* 101, 2195–2206. doi: 10.1021/jp962815t

Aurbach, D., Markovsky, B., Talyosef, Y., Salitra, G., Kim, H. J., and Choi, S. (2006). Studies of cycling behavior, ageing, and interfacial reactions of LiNi 0.5Mn1.5O4 and carbon electrodes for lithium-ion 5-volt cells. *J. Power Sources* 162, 780–789. doi: 10.1016/j.jpowsour.2005.07.009

Bai, Y., Wang, Z., Wu, C., Xu, R., Wu, F., Liu, Y., et al. (2015). Hard carbon originated from polyvinyl chloride nanofibers as high-performance anode material for Na-ion battery. *ACS Appl. Mater. Interfaces* 7, 5598–5604. doi: 10.1021/acsami.5b00861

Bao, C., Yao, W., Wang, E., Chen, C., Avila, J., Asensio, M. C., et al. (2017). Stacking-dependent electronic structure of trilayer graphene resolved by nanospot angle-resolved photoemission spectroscopy. *Nano Lett.* 17, 1564–1568. doi: 10.1021/acs.nanolett.6b04698

Bobrikov, I. A., Balagurov, A. M., Hu, C. W., Lee, C. H., Chen, T. Y., Deleg, S., et al. (2014). Structural evolution in LiFePO4-based battery materials: *in-situ* and *ex-situ* time-of-flight neutron diffraction study. *J. Power Sources* 258, 356–364. doi: 10.1016/j.jpowsour.2014.02.060

Bodenes, L., Dedryvère, R., Martinez, H., Fischer, F., Tessier, C., and f Pérès, P. (2012). Lithium-ion batteries working at 85°C: aging phenomena and electrode/electrolyte interfaces studied by XPS. *J.Electrochem. Soc.* 159, A1739–A1746. doi: 10.1149/2.061210jes

Boehm, R. C., and Banerjee, A. (1992). Theoretical study of lithium intercalated graphite. *J. Chem. Phys.* 96, 1150–1157. doi: 10.1063/1.462202

Bommier, C., and Ji, X. L. (2015). Recent development on anodes for Na-ion batteries. *Israel J. Chem*. 55, 486–507. doi: 10.1002/ijch.201400118

Bridges, C. A., Sun, X. G., Guo, B. K., Heller, W. T., He, L. L., Paranthaman, M. P., et al. (2017). Observing framework expansion of ordered mesoporous hard carbon anodes with ionic liquid electrolytes via *in situ* small-angle neutron scattering. *ACS Energy Lett*. 2, 1698–1704. doi: 10.1021/acsenergylett.7b00472

Bridges, C. A., Sun, X. G., Zhao, J. K., Paranthaman, M. P., and Dai, S. (2012). *In situ* observation of solid electrolyte interphase formation in ordered mesoporous hard carbon by small-angle neutron scattering. *J. Phys. Chem. C.* 116, 7701–7711. doi: 10.1021/jp3012393

Broussely, M., Herreyre, S., Biensan, P., Kasztejna, P., Nechev, K., and Staniewicz, R. J. (2001). Aging mechanism in Li ion cells and calendar life predictions. *J. Power Sources* 97–98, 13–21. doi: 10.1016/S0378-7753(01)00722-4

Bryngelsson, H., Stjerndahl, M., Gustafsson, T., and Edström, K. (2007). How dynamic is the SEI? *J. Power Sources* 174, 970–975. doi: 10.1016/j.jpowsour.2007.06.050

Cao, Y., Xiao, L., Sushko, M. L., Wang, W., Schwenzer, B., Xiao, J., et al. (2012). Sodium ion insertion in hollow carbon nanowires for battery applications. *Nano Lett.* 12, 3783–3787. doi: 10.1021/nl3016957

Cheng, F., Tao, Z., Liang, J., and Chen, J. (2008). Template-directed materials for rechargeable lithium-ion batteries†. *Chem. Mater.* 20, 667–681. doi: 10.1021/cm702091q

Churikov, A. V. (2001). Transfer mechanism in solid-electrolyte layers on lithium: influence of temperature and polarization. *Electrochim. Acta* 46, 2415–2426. doi: 10.1016/S0013-4686(01)00439-X

Cohn, A. P., Muralidharan, N., Carter, R., Share, K., Oakes, L., and Pint, C. L. (2016). Durable potassium ion battery electrodes from high-rate cointercalation into graphitic carbons. *J. Mater. Chem. A*. 4, 14954–14959. doi: 10.1039/C6TA06797B

Dahn, J. R. (1991). Phase diagram of LixC6. *Phys. Rev. B Condens. Matter*. 44, 9170–9177. doi: 10.1103/PhysRevB.44.9170

Ding, J., Wang, H. L., Li, Z., Kohandehghan, A., Cui, K., Xu, Z. W., et al. (2013). Carbon nanosheet frameworks derived from peat moss as high performance sodium ion battery anodes. *Acs Nano* 7, 11004–11015. doi: 10.1021/nn404640c

Domi, Y., Ochida, M., Tsubouchi, S., Nakagawa, H., Yamanaka, T., Doi, T., et al. (2011). *In situ* AFM study of surface film formation on the edge plane of HOPG for lithium-ion batteries. *J. Phys. Chem. C*. 115, 25484–25489. doi: 10.1021/jp2064672

Domi, Y., Ochida, M., Tsubouchi, S., Nakagawa, H., Yamanaka, T., Doi, T., et al. (2012). Electrochemical AFM observation of the HOPG edge plane in ethylene carbonate-based electrolytes containing film-forming additives. *J. Electrochem. Soc*. 159, A1292–A1297. doi: 10.1149/2.059208jes

Dresselhaus, M. S., and Dresselhaus, G. (2002). Intercalation compounds of graphite. *Adv. Phys.* 51, 1–186. doi: 10.1080/000187301101013644

Dunn, B., Kamath, H., and Tarascon, J-M. (2011). Electrical energy storage for the Grid A battery. *Science* 334, 928–935. doi: 10.1126/science.1212741

Edström, K., Herstedt, M., and Abraham, D. P. (2006). A new look at the solid electrolyte interphase on graphite anodes in Li-ion batteries. *Power Sources J.* 153, 380–384. doi: 10.1016/j.jpowsour.2005.05.062

Ein-Eli, Y., Markovsky, B., Aurbach, D., Carmeli, Y., Yamin, H., and Luski, S. (1994). The dependence of the performance of Li-C intercalation anodes for Li-ion secondary batteries on the electrolyte solution composition. *Electrochim. Acta* 39, 2559–2569. doi: 10.1016/0013-4686(94)00221-5

Gaddam, R. R., Yang, D., Narayan, R., Raju, K., Kumar, N. A., and Zhao, X. S. (2016). Biomass derived carbon nanoparticle as anodes for high performance sodium and lithium ion batteries. *Nano Energy*. 26, 346–352. doi: 10.1016/j.nanoen.2016.05.047

Gerald, R. E., Sanchez, J., Johnson, C. S., Klingler, R. J., and Rathke, J. W. (2001). *In situ* nuclear magnetic resonance investigations of lithium ions in carbon electrode materials using a novel detector. J. *Phys. Condens. Mat.* 13, 8269–8285. doi: 10.1088/0953-8984/13/36/304

Ghannoum, A., Norris, R. C., Iyer, K., Zdravkova, L., Yu, A., and Nieva, P. (2016). Optical characterization of commercial lithiated graphite battery electrodes and *in situ* fiber optic evanescent wave spectroscopy. *ACS Appl. Mater. Interfaces* 8, 18763–18769. doi: 10.1021/acsami.6b03638

Gu, D., Li, W., Wang, F., Bongard, H., Spliethoff, B., Schmidt, W., et al. (2015). Controllable synthesis of mesoporous peapod-like Co3O4@carbon nanotube arrays for high-performance lithium-ion batteries. *Angew. Chem.* 127, 7166–7170. doi: 10.1002/ange.201501475

Harks, P. P. R. M. L., Mulder, F. M., and Notten, P. H. L. (2015). *In situ* methods for Li-ion battery research: a review of recent developments. *Power Sources J.* 288, 92–105. doi: 10.1016/j.jpowsour.2015.04.084

He, H., Huang, C., Luo, C.-W., and Liu, J.-J., and Chao, Z.-S. (2013). Dynamic study of Li intercalation into graphite by *in situ* high energy synchrotron XRD. *Electrochim. Acta* 92, 148–152. doi: 10.1016/j.electacta.2012.12.135

Hong, K.-I., Qie, L., Zeng, R. Z.-Q. Yi, Z. W., Wang, D., Yin, W., et al. (2014). Biomass derived hard carbon used as a high performance anode material for sodium ion batteries. *J. Mater. Chem. A*. 2, 12733–12738. doi: 10.1039/C4TA02068E

Hou, H., Banks, C. E., Jing, M., Zhang, Y., and Ji, X. (2015). Carbon quantum dots and their derivative 3D porous carbon frameworks for sodium-ion batteries with ultralong cycle life. *Adv. Mater.* 27, 7861–7866. doi: 10.1002/adma.201503816

Hou, H., Qiu, X., Wei, W., Zhang, Y., and Ji, X. (2017). Carbon anode materials for advanced sodium-ion batteries. *Adv. Energy Mater.* 7:1602898. doi: 10.1002/aenm.201602898

Hu, Y. S., Adelhelm, P., Smarsly, B. M., Hore, S., Antonietti, M., and Maier, J. (2007). Synthesis of hierarchically porous carbon monoliths with highly ordered microstructure and their application in rechargeable lithium batteries with high-rate capability. *Adv. Funct. Mater.* 17, 1873–1878. doi: 10.1002/adfm.200601152

Jafta, C. J., X.-,Sun, G., Veith, G. M., Jensen, G. V., Mahurin, S. M., Paranthaman, M. P., et al. (2019). Probing microstructure and electrolyte concentration dependent cell chemistry via operando small angle neutron scattering. *Energy Environ. Sci.* 12, 1866–1877. doi: 10.1039/C8EE02703J

Jahel, A., Ghimbeu, C. M., Darwiche, A., Vidal, L., Hajjar-Garreau, S., Vix-Guterl, C., et al. (2015). Exceptionally highly performing Na-ion battery anode using crystalline SnO2 nanoparticles confined in mesoporous carbon. *J. Mater. Chem. A.* 3, 11960–11969. doi: 10.1039/C5TA01963J

Jahel, A., Ghimbeu, C. M., Monconduit, L., and Vix-Guterl, C. (2014). Confined ultrasmall SnO2 particles in micro/mesoporous carbon as an extremely long cycle-life anode material for li-ion batteries. *Adv. Energy Mater.* 4:1400025. doi: 10.1002/aenm.201400025

Jeong, S.-K., Inaba, M., Mogi, R., Iriyama, Y., Abe, T., and Ogumi, Z. (2001). Surface film formation on a graphite negative electrode in lithium-ion batteries: atomic force microscopy study on the effects of film-forming additives in propylene carbonate solutions. *Langmuir* 17, 8281–8286. doi: 10.1021/la015553h

Ji, L., Lin, Z., Alcoutlabi, M., and Zhang, X. (2011). Recent developments in nanostructured anode materials for rechargeable lithium-ion batteries. *Energy Environ. Sci.* 4, 2682–2699. doi: 10.1039/c0ee00699h

Jian, Z., Luo, W., and Ji, X. (2015). Carbon electrodes for K-ion batteries. *J. Am. Chem. Soc.* 137, 11566–11569. doi: 10.1021/jacs.5b06809

Jin, Y., N.-,Kneusels, J. H., P. C., Magusin, M. M., Kim, G., Castillo-Martínez, E., et al. (2017). Identifying the structural basis for the increased stability of the solid electrolyte interphase formed on silicon with the additive fluoroethylene carbonate. *J. Am. Chem. Soc.* 139, 14992–15004. doi: 10.1021/jacs.7b06834

Kang, S. H., Abraham, D. P., Xiao, A., and Lucht, B. L. (2008). Investigating the solid electrolyte interphase using binder-free graphite electrodes. *Power Sources J.* 175, 526–532. doi: 10.1016/j.jpowsour.2007.08.112

Kim, H., Hong, J., Yoon, G., Kim, H., K.-,Park, Y., M.-,Park, S., et al. (2015). Sodium intercalation chemistry in graphite. *Energy Environ. Sci.* 8, 2963–2969. doi: 10.1039/C5EE02051D

Kim, M.-S., Bhattacharjya, D., Fang, B., D.-,Yang, S., T.-,Bae, S., and Yu, J.- S. (2013). Morphology-dependent li storage performance of ordered mesoporous carbon as anode material. *Langmuir* 29, 6754–6761. doi: 10.1021/la401150t

Kim, M.-S., Fang, B., Kim, J. H., Yang, D., Kim, Y. K., T.-, Bae, S., et al. (2011). Ultra-high Li storage capacity achieved by hollow carbon capsules with hierarchical nanoarchitecture. *J. Mater. Chem. A.* 21, 19362–19367. doi: 10.1039/c1jm13753k

Lai, Y., Cao, Z., Song, H., Zhang, Z., Chen, X., Lu, H., et al. (2012). Influence of Fe (II) species in electrolyte on performance of graphite anode for lithium-ion batteries. *J. Electrochem. Soc.* 159, A1961–A1966. doi: 10.1149/2.044212jes

Lee, J. K., Oh, C., Kim, N., Jang-Yeon, H., and Sun, Y. K. (2016). Rational design of silicon-based composites for high-energy storage devices. *J. Mater. Chem. A* 4, 5366–5384. doi: 10.1039/C6TA00265J

Lee, S.-B., and Pyun, S.-I. (2002). The effect of electrolyte temperature on the passivity of solid electrolyte interphase formed on a graphite electrode. *Carbon* 40, 2333–2339. doi: 10.1016/S0008-6223(02)00144-6

Letellier, M., Chevallier, F., and Béguin, F. (2006). *In situ* 7Li NMR during lithium electrochemical insertion into graphite and a carbon/carbon composite. *J. Phys. Chem. Solids.* 67, 1228–1232. doi: 10.1016/j.jpcs.2006.01.088

Letellier, M., Chevallier, F., Clinard, C., Frackowiak, E., J.-,Rouzaud, N., Béguin, F., et al. (2003). The first *in situ* 7Li nuclear magnetic resonance study of lithium insertion in hard-carbon anode materials for Li-ion batteries. *J. Chem. Phys.* 118, 6038–6045. doi: 10.1063/1.1556092

Li, J., Murphy, E., Winnick, J., and Kohl, P. A. (2001). Studies on the cycle life of commercial lithium ion batteries during rapid charge–discharge cycling. *Power Sources J.* 102, 294–301. doi: 10.1016/S0378-7753(01)00821-7

Li, J., Su, H., Huang, L., and Sun, S. (2013). Investigation of interfacial processes in graphite thin film anodes of lithium-ion batteries by both *in situ* and *ex situ* infrared spectroscopy. *Sci. China Chem.* 56, 992–996. doi: 10.1007/s11426-013-4844-6

Li, T., Senesi, A. J., and Lee, B. (2016). Small angle X-ray scattering for nanoparticle research. *Chem. Rev.* 116, 11128–11180. doi: 10.1021/acs.chemrev.5b00690

Li, Y., Lu, Y., Adelhelm, P., Titirici, M. M., and Hu, Y. S. (2019). Intercalation chemistry of graphite: alkali metal ions and beyond. *Chem. Soc. Rev.* 48, 4655–4687. doi: 10.1039/C9CS00162J

Liang, C., Hong, K., Guiochon, G. A., Mays, J. W., and Dai, S. (2004). Synthesis of a large-scale highly ordered porous carbon film by self-assembly of block copolymers. *Angew. Chem. Int. Edit.* 43, 5785–5789. doi: 10.1002/anie.200461051

Liebenow, C., Wagner, M. W., Lühder, K., Lobitz, P., and Besenhard, J. O. (1995). Electrochemical behaviour of coated lithium-carbon electrodes. *Power Sources J.* 54, 369–372. doi: 10.1016/0378-7753(94)02104-B

Lier, G. V., Alsenoy, C. V., Doren, V. V., and Geerlings, P. (2000). *Ab initio* study of the elastic properties of single-walled carbon nanotubes and graphene. *Chem. Phys. Lett.* 326, 181–185. doi: 10.1016/S0009-2614(00)00764-8

Liew, K. M., Lei, Z. X., and Zhang, L. W. (2015). Mechanical analysis of functionally graded carbon nanotube reinforced composites: a review. *Compos. Struct.* 120, 90–97. doi: 10.1016/j.compstruct.2014.09.041

Liu, H., Jia, M., Sun, N., Cao, B., Chen, R., Zhu, Q., et al. (2015). Nitrogen-rich mesoporous carbon as anode material for high-performance sodium-ion batteries. *ACS App. Mater. Interfaces* 7, 27124–27130. doi: 10.1021/acsami.5b06898

Liu, J., Yin, T., Tian, B., Zhang, B., Qian, C., Wang, Z., et al. (2019). Unraveling the potassium storage mechanism in graphite foam. *Adv. Energy Mater.* 9:1900579. doi: 10.1002/aenm.201900579

Liu, T., Lin, L., Bi, X., Tian, L., Yang, K., Liu, J., et al. (2019). *In situ* quantification of interphasial chemistry in Li-ion battery. *Nat. Nanotechnol.* 14, 50–56. doi: 10.1038/s41565-018-0284-y

Liu, X.-R., Wang, L., L.-,Wan, J., and Wang, D. (2015). *In situ* observation of electrolyte-concentration-dependent solid electrolyte interphase on graphite in dimethyl sulfoxide. *ACS App. Mater. Inter.* 7, 9573–9580. doi: 10.1021/acsami.5b01024

Liu, X. H., Wang, J. W., Liu, Y., Zheng, H., Kushima, A., Huang, S., et al. (2012). *In situ* transmission electron microscopy of electrochemical lithiation, delithiation and deformation of individual graphene nanoribbons. *Carbon* 50, 3836–3844. doi: 10.1016/j.carbon.2012.04.025

Liu, Y., Fan, F., Wang, J., Liu, Y., Chen, H., Jungjohann, K. L., et al. (2014). *In situ* transmission electron microscopy study of electrochemical sodiation and potassiation of carbon nanofibers. *Nano Lett.* 14, 3445–3452. doi: 10.1021/nl500970a

Liu, Y., Merinov, B. V., and Goddard, W. A. (2016). Origin of low sodium capacity in graphite and generally weak substrate binding of Na and Mg among alkali and alkaline earth metals. *Proc. Natl. Acad. Sci. U.S.A.* 113:3735. doi: 10.1073/pnas.1602473113

Liu, Y., Zheng, H., Liu, X. H., Huang, S., Zhu, T., Wang, J., et al. (2011). Lithiation-induced embrittlement of multiwalled carbon nanotubes. *ACS Nano* 5, 7245–7253. doi: 10.1021/nn202071y

Mao, Y., Duan, H., Xu, B., Zhang, L., Hu, Y., Zhao, C., et al. (2012). Lithium storage in nitrogen-rich mesoporous carbon materials. *Energy Environ. Sci.* 5, 7950–7955. doi: 10.1039/c2ee21817h

Mathiesen, J. K., Johnsen, R. E., Blennow, A. S., and Norby, P. (2019). Understanding the structural changes in lithiated graphite through high-resolution operando powder X-ray diffraction. *Carbon* 153, 347–354. doi: 10.1016/j.carbon.2019.06.103

Meunier, V., Kephart, J., Roland, C., and Bernholc, J. (2002). *Ab initio* investigations of lithium diffusion in carbon nanotube systems. *Phys. Rev. Lett.* 88:075506. doi: 10.1103/PhysRevLett.88.075506

Mizushima, K., Jones, P. C., Wiseman, P. J., and Goodenough, J. B. (1981). LixCoO2 (0<x<1): a new cathode material for batteries of high energy density. *Solid State Ionics* 3–4, 171–174.

Moss, P., Au, G., Plichta, E., and Zheng, J. (2010). Study of capacity fade of lithium-ion polymer rechargeable batteries with continuous cycling. *J. Electrochem. Soc.* 157, A1–A7. doi: 10.1149/1.3246001

Nobuhara, K., Nakayama, H., Nose, M., Nakanishi, S., and Iba, H. (2013). First-principles study of alkali metal-graphite intercalation compounds. *Power Sources J.* 243, 585–587. doi: 10.1016/j.jpowsour.2013.06.057

Novák, P., Panitz, J. C., Joho, F., Lanz, M., Imhof, R., and Coluccia, M. (2000). Advanced *in situ* methods for the characterization of practical electrodes in lithium-ion batteries. *Power Sources J.* 90, 52–58. doi: 10.1016/S0378-7753(00)00447-X

Ohzuku, T., Iwakoshi, Y., and Sawai, K. (1993). Cheminform abstract: formation of lithium-graphite intercalation compounds in nonaqueous electrolytes and their application as a negative electrode for a lithium ion (Shuttlecock) cell. *ChemInform*. 24:8. doi: 10.1002/chin.199351008

Okamoto, Y. (2014). Density functional theory calculations of alkali metal (Li, Na, and K) graphite intercalation compounds. *J. Phys. Chem.* C 118, 16–19. doi: 10.1021/jp4063753

Pan, Z., Ren, J., Guan, G., Fang, X., Wang, B., S., Doo, G., et al. (2016). Synthesizing nitrogen-doped core–sheath carbon nanotube films for flexible lithium ion batteries. *Adv. Energy Mater*. 6:1600271. doi: 10.1002/aenm.201600271

Pang, W. K., Alam, M., Peterson, V., and Sharma, N. (2014). Structural evolution of electrodes in the NCR and CGR cathode-containing commercial lithium-ion batteries cycled between 3.0 and 4.5 V: an operando neutron powder-diffraction study. *J. Mater. Res.* 30, 373–380. doi: 10.1557/jmr.2014.297

Park, G., Nakamura, H., Lee, Y., and Yoshio, M. (2009). The important role of additives for improved lithium ion battery safety. *Power Sources J.* 189, 602–606. doi: 10.1016/j.jpowsour.2008.09.088

Pollak, E., Geng, K.-B., Jeon, J., Lucas, I. T., Richardson, T. J., Wang, F., et al. (2010). The Interaction of Li+ with single-layer and few-layer graphene. *Nano Lett.* 10, 3386–3388. doi: 10.1021/nl101223k

Pramudita, J. C., Sehrawat, D., Goonetilleke, D., and Sharma, N. (2017). An initial review of the status of electrode materials for potassium-ion batteries. *Adv. Energy Mater*. 7:1602911. doi: 10.1002/aenm.201602911

Rhodes, K., Kirkham, M., Meisner, R., Parish, C. M., Dudney, N., and Daniel, C. (2011). Novel cell design for combined *in situ* acoustic emission and x-ray diffraction study during electrochemical cycling of batteries. *Rev. Sci. Instrum*. 82:075107. doi: 10.1063/1.3607961

Ridgway, P., Zheng, H., Bello, A., Song, X., Xun, S., Chong, J., et al. (2012). Comparison of cycling performance of lithium ion cell anode graphites. *J. Electrochem. Soc*. 159:A520. doi: 10.1149/2.006205jes

Sandí, G. (1999). Carbons for lithium battery applications prepared using sepiolite as inorganic template. *J. Electrochem. Soc*. 146:3644. doi: 10.1149/1.1392527

Saurel, D., Orayech, B., Xiao, B., Carriazo, D., Li, X., and Rojo, T. (2018). From charge storage mechanism to performance: a roadmap toward high specific energy sodium-ion batteries through carbon anode optimization. *Adv. Energy Mater*. 8:1703268. doi: 10.1002/aenm.201703268

Schweidler, S., de Biasi, L., Schiele, A., Hartmann, P., Brezesinski, T., and Janek, J. (2018). Volume changes of graphite anodes revisited: a combined operando X-ray diffraction and *in situ* pressure analysis study. *J. Phys. Chem. C*. 122, 8829–8835. doi: 10.1021/acs.jpcc.8b01873

Seidl, L., Martens, S., Ma, J., Stimming, U., and Schneider, O. (2016). *In situ* scanning tunneling microscopy studies of the SEI formation on graphite electrodes for Li+-ion batteries. *Nanoscale* 8, 14004–14014. doi: 10.1039/C6NR00825A

Shan, X.-Y., Zhou, G., Yin, L-C., Yu, W.-J., Li, H.-F., and Cheng, M. (2014). Visualizing the roles of graphene for excellent lithium storage. *J. Mater. Chem. A*. 2, 17808–17814. doi: 10.1039/C4TA04460F

Share, K., Cohn, A. P., Carter, R. E., and Pint, C. L. (2016). Mechanism of potassium ion intercalation staging in few layered graphene from *in situ* Raman spectroscopy. *Nanoscale* 8, 16435–16439. doi: 10.1039/C6NR04084E

Sharma, N., Peterson, V. K., Elcombe, M. M., Avdeev, M., Studer, A. J., Blagojevic, N., et al. (2010). Structural changes in a commercial lithium-ion battery during electrochemical cycling: an *in situ* neutron diffraction study. *J. Power Sources* 195, 8258–8266. doi: 10.1016/j.jpowsour.2010.06.114

Shen, F., Luo, W., Dai, J., Yao, Y., Zhu, M., Hitz, E., et al. (2016). Ultra-thick, low-tortuosity, and mesoporous wood carbon anode for high-performance sodium-ion batteries. *Adv. Energy Mater*. 6:1600377. doi: 10.1002/aenm.201600377

Shi, H. (1996). Structure and lithium intercalation properties of synthetic and natural graphite. *J. Electrochem. Soc*. 143:3466. doi: 10.1149/1.1837238

Shi, H., Barker, J., Saïdi, M. Y., Koksbang, R., and Morris, L. (1997). Graphite structure and lithium intercalation. *Power Sources J.* 68, 291–295. doi: 10.1016/S0378-7753(96)02562-1

Shim, J., and Striebel, K. A. (2004). The dependence of natural graphite anode performance on electrode density. *Power Sources J.* 130, 247–253. doi: 10.1016/j.jpowsour.2003.12.015

Smith, A., Dahn, H., Burns, J., and Dahn, J. (2012). Long-term low-rate cycling of LiCoO2/graphite li-ion cells at 55 degrees C. *J. Electrochem. Soc*. 159:A705. doi: 10.1149/2.056206jes

Sole, C., Drewett, N. E., and Hardwick, L. J. (2014). *In situ* Raman study of lithium-ion intercalation into microcrystalline graphite. *Faraday Discuss*. 172, 223–237. doi: 10.1039/C4FD00079J

Song, X. Y., Kinoshita, K., and Tran, T. D. (1996). Microstructural characterization of lithiated graphite. *J. Electrochem. Soc.* 143, L120–L123. doi: 10.1149/1.1836896

Stevens, D. A., and Dahn, J. R. (2000a). High capacity anode materials for rechargeable sodium-ion batteries. *J. Electrochem. Soc.* 147:1271. doi: 10.1149/1.1393348

Stevens, D. A., and Dahn, J. R. (2000b). An *in situ* small-angle X-ray scattering study of sodium insertion into a nanoporous carbon anode material within an operating electrochemical cell. *J. Electrochem. Soc*. 147:4428. doi: 10.1149/1.1394081

Sun, Y., Liu, N., and Cui, Y. (2016). Promises and challenges of nanomaterials for lithium-based rechargeable batteries. *Nat. Energy*. 1:16071. doi: 10.1038/nenergy.2016.71

Sun, Z., Jin, S., Jin, H., Du, Z., Zhu, Y., Cao, A., et al. (2018). Robust expandable carbon nanotube scaffold for ultrahigh-capacity lithium-metal anodes. *Adv. Mater*. 30:1800884.1-7. doi: 10.1002/adma.201800884

Tang, K., Fu, L., White, R. J., Yu, L. M.,Titirici, M., Antonietti, M., et al. (2012). Hollow carbon nanospheres with superior rate capability for sodium-based batteries. *Adv. Energy Mater*. 2, 873–877. doi: 10.1002/aenm.201100691

Tang, W., B.-,Goh, M., Hu, M. Y., Wan, C., Tian, B., Deng, X., et al. (2016). *In situ* raman and nuclear magnetic resonance study of trapped lithium in the solid electrolyte interface of reduced graphene oxide. *J. Phys. Chem. C* 120, 2600–2608. doi: 10.1021/acs.jpcc.5b12551

The Nobel Prize in Chemistry (2019). Available online at: https://www.nobelprize.org/prizes/chemistry/2019/summary/ (accessed October 9, 2019).

Thess, A., Lee, R., Nikolaev, P., Dai, H., Petit, P., Robert, J., et al. (1996). Crystalline ropes of metallic carbon nanotubes. *Science* 273:483. doi: 10.1126/science.273.5274.483

Thostenson, E. T., Ren, Z., and Chou, T.-W. (2001). Advances in the science and technology of carbon nanotubes and their composites: a review. *Compos. Sci. Technol*. 61, 1899–1912. doi: 10.1016/S0266-3538(01)00094-X

Treacy, M. J. M., and Ebbesen, and, W. T. (1996). Exceptionally high Young's modulus observed for individual carbon nanotubes. *Nature* 381, 678–680. doi: 10.1038/381678a0

Wan, J., Shen, F., Luo, W., Zhou, L., Dai, J., Han, X., et al. (2016). *In situ* transmission electron microscopy observation of sodiation–desodiation in a long cycle, high-capacity reduced graphene oxide sodium-ion battery anode. *Chem. Mater*. 28, 6528–6535. doi: 10.1021/acs.chemmater.6b01959

Wang, H.-G. Z., Wu, F.-I., Meng, D.-I., Ma, X.-I., Huang, L.-M., Wang, X., et al. (2013). Nitrogen-doped porous carbon nanosheets as low-cost, high-performance anode material for sodium-ion batteries. *ChemSusChem* 6, 56–60. doi: 10.1002/cssc.201200680

Wang, J., Nie, P., Ding, B., Dong, S., Hao, X., Dou, H., et al. (2017). Biomass derived carbon for energy storage devices. *J. Mater. Chem. A*. 5, 2411–2428. doi: 10.1039/C6TA08742F

Wang, K., Xu, Y., Li, Y., Dravid, V., Wu, J., and Huang, Y. (2019). Sodium storage in hard carbon with curved graphene platelets as the basic structural units. *J. Mater. Chem. A*. 7, 3327–3335. doi: 10.1039/C8TA11510A

Wang, Y., Wen, X., Chen, J., and Wang, S. (2015). Foamed mesoporous carbon/silicon composite nanofiber anode for lithium ion batteries. *Power Sources J.* 281, 285–292. doi: 10.1016/j.jpowsour.2015.01.184

Wang, Z., Selbach, S., and Grande, T. (2014). Van der Waals density functional study of the energetics of alkali metal intercalation in graphite. *RSC Adv*. 4, 4069–4079. doi: 10.1039/C3RA47187J

Wen, Y., He, K., Zhu, Y., Han, F., Xu, Y., Matsuda, I., et al. (2014). Expanded graphite as superior anode for sodium-ion batteries. *Nat. Commun.* 5:4033. doi: 10.1038/ncomms5033

Whittingham, M. S. (1976). Electrical energy storage and intercalation chemistry. *Science* 192, 1126–1127. doi: 10.1126/science.192.4244.1126

Winter, M. (2009). The solid electrolyte interphase – the most important and the least understood solid electrolyte in rechargeable Li Batteries. *Z. Phys. Chem.* 223, 1395–1406. doi: 10.1524/zpch.2009.6086

Winter, M., Barnett, B., and Xu, K. (2018). Before Li ion batteries. *Chem. Rev.* 118, 11433–11456. doi: 10.1021/acs.chemrev.8b00422

Winter, M., Besenhard, J. O., Spahr, M. E., and Novák, P. (1998). Insertion electrode materials for rechargeable lithium batteries. *Adv. Mater.* 10, 725–763.

Woo, S.-W., Dokko, K., Nakano, H., and Kanamura, K. (2007). Bimodal porous carbon as a negative electrode material for lithium-ion capacitors. *Electrochem* 75, 635–640. doi: 10.5796/electrochemistry.75.635

Wu, Y. P., Rahm, E., and Holze, R. (2003). Carbon anode materials for lithium ion batteries. *Power Sources J.* 114, 228–236. doi: 10.1016/S0378-7753(02)00596-7

Xin, D., Xingrui, L., Huijuan, Y., Dong, W., and Lijun, W. (2014). Morphology and modulus evolution of graphite anode in lithium ion battery: an *in situ* AFM investigation. *Sci. China Chem.* 2014, 178–183. doi: 10.1007/s11426-013-4988-4

Xing, Z., Gao, N., Qi, Y., Ji, X., and Liu, H. (2017a). Influence of enhanced carbon crystallinity of nanoporous graphite on the cathode performance of microbial fuel cells. *Carbon* 115, 271–278. doi: 10.1016/j.carbon.2017.01.014

Xing, Z., Luo, X., Qi, Y., Stickle, W. F., Amine, K., Lu, J., et al. (2016). Nitrogen-doped nanoporous graphenic carbon: an efficient conducting support for O2 cathode. *ChemNanoMat* 2, 692–697. doi: 10.1002/cnma.201600112

Xing, Z., Qi, Y., Jian, Z., and Ji, X. (2017c). Polynanocrystalline graphite: a new carbon anode with superior cycling performance for K-ion batteries. *ACS Appl. Mater. Interfaces* 9, 4343–4351. doi: 10.1021/acsami.6b06767

Xing, Z., Qi, Y., Tian, Z., Xu, J., Yuan, Y., Bommier, C., et al. (2017b). Identify the removable substructure in carbon activation. *Chem. Mater.* 29, 7288–7295. doi: 10.1021/acs.chemmater.7b01937

Xing, Z., Wang, B., Halsted, J. K., Subashchandrabose, R., Stickle, W. F., and Ji, X. (2015). Direct fabrication of nanoporous graphene from graphene oxide by adding a gasification agent to a magnesiothermic reaction. *Chem. Commun.* 51, 1969–1971. doi: 10.1039/C4CC08977D

Yamada, H., Watanabe, Y., Moriguchi, I., and Kudo, T. (2008). Rate capability of lithium intercalation into nano-porous graphitized carbons. *Solid State Ionics.* 179, 1706–1709. doi: 10.1016/j.ssi.2008.02.022

Yan, Y., Yin, Y. X., Guo, Y. G., and Wan, L. J. (2014). A sandwich-like hierarchically porous carbon/graphene composite as a high-performance anode material for sodium-ion batteries. *Adv. Energy Mater.* 4:1301584. doi: 10.1002/aenm.201301584

Yang, F., Zhang, Z., Du, K., Zhao, X., Chen, W., Lai, Y., et al. (2015). Dopamine derived nitrogen-doped carbon sheets as anode materials for high-performance sodium ion batteries. *Carbon* 91, 88–95. doi: 10.1016/j.carbon.2015.04.049

Yang, J., Muhammad, S., Jo, M. R., Kim, H., Song, K., Agyeman, D. A., et al. (2016). *In situ* analyses for ion storage materials. *Chem. Soc. Rev.* 45, 5717–5770. doi: 10.1002/chin.201647298

Yang, S., Huo, J., Song, H., and Chen, X. (2008). A comparative study of electrochemical properties of two kinds of carbon nanotubes as anode materials for lithium ion batteries. *Electrochim. Acta.* 53, 2238–2244. doi: 10.1016/j.electacta.2007.09.040

Yang, Y., Jin, S., Zhang, Z., Du, Z., Liu, H., Yang, J., et al. (2017). Nitrogen-doped hollow carbon nanospheres for high-performance li-ion batteries. *ACS Appl. Mater. Interfaces* 9, 14180–14186. doi: 10.1021/acsami.6b14840

Yazami, R., and Reynier, Y. F. (2002). Mechanism of self-discharge in graphite–lithium anode. *Electrochim. Acta* 47, 1217–1223. doi: 10.1016/S0013-4686(01)00827-1

Yazami, R., and Touzain, P. (1983). A reversible graphite-lithium negative electrode for electrochemical generators. *Power Sources J.* 9, 365–371. doi: 10.1016/0378-7753(83)87040-2

Yoon, G., Kim, H., Park, I., and Kang, K. (2017). Conditions for reversible na intercalation in graphite: theoretical studies on the interplay among guest ions, solvent, and graphite host. *Adv. Energy Mater.* 7:1601519. doi: 10.1002/aenm.201601519

Yoshino, A. (2012). The birth of the lithium-ion battery. *Angew. Chem. Int. Edit.* 51, 5798–5800. doi: 10.1002/anie.201105006

Yoshino, A., Sanechika, K., and Nakajima, T. (1987). *Secondary Battery*. U.S. Patent No. 4,668,595.

Yu, M. F., Lourie, O., Dyer, M. J., Moloni, K., Kelly, T. F., and Ruoff, R. S. (2000). Strength and breaking mechanism of multiwall carbon nanotubes under tensile load. *Science.* 287, 637–640. doi: 10.1126/science.287.5453.637

Yuan, Y., Amine, K., Lu, J., and Shahbazian-Yassar, R. (2017). Understanding materials challenges for rechargeable ion batteries with *in situ* transmission electron microscopy. *Nat. Commun.* 8:15806. doi: 10.1038/ncomms15806

Yun Zhao, Y. K., Yuhong, J., Li, W., Guangyu, T., and He, X. (2019). Silicon-based and -related materials for lithium-ion batteries. *Prog. Chem.* 31, 613–630. doi: 10.7536/PC150155

Yuqin, C., Hong, L., Lie, W., and Tianhong, L. (1997). Irreversible capacity loss of graphite electrode in lithium-ion batteries. *Power Sources J.* 68, 187–190. doi: 10.1016/S0378-7753(96)02549-9

Zaghib, K., Nadeau, G., and Kinoshita, K. (2000). Effects of graphite particle size on irreversible capacityloss. *J. Electrochem. Soc.* 147, 2110–2115. doi: 10.1149/1.1393493

Zanini, M., Basu, S., and Fischer, J. E. (1978). Alternate synthesis and reflectivity spectrum of stage 1 lithium—graphite intercalation compound. *Carbon* 16, 211–212. doi: 10.1016/0008-6223(78)90026-X

Zhang, S., Yao, F., Yang, L., Zhang, F., and Xu, S. (2015). Sulfur-doped mesoporous carbon from surfactant-intercalated layered double hydroxide precursor as high-performance anode nanomaterials for both Li-ion and Na-ion batteries. *Carbon* 93, 143–150. doi: 10.1016/j.carbon.2015.04.091

Zheng, G., Lee, S. W., Liang, Z., H.-,Lee, W., Yan, K., Yao, H., et al. (2014). Interconnected hollow carbon nanospheres for stable lithium metal anodes. *Nat. Nanotechnol.* 9, 618–623. doi: 10.1038/nnano.2014.152

Zhou, H., An, K., Allu, S., Pannala, S., Li, J., Bilheux, H. Z., et al. (2016). Probing multiscale transport and inhomogeneity in a lithium-ion pouch cell using *in situ* neutron methods. *ACS Energy Lett.* 1, 981–986. doi: 10.1021/acsenergylett.6b00353

Zhu, H., Huang, Y., Zhu, H., Wang, L., Lan, S., Xia, X., et al. (2019). *In situ* probing multiple-scale structures of energy materials for li-ion batteries. *Small Method* 4:1900223. doi: 10.1002/smtd.201900223

Zhu, J., Chen, C., Lu, Y., Ge, Y., Jiang, H., Fu, K., et al. (2015). Nitrogen-doped carbon nanofibers derived from polyacrylonitrile for use as anode material in sodium-ion batteries. *Carbon* 94, 189–195. doi: 10.1016/j.carbon.2015.06.076

Zou, J., Sole, C., Drewett, N. E., Velický, M., and Hardwick, L. J. (2016). *In situ* study of Li intercalation into highly crystalline graphitic flakes of varying thicknesses. *J. Phys. Chem. Lett.* 7, 4291–4296. doi: 10.1021/acs.jpclett.6b01886

Conflict of Interest: The authors declare that the research was conducted in the absence of any commercial or financial relationships that could be construed as a potential conflict of interest.

frontiers in Chemistry

REVIEW
published: 10 February 2021
doi: 10.3389/fchem.2020.620153

Recent Advances in the Direct Electron Transfer-Enabled Enzymatic Fuel Cells

*Sooyoun Yu and Nosang V. Myung**

Department of Chemical and Biomolecular Engineering, University of Notre Dame, Notre Dame, IN, United States

Direct electron transfer (DET), which requires no mediator to shuttle electrons from enzyme active site to the electrode surface, minimizes complexity caused by the mediator and can further enable miniaturization for biocompatible and implantable devices. However, because the redox cofactors are typically deeply embedded in the protein matrix of the enzymes, electrons generated from oxidation reaction cannot easily transfer to the electrode surface. In this review, methods to improve the DET rate for enhancement of enzymatic fuel cell performances are summarized, with a focus on the more recent works (past 10 years). Finally, progress on the application of DET-enabled EFC to some biomedical and implantable devices are reported.

Keywords: enzymatic fuel cell, direct electron transfer, glucose oxidase, nanostructure, biocatalyst

OPEN ACCESS

Edited by:
Sri Narayan,
University of Southern California,
United States

Reviewed by:
Seung Woo Lee,
Georgia Institute of Technology,
United States
Federico Tasca,
University of Santiago, Chile

***Correspondence:**
Nosang V. Myung
nmyung@nd.edu

Specialty section:
This article was submitted to Electrochemistry, a section of the journal Frontiers in Chemistry

Received: *22 October 2020*
Accepted: *09 December 2020*
Published: *10 February 2021*

Citation:
Yu S and Myung NV (2021) Recent Advances in the Direct Electron Transfer-Enabled Enzymatic Fuel Cells. Front. Chem. 8:620153. doi: 10.3389/fchem.2020.620153

INTRODUCTION

Since its first demonstration of concept by Yahiro et al. (1964), enzymatic fuel cell (EFC) has gained much research interest as one of the environmentally friendly and renewable source of power generation. Utilizing isolated enzymes from microorganisms as biocatalysts at either or both of electrodes, EFC is particularly attractive as the substrate specificity of the biocatalysts essentially removes the need for compartmentalization of each electrode, allowing for wider applications *via* miniaturization. The biocatalyst at the anode catalyzes the oxidation reaction of a fuel, from which electrons are released and then transferred to the electrode surface. The electrons then travel through the circuit to the cathode, where they are consumed in the reduction reaction of an oxidant, typically oxygen to produce water as byproduct. In an EFC, there are two possible electron transport mechanisms from the redox center of the biocatalyst at the anode (i.e., bioanodic enzyme) to the electrode surface: direct electron transfer (DET) and mediated electron transfer (MET). When an electron generated from oxidation catalyzed by the redox center of a bioanodic enzyme travels directly to the electrode surface and is collected as current, the enzyme is known to undergo DET; when an additional component is utilized between the enzymatic catalyst and electrode surface to act as a mediator to shuttle the electron, it is referred to as MET. Early works with EFC typically involved electron mediators, such as hydroquinone, benzoquinone, and ferricyanide salt to obtain current (Hunger et al., 1966; Davis and Yarbrough, 1967). Though first report of DET may date back to as early as 1972 (Betso et al., 1972), it was not until 1978 when works by Berezin et al. pioneered the DET mechanism to collect current with a laccase (Lc) directly adsorbed onto graphite electrodes (Berezin et al., 1978).

Despite over a half of a century worth of research, there is yet to be a consensus on whether DET or MET surpasses one another in terms of EFC performance. On one hand, MET-enabled EFC theoretically provides higher current and power density as the mediator would minimize the number of electrons that fail to reach the electrode due to its small tunneling distance (~10 Å);

on the other hand, DET-enabled EFC offers simpler configuration and can bypass potential toxicity or low stability of some mediators (Mazurenko et al., 2017a; Mani et al., 2018). Furthermore, not using a mediator means the redox enzymes can operate at a potential close to their natural standard redox potentials, leading to lower chances of interfering reactions as well as higher open-circuit potential and thus higher power density (Kawai et al., 2014).

When evaluating the performance of EFC, several properties are commonly characterized or quantified: power density, current density, the amount of decay in power density over time, and open-circuit potential (OCP). The power and current density and the OCP correlate to the overall power output by the EFC, while the time-dependent decay of the power density can be translated into the stability of the EFC. While DET seems like a more favorable method of electron transfer to optimize the EFC performance, the small electron tunneling distance greatly limits the type of oxidoreductases that can be used for this configuration. Typically, the redox center is deeply embedded within a protein matrix, the size of which often exceeds 10 Å. In fact, only about a 100 of 1,700 known oxidoreductase enzymes can facilitate DET (Shleev et al., 2016). In an effort to not only increase this number but also enhance the fuel cell performance utilizing DET, a number of components of EFC could be improved: protein engineering to increase the efficiency of the direct electron transfer; immobilization of the biocatalysts on the electrode to decrease the tunneling distance and enhance the stability; and use of functional nanomaterials as electrodes to maximize enzyme loading while minimizing IR drop and tunneling distance for efficient charge transfer.

Herein, methods to enhance the performance of DET-enabled EFC that have recently been popular are summarized, and the outlook on these EFCs, including their applications are presented.

BIOCATALYST ENGINEERING

One of the major drawbacks of using native enzymes as biocatalysts for EFCs is that some redox cofactors, molecules that change their oxidation state during catalytic redox reaction of the substrate, are deeply embedded inside the enzyme, and thus it is difficult for the electrons generated from the oxidation reaction to transfer successfully to the electrode surface (Hecht et al., 1993). For many enzymes, this means the electrons must be able to travel far beyond their 10-Å limit to reach the electrode, and most, if not all, of the electrons are not collected as current without any modification on the enzymes.

Enzyme Choice and Protein Engineering

Glucose oxidase (GOx), one of the most extensively studied oxidoreductase enzyme for catalysis of glucose oxidation, is well-known for its flavin adenine dinucleotide (FAD) cofactor embedded within the protein matrix as far as 15–26 Å from the surface (Luong et al., 2017). Due to the large depth in which the FAD is located, some works have claimed that native GOx does not undergo DET at all (Wilson, 2016; Bartlett and Al-lolage, 2018). In these works, the redox peaks at $E^0 = -0.46$ V (vs. Ag/AgCl) famously known to represent the GOx activity by the redox of FAD/$FADH_2$ cofactor were argued to be inaccurate, as their electroanalytical methods with various control experiments suggested the redox peaks were due to the enzymatic activity of the FAD cofactors that have denatured from GOx itself, rather than the electroactivity.

Despite these claims, efforts toward DET-enabled GOx-based EFC have continued. Furthermore, other enzyme catalysts for both anode and cathode have been engineered and utilized for enhancement of EFC performance. This section describes various methods to modify or engineer enzymes for increasing the stability of enzyme immobilization and decreasing enzyme-to-electrode distance, thereby increasing the chance of DET for higher power density.

One of the drawbacks of using native GOx as the anodic biocatalyst is its sensitivity to oxygen. In addition to its primary substrate, glucose, GOx also interacts with oxygen as a natural electron acceptor and catalyzes its reduction to hydrogen peroxide. This can not only result in a lower coulombic efficiency, but also affect the cathode by depleting the available oxygen to be reduced (Navaee and Salimi, 2018).

As one of the alternatives, FAD-dependent glucose dehydrogenase (referred to as FAD-GDH) has been suggested as a promising enzyme. GDH is available with three different cofactors—pyrroloquinoline quinone (PQQ), nicotine adenine dinucleotide (NAD), and FAD. Though GDH based on all three cofactors have been utilized as anodic enzyme catalyst for EFC applications (Saleh et al., 2011; Schubart et al., 2012; Scherbahn et al., 2014), the low substrate selectivity and poor thermal stability of PQQ-dependent GDH (Aiba et al., 2015) and denaturing of NAD cofactor suggest there are room for improvement for them to be stronger candidates for glucose-oxidizing enzyme for EFCs. FAD-GDH, on the other hand, have been steadily used as an oxygen-insensitive alternative, immobilized in various EFC setups. Desriani et al. demonstrated FAD-GDH-based enzymatic fuel cell by casting FAD-GDH/carbon ink mixture on carbon cloth to fabricate the bioanode (Desriani et al., 2010). Combined with the cathode functionalized with bilirubin oxidase (BOD), the EFC produced up to 9.3 $\mu W/cm^2$ power density with cellobiose as substrate. Muguruma et al. employed debundled single-walled carbon nanotubes (SWNTs), which were small enough in diameter (1.2 nm) to be plugged into the grooves of FAD-GDH to minimize the distance between enzyme cofactor and the electrode. Glucose concentration-dependent current response was only observed when debundled SWNTs were utilized as opposed to SWNT aggregates or multi-walled carbon nanotubes (MWNTs), despite the oxygen insensitivity of FAD-GDH (**Figure 1**) (Muguruma et al., 2017). Lee et al. studied the electrochemical behavior of FAD-GDH *via* chronoamperometry. Not only was DET achieved, but also the distance between enzyme cofactor and electrode surface was controlled by different self-assembly monolayers (SAM) to show its significance in enhancing the current response (Lee et al., 2018). Furthermore, the chemisorption between the thiol residue of SAM and gold electrode, combined with the covalent bond between the amino groups of the FAD-GDH and

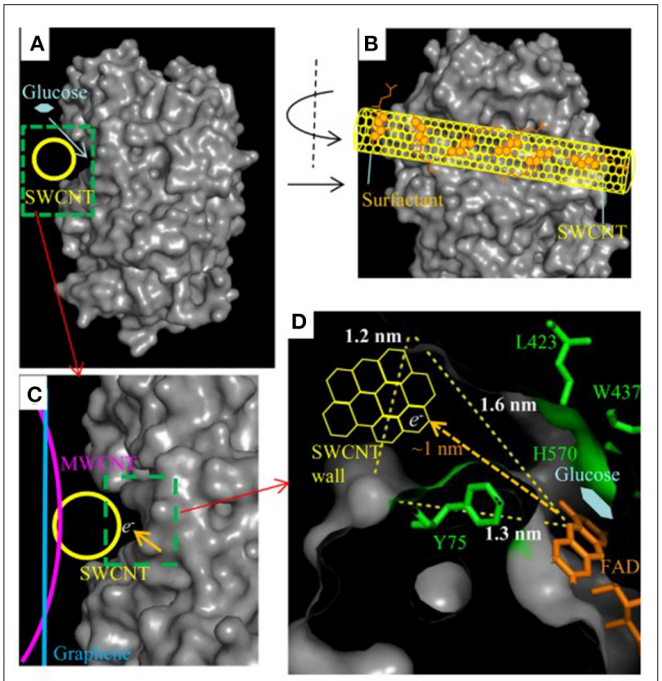

FIGURE 1 | Schematic of possible DET route between FAD-GDH and debundled SWNT. **(A)** and **(B)** show possible location of debundled SWNT in the indentation of FAD-GDH; **(C)** compares the locations of MWNT, graphene, and debundled SWNT with respect to the FAD-GDH; **(D)** visualizes the reduced distance for electrons to travel from the FAD cofactor to the debundled SWNT (Muguruma et al., 2017).

succinimide groups of SAM, strengthened the stability of enzyme immobilization on the electrode surface for more efficient DET.

Another method to overcome the weak DET rate by GOx is genetic modification for ready functionalization with metallic nanomaterials or more intricate structure with supporting materials. Prévoteau et al. demonstrated that deglycosylated glucose oxidase exhibited more negative surface charge than native GOx, which allowed for stronger electrostatic interaction with positively charged hydrogels used to immobilize the enzymes (Prévoteau et al., 2010). Electrodes functionalized with deglycosylated GOx showed higher current density to fixed amount of glucose than native GOx, which was attributed to the smaller enzyme-electrode distance and higher enzyme loading due to stronger attraction toward the hydrogel and thus the electrode surface. Other enzymes such as cellobiose dehydrogenase (CDH) was also deglycosylated to show up to 65% higher current response in the presence of substrate than the glycosylated enzymes (Ortiz et al., 2012). One of the advantages that contributed to this increase was the smaller hydrodynamic radius of the deglycosylated CDH, which allowed for higher amount of enzymes to be packed on the electrode surface. Holland et al. made direct mutations at various locations of GOx to add a cysteine side chain, which revealed a thiol group at a distance from 14 to 29 Å from the FAD cofactor. The thiol group attached to the GOx readily bound to gold nanoparticles, which facilitated direct electron transfer when functionalized onto electrode surface (Holland et al., 2011). Electroanalytical methods on electrodes modified with five mutated GOx showed only the enzyme with the thiol group closest to the FAD exhibited electroactivity, reinforcing the significance of minimizing enzyme-to-electrode distance for efficient DET. Other enzymatic catalysts such as fructose dehydrogenase (Hibino et al., 2017; Kaida et al., 2019), laccase (Lalaoui et al., 2016a), and pyranose 2-oxidase (Spadiut et al., 2009) have been modified for more stable immobilization as well as enhanced enzymatic activity.

Orientation of Enzymes

Oxidoreductase enzymes are relatively large and measure few nanometers in diameter; the redox center is typically embedded within the protein matrix, at times tens of angstroms from the surface of the enzyme, which is well over the maximum electron tunneling distance of up to 20 Å (Moser et al., 1992). Because of this, it is essential to achieve favorable orientation of the enzyme when immobilizing on the electrode; that is, in a way that the redox cofactor is closest to the electrode surface (Lopez et al., 2018). The difficulties associated with obtaining such orientation, parameters that affect the orientation, and the electrode properties that are affected by the enzyme orientation are reviewed in great detail by Hitaishi et al. (2018). Thus, in this review, several recent works that demonstrated fine tuning of enzyme orientation by protein and electrode engineering for more efficient direct electron transfer are presented.

The general idea behind achieving good orientation for DET is to promote electrostatic interaction or covalent binding between the enzyme and the electrode surface so that the cofactor is located at a compatible distance from the electrode for electron transfer. For example, gold nanoparticles immobilized on highly oriented graphite electrode were functionalized with aminophenyl groups, which allowed for covalent binding between the nanoparticles and laccase enzyme. Two-step immobilization was proposed for this work: (i) the amino groups on the gold nanoparticles reacted with the oxidized sugar residues on the Lc, while (ii) amide bonds were formed between carboxylic groups of the enzyme and amino groups on the graphite electrode (Gutiérrez-Sánchez et al., 2012). Lalaoui et al. modified a specific location of laccase (Lc) with a pyrene molecule near the T1 copper redox center of the enzyme, so that when the pyrene group on the Lc bound to the CNT-bound gold nanoparticle, the redox center was closest to the electrode surface to maximize the current density output (**Figure 2**) (Lalaoui et al., 2016a).

Ma et al. engineered seven different mutants of cellobiose dehydrogenase to vary the orientation at which the enzyme was immobilized on the electrode surface. All enzymes but the wild type one were covalently bound to either gold or glassy carbon electrode, which was confirmed by surface plasmon resonance and cyclic voltammetry. The orientation of the enzyme immobilized on the electrode surface affected the mobility of the cytochrome domain, which moves between closed and open state to take the electron from the FAD cofactor to donate to the electrode. In the presence and absence of a mediator, they confirmed the enzyme cofactor-to-electrode distance controlled by the enzyme orientation greatly affected the DET/MET ratio

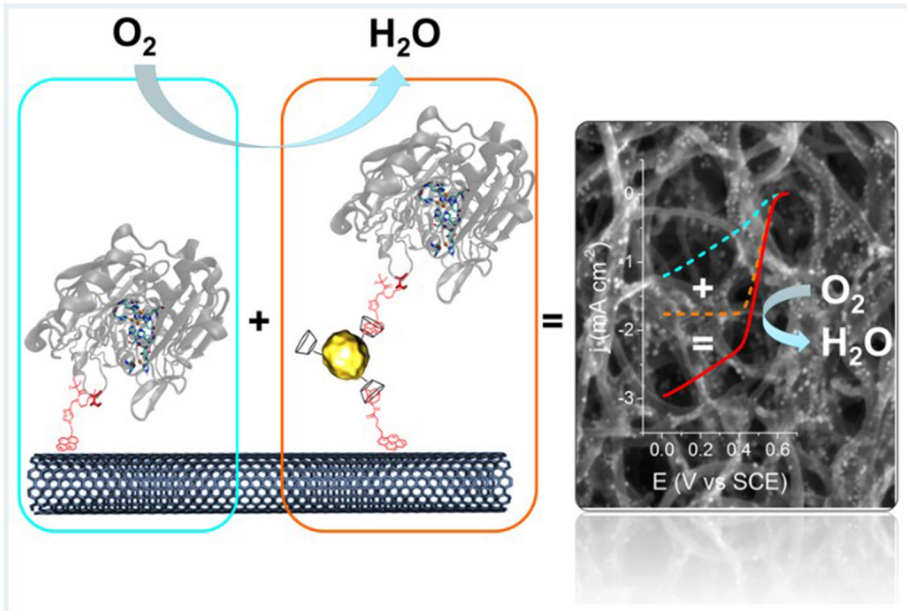

FIGURE 2 | Schematic representing direct bioelectrocatalysis of pyrene-modified laccase immobilized by β-cyclodextrin-modified gold nanoparticles bound to carbon nanotube (Lalaoui et al., 2016b).

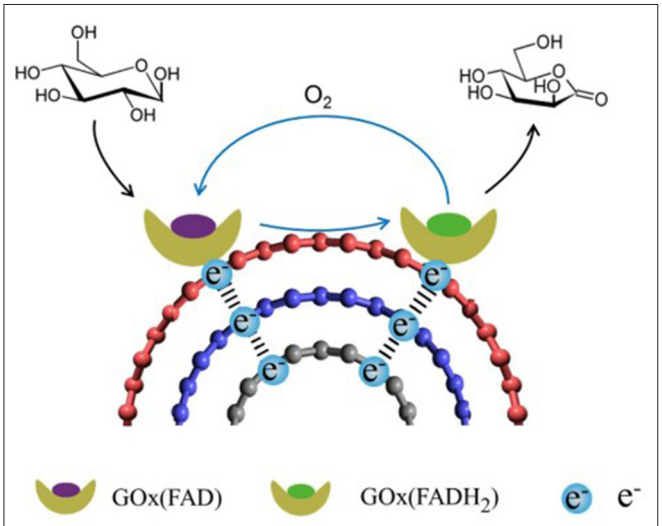

FIGURE 3 | Schematic of proposed route of DET for GOx physisorbed with multi-walled carbon nanotubes (Liu et al., 2018) (https://pubs.acs.org/doi/full/10.1021/acsomega.7b01633. Further permissions related to the material should be directed to ACS).

(Ma et al., 2019). Though not employed in an enzymatic fuel cell setup, they electrochemically demonstrated this effect with increased current density in the presence of a substrate at a fixed concentration when the enzyme was in a DET-favorable orientation. Tasca et al. enhanced the direct electron transfer by modifying single-walled carbon nanotubes with *p*-aminobenzoic acid or *p*-phenylenediamine using aryl diazonium salts, and cellobiose dehydrogenase (CDH) was immobilized onto these surface-modified SWNTs as the bioanodic enzyme (Tasca et al., 2011). The functional groups provided a positively or negatively charged surface to increase the interaction between the enzyme and the electrode as well as to facilitate specific orientation of the enzyme. Tasca et al. further explained that at low pH (i.e., pH3.5), which exhibits high surface concentration of negatively charged amino acid residues, the protonated (i.e., positively charged) *p*-phenylenediamine could create a less electrostatically repulsive environment for CDH, thus enhancing the DET. This effort was continued by the same group, and a similar bioanodic setup was used to fabricate a third-generation biosensor to detect lactose (Tasca et al., 2013).

BIOCATALYST IMMOBILIZATION METHODS

Stability of enzymatic fuel cells can also be enhanced by securely immobilizing the catalyst on the electrode surface (Bahar, 2019). Without proper anchoring down or protection, biocatalysts could easily denature and lose their activity or desorb from the electrode surface. Several immobilization methods have been developed based on covalent bonding, affinity of biocatalysts, entrapment, crosslinking, and more. With the ample potential for miniaturization for applications in biomedical, biocompatible, and even implantable devices, it is critical to maximize the stability of the biocatalysts and thus of the device performance.

Physisorption

Physisorption, typically done by dropcasting of enzyme solution onto the electrode surface followed by air-drying, is by far the

simplest and cheapest method to fabricate enzyme electrodes. However, because the enzymes are immobilized by weak van der Waals forces or hydrophobic-hydrophilic interactions, they can easily desorb or leach off the electrode surface (Strack et al., 2013; Narváez Villarrubia et al., 2014). Because of this, physisorption is often avoided, and rather, novel methods of enzyme immobilization or development of composite electrode materials are sought, and thus physisorption is only briefly described in this review. However, there are still recent efforts to improve the stability of physisorbed enzyme catalysts, including composite materials to co-deposit with the enzyme solution. Das et al. utilized composite electrode consisting of reduced graphene oxide (rGO) and gold nanoparticles (AuNPs) to immobilize GOx, which showed higher electron transfer rate than when rGO or AuNPs were used individually. The improved performance of laboratory scale fuel cell built from this bioanode was attributed to the increase specific surface area and electronic conductivity of rGO combined with better attachment between GOx and AuNPs *via* sulfur-containing amino acids of the enzyme (Das et al., 2014). Liu et al. studied the effect of MWNTs on the DET and electroactivity of GOx by co-depositing carbon nanotubes of various numbers of layers for various electroanalytical methods, which suggested that the electrons generated from GOx was shuttled from outer to inner wall of the MWNTs (**Figure 3**) (Liu et al., 2018).

Entrapment and Conducting Polymers

Organic molecules with metallic or semiconducting electrical properties called conducting polymers can be an effective agent to entrap the enzyme catalysts and help transfer electrons to the electrodes. In addition to these benefits, polypyrrole (Ppy) helps prevent some undesired reactions, explaining its continued use since its implementation in EFC setups in 1986 (Umaña and Waller, 1986). Recently, more complex bioanode setups with single- or multiwalled carbon nanotubes, nanocellulose, graphene, or various Ppy nanostructures, immobilizing a wide range of enzymes such as fructose dehydrogenase (Kizling et al., 2015, 2016), glucose oxidase (Kim et al., 2009; Min et al., 2010; Liu C. et al., 2011), and alcohol dehydrogenase (Gutiérrez-Domínguez et al., 2013). Many works suggested the enhanced power density was owed to the conductive polymer matrix allowing for proper orientation of the enzymes, good mass transport rates, and improved stability.

Polyethyleneimine (PEI) is also widely used to immobilize enzymes while exhibiting water miscibility and high biocompatibility as well as offering various surface chemistries for stable binding to electrode surfaces or other nanomaterials (**Figure 4**) (Christwardana et al., 2017; Sapountzi et al., 2017; Tavahodi et al., 2017). PEI is typically used along with carbon nanotubes (Christwardana et al., 2016, 2017) or metallic nanoparticles (Zeng et al., 2015; Chung et al., 2017a; Christwardana et al., 2018) to increase the stability of enzyme immobilization.

Polyaniline (PANI), discovered over 150 years ago, only started gaining research interest until 1980's due to its high electrical conductivity, and was first demonstrated for its utility as enzymatic electrode in 1999 by immobilizing lactate dehydrogenase on electrochemically prepared PANI film (Gerard et al., 1999). Since then, PANI has been utilized as composite materials or prepared as nanofibers (Kim et al., 2011, 2014; Mishra et al., 2017), mainly due to its multifaceted functionality and biocompatibility (Yan et al., 2010). PANI can be directly electrochemically polymerized or functionalized onto various carbonaceous nanomaterials including graphene, graphene oxide, or carbon nanotubes for enhanced electrical conductivity and enzymatic activity (Schubart et al., 2012; Kashyap et al., 2015; Kumar et al., 2016; Kang et al., 2017).

DNA as Scaffolds or Electron Acceptors

DNA has been employed as an effective method to immobilize single or multiple enzymes in a specific order for efficient cascade reactions. The terminals of the DNA can be modified for strong covalent bonds onto the electrode surface for stable anchoring of the enzyme catalysts. Xia et al. demonstrated a fully assembled methanol enzymatic fuel cell by immobilizing alcohol dehydrogenase and aldehyde dehydrogenase using zing-finger protein (Xia L. et al., 2017). The cascade reaction catalyzed by the two enzyme catalysts successfully hydrolyzed methanol to produce power density of 24.5 $\mu W/cm^2$. DNA nanostructures have also been used to couple synergistic enzymatic reactions into a cascade system (Müller and Niemeyer, 2008; Conrado et al., 2012; Fu et al., 2012), up to five enzymes for sequential hydrolysis of cellulose (**Figure 5**) (Chen et al., 2017).

Other 3D structures utilizing DNA such as nano-chambers (Linko et al., 2015) and nanocages (Zhao et al., 2016) were fabricated for self-assembly of enzyme cascades by GOx and horseradish peroxidase (HRP), which showed enhanced activity compared to when the two enzymes were freely in solution. Chakraborty et al. studied an oxygen-reducing cathode catalyzed by bilirubin oxidase (BOD) (Chakraborty et al., 2015). They used DNA as a template to fabricate gold nanoclusters (AuNC), which enhanced the electron transfer, shown by 15 mV lower overpotential as well as 5.5 times higher current than when typical plasmonic gold nanoparticle was used in the same configuration. Furthermore, rolling circle amplification was utilized to assemble multiple copies of the enzyme catalysts for enhanced catalytic activity toward reactions that are otherwise impossible to achieve with a single enzyme (Wilner et al., 2009; Sun and Chen, 2016). Though some of these examples were not readily applied to EFC setups, it is worth noting their potential for future applications in EFC with enhanced catalytic activity and stability.

NANOMATERIAL-BASED ELECTRODES

The high surface area-to-volume ratio and variability of physical and chemical properties by precise control of morphologies have made nanomaterials attractive and superior to their bulk counterparts in numerous applications. Taking advantage of such properties to increase not only the enzyme loading but also protection around the enzyme catalysts can allow the nanomaterial-based EFC electrodes to increase stability and decrease the enzyme-to-electrode distance for more efficient direct electron transfer (Mazurenko et al., 2018).

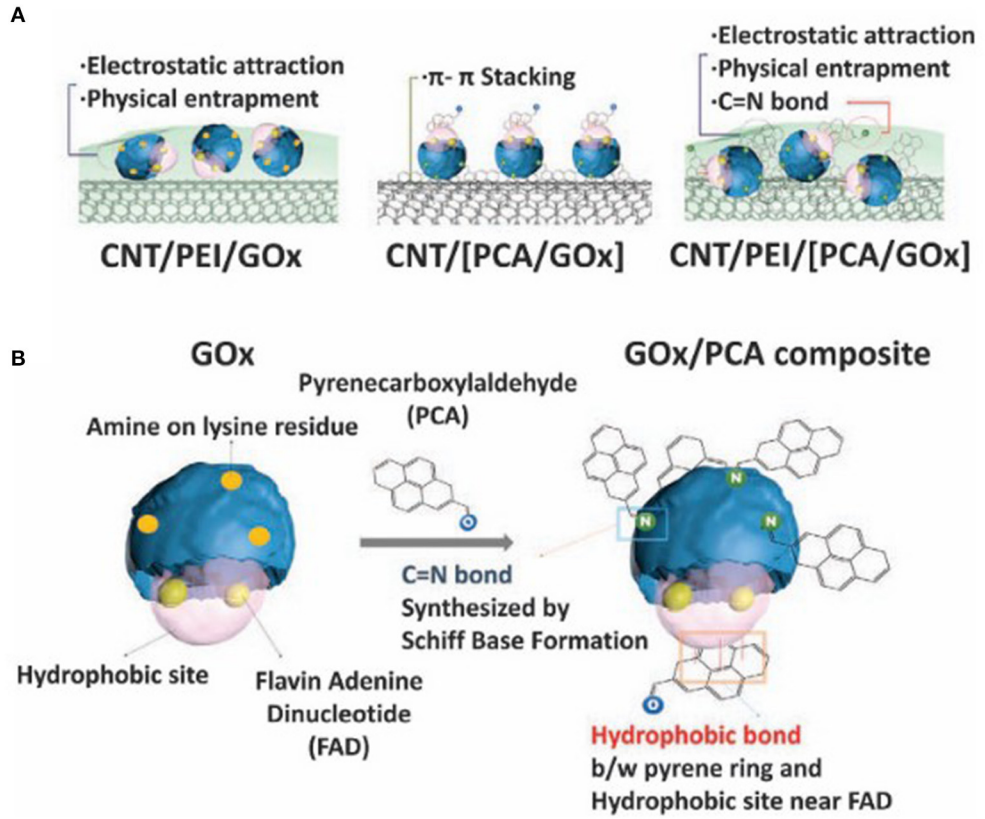

FIGURE 4 | Schematic of **(A)** fabrication of various GOx-functionalized electrodes and their mechanism of immobilization; **(B)** comparison between native GOx and GOx/PCA composite (Christwardana et al., 2017).

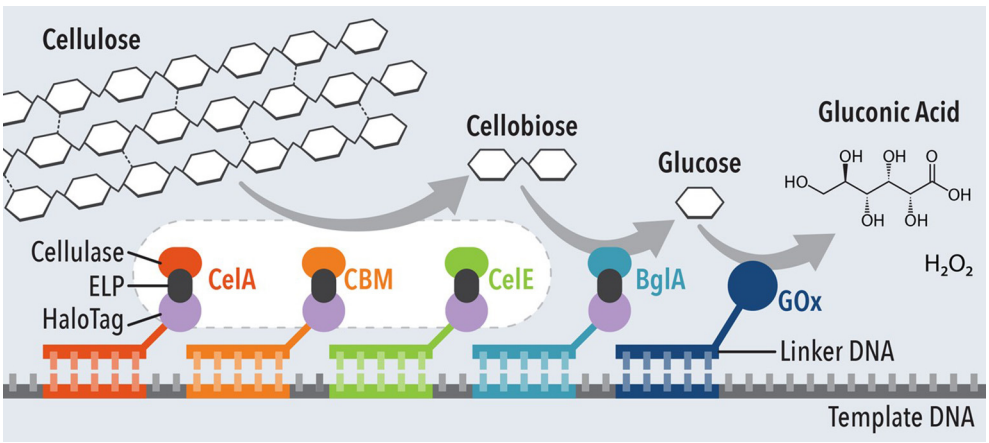

FIGURE 5 | Schematic of five-enzyme cascade system for hydrolysis of cellulose and glucose oxidation. Adapted from Chen et al. (2017).

Carbonaceous Materials

Carbon-based nanomaterials exhibit high electrical conductivity and good mechanical properties, as well as various physical and electrical properties depending on the control of their morphologies. Various carbonaceous materials such as carbon fibers or papers (Xu and Minteer, 2012; Kuo et al., 2013), carbon black (Kamitaka et al., 2007; Gupta et al., 2011; Haneda et al., 2012; Xia et al., 2016a), carbon nanoparticles (Selloum et al., 2014), graphene (Chen et al., 2012; Campbell et al., 2015; Song et al., 2015), graphite (Tasca et al., 2015; Antiochia et al., 2019), and carbon nanotubes (Gao et al., 2010; Ciaccafava et al., 2012; Agnès et al., 2013) have been

employed as EFC electrode materials. For example, buckypaper form of multiwalled carbon nanotubes (MWNTs) demonstrated excellent potential as enzymatic electrode material by 68-fold increase in current density from oxygen reduction reaction catalyzed by laccase compared to as-prepared agglomerates of MWNTs (Hussein et al., 2011). Hussein et al. attributed this significant enhancement to reduced diffusional mass transfer limitations and enhanced electrical conductivity when MWNTs were dispersed into a buckypaper form, which also exhibited highly mesoporous structures and good mechanical stability. Filip et al. demonstrated a low-cost biofuel cell by integrating carbon nanoparticle-nanotube composite-based bioanode and biocathode containing fructose dehydrogenase and bilirubin oxidase, respectively (Filip et al., 2013). In addition to combining two different carbon nanostructures to achieve high surface area as well as efficient interconnection for high electrical conductivity, this work by Filip et al. further attributed the high current density of the biocathode to the chitosan that acted as a "glue" to hold Ketjen Black-CNT composite, facilitating favorable orientation of the bilirubin oxidase for DET by electrostatic interaction between the positively charged chitosan and negatively charged enzyme as well as reducing charge transfer resistance and overpotential for oxygen reduction.

First discovered by Ijima et al. in 1991 (Iijima, 1991), carbon nanotubes (CNTs) now are one of the most widely used nanomaterials for fabrication of enzyme electrodes, largely due to high surface area-to-volume ratio and flexibility toward surface chemistry manipulation to enhance enzyme immobilization (Liu X. et al., 2011; Yan et al., 2011). For example, Zebda et al. demonstrated mediatorless glucose/oxygen biofuel cell based on GOx and Lc mechanically compressed with carbon nanotubes into bioanode and biocathode, respectively (Zebda et al., 2011). The high porosity and electrical conductivity of the CNT matrix contributed to good diffusion and electrical connection for the enzymes. Zebda et al. also suggested that the mechanical compression facilitated nanoscale proximity between the enzymes and the three-dimensional electrode surface, which attributed to the DET without any loss in enzymatic activity. In fact, power density of 1 mW/cm^2 and open-circuit voltage of 0.95 V was largely retained for 1 month under physiological conditions. Though carbon nanotubes are typically physisorbed or compressed with enzyme catalyst of choice, followed by coating of semi-permeable polymer like Nafion to prevent desorption or leaching of the enzymes, more complex setups have been reported to enhance the immobilization of the enzyme as well as electron transfer by using electrode materials of higher surface area and electrical conductivity. Carbon-based electrode materials were chemically modified or doped for increased enzyme loading and stability of enzyme immobilization (Meredith et al., 2011; Karaśkiewicz et al., 2012; Wei et al., 2012; Giroud and Minteer, 2013), decorated with metallic nanomaterials for covalent bonding of enzymes and enhanced electron transfer (Naruse et al., 2011; Lalaoui et al., 2016a), or combined with various carbonaceous nanomaterials to form composite electrodes (Wu et al., 2013; Campbell et al., 2015; Escalona-Villalpando et al., 2018). For example, carbon nanotubes functionalized with naphthalene, an aromatic group toward which laccase exhibited affinity due to its hydrophobic pocket, were efficient electrode materials in not only ensuring electrical wiring between enzyme cofactor and the electrode surface but also increasing the amount of enzymes in favorable orientation for DET (Karaśkiewicz et al., 2012). Biofuel cell assembled with this electrode exhibited power density of 131 $\mu W/cm^2$, 80% of which were retained after 24 h. Iron- and nitrogen-codoped carbon nanotubes were used by Ji et al. to enhance the overall catalytic activity of GOx-based bioanode by catalyzing oxidation reaction of hydrogen peroxide, a byproduct of glucose oxidation commonly known to inhibit enzyme activity (Ji et al., 2020). They also demonstrated their enzymatic fuel cell based on this electrode with power density of 63 $\mu W/cm^2$, and ~80% of the bioanodic current density of 347.1 $\mu A/cm^2$ was retained after 4 weeks.

Porous Nanostructure

The ultra-large surface area-to-volume ratio with fine-tunable pore size, density, and overall nanostructure dimensions, porous nanostructures have shown to be excellent candidates for EFC electrode materials. Though enzymeless, catalytic glucose oxidation by Rong et al. described the high porosity of the polymer matrix employed around the gold nanoparticle catalyst provided size-selective protection against larger molecules (Rong et al., 2014). Similar to this work, enzymatic electrodes are also fabricated based on porous structures in order to protect the enzyme catalysts, while allowing more contact area to enhance the DET rate. The significance of mesoporous electrodes (i.e., containing pores of diameter between 2 and 50 nm) is supported by (i) the curvature effect (Sugimoto et al., 2016, 2017), in which the current density largely increases as pore diameter approaches that of a single enzyme; as well as (ii) the electrostatic interaction between the enzyme and the electrode, where the surface charge of the electrodes can promote the preferred orientation of the enzymes so that the distance between the enzyme active site and the electrode is minimized (Sugimoto et al., 2015; Lalaoui et al., 2016b; Xia et al., 2016b; Xia H. et al., 2017). With these in mind, meso- and microporous electrodes were fabricated based on glassy carbon electrodes modified with Ketjen Black and gold nanoparticles to improve the direct electron transfer kinetics of several redox enzymes such as bilirubin oxidase, hydrogenase, and formate dehydrogenase (**Figure 6**) (Sakai et al., 2018). Based on the electrochemical behavior of these electrodes characterized by cyclic voltammetry, combined with electrostatic charge distribution visualized by PyMOL, it was suggested that electrodes with controlled morphology such as mesoporous structure was a predominant factor in facilitating DET of the three enzymes. The mechanism of DET based on porous electrodes and the optimum porous nanomaterial for DET were mathematically modeled and experimentally validated by Do et al. (2014) and Mazurenko et al. (2017b) respectively.

Various porous materials were utilized as electrodes to be functionalized with enzyme catalysts. Wang et al. deposited single-walled carbon nanotube on gold-coated porous silicon substrates, onto which GOx and Lc were electrochemically immobilized to fabricate bioanode and biocathode, respectively. Enzymatic fuel cell built with these electrodes produced peak

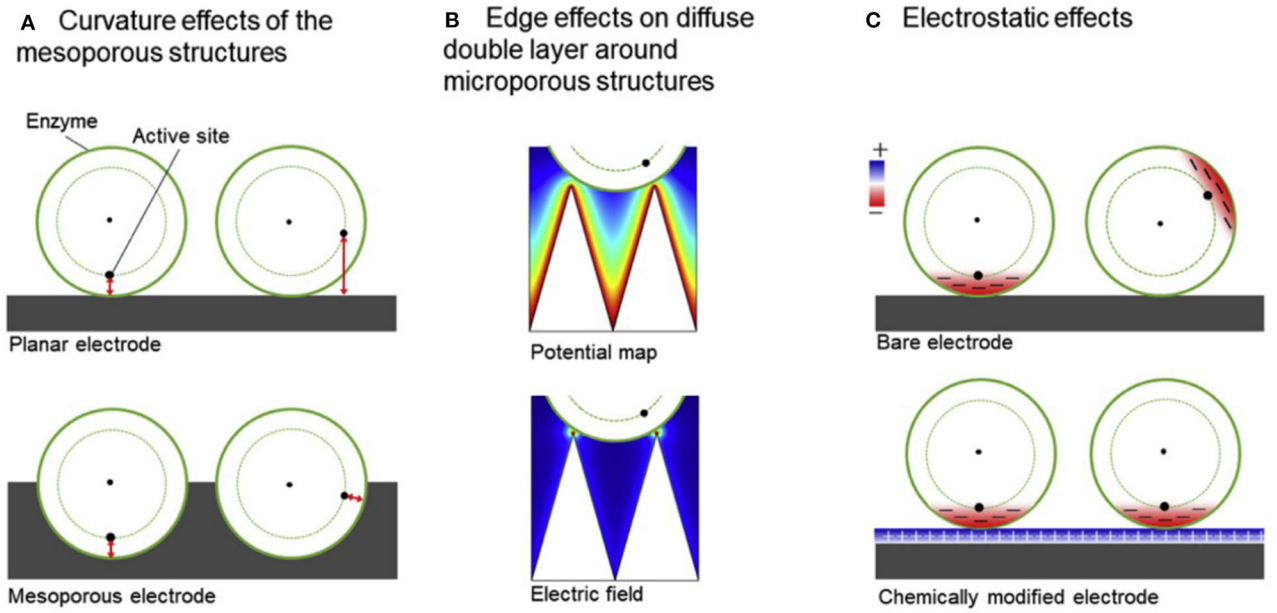

FIGURE 6 | Schematics showing **(A)** curvature effect **(B)** edge effect **(C)** electrostatic effect that are taken into account for meso- and microporous structures (Sakai et al., 2018).

power density of 1.38 $\mu W/cm^2$ for up to 24 h (Wang et al., 2009a). Though the power density output was not as high compared to similar works, it was important to note that both membrane- and mediator-free enzymatic fuel cell was demonstrated with glucose at a near-physiological concentration for potential in biomedical application. Improved peak power density and stability of up to 12 $\mu W/cm^2$ and 48 h, respectively, were later demonstrated by the same setup and group later that year (Wang et al., 2009b). A work by du Toit and Di Lorenzo demonstrated the feasibility of highly porous gold electrodes for use in biofuel cell with GOx and laccase as anodic and cathodic catalysts, respectively, producing peak power density of 6 $\mu W/cm^2$ (Du Toit and Di Lorenzo, 2014), a comparable value to other miniature EFCs (Beneyton et al., 2013; Falk et al., 2013). Their effort continued to develop a flow-through glucose/oxygen fuel cell based on highly porous gold electrodes for continuous power generation for up to 24 h (du Toit and Di Lorenzo, 2015). Salaj-Kosla et al. also utilized nanoporous gold electrodes to immobilize bilirubin oxidase by physisorption to produce catalytic current density of 0.8 mA/cm^2 (Salaj-kosla et al., 2012). More recently, bioelectrocatalysis by bilirubin oxidase was further improved by immobilizing it onto porous gold (Takahashi et al., 2019a) and mesoporous carbon electrodes (Takahashi et al., 2019b), which was attributed to the appropriate pore size distribution as well as promotion of favorable orientation of the enzyme for direct electron transfer.

Gold Nanoparticles

Due to their unique physical and electrical properties, gold nanoparticles (AuNPs) are among popular materials with which to functionalize EFC electrodes. In addition, the various facile synthesis protocols and size control techniques make AuNPs more attractive in enhancing the enzyme electrode performance. AuNPs themselves can be modified with functional groups such as thiols to covalently attach to electrode surface, improving the stability when the enzymes are adsorbed onto the AuNP functionalized electrodes, in which the AuNPs act as electronic bridges between the enzyme active site and the electrode surface. Monsalve et al. used a thiolated AuNPs of various sizes to covalently bind to a hydrogenase for bioanode fabrication, during which the smallest AuNPs were found to exhibit the highest surface area, leading to a 170-fold increase in current density from DET-based hydrogen oxidation compared to using unmodified bulk gold electrode (Monsalve et al., 2015). Combined with BOD-modified cathode, the as-fabricated EFC produced power density of up to 0.25 mW/cm^2. Ratautas et al. fabricated a bioanode with AuNP modified with 4-aminothiophenol (4-ATP), which contained oxidized derivatives that allowed for stable immobilization of glucose dehydrogenase, and confirmed its mediator-free glucose oxidation electrochemically (Ratautas et al., 2016). Biocathodes based on AuNPs as electronic bridges for laccase were also fabricated by Kang et al.; laccase was immobilized onto naphthalenethiol-modified AuNPs, which promoted the electron transfer to the polyethyleneimine-carbon nanotube electrode (Kang S. et al., 2018). The high-surface area electrode also increased the enzyme loading, producing 13 $\mu W/cm^2$ power density when put together into EFC. AuNPs were employed in both anode and cathode for sugar/oxygen EFC with cellobiose dehydrogenase and bilirubin oxidase as anodic and cathodic catalyst, respectively; the EFC showed improved performance than previously fabricated EFCs (i.e., power density of 15 $\mu W/cm^2$ in buffer and 3 $\mu W/cm^2$ in human blood), which was attributed to the use of 3D AuNP-modified electrodes (Wang et al., 2012). AuNPs are also used with other electrically

conductive materials such as conducting polymers and carbon nanotubes to further enhance the electrical properties for more stable DET (Krikstolaityte et al., 2014; Tavahodi et al., 2017).

Recently, gold nanoparticle-carbon nanotube hybrid fibers were utilized as electrode materials for high-performance glucose/O_2 enzymatic fuel cell (Kwon et al., 2019). GOx, the bioanodic enzyme of choice, and the gold nanoparticles were alternately assembled layer by layer to combine covalent and electrostatic bonding, leading to enhanced electron transfer and stability. This highly electrically conductive material allowed for fast electron transfer between the active site of GOx and the electrode surface, exhibited by the small redox peak separation of ∼0.11 V. Furthermore, the assembled enzymatic fuel cell outputted power density and open-circuit voltage of 1.2 mW/cm^2 and 0.98 V, respectively. In the presence of a low concentration of glucose to mimic the physiological conditions (i.e., 10 mmol/L glucose), the EFC still exhibited 0.6 mW/cm^2 of power density and 0.72 V of open-circuit voltage, showing great promise in the biomedical applications. The same layer-by-layer assembly method was employed to fabricate GOx-coated metallic cotton fiber as the bioanode, exhibiting excellent electrical communication between the enzyme and the electrode for enhanced electron transfer (Kwon et al., 2018). Combined with the high conductivity of the cotton fibers ($>2.1 \times 10^4$ S/cm), the GOx/AuNP/metallic cotton fiber-based electrode showed an impressive power density of 3.7 mW/cm^2 when assembled into EFC.

RECENT PERFORMANCES OF DET-ENABLED ANODES, CATHODES, AND EFCs

Combining methods discussed in the previous sections, recent studies have demonstrated enhanced performances of electrodes and enzymatic fuel cells operating in direct electron transfer. Studies worth highlighting are summarized in **Table 1**.

Bioanode with one of the highest performances was demonstrated by Gineityte et al.; GDH was immobilized onto cysteamine-modified gold nanoparticles, which was tethered to polyaniline (Gineityte et al., 2019). The unique combination of conductive polymer directly electropolymerized on the electrode surface and positively charged monolayer of gold nanoparticles attributed to the enhanced electron transfer between the bioanodic enzyme and the electrode. This study further demonstrated the bioanode performance in human blood samples, in which the average current density was ∼65% of that in blood-mimicking buffer solution. One of the highest power densities in an enzymatic fuel cell was reported by Chung et al., who utilized a two-step crosslinking method to first form a TPA/GOx composite and then immobilize onto PEI/CNT electrode (Chung et al., 2017b). The large power density of 1,620 μW/cm^2 was attributed to the enhanced electron transfer due to electron delocalization by π conjugation as well as the enhanced stability of the enzyme. Because the GOx denaturation was reduced by the strong chemical bonds immobilizing the bioanodic enzyme on the electrode surface, the assembled EFC retained ∼75% of its power density for 4 weeks, which highlighted the increased stability.

Some other methods that are interesting to note include extending the EFC lifetime by functionalizing magnetic nanoparticles with bioanodic enzymes to replenish the bioanode with a fresh batch of biocatalysts (Herkendell et al., 2019). Though power density of only 160 μW/cm^2 was reported for this EFC, the idea of removing and reloading the biocatalysts by a magnetically assisted methodology was unique, which showed the EFC lifetime was extended from ∼20 to 70 h.

RECENT PROGRESS IN BIOMEDICAL APPLICATION OF DET-ENABLED EFC

Implantable devices powered by EFCs are increasingly attracting research attention since high substrate specificity of enzyme catalysts removes the need for compartments or membranes, allowing for miniaturization. Furthermore, use of biocompatible nanomaterials for electrodes has shown great potential in implantable EFC devices. Though mediated electron transfer-based EFCs have shown potential for implantable device applications earlier and consistently grown (Mano et al., 2003, 2004; Miyake et al., 2011; Sales et al., 2013), DET-enabled EFCs closely followed the trend. Starting from those fueled by clams (Szczupak et al., 2012) and lobsters (MacVittie et al., 2013), DET-driven EFCs were surgically implanted on an exposed rat tissue (Castorena-Gonzalez et al., 2013) and finally in the abdominal cavity of a rat to truly show the potential of biocompatible, implantable EFC to power devices, which was demonstrated by the powering of light-emitting diode (LED) and a digital thermometer (Zebda et al., 2013). To accomplish this, Zebda et al. wrapped the enzyme electrodes in silicone bags, followed by a dialysis bag filled with sterile solution and then an autoclaved commercial sleeve to avoid inflammation or toxicity issue with the rat tissue. Halámková et al. demonstrated a glucose/oxygen fuel cell based on PQQ-GDH noncovalently bound to carbon nanotubes and Lc as bioanodic and biocathodic catalyst, respectively, and generated maximum power density of 30 μW/cm^2 and continuously operated as glucose was regenerated by the snail's feedings and relaxing (**Figure 7**) (Halámková et al., 2012).

The effort toward implantable EFC-powered devices for humans have also been consistent. Bollella et al. demonstrated a proof of concept with a FAD-based CDH and Lc as bioanodic and biocathodic enzyme catalyst, respectively, immobilized on a gold nanoparticle-functionalized graphene screen-printed electrode; the EFC with both enzyme catalysts co-immobilized on the same electrode showed power output of 1.10 μW/cm^2 and open-circuit voltage of 0.41 V in real human saliva samples, hinting at a potential non-invasive autonomous biodevices (Bollella et al., 2018). DET-enabled EFCs also exhibited stable operation in other human liquids such as serum, saliva, and urine, ranging in power density of 12–18 μW/cm^2 (Göbel et al., 2016). Operation of mediatorless EFC utilizing various enzymes such as PQQ-GDH and cellobiose dehydrogenase in real or synthetic

TABLE 1 | Performances of electrodes and enzymatic fuel cells operating on direct electron transfer.

Bioanodic enzyme/ material	Biocathodic enzyme/ material	Fuel/oxidant	Electrode/cell current density [$\mu A/cm^2$]	Power density [$\mu W/cm^2$]	OCP [V]	Lifetime [h]	% current or power density retained during lifetime	References
CDH/SWNT/GC	-	Lactose/-	500	-	-	50	85	Tasca et al., 2011
CDH/graphite	-	Lactose/-	4.79	-	-	-	-	Ortiz et al., 2012
CDH/SWNT/GC	-	Lactose/-	500	-	-	288	50	Tasca et al., 2013
-	Lc/CNT/Ta	-/O_2	840	-	-	168	75	Singh et al., 2020
GOx/hydroquinone/SWNT/Au	Lc/SWNT/Au	Glucose/O_2	-	240	0.52	-	-	Bojórquez-Vázquez et al., 2018
Py_2Ox/CAT/GC	Py_2Ox/HRP/CNT-CMF-CC	H_2/glucose	-	530	1.15	10	50	Ruff et al., 2018
GDH/PANI/AuNP/Au	-	Glucose/-	1,000	-	-	24	79	Gineityte et al., 2019
GOx/NQ/MWNT	HRP/MWNT	Glucose/H_2O_2	-	700	0.6	-	-	Abreu et al., 2018
GOx/TPA/PEI/CNT	Pt/C	Glucose/O_2	78.6	1,620	-	672	75.8	Chung et al., 2017b
GOx/PANI/GC	Lc/PANI/GC	Glucose/O_2	-	1,120	0.78	336	82.9	Kang Z. et al., 2018
FAD-GDH/Th-AuNP/CNT/GC	BOD/GR/CNT/GC	Glucose/O_2	925	269	0.71	-	-	Navaee and Salimi, 2018
GOx/Naph-SH/AgNP/PEI/CNT	Pt/C	Glucose/O_2	-	1,460	-	840	83	Christwardana et al., 2018
GOx/graphene	-	Glucose/O_2	-	164	0.44	168	60	Babadi et al., 2019
GOx/PVP-RPPy/NiF	Lc/PVP-RPPy/NiF	Glucose/O_2	-	350	1.16	336	82	Kang et al., 2019
Zn	BOD/MWNT/rGO/PG	-/O_2	650	775	1.68	-	-	Torrinha et al., 2020
-	MoBOD/MWNT	-/O_2	4,000	-	-	24	73	Gentil et al., 2018
GDH/GO/GC	Lc/AuNP/Au	Glucose/O_2	1,100	400	0.86	576	93	Maleki et al., 2019

CDH, cellobiose dehydrogenase; SWNT, single-walled carbon nanotube; GC, glassy carbon; GOx, glucose oxidase; Py_2Ox, pyranose oxidase; CAT, catalase; GDH, glucose dehydrogenase; PANI, polyaniline; NP, nanoparticles; NQ, naphthoquinone; MWNT, multi-walled carbon nanotube; TPA, terephthalaldehyde; PEI, polyethyleneimine; CNT, carbon nanotube; FAD-GDH, flavin adenine dinucleotide-dependent GDH; Th, thionine; Naph-SH, naphthalene-thiol; PVP-RPPy, polyvinylpyrrolidone-rectangular polypyrrole; GO, graphene oxide; Lc, laccase; HRP, horseradish peroxidase; CMF, carbon microfibers; CC, carbon cloth; BOD, bilirubin oxidase; rGO, reduced raphene oxide; PG, pencil graphite; MoBOD, BOD from Magnaporthe orizae.

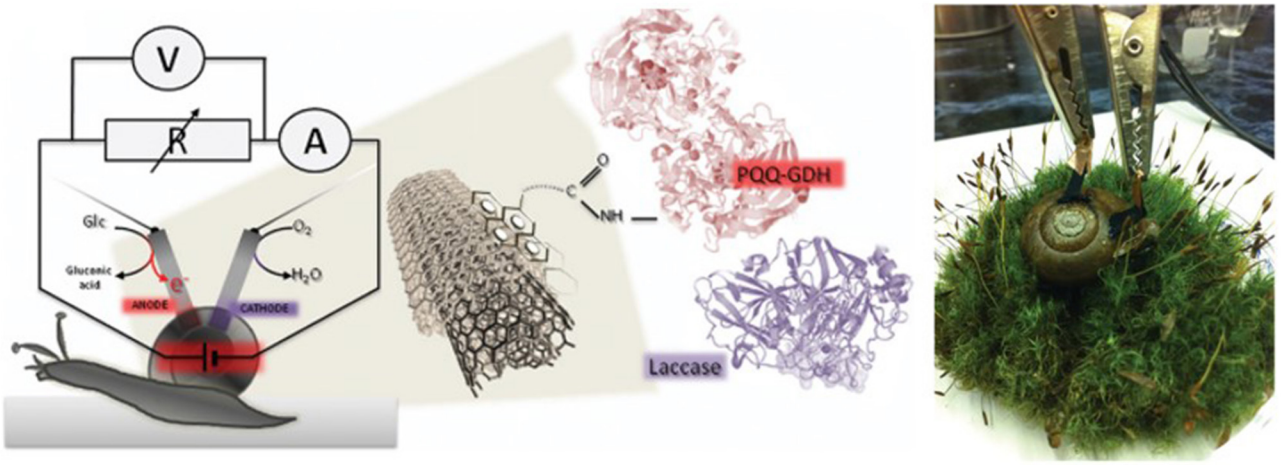

FIGURE 7 | Schematic of enzymatic fuel cell using live snail. Figures are from work by Halámková et al. (2012).

human tear was observed, giving possibility of EFCs powering "smart" contact lenses (Falk et al., 2012; Reid et al., 2015). Other electrochemical devices for transdermal biosensing were reviewed by Tasca et al. (2019); minimally invasive diagnostic devices have gained some momentum, leading to microneedle-based biosensors penetrating the skin at the dermis (i.e., 1–2,000 μm) level to detect analytes in human body such as glucose, lactate, potassium ions, and glutamate.

Pankratov et al. utilized transparent, flexible substrate upon which CDH and BOx were immobilized was used to produce maximum of 0.6 $\mu W/cm^2$ and maintain ∼80% of the initial power density after 12 h of operation (Pankratov et al., 2015). The use of the transparent substrate and the minimal impact on the transparency upon enzyme immobilization, combined with relatively stable operation of the EFC, suggests its potential as a power source for smart contact lenses. The low power output of the implantable DET-enabled EFC in human physiological fluids [compared to ∼40 $\mu W/cm^2$ achieved by Milton et al. *via* mediated glucose oxidation in human serum at 21 °C (Milton et al., 2015)] was primarily attributed to the extremely low glucose concentration, but given that some cases of MET-based EFC was able to show higher power outputs, there are certainly more optimization and improvements needed before implementing DET-based EFCs to power implantable devices.

CONCLUSIONS AND OUTLOOK

In addition to being a method of green energy production, enzymatic fuel cells offer many advantages such as potential for miniaturization and flexibility of fuels. With proper engineering of various components of the EFC, scientific community has come a long way in enhancing the EFC performance including power density and open circuit potential in a push toward real-life applications, especially in the biomedical field. Both biocatalysts and electrodes were engineered to promote higher catalytic activity, more efficient electron transfer, and faster current collection to maximize power generation. Some engineering methods have been employed to prolong the activity of the biocatalysts and therefore the stability of the EFC performance.

Even though many potential applications have been explored, some of which were very promising, EFCs still suffer greatly from lack of long-term stability and low power density with fuel concentrations as low as physiological conditions. However, the ongoing debate on whether or not MET is better than DET or vice versa may be the bottleneck that takes away the focus from realization of EFCs in real-life applications. More research based on fundamentals of enzymatic and electroactivity of the biocatalysts may be necessary to undeniably support or refute the direct electron transfer of some popular enzymes like glucose oxidase.

AUTHOR CONTRIBUTIONS

SY prepared the manuscript and obtained permission to reuse figures from appropriate parties. All authors contributed to the article and approved the submitted version.

REFERENCES

Abreu, C., Nedellec, Y., Ondel, O., Buret, F., Cosnier, S., Le Goff, A., et al. (2018). Glucose oxidase bioanodes for glucose conversion and H_2O_2 production for horseradish peroxidase biocathodes in a Fl Ow through glucose biofuel cell design. *J. Power Sources* 392, 176–180. doi: 10.1016/j.jpowsour.2018.04.104

Agnès, C., Reuillard, B., Le Goff, A., Holzinger, M., and Cosnier, S. (2013). A double-walled carbon nanotube-based glucose/H_2O_2 biofuel cell

operating under physiological conditions. *Electrochem. Commun.* 34, 105–108. doi: 10.1016/j.elecom.2013.05.018

Aiba, H., Nishiya, Y., Azuma, M., Yokooji, Y., Atomi, H., and Imanaka, T. (2015). Characterization of a thermostable glucose dehydrogenase with strict substrate specificity from a hyperthermophilic archaeon thermoproteus Sp. GDH-1. *Biosci. Biotechnol. Biochem.* 79, 1094–1102. doi: 10.1080/09168451.2015.1018120

Antiochia, R., Oyarzun, D., Sanchez, J., and Tasca, F. (2019). Comparison of direct and mediated electron transfer for bilirubin oxidase from myrothecium verrucaria. Reduction reaction. *Catalysts* 9:121056. doi: 10.3390/catal9121056

Babadi, A. A., Wan-Mohtar, W. A. A. Q. I., Chang, J. S., Ilham, Z., Jamaludin, A. A., Zamiri, G., et al. (2019). High-performance enzymatic biofuel cell based on three-dimensional graphene. *Int. J. Hydrogen Energy* 44, 30367–30374. doi: 10.1016/j.ijhydene.2019.09.185

Bahar, T. (2019). Stability improvement by crosslinking of previously immobilized glucose oxidase on carbon nanotube-based bioanode. *Turkish J. Chem.* 43, 1570–1579. doi: 10.3906/kim-1905-35

Bartlett, P. N., and Al-lolage, F. A. (2018). There is no evidence to support literature claims of direct electron transfer (DET) for native glucose oxidase (GOx) at carbon nanotubes or graphene. *J. Electroanal. Chem.* 819, 26–37. doi: 10.1016/j.jelechem.2017.06.021

Beneyton, T., Wijaya, I. P. M., Salem, C., Griffiths, A. D., and Taly, V. (2013). Membraneless glucose/O_2 microfluidic biofuel cells using covalently bound enzymes. *Chem. Commun.* 49, 1094–1096. doi: 10.1039/c2cc37906f

Berezin, I. V., Bogdanovskaya, V. A., Varfolomeev, S. D., Tarasevich, M. R., and Yaropolov, A. I. (1978). *Dokl. Akad. Nauk SSSR* 240, 615–618.

Betso, S. R., Klapper, M. H., and Anderson, L. B. (1972). Electrochemical studies of heme proteins. Coulometric, polarographic, and combined spectroelectrochemical methods for reduction of the heme prosthetic group in cytochrome C. *J. Am. Chem. Soc.* 94, 8197–8204. doi: 10.1021/ja00778a042

Bojórquez-Vázquez, L. A., Cano-Castillo, U., and Vazquez-Duhalt, R. (2018). Membrane-less enzymatic fuel cell operated under acidic conditions. *J. Electroanal. Chem.* 830–831, 56–62. doi: 10.1016/j.jelechem.2018.10.027

Bollella, P., Fusco, G., Stevar, D., Gorton, L., Ludwig, R., Ma, S., et al. (2018). A glucose/oxygen enzymatic fuel cell based on gold nanoparticles modified graphene screen-printed electrode. Proof-of-concept in human Saliva. *Sensors Actuat. B Chem.* 256, 921–930. doi: 10.1016/j.snb.2017.10.025

Campbell, A. S., Jeong, Y. J., Geier, S. M., Koepsel, R. R., Russell, A. J., and Islam, M. F. (2015). Membrane/mediator-free rechargeable enzymatic biofuel cell utilizing graphene/single-wall carbon nanotube cogel electrodes. *ACS Appl. Mater. Interfaces* 7, 4056–4065. doi: 10.1021/am507801x

Castorena-Gonzalez, J. A., Foote, C., MacVittie, K., Halámek, J., Halámková, L., Martinez-Lemus, L. A., et al. (2013). Biofuel cell operating *in vivo* in rat. *Electroanalysis* 25, 1579–1584. doi: 10.1002/elan.201300136

Chakraborty, S., Babanova, S., Rocha, R. C., Desireddy, A., Artyushkova, K., Boncella, A. E., et al. (2015). A hybrid DNA-templated gold nanocluster for enhanced enzymatic reduction of oxygen. *J. Am. Chem. Soc.* 137, 11678–11687. doi: 10.1021/jacs.5b05338

Chen, J., Zheng, X., Miao, F., Zhang, J., Cui, X., and Zhen, W. (2012). Engineering graphene/carbon nanotube hybrid for direct electron transfer of glucose oxidase and glucose biosensor. *J. Appl. Electrochem.* 42, 875–881. doi: 10.1007/s10800-012-0461-x

Chen, Q., Yu, S., Myung, N., and Chen, W. (2017). DNA-guided assembly of a five-component enzyme cascade for enhanced conversion of cellulose to gluconic acid and H_2O_2. *J. Biotechnol.* 263, 30–35. doi: 10.1016/j.jbiotec.2017.10.006

Christwardana, M., Chung, Y., and Kwon, Y. (2017). A new biocatalyst employing pyrenecarboxaldehyde as an anodic catalyst for enhancing the performance and stability of an enzymatic biofuel cell. *NPG Asia Mater.* 9, 1–9. doi: 10.1038/am.2017.75

Christwardana, M., Kim, D. H., Chung, Y., and Kwon, Y. (2018). A hybrid biocatalyst consisting of silver nanoparticle and naphthalenethiol self-assembled monolayer prepared for anchoring glucose oxidase and its use for an enzymatic biofuel cell. *Appl. Surf. Sci.* 429, 180–186. doi: 10.1016/j.apsusc.2017.07.023

Christwardana, M., Kim, K. J., and Kwon, Y. (2016). Fabrication of mediatorless/membraneless glucose/oxygen based biofuel cell using biocatalysts including glucose oxidase and laccase enzymes. *Sci. Rep.* 6, 1–10. doi: 10.1038/srep30128

Chung, Y., Ahn, Y., Kim, D. H., and Kwon, Y. (2017a). Amide group anchored glucose oxidase based anodic catalysts for high performance enzymatic biofuel cell. *J. Power Sources* 337, 152–158. doi: 10.1016/j.jpowsour.2016.10.092

Chung, Y., Christwardana, M., Tannia, D. C., Kim, K. J., and Kwon, Y. (2017b). Biocatalyst including porous enzyme cluster composite immobilized by two-step crosslinking and its utilization as enzymatic biofuel cell. *J. Power Sources* 360, 172–179. doi: 10.1016/j.jpowsour.2017.06.012

Ciaccafava, A., Poulpiquet, A., De Techer, V., Giudici-orticoni, M. T., Tingry, S., Innocent, C., et al. (2012). Electrochemistry communications an innovative powerful and mediatorless H_2/O_2 biofuel cell based on an outstanding bioanode. *Electrochem. Commun.* 23, 25–28. doi: 10.1016/j.elecom.2012.06.035

Conrado, R. J., Wu, G. C., Boock, J. T., Xu, H., Chen, S. Y., Lebar, T., et al. (2012). DNA-guided assembly of biosynthetic pathways promotes improved catalytic efficiency. *Nucl. Acids Res.* 40, 1879–1889. doi: 10.1093/nar/gkr888

Das, D., Ghosh, S., and Basumallick, I. (2014). Electrochemical studies on glucose oxidation in an enzymatic fuel cell with enzyme immobilized on to reduced graphene oxide surface. *Electroanalysis* 26, 2408–2418. doi: 10.1002/elan.201400245

Davis, J., and Yarbrough, H. (1967). *Microbial oxygenated fuel cell*. U.S. Patent 3,331,848.

Desriani, Hanashi, T., Yamazaki, T., Tsugawa, W., and Sode, K. (2010). Enzyme fuel cell for cellulolytic sugar conversion employing FAD glucose dehydrogenase and carbon cloth electrode based on direct electron transfer principle. *Open Electrochem. J.* 2, 6–10. doi: 10.2174/1876505X01002010006

Do, T. Q. N., Varničić, M., Hanke-Rauschenbach, R., Vidaković-Koch, T., and Sundmacher, K. (2014). Mathematical modeling of a porous enzymatic electrode with direct electron transfer mechanism. *Electrochim. Acta* 137, 616–626. doi: 10.1016/j.electacta.2014.06.031

Du Toit, H., and Di Lorenzo, M. (2014). Glucose oxidase directly immobilized onto highly porous gold electrodes for sensing and fuel cell applications. *Electrochim. Acta* 138, 86–92. doi: 10.1016/j.electacta.2014.06.074

du Toit, H., and Di Lorenzo, M. (2015). Continuous power generation from glucose with two different miniature flow-through enzymatic biofuel cells. *Biosens. Bioelectron.* 69, 199–205. doi: 10.1016/j.bios.2015.02.036

Escalona-Villalpando, R. A., Martínez-Maciel, A. C., Espinosa-Ángeles, J. C., Ortiz-Ortega, E., Arjona, N., Arriaga, L. G., et al. (2018). Evaluation of hybrid and enzymatic nanofluidic fuel cells using 3D carbon structures. *Int. J. Hydrogen Energy* 43, 11847–11852. doi: 10.1016/j.ijhydene.2018.04.016

Falk, M., Andoralov, V., Blum, Z., Sotres, J., Suyatin, D. B., Ruzgas, T., et al. (2012). Biofuel cell as a power source for electronic contact lenses. *Biosens. Bioelectron.* 37, 38–45. doi: 10.1016/j.bios.2012.04.030

Falk, M., Andoralov, V., Silow, M., Toscano, M. D., and Shleev, S. (2013). Miniature biofuel cell as a potential power source for glucose-sensing contact lenses. *Anal. Chem.* 85, 6342–6348. doi: 10.1021/ac4006793

Filip, J., Šefčovičová, J., and Gemeiner, P., Tkac, J. (2013). Electrochemistry of bilirubin oxidase and its use in preparation of a low cost enzymatic biofuel cell based on a renewable composite binder chitosan. *Electrochim. Acta* 87, 366–374. doi: 10.1016/j.electacta.2012.09.054

Fu, J., Liu, M., Liu, Y., Woodbury, N. W., and Yan, H. (2012). Interenzyme substrate diffusion for an enzyme cascade organized on spatially addressable DNA nanostructures. *J. Am. Chem. Soc.* 134, 5516–5519. doi: 10.1021/ja300897h

Gao, F., Viry, L., Maugey, M., Poulin, P., and Mano, N. (2010). Engineering hybrid nanotube wires for high-power biofuel cells. *Nat. Commun.* 1:1000. doi: 10.1038/ncomms1000

Gentil, S., Carriere, M., Cosnier, S., Gounel, S., Mano, N., and Le Goff, A. (2018). Direct electrochemistry of bilirubin oxidase from magnaporthe orizae on covalently-functionalized MWCNT for the design of. *Chem. A Eur. J.* 24, 8404–8408. doi: 10.1002/chem.201800774

Gerard, M., Ramanathan, K., Chaubey, A., and Malhotra, B. D. (1999). Immobilization of lactate dehydrogenase on electrochemically prepared polyaniline films. *Electroanalysis* 11, 450–452. doi: 10.1002/(SICI)1521-4109(199905)11:6<450::AID-ELAN450>3.0.CO;2-R

Gineityte, J., Meskys, R., Dagys, M., and Ratautas, D. (2019). Highly efficient direct electron transfer bioanode containing glucose

dehydrogenase operating in human blood. *J. Power Sources* 441:227163. doi: 10.1016/j.jpowsour.2019.227163

Giroud, F., and Minteer, S. D. (2013). Anthracene-modified pyrenes immobilized on carbon nanotubes for direct electroreduction of O_2 by laccase. *Electrochem. Commun.* 34, 157–160. doi: 10.1016/j.elecom.2013.06.006

Göbel, G., Beltran, M. L., Mundhenk, J., Heinlein, T., Schneider, J., and Lisdat, F. (2016). Operation of a carbon nanotube-based glucose/oxygen biofuel cell in human body liquids — performance factors and characteristics. *Electrochim. Acta* 218, 278–284. doi: 10.1016/j.electacta.2016.09.128

Gupta, G., Lau, C., Branch, B., Rajendran, V., Ivnitski, D., and Atanassov, P. (2011). Direct bio-electrocatalysis by multi-copper oxidases : gas-diffusion laccase-catalyzed cathodes for biofuel cells. *Electrochim. Acta* 56, 10767–10771. doi: 10.1016/j.electacta.2011.01.089

Gutiérrez-Domínguez, D. E., Pacheco-Catalán, D. E., Patiño-Diaz, R., Canto-Canché, B., and Smit, M. A. (2013). Development of alcohol dehydrogenase-polypyrrole electrodes by adsorption and crosslinking for ethanol oxidation. *Int. J. Hydrogen Energy* 38, 12610–12616. doi: 10.1016/j.ijhydene.2012.11.086

Gutiérrez-Sánchez, C., Pita, M., Vaz-Domínguez, C., Shleev, S., and De Lacey, A. L. (2012). Gold nanoparticles as electronic bridges for laccase-based biocathodes. *J. Am. Chem. Soc.* 134, 17212–17220. doi: 10.1021/ja307308j

Halámková, L., Halámek, J., Bocharova, V., Szczupak, A., Alfonta, L., and Katz, E. (2012). Implanted biofuel cell operating in a living snail. *J. Am. Chem. Soc.* 134, 5040–5043. doi: 10.1021/ja211714w

Haneda, K., Yoshino, S., Ofuji, T., Miyake, T., and Nishizawa, M. (2012). Sheet-shaped biofuel cell constructed from enzyme-modified nanoengineered carbon fabric. *Electrochim. Acta* 82, 175–178. doi: 10.1016/j.electacta.2012.01.112

Hecht, H. J., Kalisz, H. M., Hendle, J., Schmid, R. D., and Schomburg, D. (1993). Crystal structure of glucose oxidase from aspergillus niger refined at 2.3 Å reslution. *J. Mol. Biol.* 229, 153–172. doi: 10.1006/jmbi.1993.1015

Herkendell, K., Stemmer, A., and Tel-Vered, R. (2019). Extending the operational lifetimes of all-direct electron transfer enzymatic biofuel cells by magnetically assembling and exchanging the active biocatalyst layers on stationary electrodes. *Nano Res.* 12, 767–775. doi: 10.1007/s12274-019-2285-z

Hibino, Y., Kawai, S., Kitazumi, Y., Shirai, O., and Kano, K. (2017). Construction of a protein-engineered variant of D -fructose dehydrogenase for direct electron transfer-type bioelectrocatalysis. *Electrochem. Commun.* 77, 112–115. doi: 10.1016/j.elecom.2017.03.005

Hitaishi, V. P., Clement, R., Bourassin, N., Baaden, M., de Poulpiquet, A., Sacquin-Mora, S., et al. (2018). Controlling redox enzyme orientation at planar electrodes. *Catalysts* 8, 1–38. doi: 10.3390/catal8050192

Holland, J. T., Lau, C., Brozik, S., Atanassov, P., and Banta, S. (2011). Engineering of glucose oxidase for direct electron transfer *via* site-specific gold nanoparticle conjugation. *J. Am. Chem. Soc.* 133, 19262–19265. doi: 10.1021/ja2071237

Hunger, H., Branch, L., and Perry, J. (1966). *Biochemical Fuel Cell*.

Hussein, L., Rubenwolf, S., von Stetten, F., Urban, G., Zengerle, R., Krueger, M., et al. (2011). A highly efficient buckypaper-based electrode material for mediatorless laccase-catalyzed dioxygen reduction. *Biosens. Bioelectron.* 26, 4133–4138. doi: 10.1016/j.bios.2011.04.008

Iijima, S. (1991). Helical microtubules of graphitic carbon. *Nature* 354, 56–58. doi: 10.1038/354056a0

Ji, J., Woo, J., Chung, Y., Joo, S. H., and Kwon, Y. (2020). Dual catalytic functions of biomimetic, atomically dispersed iron-nitrogen doped carbon catalysts for efficient enzymatic biofuel cells. *Chem. Eng. J.* 381:122679. doi: 10.1016/j.cej.2019.122679

Kaida, Y., Hibino, Y., Kitazumi, Y., Shirai, O., and Kano, K. (2019). Ultimate downsizing of D -fructose dehydrogenase for improving the performance of direct electron transfer-type bioelectrocatalysis. *Electrochem. Commun.* 98, 101–105. doi: 10.1016/j.elecom.2018.12.001

Kamitaka, Y., Tsujimura, S., Setoyama, N., Kajino, T., and Kano, K. (2007). Fructose/dioxygen biofuel cell based on direct electron transfer-type bioelectrocatalysis. *Phys. Chem. Chem. Phys.* 9, 1793–1801. doi: 10.1039/b617650j

Kang, S., Yoo, K. S., Chung, Y., and Kwon, Y. (2018). Cathodic biocatalyst consisting of laccase and gold nanoparticle for improving oxygen reduction reaction rate and enzymatic biofuel cell performance. *J. Ind. Eng. Chem.* 62, 329–332. doi: 10.1016/j.jiec.2018.01.011

Kang, Z., Jiao, K., Cheng, J., Peng, R., Jiao, S., and Hu, Z. (2018). A novel three-dimensional carbonized PANI 1600 @ CNTs network for enhanced enzymatic biofuel cell. *Biosens. Bioelectron.* 101, 60–65. doi: 10.1016/j.bios.2017.10.008

Kang, Z., Jiao, K., Xu, X., Peng, R., Jiao, S., and Hu, Z. (2017). Graphene oxide-supported carbon nanofiber-like network derived from polyaniline: a novel composite for enhanced glucose oxidase bioelectrode performance. *Biosens. Bioelectron.* 96, 367–372. doi: 10.1016/j.bios.2017.05.025

Kang, Z., Zhang, Y. P. J., and Zhu, Z. (2019). A shriveled rectangular carbon tube with the concave surface for high- performance enzymatic glucose/O_2 biofuel cells. *Biosens. Bioelectron.* 132, 76–83. doi: 10.1016/j.bios.2019.02.044

Karaśkiewicz, M., Nazaruk, E., Zelechowska, K., Biernat, J. F., and Rogalski, J., Bilewicz, R. (2012). Fully enzymatic mediatorless fuel cell with efficient naphthylated carbon nanotube – laccase composite cathodes. *Electrochem. Commun.* 20, 124–127. doi: 10.1016/j.elecom.2012.04.011

Kashyap, D., Kim, C., Kim, S. Y., Kim, Y. H., Kim, G. M., Dwivedi, P. K., et al. (2015). Multi walled carbon nanotube and polyaniline coated pencil graphite based bio-cathode for enzymatic biofuel cell. *Int. J. Hydrogen Energy* 40, 9515–9522. doi: 10.1016/j.ijhydene.2015.05.120

Kawai, S., Yakushi, T., Matsushita, K., Kitazumi, Y., Shirai, O., and Kano, K. (2014). The electron transfer pathway in direct electrochemical communication of fructose dehydrogenase with electrodes. *Electrochem. Commun.* 38, 28–31. doi: 10.1016/j.elecom.2013.10.024

Kim, H., Lee, I., Kwon, Y., Kim, B. C., Ha, S., Lee, J., et al. (2011). Immobilization of glucose oxidase into polyaniline nanofiber matrix for biofuel cell applications. *Biosens. Bioelectron.* 26, 3908–3913. doi: 10.1016/j.bios.2011.03.008

Kim, J., Kim, S. I., and Yoo, K. H. (2009). Polypyrrole nanowire-based enzymatic biofuel cells. *Biosens. Bioelectron.* 25, 350–355. doi: 10.1016/j.bios.2009.07.020

Kim, R. E., Hong, S. G., Ha, S., and Kim, J. (2014). Enzyme adsorption, precipitation and crosslinking of glucose oxidase and laccase on polyaniline nanofibers for highly stable enzymatic biofuel cells. *Enzyme Microb. Technol.* 66, 35–41. doi: 10.1016/j.enzmictec.2014.08.001

Kizling, M., Stolarczyk, K., Kiat, J. S. S., Tammela, P., Wang, Z., Nyholm, L., et al. (2015). Pseudocapacitive polypyrrole-nanocellulose composite for sugar-air enzymatic fuel cells. *Electrochem. Commun.* 50, 55–59. doi: 10.1016/j.elecom.2014.11.008

Kizling, M., Stolarczyk, K., Tammela, P., Wang, Z., Nyholm, L., Golimowski, J., et al. (2016). Bioelectrodes based on pseudocapacitive cellulose/polypyrrole composite improve performance of biofuel cell. *Bioelectrochemistry* 112, 184–190. doi: 10.1016/j.bioelechem.2016.01.004

Krikstolaityte, V., Lamberg, P., Toscano, M. D., Silow, M., Eicher-Lorka, O., Ramanavicius, A., et al. (2014). Mediatorless carbohydrate/oxygen biofuel cells with improved cellobiose dehydrogenase based bioanode. *Fuel Cells* 14, 792–800. doi: 10.1002/fuce.201400003

Kumar, R., Bhuvana, T., Mishra, G., and Sharma, A. (2016). A polyaniline wrapped aminated graphene composite on nickel foam as three-dimensional electrodes for enzymatic microfuel cells. *RSC Adv.* 6, 73496–73505. doi: 10.1039/C6RA08195A

Kuo, C. H., Huang, W. H., Lee, C. K., Liu, Y. C., Chang, C. M., Yang, H., et al. (2013). Biofuel cells composed by using glucose oxidase on chitosan coated carbon fiber cloth. *Int. J. Electrochem. Sci.* 8, 9242–9255.

Kwon, C. H., Ko, Y., Shin, D., Kwon, M., Park, J., Bae, W. K., et al. (2018). High-power hybrid biofuel cells using layer-by-layer assembled glucose oxidase-coated metallic cotton fibers. *Nat. Commun.* 9:5. doi: 10.1038/s41467-018-06994-5

Kwon, C. H., Ko, Y., Shin, D., Lee, S. W., and Cho, J. (2019). Highly conductive electrocatalytic gold nanoparticle-assembled carbon fiber electrode for high-performance glucose-based biofuel cells. *J. Mater. Chem. A* 7, 13495–13505. doi: 10.1039/C8TA12342J

Lalaoui, N., Holzinger, M., Le Goff, A., and Cosnier, S. (2016b). Diazonium functionalisation of carbon nanotubes for specific orientation of multicopper oxidases: controlling electron entry points and oxygen diffusion to the enzyme. *Chem. A Eur. J.* 22, 10494–10500. doi: 10.1002/chem.201601377

Lalaoui, N., Rousselot-Pailley, P., Robert, V., Mekmouche, Y., Villalonga, R., Holzinger, M., et al. (2016a). Direct electron transfer between a site-specific pyrene-modified laccase and carbon nanotube/gold nanoparticle supramolecular assemblies for bioelectrocatalytic dioxygen reduction. *ACS Catal.* 6, 1894–1900. doi: 10.1021/acscatal.5b02442

Lee, I., Loew, N., Tsugawa, W., Lin, C. E., Probst, D., La Belle, J. T., et al. (2018). The electrochemical behavior of a FAD dependent glucose dehydrogenase with direct electron transfer subunit by immobilization on self-assembled monolayers. *Bioelectrochemistry* 121, 1–6. doi: 10.1016/j.bioelechem.2017.12.008

Linko, V., Eerikäinen, M., and Kostiainen, M. A. (2015). A modular DNA origami-based enzyme cascade nanoreactor. *Chem. Commun.* 51, 5351–5354. doi: 10.1039/C4CC08472A

Liu, C., Chen, Z., and Li, C. Z. (2011). Surface engineering of graphene-enzyme nanocomposites for miniaturized biofuel cell. *IEEE Trans. Nanotechnol.* 10, 59–62. doi: 10.1109/TNANO.2010.2050147

Liu, X., Tao, H., Yang, K., Zhang, S., Lee, S. T., and Liu, Z. (2011). Optimization of surface chemistry on single-walled carbon nanotubes for *in vivo* photothermal ablation of tumors. *Biomaterials* 32, 144–151. doi: 10.1016/j.biomaterials.2010.08.096

Liu, Y., Zhang, J., Cheng, Y., and Jiang, S. P. (2018). Effect of carbon nanotubes on direct electron transfer and electrocatalytic activity of immobilized glucose oxidase. *ACS Omega* 3, 667–676. doi: 10.1021/acsomega.7b01633

Lopez, F., Siepenkoetter, T., Xiao, X., Magner, E., Schuhmann, W., and Salaj-Kosla, U. (2018). Potential pulse-assisted immobilization of myrothecium verrucaria bilirubin oxidase at planar and nanoporous gold electrodes. *J. Electroanal. Chem.* 812, 194–198. doi: 10.1016/j.jelechem.2017.12.023

Luong, J. H. T., Glennon, J. D., Gedanken, A., and Vashist, S. K. (2017). Achievement and assessment of direct electron transfer of glucose oxidase in electrochemical biosensing using carbon nanotubes, graphene, and their nanocomposites. *Microchim. Acta* 184, 369–388. doi: 10.1007/s00604-016-2049-3

Ma, S., Laurent, C. V. F. P., Meneghello, M., Tuoriniemi, J., Oostenbrink, C., Gorton, L., et al. (2019). Direct electron-transfer anisotropy of a site-specifically immobilized cellobiose dehydrogenase. *ACS Catal.* 9, 7607–7615. doi: 10.1021/acscatal.9b02014

MacVittie, K., Halámek, J., Halámková, L., Southcott, M., Jemison, W. D., Lobel, R., et al. (2013). From "Cyborg" lobsters to a pacemaker powered by implantable biofuel cells. *Energy Environ. Sci.* 6, 81–86. doi: 10.1039/C2EE23209J

Maleki, N., Kashanian, S., Nazari, M., and Shahabadi, N. (2019). A novel and enhanced membrane-free performance of glucose/O_2 biofuel cell, integrated with biocompatible laccase nanoflower biocathode and glucose. *IEEE Sens. J.* 19, 11988–11994. doi: 10.1109/JSEN.2019.2937814

Mani, P., Kumar, V. T. F., Keshavarz, T., Sainathan Chandra, T., and Kyazze, G. (2018). The role of natural laccase redox mediators in simultaneous dye decolorization and power production in microbial fuel cells. *Energies* 11, 1–12. doi: 10.3390/en11123455

Mano, N., Mao, F., and Heller, A. (2003). Characteristics of a miniature compartment-less glucose-O_2 biofuel cell and its operation in a living plant. *J. Am. Chem. Soc.* 125, 6588–6594. doi: 10.1021/ja0346328

Mano, N., Mao, F., and Heller, A. (2004). A miniature membrane-less biofuel cell operating at +0.60 V under physiological conditions. *ChemBioChem* 5, 1703–1705. doi: 10.1002/cbic.200400275

Mazurenko, I., Clément, R., Byrne-Kodjabachian, D., de Poulpiquet, A., Tsujimura, S., and Lojou, E. (2018). Pore size effect of MgO-templated carbon on enzymatic H_2 oxidation by the hyperthermophilic hydrogenase from aquifex aeolicus. *J. Electroanal. Chem.* 812, 221–226. doi: 10.1016/j.jelechem.2017.12.041

Mazurenko, I., Monsalve, K., Infossi, P., Giudici-Orticoni, M. T., Topin, F., Mano, N., et al. (2017b). Impact of substrate diffusion and enzyme distribution in 3D-porous electrodes: a combined electrochemical and modelling study of a thermostable H_2/O_2 enzymatic fuel cell. *Energy Environ. Sci.* 10, 1966–1982. doi: 10.1039/C7EE01830D

Mazurenko, I., Wang, X., De Poulpiquet, A., and Lojou, E. (2017a). H_2/O_2 enzymatic fuel cells: from proof-of-concept to powerful devices. *Sustain. Energy Fuels* 1, 1475–1501. doi: 10.1039/C7SE00180K

Meredith, M. T., Minson, M., Hickey, D., Artyushkova, K., Glatzhofer, D. T., and Minteer, S. D. (2011). Anthracene-modified multi-walled carbon nanotubes as direct electron transfer scaffolds for enzymatic oxygen reduction. *ACS Catal.* 1, 1683–1690. doi: 10.1021/cs200475q

Milton, R. D., Lim, K., Hickey, D. P., and Minteer, S. D. (2015). Employing FAD-dependent glucose dehydrogenase within a glucose/oxygen enzymatic fuel cell operating in human serum. *Bioelectrochemistry* 106, 56–63. doi: 10.1016/j.bioelechem.2015.04.005

Min, K., Ryu, J. H., and Yoo, Y. J. (2010). Mediator-free glucose/O_2 biofuel cell based on a 3-dimensional glucose oxidase/swnt/polypyrrole composite electrode. *Biotechnol. Bioprocess Eng.* 15, 371–375. doi: 10.1007/s12257-009-3034-z

Mishra, P., Lakshmi, G. B. V. S., Mishra, S., Avasthi, D. K., Swart, H. C., Turner, A. P. F., et al. (2017). Electrocatalytic biofuel cell based on highly efficient metal-polymer nano-architectured bioelectrodes. *Nano Energy* 39, 601–607. doi: 10.1016/j.nanoen.2017.06.023

Miyake, T., Haneda, K., Nagai, N., Yatagawa, Y., Onami, H., Yoshino, S., et al. (2011). Enzymatic biofuel cells designed for direct power generation from biofluids in living organisms. *Energy Environ. Sci.* 4, 5008–5012. doi: 10.1039/c1ee02200h

Monsalve, K., Roger, M., Gutierrez-Sanchez, C., Ilbert, M., Nitsche, S., Byrne-Kodjabachian, D., et al. (2015). Hydrogen bioelectrooxidation on gold nanoparticle-based electrodes modified by aquifex aeolicus hydrogenase: application to hydrogen/oxygen enzymatic biofuel cells. *Bioelectrochemistry* 106, 47–55. doi: 10.1016/j.bioelechem.2015.04.010

Moser, C. C., Keske, J. M., Warncke, K., Farid, R. S., and Dutton, P. L. (1992). Nature of biological electron transfer. *Nature* 355, 796–802. doi: 10.1038/355796a0

Muguruma, H., Iwasa, H., Hidaka, H., Hiratsuka, A., and Uzawa, H. (2017). Mediatorless direct electron transfer between flavin adenine dinucleotide-dependent glucose dehydrogenase and single-walled carbon nanotubes. *ACS Catal.* 7, 725–734. doi: 10.1021/acscatal.6b02470

Müller, J., and Niemeyer, C. M. (2008). DNA-directed assembly of artificial multienzyme complexes. *Biochem. Biophys. Res. Commun.* 377, 62–67. doi: 10.1016/j.bbrc.2008.09.078

Naruse, J., Hoa, L. Q., Sugano, Y., Ikeuchi, T., Yoshikawa, H., Saito, M., et al. (2011). Development of biofuel cells based on gold nanoparticle decorated multi-walled carbon nanotubes. *Biosens. Bioelectron.* 30, 204–210. doi: 10.1016/j.bios.2011.09.012

Narváez Villarrubia, C. W., Lau, C., Ciniciato, G. P. M. K., Garcia, S. O., Sibbett, S. S., Petsev, D. N., et al. (2014). Practical electricity generation from a paper based biofuel cell powered by glucose in ubiquitous liquids. *Electrochem. Commun.* 45, 44–47. doi: 10.1016/j.elecom.2014.05.010

Navaee, A., and Salimi, A. (2018). FAD-based glucose dehydrogenase immobilized on thionine/AuNPs frameworks grafted on amino-CNTs: development of high power glucose biofuel cell and biosensor. *J. Electroanal. Chem.* 815, 105–113. doi: 10.1016/j.jelechem.2018.02.064

Ortiz, R., Matsumura, H., Tasca, F., Zahma, K., Samejima, M., Igarashi, K., et al. (2012). Effect of deglycosylation of cellobiose dehydrogenases on the enhancement of direct electron transfer with electrodes. *Anal. Chem.* 5, 10315–10323. doi: 10.1021/ac3022899

Pankratov, D., Sundberg, R., Sotres, J., Maximov, I., Graczyk, M., Suyatin, D. B., et al. (2015). Transparent and flexible, nanostructured and mediatorless glucose/oxygen enzymatic fuel cells. *J. Power Sources* 294, 501–506. doi: 10.1016/j.jpowsour.2015.06.041

Prévoteau, A., Courjean, O., and Mano, N. (2010). Deglycosylation of glucose oxidase to improve biosensors and biofuel cells. *Electrochem. Commun.* 12, 213–215. doi: 10.1016/j.elecom.2009.11.027

Ratautas, D., Laurynenas, A., Dagys, M., Marcinkevičiene, L., Meškys, R., and Kulys, J. (2016). High current, low redox potential mediatorless bioanode based on gold nanoparticles and glucose dehydrogenase from Ewingella Americana. *Electrochim. Acta* 199, 254–260. doi: 10.1016/j.electacta.2016.03.087

Reid, R. C., Minteer, S. D., and Gale, B. K. (2015). Contact lens biofuel cell tested in a synthetic tear solution. *Biosens. Bioelectron.* 68, 142–148. doi: 10.1016/j.bios.2014.12.034

Rong, Y., Malpass-Evans, R., Carta, M., Mckeown, N. B., Attard, G. A., and Marken, F. (2014). Intrinsically porous polymer protects catalytic gold particles for enzymeless glucose oxidation. *Electroanalysis* 26, 904–909. doi: 10.1002/elan.201400085

Ruff, A., Szczesny, J., Markovic, N., Conzuelo, F., Zacarias, S., Pereira, I. A. C., et al. (2018). A fully protected hydrogenase/polymer-based bioanode for high-performance hydrogen/glucose biofuel cells. *Nat. Commun.* 9:3675. doi: 10.1038/s41467-018-06106-3

Sakai, K., Xia, H., Kitazumi, Y., Shirai, O., and Kano, K. (2018). Assembly of direct-electron-transfer-type bioelectrodes with high performance. *Electrochim. Acta* 271, 305–311. doi: 10.1016/j.electacta.2018.03.163

Salaj-kosla, U., Pöller, S., Beyl, Y., Scanlon, M. D., Beloshapkin, S., Shleev, S., et al. (2012). Direct electron transfer of bilirubin oxidase (Myrothecium Verrucaria) at an unmodified nanoporous gold biocathode. *Electrochem. Commun.* 16, 92–95. doi: 10.1016/j.elecom.2011.12.007

Saleh, F. S., Mao, L., and Ohsaka, T. (2011). Development of a dehydrogenase-based glucose anode using a molecular assembly composed of nile blue and functionalized SWCNTs and its applications to a glucose sensor and glucose/O_2 biofuel cell. *Sensors Actuat. B Chem.* 152, 130–135. doi: 10.1016/j.snb.2010.07.054

Sales, F. C. P. F., Iost, R. M., Martins, M. V. A., Almeida, M. C., and Crespilho, F. N. (2013). An intravenous implantable glucose/dioxygen biofuel cell with modified flexible carbon fiber electrodes. *Lab Chip* 13, 468–474. doi: 10.1039/C2LC41007A

Sapountzi, E., Braiek, M., Vocanson, F., Chateaux, J. F., Jaffrezic-Renault, N., and Lagarde, F. (2017). Gold nanoparticles assembly on electrospun poly(vinyl alcohol)/poly(ethyleneimine)/glucose oxidase nanofibers for ultrasensitive electrochemical glucose biosensing. *Sensors Actuat. B Chem.* 238, 392–401. doi: 10.1016/j.snb.2016.07.062

Scherbahn, V., Putze, M. T., Dietzel, B., Heinlein, T., Schneider, J. J., and Lisdat, F. (2014). Biofuel cells based on direct enzyme-electrode contacts using PQQ-dependent glucose dehydrogenase/bilirubin oxidase and modified carbon nanotube materials. *Biosens. Bioelectron.* 61, 631–638. doi: 10.1016/j.bios.2014.05.027

Schubart, I. W., Göbel, G., and Lisdat, F. (2012). A pyrroloquinolinequinone-dependent glucose dehydrogenase (PQQ-GDH)-electrode with direct electron transfer based on polyaniline modified carbon nanotubes for biofuel cell application. *Electrochim. Acta* 82, 224–232. doi: 10.1016/j.electacta.2012.03.128

Selloum, D., Tingry, S., Techer, V., Renaud, L., Innocent, C., and Zouaoui, A. (2014). Optimized electrode arrangement and activation of bioelectrodes activity by carbon nanoparticles for efficient ethanol microfluidic biofuel cells. *J. Power Sources* 269, 834–840. doi: 10.1016/j.jpowsour.2014.07.052

Shleev, S., Andoralov, V., Pankratov, D., Falk, M., Aleksejeva, O., and Blum, Z. (2016). Oxygen electroreduction vs. bioelectroreduction: direct electron transfer approach. *Electroanalysis* 28, 2270–2287. doi: 10.1002/elan.201600280

Singh, M., Nolan, H., Tabrizian, M., and Cosnier, S. (2020). Functionalization of contacted carbon nanotube forests by dip coating for high-performance biocathodes. *ChemElectroChem* 7, 4685–4689. doi: 10.1002/celc.202001334

Song, Y., Chen, C., and Wang, C. (2015). Graphene/enzyme-encrusted three-dimensional carbon micropillar arrays for mediatorless micro-biofuel cells. *Nanoscale* 7, 7084–7090. doi: 10.1039/C4NR06856D

Spadiut, O., Pisanelli, I., Maischberger, T., Peterbauer, C., Gorton, L., Chaiyen, P., et al. (2009). Engineering of pyranose 2-oxidase: improvement for biofuel cell and food applications through semi-rational protein design. *J. Biotechnol.* 139, 250–257. doi: 10.1016/j.jbiotec.2008.11.004

Strack, G., Luckarift, H. R., Sizemore, S. R., Nichols, R. K., Farrington, K. E., Wu, P. K., et al. (2013). Power generation from a hybrid biological fuel cell in seawater. *Bioresour. Technol.* 128, 222–228. doi: 10.1016/j.biortech.2012.10.104

Sugimoto, Y., Kitazumi, Y., Shirai, O., and Kano, K. (2017). Effects of mesoporous structures on direct electron transfer-type bioelectrocatalysis: facts and simulation on a three-dimensional model of random orientation of enzymes. *Electrochemistry* 85, 82–87. doi: 10.5796/electrochemistry.85.82

Sugimoto, Y., Kitazumi, Y., Tsujimura, S., Shirai, O., Yamamoto, M., and Kano, K. (2015). Electrostatic interaction between an enzyme and electrodes in the electric double layer examined in a view of direct electron transfer-type bioelectrocatalysis. *Biosens. Bioelectron.* 63, 138–144. doi: 10.1016/j.bios.2014.07.025

Sugimoto, Y., Takeuchi, R., Kitazumi, Y., Shirai, O., and Kano, K. (2016). Significance of mesoporous electrodes for noncatalytic faradaic process of randomly oriented redox proteins. *J. Phys. Chem. C* 120, 26270–26277. doi: 10.1021/acs.jpcc.6b07413

Sun, Q., and Chen, W. (2016). HaloTag mediated artificial cellulosome assembly on a rolling circle amplification DNA template for efficient cellulose hydrolysis. *Chem. Commun.* 52, 6701–6704. doi: 10.1039/C6CC02035F

Szczupak, A., Halámek, J., Halámková, L., Bocharova, V., Alfonta, L., and Katz, E. (2012). Living battery - biofuel cells operating *in vivo* in clams. *Energy Environ. Sci.* 5, 8891–8895. doi: 10.1039/c2ee21626d

Takahashi, Y., Kitazumi, Y., Shirai, O., and Kano, K. (2019b). Improved direct electron transfer-type bioelectrocatalysis of bilirubin oxidase using thiol-modified gold nanoparticles on mesoporous carbon electrode. *J. Electroanal. Chem.* 832, 158–164. doi: 10.1016/j.jelechem.2018.10.048

Takahashi, Y., Wanibuchi, M., Kitazumi, Y., Shirai, O., and Kano, K. (2019a). Improved direct electron transfer-type bioelectrocatalysis of bilirubin oxidase using porous gold electrodes. *J. Electroanal. Chem.* 843, 47–53. doi: 10.1016/j.jelechem.2019.05.007

Tasca, F., Farias, D., Castro, C., and Acuna-rougier, C. (2015). Bilirubin oxidase from myrothecium verrucaria physically absorbed on graphite electrodes. Insights into the alternative resting form and the sources of activity loss. *PLoS ONE* 2015:132181. doi: 10.1371/journal.pone.0132181

Tasca, F., Harreither, W., Ludwig, R., Gooding, J. J., and Gorton, L. (2011). Cellobiose dehydrogenase aryl diazonium modified single walled carbon nanotubes: enhanced direct electron transfer through a positively charged surface. *Anal. Chem.* 83, 3042–3049. doi: 10.1021/ac103250b

Tasca, F., Ludwig, R., Gorton, L., and Antiochia, R. (2013). Determination of lactose by a novel third generation biosensor based on a cellobiose dehydrogenase and aryl diazonium modified single wall carbon nanotubes electrode. *Sensors Actuat. B. Chem.* 177, 64–69. doi: 10.1016/j.snb.2012.10.114

Tasca, F., Tortolini, C., Bollella, P., and Antiochia, R. (2019). Microneedle-based electrochemical devices for transdermal biosensing : a review. *Curr. Opin. Electrochem.* 16, 42–49. doi: 10.1016/j.coelec.2019.04.003

Tavahodi, M., Ortiz, R., Schulz, C., Ekhtiari, A., Ludwig, R., Haghighi, B., et al. (2017). Direct electron transfer of cellobiose dehydrogenase on positively charged polyethyleneimine gold nanoparticles. *Chempluschem* 82, 546–552. doi: 10.1002/cplu.201600453

Torrinha, Á., Jiyane, N., Sabela, M., Bisetty, K., Montenegro, M. C. B. S. M., and Araújo, A. N. (2020). Nanostructured pencil graphite electrodes for application as high power biocathodes in miniaturized biofuel cells and bio-batteries. *Sci. Rep.* 10:7. doi: 10.1038/s41598-020-73635-7

Umaña, M., and Waller, J. (1986). Protein-modified electrodes. The glucose oxidase/polypyrrole system. *Anal. Chem.* 58, 2979–2983. doi: 10.1021/ac00127a018

Wang, S. C., Patlolla, A., and Iqbai, Z. (2009b). Carbon nanotube-based, membrane-less and mediator-free enzymatic biofuel cells. *ECS* 19, 55–60. doi: 10.1149/1.3236794

Wang, S. C., Yang, F., Silva, M., Zarow, A., Wang, Y., and Iqbal, Z. (2009a). Membrane-less and mediator-free enzymatic biofuel cell using carbon nanotube/porous silicon electrodes. *Electrochem. Commun.* 11, 34–37. doi: 10.1016/j.elecom.2008.10.019

Wang, X., Falk, M., Ortiz, R., Matsumura, H., Bobacka, J., Ludwig, R., et al. (2012). Mediatorless sugar/oxygen enzymatic fuel cells based on gold nanoparticle-modified electrodes. *Biosens. Bioelectron.* 31, 219–225. doi: 10.1016/j.bios.2011.10.020

Wei, W., Li, P., Li, Y., Cao, X., and Liu, S. (2012). Nitrogen-doped carbon nanotubes enhanced laccase enzymatic reactivity towards oxygen reduction and its application in biofuel cell. *Electrochem. Commun.* 22, 181–184. doi: 10.1016/j.elecom.2012.06.021

Wilner, O. I., Shimron, S., Weizmann, Y., Wang, Z. G., and Willner, I. (2009). Self-assembly of enzymes on DNA scaffolds: en route to biocatalytic cascades and the synthesis of metallic nanowires. *Nano Lett.* 9, 2040–2043. doi: 10.1021/nl900302z

Wilson, G. S. (2016). Native glucose oxidase does not undergo direct electron transfer. *Biosens. Bioelectr.* 83, vii–viii. doi: 10.1016/j.bios.2016.04.083

Wu, X. E., Guo, Y. Z., Chen, M. Y., and Chen, X. D. (2013). Fabrication of flexible and disposable enzymatic biofuel cells. *Electrochim. Acta* 98, 20–24. doi: 10.1016/j.electacta.2013.03.024

Xia, H., Kitazumi, Y., Shirai, O., Ozawa, H., Onizuka, M., Komukai, T., et al. (2017). Factors affecting the interaction between carbon nanotubes and redox enzymes in direct electron transfer-type bioelectrocatalysis. *Bioelectrochemistry* 118, 70–74. doi: 10.1016/j.bioelechem.2017.07.003

Xia, H.-q., Kitazumi, Y., Shirai, O., and Kano, K. (2016b). Enhanced direct electron transfer-type bioelectrocatalysis of bilirubin oxidase on negatively charged

aromatic compound-modified carbon electrode. *J. Electroanal. Chem.* 763, 104–109. doi: 10.1016/j.jelechem.2015.12.043

Xia, H.-q., So, K., Kitazumi, Y., Shirai, O., Nishikawa, K., Higuchi, Y., et al. (2016a). Dual gas-diffusion membrane- and mediatorless dihydrogen/air-breathing biofuel cell operating at room temperature. *J. Power Sources* 335, 105–112. doi: 10.1016/j.jpowsour.2016.10.030

Xia, L., Van Nguyen, K., Holade, Y., Han, H., Dooley, K., Atanassov, P., et al. (2017). Improving the performance of methanol biofuel cells utilizing an enzyme cascade bioanode with DNA-bridged substrate channeling. *ACS Energy Lett.* 2, 1435–1438. doi: 10.1021/acsenergylett.7b00134

Xu, S., and Minteer, S. D. (2012). Enzymatic biofuel cell for oxidation of glucose to CO_2. *ACS Catal.* 2, 91–94. doi: 10.1021/cs200523s

Yahiro, A. T., Lee, S. M., and Kimble, D. O. (1964). Bioelectrochemistry. I. Enzyme utilizing bio-fuel cell studies. *BBA* 88, 375–383. doi: 10.1016/0926-6577(64)90192-5

Yan, L., Zhao, F., Li, S., Hu, Z., and Zhao, Y. (2011). Low-toxic and safe nanomaterials by surface-chemical design, carbon nanotubes, fullerenes, metallofullerenes, and graphenes. *Nanoscale* 3, 362–382. doi: 10.1039/C0NR00647E

Yan, X., Chen, J., Yang, J., Xue, Q., and Miele, P. (2010). Fabrication of free-standing, electrochemically active, and biocompatible graphene oxide-polyaniline and graphene-polyaniline hybrid papers. *ACS Appl. Mater. Interfaces* 2, 2521–2529. doi: 10.1021/am100293r

Zebda, A., Cosnier, S., Alcaraz, J. P., Holzinger, M., Le Goff, A., Gondran, C., et al. (2013). Single glucose biofuel cells implanted in rats power electronic devices. *Sci. Rep.* 3, 1–5. doi: 10.1038/srep01516

Zebda, A., Gondran, C., Le Goff, A., Holzinger, M., Cinquin, P., and Cosnier, S. X. (2011). Mediatorless high-power glucose biofuel cells based on compressed carbon nanotube-enzyme electrodes. *Nat. Commun.* 2:1365. doi: 10.1038/ncomms1365

Zeng, T., Pankratov, D., Falk, M., Leimkühler, S., Shleev, S., and Wollenberger, U. (2015). Miniature direct electron transfer based sulphite/oxygen enzymatic fuel cells. *Biosens. Bioelectron.* 66, 39–42. doi: 10.1016/j.bios.2014.10.080

Zhao, Z., Fu, J., Dhakal, S., Johnson-Buck, A., Liu, M., Zhang, T., et al. (2016). Nanocaged enzymes with enhanced catalytic activity and increased stability against protease digestion. *Nat. Commun.* 7:10619. doi: 10.1038/ncomms10619

Conflict of Interest: The authors declare that the research was conducted in the absence of any commercial or financial relationships that could be construed as a potential conflict of interest.

Advantages of publishing in Frontiers

OPEN ACCESS
Articles are free to read for greatest visibility and readership

FAST PUBLICATION
Around 90 days from submission to decision

HIGH QUALITY PEER-REVIEW
Rigorous, collaborative, and constructive peer-review

TRANSPARENT PEER-REVIEW
Editors and reviewers acknowledged by name on published articles

Frontiers
Avenue du Tribunal-Fédéral 34
1005 Lausanne | Switzerland

Visit us: www.frontiersin.org
Contact us: frontiersin.org/about/contact

REPRODUCIBILITY OF RESEARCH
Support open data and methods to enhance research reproducibility

DIGITAL PUBLISHING
Articles designed for optimal readership across devices

FOLLOW US
@frontiersin

IMPACT METRICS
Advanced article metrics track visibility across digital media

EXTENSIVE PROMOTION
Marketing and promotion of impactful research

LOOP RESEARCH NETWORK
Our network increases your article's readership